UNIVERSITÀ DI SIENA 1240

Department of Molecular and Developmental Medicine

PhD program in Molecular Medicine

XXXVI° Cycle

Coordinator: Prof. Vincenzo Sorrentino, PhD

Oxidative and bioenergetic balance as key determinants of neural viability in the retina: insights from retinal neurodegenerative diseases

Scientific disciplinary sector: Physiology (BIO/09)

PhD CANDIDATE

Alessio Canovai

Department of Biology, University of Pisa

Firmato digitalmente dal candidato

Alessio Canovai Firmato il 17-05-2024

Supervisor

Prof. Massimo Dal Monte, PhD

Department of Biology, University of Pisa

Co-supervisor

Prof. Maurizio Cammalleri, PhD

Department of Biology, University of Pisa

Academic year

2022/2023

Università degli Studi di Siena
Dottorato in Medicina Molecolare
XXXVI° Ciclo

Data dell'esame finale
30/05/2024

Commissione giudicatrice
Prof.ssa Daniela Rossi
Dr.ssa Marianna Vitiello
Dr.ssa Elena Sticchi

Supplenti
Dr. Rosario Amato

Index

List of abbreviations

4-HNE 4-hydroxynonenal
8-OH-dG 8-hydroxy-deoxyguanosine
AGE Advanced glycation end products
AMD Age-related macular degeneration
AMP Adenosine monophosphate
ANOVA Analysis of variance
ARE Antioxidant response element
ATP Adenosine triphosphate
ATP5a1 ATP synthase F1 subunit alpha
BDNF Brain-derived neurotrophic factor
BRB Blood retinal barrier
BSA Bovine serum albumin
C3G Cyanidin-3-glucoside
cGMP Cyclic GMP
CNS Central nervous system
CoQ Coenzyme Q
DAPI 4′, 6-diamidino-2-phenylindole
DCF Dichlorofluorescein
DCFH Dichlorodihydrofluorescein
DCFH-DA 2′,7′-dichlorodihydrofluorescein diacetate
DEV Days ex vivo
DME Diabetic macular edema
DMSO Dimethyl sulfoxide
DR Diabetic retinopathy
ERG Electroretinogram
ETC Electron transport chain
FAD Flavin adenine dinucleotide
$FADH_2$ Flavin adenine dinucleotide + hydrogen
FDR False discovery rate
FMN Flavin mononucleotide
GDP Guanosine diphosphate
GFAP Glial fibrillary acidic protein
GFP Green fluorescent protein
GMO Genetically modified organism
GSH Glutathione
GTP Guanosine triphosphate
HBSS Hank's balanced salt solution
HC Hierarchical clustering
HIF-1 Hypoxia inducible factor-1
HO-1 Heme oxygenase-1
HRE Hypoxia response element
IL Interleukin
INL Inner nuclear layer
IOP Intraocular pressure
IPL Inner plexiform layer
IS Inner segment
KEGG Kyoto Encyclopedia of Genes and Genomes
LD Light damage
MCE Methylcellulose
MDA Malondialdehyde
mt-CO Mitochondrially Encoded Cytochrome C Oxidase
mtDNA Mitochondrial DNA
NAD Nicotinamide adenine dinucleotide
NADH Nicotinamide adenine dinucleotide + hydrogen
NDUFB8 NADH:Ubiquinone Oxidoreductase Subunit B8
NF-kB Nuclear factor kappa-light-chain-enhancer of activated B cells
NFL Nerve fiber layer
NGF Nerve growth factor
NPDR Non-proliferative diabetic retinopathy
Nrf2 Nuclear factor erythroid 2-related factor 2
NVU Neurovascular unit
OD Optical density
ON Optic nerve
ONH Optic nerve head
ONL Outer nuclear layer
OPL Outer plexiform layer
OS Outer segment
OXPHOS Oxidative phosphorylation
PBS Phosphate-buffered saline
PCA Principal component analysis
PDR Proliferative diabetic retinopathy
PERG Pattern ERG
PFA Paraformaldehyde
PGC-1α Proliferator-activated receptor-gamma coactivator alpha
PhNR Photopic negative response
PKC Protein kinase C
PQQ Pyrroloquinoline quinone
QC Quality control
RA Rosmarinic acid
RBPMS RNA-binding protein with multiple splicing
RGC Retinal ganglion cell
RIPA Radioimmuneprecipitation assay
ROS Reactive oxygen species
RP Retinitis pigmentosa
RPE Retinal pigment epithelium
SD Standard deviation
SDHB Succinate dehydrogenase complex iron sulfur subunit B
SEM Standard error of the mean
SPE Spearmint extract
STZ Streptozotocin
TBS Tris-buffered saline
TCA Tricarboxylic acid
TFAM Mitochondrial transcription factor A
UQCRC2 Ubiquinol-cytochrome c reductase core protein 2
VEGF Vascular endothelial growth factor
YFP Yellow fluorescent protein
ZO-1 Zonula occludens-1

Abstract of the thesis

The study of the mechanisms regulating retinal neuron viability can unravel the role of key determinants for neuronal survival potentially suitable as therapeutic targets. The elevated metabolism of the retina may increase retinal neuron susceptibility to metabolic stressors, which can damage retinal cells by altering mitochondrial activity and unbalancing the bioenergetic and oxidative status. Many studies have reported an early dysregulation of bioenergetic and oxidative mechanisms prior to cell death in the pathogenesis of many retinal neurodegenerative disorders induced by different type of stressors, suggesting the key role of the maintenance of metabolic and oxidative processes as a general mechanism for retinal survival and a potential target for new therapies. Therefore, this thesis is focused on providing further insights into the role of the bioenergetic and oxidative balance as determinants of retinal neuron viability and suggesting possible novel non-invasive approaches for neuroprotection in different retinal disorders. In particular, the effects of a positive modulation of cell bioenergetic and oxidative status have been assessed in models of retinal neurodegenerative diseases by the non-invasive administration of natural antioxidant and ATP-boosting molecules. In particular, the effects of a positive modulation in the oxidative balance by the dietary administration of an antioxidant compound including cyanidin-3-glucoside (C3G), verbascoside and zinc, was first tested in a model of streptozotocin (STZ)-induced diabetic retinopathy (DR), where oxidative stress occurs as a result of a hyperactivated mitochondrial activity promoted by hyperglycemia. In this model, the counteraction of the oxidative stress and its related inflammation by the compound was effective in reducing the hyperglycemia-induced vascular and neuronal alterations, including BRB dysfunction, retinal cell degeneration and visual loss. Thus, these findings demonstrate the beneficial regulation of oxidative balance in counteracting the high glucose-induced neurovascular alterations, suggesting novel molecules for the treatment of DR. Oxidative stress can also result from mitochondrial hypoactivity, as occurs under light damage (LD). Since the oxidative stress is a shared pathological event both in LD and DR, a similar antioxidant strategy and similar molecules used in the STZ model were used to test the beneficial effects of the oxidative stress counteraction in a model of LD. In particular, the dietary supplementation of antioxidant molecules, including lutein and C3G, administered either alone or in combination, prevented the LD-driven oxidative stress and inflammation, protecting photoreceptors from degeneration and functional impairment. In addition, the protective efficacy of lutein and C3G was also confirmed in a more complex antioxidant multicomponent formula with verbascoside and zinc, confirming the potential of these molecules as novel treatment option for the oxidative stress-related retinal disorders. Considering that an antioxidant strategy was effective in reducing retinal cell degeneration under reduced mitochondrial activity promoted by LD, it was investigated whether the modulation of the oxidative balance was sufficient to counteract the impairment of retinal cell viability in a multifactorial context. In this respect, glaucoma was used as a model of multifactorial disease, representing a retinal ganglion cell (RGC) specific disorder where metabolic disturbances and reduced mitochondrial activity concur with other pathophysiological events to determine RGC degeneration. The efficacy of antioxidant molecules included in the spearmint extract (SPE) was investigated in a model of methylcellulose (MCE)-induced glaucoma, where the elevated intraocular pressure (IOP) reproduces a glaucomatous stress. The administration of SPE in this model resulted in a dose-dependent improvement of RGC activity, density and trophism, showing an antioxidant and anti-inflammatory effect evidenced by the reduction of oxidative stress- and inflammation-related markers, together with an increase in the retinal antioxidant defense. These findings demonstrate the capacity of SPE to counteract glaucoma-related oxidative stress and improve RGC viability and function, thus suggesting a novel complementary strategy for the management of the disease. The protective effect associated with the positive regulation of RGC redox balance under glaucomatous stress suggested the potential to target the upstream mitochondrial and metabolic mechanisms to

improve RGC viability under metabolic stress. RGCs were therefore used as a model to investigate whether the positive improvement of cell bioenergetics improves RGC health under metabolic stress by using pyrroloquinoline quinone (PQQ), which has been identified as a metabolic regulator in non-neuronal systems. The metabolic capacity of PQQ was confirmed in a retinal context by assessing the increase in ATP production in *in vitro* and *in vivo* RGC-related tissues. Moreover, the administration of PQQ was associated with moderate influence on molecular and morphological changes in RGC mitochondria and altered metabolic profile of RGC-related tissues, suggesting possible mechanisms by which PQQ may exert its metabolic effect. Given its ATP-boosting activity, the neuroprotective efficacy of PQQ was investigated in different models of RGC stress where bioenergetic capacity has been compromised. PQQ neuroprotection was first tested in an *ex vivo* model of retinal axotomy, where the administration of PQQ partially prevented the RGC loss observed in this model. In addition, the neuroprotective properties of PQQ have been confirmed in an *in vivo* model of rotenone-induced RGC degeneration, where the treatment with PQQ prevented RGC death. Therefore, PQQ may be used as a novel compound providing bioenergetic support to improve RGC resiliency under metabolic stress. Taken together, the data reported in this thesis provide further insights on the role of the bioenergetic and oxidative balance as determinants of retinal neuron viability and suggest possible novel non-invasive complementary approaches for neuroprotection in different retinal disorders.

Chapter 1

Introduction

The retina is the organ involved in light perception and it needs a constant and regulated functionality to guarantee its role in vision. Many different cellular mechanisms concur together to preserve the physiological processes involved in the maintenance of efficient retinal function. In this context, a balanced metabolism is fundamental to provide bioenergetic support to retinal cells for their functioning and survival.

1.1 Retinal metabolism

The retina has a highly activate metabolism and it is probably one of the most demanding structures in the central nervous system (CNS). Being involved in visual processing, the retina has a huge energy demand since retinal cells consume a vast amount of ATP to efficiently sustain the cell processes mediating the light perception. The replenishment of the consumed ATP in retinal cells is guaranteed by a proper balanced ATP synthesis through finely regulated metabolic pathways, together with a constant supply of nutrients and oxygen (O_2) as metabolic substrates. In this context, the mitochondrial oxidative phosphorylation (OXPHOS) provides an enormous contribution in producing ATP in retinal neurons, giving its high yield of ATP compared to other metabolic processes (Casson et al., 2021). In the OXPHOS, reduced cofactors, such as NADH and $FADH_2$, are re-oxidized by the controlled transfer of electrons through several redox reactions across the electron transport chain (ETC), made by different electron acceptors organized in macromolecular complexes (C) and situated in the mitochondrial inner membrane (Zhao et al., 2019). At the end of the ETC, O_2 acts as the final electron acceptor that is finally converted into H_2O in the mitochondrial matrix. The electron transfer through the ETC, in particular at CI, CIII and CIV, favors the movement of protons into the intermembrane space, creating an electrochemical gradient, known also as mitochondrial membrane potential ($\Delta\Psi$). This gradient is then dissipated by the re-entering of protons into the matrix through the ATP synthase (also known as CV), which couples the passage of protons to the synthesis of ATP (Zhao et al., 2019). Since the OXPHOS is the main physiological cell process consuming O_2 in retinal neurons, the high metabolic activity of these cells justifies the overall high oxygen demand in the retina (Casson et al., 2021). In this respect, the distribution of mitochondria in the retina is strictly correlated to the demand of ATP in the different regions and cell types (Figure 1). Among retinal

neurons, photoreceptors and retinal ganglion cells (RGCs) are the most highly metabolically active neurons.

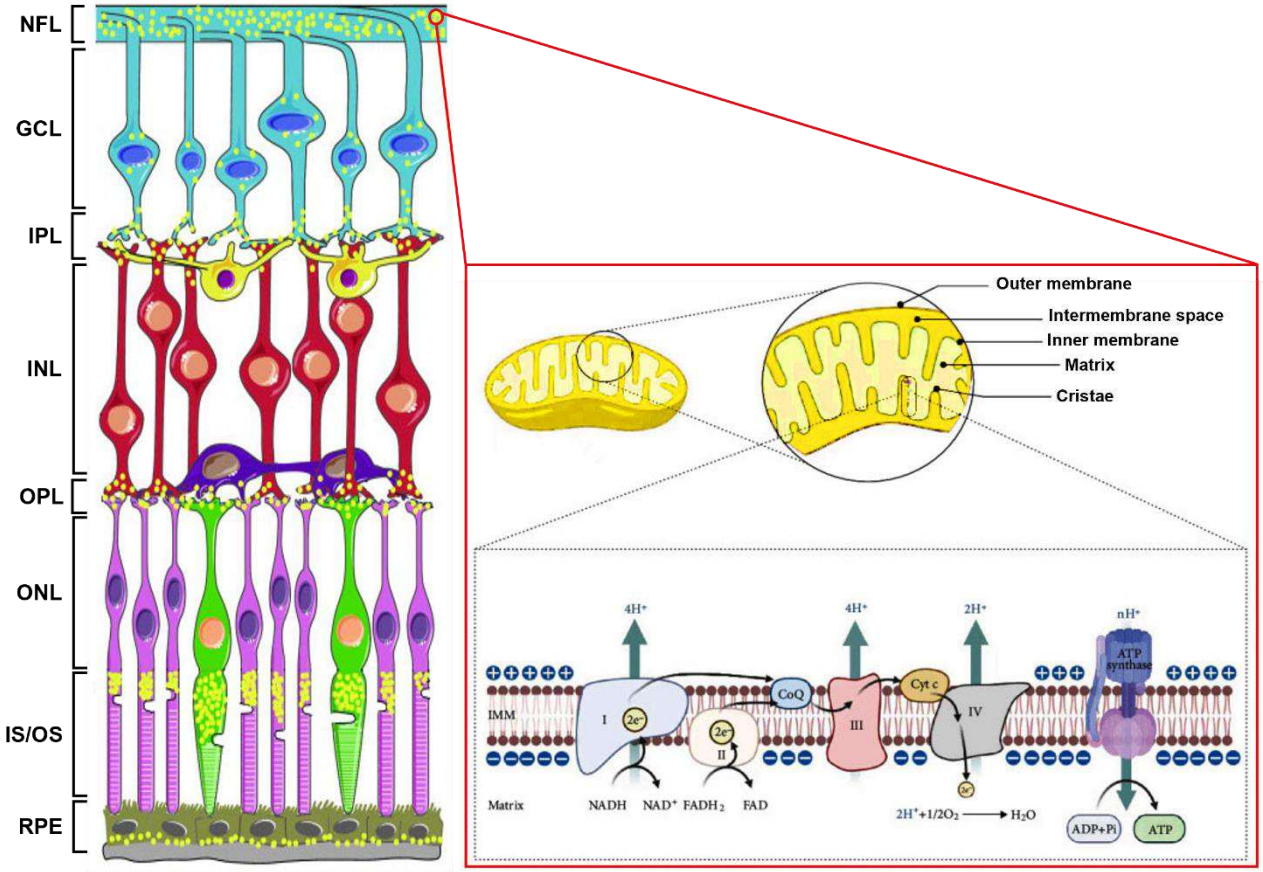

Figure 1. Schematic representation of retinal layers and the major distribution of mitochondria (yellow dots) in retinal neurons. The red inset delimits a particular of mitochondrial structure with the components of ETC and the direction of the electron transfer occurring in OXPHOS. GCL, ganglion cell layer. IMM, inner mitochondrial membrane. INL, inner nuclear layer. IPL, inner plexiform layer. IS, photoreceptor inner segment. NFL, nerve fiber layer. ONL, outer nuclear layer. OPL, outer plexiform layer. OS, photoreceptor outer segment. RPE, retinal pigment epithelium. Modified from Tao, Zhou and Zhu, 2019 and Yuan et al., 2022.

1.1.1 Photoreceptors

Being the cell type implicated in phototransduction, photoreceptors are one of the most metabolically active cell types in the retina. The energy consumption of photoreceptors has the peculiarity of being compartmentalized and light dependent (Narayan et al., 2017). In particular, the inner segment (IS) and the synaptic terminals are the regions of the highest ATP consumption under darkness, whereas during light conditions most of the energy is required primarily in the outer segments (OS) (Narayan et al., 2017). In darkness the maintenance of the dark current and the synaptic transmission are the main mechanisms consuming ATP in photoreceptors. In this context, the activity of the ATPase ion pumps is extremely important to maintain the electrochemical gradients for the movement of ions

maintaining the dark current and for the synaptic transmission. In particular, the Na^+/K^+ ATPase pumps located in the IS consumes ATP to maintain a constant Na^+ gradient, which in turn allows the influx of Na^+ into the cell responsible for the dark current. Moreover, the Ca^{2+} ATPase pumps at the synaptic terminal spend ATP to maintain a Ca^{2+} gradient necessary for promoting the influx of Ca^{2+} driving the release of glutamate (Okawa et al., 2008). Conversely, during light conditions photoreceptors use a high amount of energy to sustain the mechanisms involved in the termination of the phototransduction cascade occurring mainly in the OS. In particular, the inactivation of the visual pigment by phosphorylation and the conversion of GTP into GDP to inactivate transducin are all processes involved in the phototransduction termination requiring the consumption of ATP (Wong-Riley, 2010). Among all these processes occurring both in light and darkness, the maintenance of the dark current seems to be the most demanding in terms of ATP consumption. Coherently, the metabolic demand in photoreceptors is higher in darkness, with a four-fold increase in ATP consumptions compared to that in light conditions (Okawa et al., 2008). The contribution of OXPHOS is important to provide ATP in photoreceptors for the maintenance of such mechanisms. In this respect, it has been reported that the highest oxygen consumption rate in a vascularized retina was in the inner segments of photoreceptors and in the outer plexiform layer (OPL), which contains the synaptic terminals of photoreceptors (Cringle et al., 2002). Accordingly, the highest density of mitochondria, as well as the most elevated activity of OXPHOS enzymes, was documented in the photoreceptor inner segments and in the synaptic terminals (Hoang et al., 2002; Chidlow et al., 2019; Joyal, Gantner and Smith, 2019).

1.1.2 Retinal ganglion cells

RGCs represent the only output of the retina sending the visual information to the extraretinal regions. RGCs are long projecting neurons located in the inner part of the retina, with cell bodies located in the ganglion cell layer (GCL) and their dendrites arborizing through the inner plexiform layer (IPL), where RGCs make synapses with amacrine processes and bipolar cell axonal terminals. Their long axons (which constitute 80% of the total RGC volume (Quigley, Dunkelberger and Green, 1988; Curcio and Allen, 1990; Morgan, 2004)) develop along the nerve fiber layer (NFL), converge into the optic nerve head (ONH), and form the optic nerve (ON), connecting the retina to primary visual centers in the brain. The different RGC subcellular components have different functions and, consequently, are characterized by distinct metabolic demands (Casson et al., 2021; Liu and Prokosch, 2021). For instance, RGC dendrites require a huge amount of ATP for the integration of

excitatory and inhibitory signals coming from synapses in the IPL (Casson et al., 2021). Conversely, ATP in the RGC somata is consumed for the biogenesis and the intracellular transport of organelles (Liu and Prokosch, 2021). Nevertheless, the most ATP requiring district of RGCs is represented by the long axon for regeneration and propagation of action potentials which need the continuous activity of ion pumps, mainly the Na+/K+ ATPase, to restore the membrane potential after depolarization. The different degree of myelination determines distinct energy requirements along the axon, with the highest energetic burden occurring in the intraocular unmyelinated region, where the highest density of constantly active Na^+/K^+ ATPases can be found (Liu and Prokosh, 2021). The elevated energy demand of RGCs is sustained by the OXPHOS to constantly produce a high amount of ATP. To this aim, RGCs are enriched in mitochondrial proteins and possess a high mitochondrial activity, with an asymmetric distribution depending on the subcellular energy demands (Chidlow et al., 2019). Indeed, a huge number of RGC mitochondria are distributed within the dendrites and the axon, although some mitochondria can be also found in the cell body located mostly around the nucleus (Liu and Prokosh, 2021). In line with the energy demands, the highest mitochondrial density can be observed in the unmyelinated portion of the axon, where mitochondria are concentrated in many axonal varicosities distributed along the entire length of this region (Wang et al., 2003). Given their extreme high energy demand, RGCs are on a metabolic knife-edge, dependent on the levels of energetic substrates and a fine-tuned metabolism for functioning, suggesting how RGCs can be metabolically fragile and susceptible to damage under metabolic stress.

1.2 Consequences of dysmetabolism and mitochondrial dysfunction

Dysmetabolism resulting from metabolic stress can alter mitochondrial activity modifying the retinal bioenergetic balance, with an impact on cell function and survival. In addition, dysfunctional mitochondria can downstream modify the cell oxidative balance, characterized by the equilibrium between the production of reactive oxygen species (ROS) and their detoxification by the cell antioxidant defense (see below). Therefore, the mitochondrion represents the key common point for the regulation of cell bioenergetic and oxidative balance, both of which can profoundly be modified by disrupted mitochondrial activity.

1.2.1 Imbalances in mitochondrial activity

An altered mitochondrial function can result in two main detrimental consequences for retinal cells, that is (i) reduced ATP synthesis and (ii) increased production of toxic ROS. On the one hand, the impaired activity of mitochondrial complexes can alter the rate of electron transfer through the ETC, consequently reducing the proton transfer into the intermembrane space and hence the $\Delta\Psi$. The decreased proton gradient reduces the activity of ATP synthase, thus resulting in impaired ATP synthesis (Neupane et al., 2019). The impairment of ETC activity can result as a consequence of structural or functional alterations in mitochondrial complexes, which lose their efficiency in transferring electrons in a controlled fashion. Alternatively, any dysmetabolism reducing the influx of metabolic substrates into metabolic pathways reactions results in changed production of NADH and $FADH_2$, leading to reduced influx of electrons into the ETC and ATP synthesis (Fernandez-Vizarra and Zeviani, 2021). Due to the high energy demand, retinal neurons continuously consume ATP, causing ATP depletion and energy exhaustion over time if the synthesis is reduced. The energetic failure resulting from the impairment of the bioenergetic balance in turn impairs a large variety of intracellular events (see paragraph 1.1), ultimately hampering cell function and viability.
On the other hand, a disrupted activity in mitochondrial ETC can lead to increased production of ROS. In effect, along the ETC the electrons can potentially leak from the electron acceptors and directly reduce the molecular O_2, thus promoting ROS production. Under physiological conditions, the electron leakage is contained by proper activity of the mitochondrial complexes and ROS production is counteracted by cell defense mechanisms against ROS (see paragraph 1.2.2). However, under unbalanced mitochondrial activity, the controlled electron transfer through the ETC is impaired, incrementing the leakage of electrons through the ETC and the direct reduction of O_2 into ROS (Mailloux, 2020). In this respect, mitochondrial CI and CIII seem to be the primary ROS production sites, although a small contribution of CII may be included in the overall mitochondrial production of ROS (Zhao et al., 2019; Figure 2). The electron leakage from the ETC can reduce O_2 and lead to the production of anion superoxide, which is the first type of produced ROS in the mitochondria potentially representing the prime step for the conversion to other highly reactive and damaging ROS, such as hydrogen peroxide, peroxynitrite, hydroxide ion and hydroperoxyl radicals (Juan et al., 2021). An increased ROS production in mitochondria can occur as a consequence of any structural/functional impairment in mitochondrial complexes resulting in decreased mitochondrial activity and favoring a higher leakage of electrons (Zhao et al., 2019). Importantly, also a higher metabolic activity, promoted by an increased influx of metabolic substrates (e.g., glucose) into metabolic reactions such as glycolysis and tricarboxylic acid (TCA) cycle, can apparently increase

the production of ROS by augmenting the production of reduced cofactors. In effect, the overproduction of reduced cofactors from metabolic pathways induces an overflow of electrons through CI and CII, generating a high ΔΨ which exceeds a threshold where the electron transfer to CIII is inhibited. The inhibition of electron transfer to CIII increases the half-life of superoxide-generating intermediates, thus favoring the reduction of O_2 into superoxide (Brownlee, 2001). Therefore, both a reduced and an excessive mitochondrial activity may result in a harmful production of ROS in mitochondria.

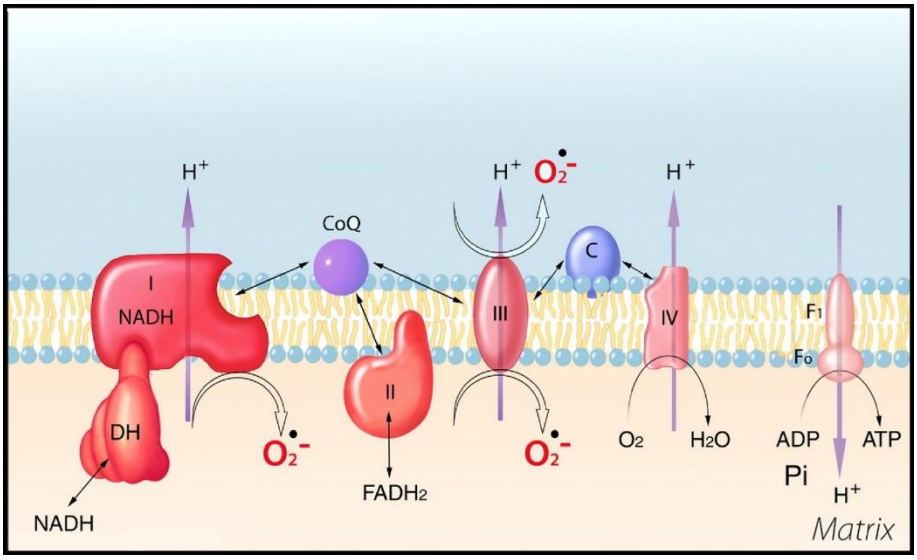

Figure 2. Schematic diagram of mitochondrial ETC evidencing the elements involved in the OXPHOS and the sites of ROS production. The electron transfer through the ETC induces the reduction of O_2 into H_2O at the level of CIV with the contemporary translocation of protons at CI, CIII and CIV out of the mitochondrial matrix. The double-edged arrows indicate the electron transfer between adjacent ETC stations. The retrograde translocation of protons into the matrix occurs through the ATP synthase, which couples the movement of protons to the synthesis of ATP. The major sites of superoxide ($O_2^{\bullet-}$) production are indicated at the level of mitochondrial CI and CIII, where most of the electron leakage occurs. Modified from Balaban, Nemoto and Finkel, 2005.

1.2.2 Oxidative stress

Under physiological conditions, the production of ROS is counterbalanced by a complex antioxidant system which buffers ROS increase by detoxifying these reactive toxic species. The antioxidant defense involves a series of both non-enzymatic and enzymatic agents acting in concert to remove excessive ROS. The non-enzymatic antioxidants include a wide range of molecules, such as glutathione (GSH), ascorbic acid and α-tocopherol, acting as radical scavengers through a direct redox interaction (Birben et al., 2012). On the other hand, the enzymatic antioxidants are represented by a class of enzymes either directly catalyzing reactions of ROS detoxification or, as in the case of some enzymes as heme oxygenase-1 (HO-1), promoting the production of antioxidant molecules

which in turn detoxify ROS. For instance, HO-1 is an enzyme involved in the degradation of the heme group producing biliruibin, one of the most abundant endogenous antioxidants in mammalian tissues acting as a scavenger of ROS (Otterbein and Choi, 2000). The expression of antioxidant enzymes is controlled by transcription factors whose activation depends on ROS levels, among which the nuclear factor erythroid 2-related factor 2 (Nrf2) is one of the most involved in mediating the transcriptional regulation of antioxidant genes. Nrf2 is stabilized upon ROS-mediated oxidation and binds to antioxidant response elements (AREs) in the promoter region of its target genes, inducing the expression of several antioxidant molecules including HO-1 (Ma, 2013).

The perfect balance between ROS production and activity of the antioxidant system guarantees a perfect cell oxidative state, which can be altered under unbalanced mitochondrial activity. In particular, if the excessive ROS production from dysfunctional mitochondria is not sufficiently counteracted by the antioxidant defenses, ROS accumulate leading to the onset of oxidative stress. During oxidative stress, ROS oxidize cell components as lipids, nucleic acids and proteins, thus leading to cell membranes destabilization, nucleic acid mutations and protein denaturation (Birben et al., 2012). As considered above, mitochondria are extremely susceptible to oxidative stress, being the primary producers of ROS. In mitochondria, ROS damage lipid membranes by lipoperoxidation and leads to cristae destabilization. In addition, the oxidation of mitochondrial proteins can destabilize the structural integrity of mitochondrial complexes thus further impairing the ETC. Moreover, increased ROS may favor mtDNA mutations, which, in turn, may modify the expression of proteins involved in mitochondrial function. All these mechanisms further impair mitochondrial respiratory function, thus promoting the imbalance in metabolic processes and leading to bioenergetic insufficiency (Guo et al., 2013).

Oxidative stress promotes a series of cell damaging pathways triggering the activation of inflammation and cell death. The accumulation of ROS stimulates some transcription factors involved in inflammatory processes, such as nuclear factor-kappa B (NF-kB), which mediates the expression of several pro-inflammatory cytokines (Mittal et al., 2014). The activation of inflammatory mechanisms also involves the recruitment of retinal microglia and the activation of Müller cells, undergoing morpho functional alterations typical of their reactive state. In particular, activated microglia changes its cell morphology into a typical ameboid shape, migrates through the retinal layers to reach the major site of damage and starts producing pro-inflammatory and neurotoxic mediators, including interleukins (ILs) and ROS (Woodburn, Bollinger and Wohleb, 2021). On the other hand, Müller glia increases in density, upregulates the glial fibrillary acid protein (GFAP), and shows dispersion of nuclear chromatin and formation of electrondense nuclear granulations, indicating the “reactive” state of these cells (Schellini et al., 1995). The induction of inflammation

further promotes ROS production, reverberating the oxidative stress and amplifying retinal cell damage. All these pathophysiological mechanisms concur to initially reduce retinal function and, if the damage persists chronically, ultimately alter retinal cell viability by the activation of caspase-mediated apoptotic mechanisms (Yang et al., 2015).

1.3 Mitochondrial dysfunction in retinal diseases

The pathophysiological mechanisms resulting from altered bioenergetic and oxidative balance due to mitochondrial dysfunction in retinal cells may influence their function and survival. Energy depletion and occurrence of oxidative stress may trigger cell death mechanisms, thus reducing the efficiency of retinal function and decreasing retinal cell survival. Many stressors converge on mitochondria and alter the rate of OXPHOS, suggesting that mitochondrial dysfunction may be a common pathophysiological condition impairing the viability of retinal neurons as occurs in different retinal disorders (Barot, Gokulgandhi and Mitra, 2011). In this context, retinal neurodegenerative diseases may be suitable models for studying the role of bioenergetic and oxidative balance in regulating retinal cell health and survival.

1.3.1 Diabetic retinopathy: excessive mitochondrial activity impairs retinal bioenergetic and oxidative balance

Diabetic retinopathy (DR) is a vision threatening disease representing one of the most common complications in patients affected by diabetes mellitus. DR has a high social impact which, due to its increasing incidence over the last decades, has raised a huge interest in the mechanisms of its pathophysiology and effective treatment approaches. Hyperglycemia represents the principal stressor inducing a series of pathological mechanisms damaging retinal vessels and neurons, ultimately leading to retinal dysfunction and blindness. Hyperglycemia-induced alterations in retinal bioenergetic and oxidative mechanisms have been reported to concur in determining cell damage and death characterizing DR pathogenesis (Miller, Cascio and Rosca, 2020).

Clinical manifestations and pathophysiology

The pathophysiology of DR is complex and affects many different intracellular pathways. The exact development of DR pathogenesis is still under debate about the nature and the mechanisms involved in the progression of the disease. In effect, clinical and experimental evidence demonstrate that high glucose can damage both vascular and neuronal components of the retina, impairing the delicate neurovascular communication responsible of the maintenance of retinal function.

Vascular alterations

Classically, the clinical manifestations of DR are described with its typical vascular defects, such as hemorrhages, aneurysms, venous beading, and vascular proliferation. The diagnosis and classification of DR have been based exclusively on vascular manifestations, leading to the establishment of two main different types of DR: the non-proliferative and proliferative DR (Wilkinson et al., 2003). Vascular defects including microaneurysms, retinal hemorrhages, microvascular abnormalities, and vessel caliber alterations characterize the non-proliferative diabetic retinopathy (NPDR), which can further progress to proliferative DR (PDR) when preretinal pathologic angiogenesis with vitreal hemorrhage and tractional retinal detachment occur (Duh, Sun and Stitt, 2017). Another clinical manifestation in DR potentially occurring in both NPDR and PDR is diabetic macular edema (DME), which occurs as a consequence of vascular leakage of fluid in the macula due to the blood-retinal barrier (BRB) breakdown (Frey and Antonetti, 2011; Zhang et al., 2014; Stitt et al., 2016). BRB can be distinguished in inner BRB (made by retinal endothelial cells) and outer BRB (made by retinal pigment epithelium (RPE) cells) (O'Leary and Campbell, 2023). Dysfunction of the inner BRB occurs following damage to retinal endothelial cells, resulting in reduced endothelial function together with pericyte loss and glial activation. In addition, hyperglycemia also causes damage to RPE and promotes the dysfunction of outer BRB (Xang et al., 2020).

The chronic exposure to high glucose induces the activation of different pathways, such as the non-enzymatic glycation end products (AGEs), the polyol pathways and the protein kinase C (PKC), which directly or indirectly alter the functionality of BRB (Brownlee, 2001). The common mechanism associated with all of these pathways and strongly damaging BRB cells in this phase is oxidative stress, occurring as the downstream effector resulting in either increased production of ROS or reduced efficiency of the antioxidant defense with consequent cell damage and death (Kang and Yang, 2020). For instance, AGEs can glycate and modify proteins which in turn binds specific AGE

receptors (RAGE), promoting ROS production (Brownlee, 2001). In addition, the activation of polyol pathways consumes NADPH, depleting the main cofactor for the synthesis of GSH, thus reducing the antioxidant capacity of cells (Lorenzi, 2007). Moreover, hyperglycemia activates the PKC involved in the activation of ROS-producing enzymes (Brownlee, 2001). The oxidative stress resulting from hyperglycemia determines pericyte loss and induces endothelial dysfunction, leading to the alteration of BRB permeability. Furthermore, the activation of AGE, PKC and other hyperglycemia-induced pathways in glial cells, RPE and macrophages, may also promote the expression of vascular permeability-enhancing factors, such as vascular endothelial growth factor (VEGF) (Wong et al., 2016). In particular, VEGF worsens BRB disruption by reducing the expression of structural proteins such as claudins and zonula occludens-1 (ZO-1), which compose the endothelial and RPE tight junctions responsible for the integrity of BRB (Kim et al., 2010). The disruption of BRB induces the leakage of plasma constituents from retinal and choroidal vessels in the surrounding retinal parenchyma, exposing retinal neurons to toxic substances that damage retinal cells and strongly affect their function and viability. Over the time, microvascular damage and the capillary occlusion exerted by recruited leukocytes, reduce retinal perfusion, establishing an ischemic condition of the retinal parenchyma. This condition may further evolve in the activation of VEGF-driven angiogenic processes leading to abnormal vascular growth as typical hallmark of PDR (Wong et al., 2016).

The VEGF upregulation derives from the activation of key transcriptional regulators, including hypoxia inducible factor-1 (HIF-1) and Nrf2. In particular, HIF-1 is a transcription factor whose activity is classically promoted under ischemic conditions to mediate the expression of several hypoxia-related genes (Wang et al., 1995). HIF-1 is a heterodimer whose de novo synthetized subunit HIF-1α is constantly degraded after its hydroxylation under normoxia (Ivan et al., 2001). In hypoxic conditions, the hydroxylation is inhibited and the half-life of HIF-1α is prolonged, allowing the accumulation, the translocation to the nucleus and the dimerization with the subunit HIF-1β (Huang et al., 1996). The activated dimer binds the hypoxia response elements (HREs) in the promoter regions of its gene targets and mediates the expression of several hypoxia-related factors, including VEGF (Arjamaa and Nikinmaa, 2006). Notably, the stability of HIF-1α may be regulated by other factors different from hypoxia, including oxidative stress (Chun, Kim and Park, 2002; Rossino et al., 2020). In particular, oxidative stress occurring in the early DR may promote HIF-1α activity through the activation of Nrf2. In effect, Nrf2 meditates the expression of HO-1, that in turn may increase HIF-1α stability through carbon monoxide deriving from the HO-1 activity (Choi et al., 2018; Rossino et al., 2020).

Neurodegeneration

The classical consideration of DR as a strict vascular-initiated disease has been recently questioned by an increasingly large body of evidence suggesting that vasculopathy occurring in DR may be preceded by dysfunctional deficits at the level of the neural retina. In the retina, neurons are connected to glia and vessels in the neurovascular unit (NVU), a functional entity represented by a complex interchange of molecular mediators to adjust the retinal metabolic supply according to neuronal activity (Metea and Newman, 2007). In particular, in the NVU, neurons communicate and activate glial cells by molecular mediators to send information on their O_2 and metabolic demand. On the other hand, activated glial cells contacts retinal vessels (composed by endothelial cells, pericytes and smooth muscle cells) by their end-feet and release vasoactive compounds in order to regulate the vascular tone depending on neuronal activity (Muoio, Persson and Sendeski, 2014). As a result, the vascular tone is directly coupled to neuronal function to guarantee the correct supply of nutrients and maintain a proper elimination of toxic byproducts deriving from neuronal metabolism.

Considering this close functional relationship between the vascular component and the neuronal/glial compartment in the retina, the view of DR as a retinal disorder exclusively based on vascular alterations may appear strongly limited. In effect, the contribution of neural retina to the onset and progression of the vascular disorders occurring in DR has been increasingly considered over the last few years. Thus, the functional and neurodegenerative processes in DR do not seem to be exclusively related to damages occurring secondarily to vascular dysfunction, but rather be a direct effect of hyperglycemia affecting function and viability of retinal neurons, which in turn may alter the NVU and favor the progression of vascular damage. As a support, functional deficits and retinal neuronal modifications have been recently reported before vascular defects in animal models of DR and retinas from diabetic donors, thus supporting the concept of neurodegeneration as an early event in DR (Barber and Baccouche, 2017; Simo, Stitt and Gardner, 2018; Amato et al., 2022). Potentially, all neuronal types in the retina can be affected by hyperglycemic conditions, although it is still not clearly established whether there is a differential susceptibility and different time response to high glucose among retinal neurons. In this respect, recent findings suggest a high susceptibility of RGCs to hyperglycemia, given their high metabolic activity and abundance of mitochondria. In particular, recent work from Amato and colleagues demonstrated RGC morpho functional alterations without overt RGC death as early as two weeks from the onset of diabetes in a mouse model of DR, when the function of the other retinal neurons seemed not to be affected (Amato et al., 2022). Supporting this, the activation of apoptotic mechanisms has been reported to occur predominantly in the inner retina at early stages of diabetes (Li et al., 2008).

Similar to the vascular defects, the main metabolic stress induced by high glucose in retinal neurons is oxidative stress, which represents the convergence of different pathways driven by hyperglycemia. For instance, the activation of polyol or hexosamine pathways, uncoupling of endothelial nitric oxide synthase, AGE production, nitrative stress are all conditions favoring the disruption of the oxidative balance by increasing ROS production and concomitantly consuming the components of the antioxidant defense (Kowluru, 2001; Coucha et al., 2015; Behl, Kaur and Kotwani, 2016). Notably, the increase in ROS may also result from altered mitochondrial activity induced by the excess in glucose, a process that might be emphasized in neurons (especially in RGCs) given their high metabolic rate and enrichment in mitochondria (Ito and Di Polo, 2017; Leveillard and Sahel, 2017). The increased oxidative stress also stimulates the inflammatory response by activating NF-kB and promoting the expression of pro-inflammatory cytokines (Liu et al., 2017a). The activation of inflammatory mechanisms contributes to retinal damage by activating macroglia and recruiting immune cells which both release toxic factors to neurons and reverberates oxidative stress by further promoting ROS production (Semeraro et al., 2015; Al-Kharashi, 2018). In this context, neuronal damage under hyperglycemia-induced oxidative stress has been reported to induce the production of VEGF, which is markedly released in retinal explants within a few days of incubation in the presence of high glucose, oxidative stress, or AGEs (Amato et al., 2016; Rossino et al., 2020). Importantly, the blockade of VEGF release under high glucose conditions increased retinal cell apoptosis, suggesting that the production of VEGF may represent an endogenous mechanism activated in acute stress conditions to protect retinal neurons from stress rather than a simple pro-angiogenic factor (Amato et al., 2016). Evidence supporting the neuroprotective role of VEGF under acute stress have been demonstrated in different contexts, such as retinal ischemia, excitotoxicity, hypertensive glaucoma model, optic nerve axotomy (Cervantes-Villagrana et al., 2010; Cervia et al., 2012; Foxton et al., 2013). Thus, the increase in VEGF seems to have an initial protective role, which is progressively lost over the establishment of DR where it can induce pathological angiogenesis and favor retinal damage. However, the confirmation of the putative VEGF survival role and the reason why this function is progressively lost over DR still needs to be established.

DR and mitochondrial dysfunction

Hyperglycemia can result in a metabolic unbalance leading to altered mitochondrial activity and ultimately inducing oxidative stress. The enhanced glucose influx in retinal cells can promote the activation of TCA cycle, providing the initial increase of reduced cofactors such as NADH and

$FADH_2$ and the activity of mitochondrial CI and CII (Brownlee 2001; Wu and Zhou, 2022). Therefore, high glucose condition seems to establish an initial transient mitochondrial activation, which has been further suggested by several studies. In particular, Masser and colleagues reported an early significant elevation of basal and ATP-linked oxygen consumption rate in the retina of diabetic rats, indicating a positive induction of mitochondrial activity (Masser et al., 2017). In addition, another study showed increased mitochondrial oxygen consumption in diabetic rats at 3 weeks of hyperglycemia, which was associated with increased specific activities of CI, CII, and CIII (Osorio-Paz et al., 2015). Similarly, a study by Han and colleagues described an increased CI-dependent mitochondrial respiration after 2 months of high glucose in a model of spontaneous diabetes in the cone-rich diurnal Nile rats (Han et al., 2017). Taken together, all these studies suggest the transient early increase in mitochondrial activity induced by hyperglycemia. Nonetheless, the excessive mitochondrial activity in CI and CII creates a high $\Delta\Psi$ and reduces the electron transfer to CIII, leading to the production of superoxide following the electron backup to coenzyme Q (CoQ; Figure 3). Notably, the hyperglycemia-induced production of superoxide has been proposed as the unifying mechanism occurring upstream to and connect all the other mechanisms influencing the onset of oxidative stress in hyperglycemia (Brownlee 2001; Wu, Tang and Chen 2014). This is further suggested by the evidence that scavenging or reducing superoxide production from mitochondria inhibits the glucose-activated induction of pathways as PKC, polyol, AGE and hexosamine pathways (Wu, Tang and Chen, 2014).

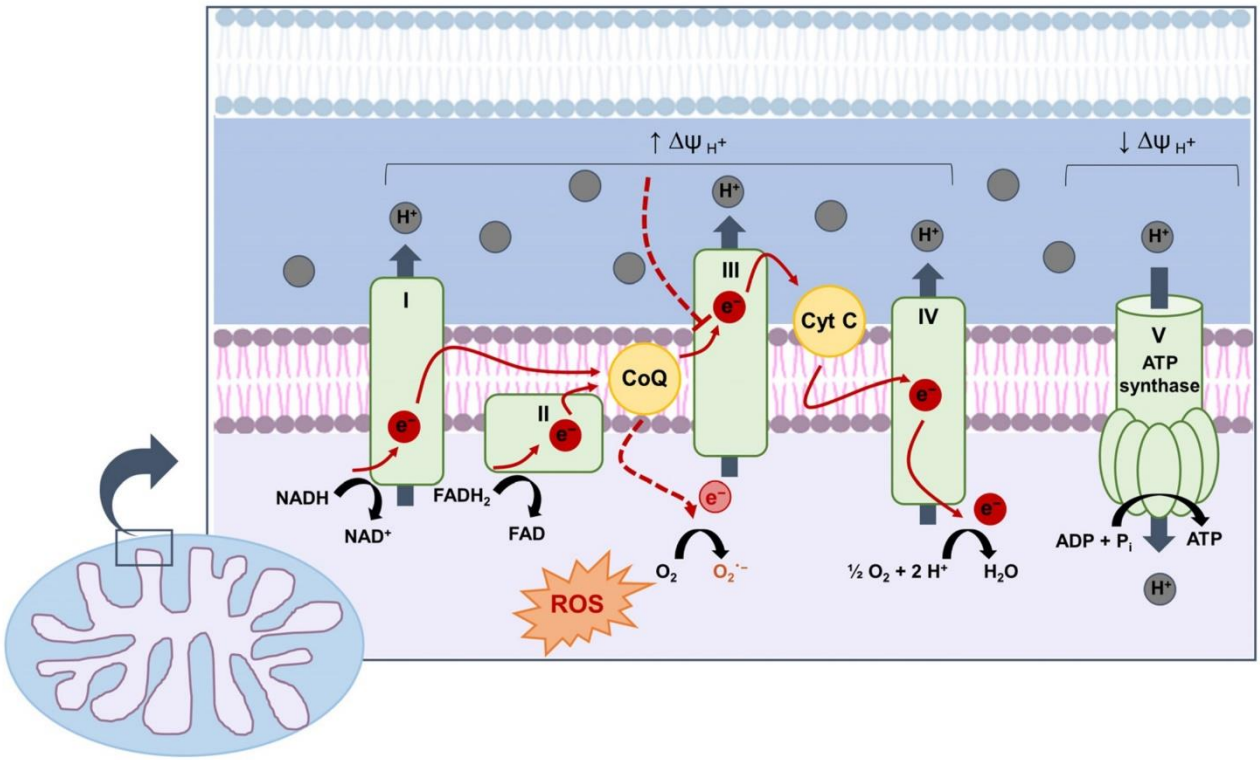

Figure 3. Schematic diagram showing the mechanism of mitochondrial superoxide production under hyperglycemia. The overflow of electrons from NADH and $FADH_2$ induces the excessive increase in proton translocation and in ΔΨ, reaching a threshold at which the electron transfer to CIII is inhibited. Therefore, the electron leakage at CoQ occurs, thus transferring electrons to the O_2 and generating more superoxide. Modified from Iacobini et al., 2021.

The increase in ROS production can overwhelm the antioxidant defenses and induce oxidative stress, leading to the alteration of mtDNA and mitochondrial proteins as mitochondria are the most direct and proximal site of ROS production. The modifications of mitochondrial elements can induce a later decline in mitochondrial function, ATP depletion and further ROS production enhancing retinal damage. In this respect, a long-term hyperglycemia in Nil diurnal rats induced a decrease in NADH-supported mitochondrial respiration and defective CIII was reported in mitochondria after several months from diabetes in mice, thus suggesting a partial impairment in mitochondrial bioenergetics when high glucose exposure becomes prolonged (Kanwar et al., 2007; Han et al., 2017). Taken together, this evidence shows how hyperglycemia can damage retinal cells through the disruption of bioenergetic and redox balance due to an altered mitochondrial activity.

Current therapies

Since DR represents a common complication of diabetes, the control of hyperglycemia is the principal target for DR management. However, DR manifests also in patients where these risk factors are

tightly controlled, dictating the necessity of additional interventions (Raman et al., 2012; Anger, 2016; Chatziralli, 2018). In this respect, most of the current therapeutic strategies for DR are focused on treating the late stages linked to severe NDPR or PDR. Laser photocoagulation is particularly used to attenuate vascular proliferation in PDR by burning and destroying the ischemic peripheral retina and reducing the production of pro-angiogenic factors (Mcdonald and Schatz, 1985). This type of surgery however includes some unavoidable side effects on retinal function and is not universally effective in preventing the impairment of retinal function induced by DR (Simo and Hernandez, 2009). Alternatively, some pharmacological strategies are available based on the neutralization of VEGF to reduce the pathological angiogenesis during PDR (Cheung, Wong and Wong, 2014). Nonetheless, the administration of anti-VEGF is an invasive procedure with some associated side effects as endophthalmitis, retinal detachment and putative deleterious effects in retinal cell viability if administered for long-term (Simo and Hernandez, 2008; Amato et al., 2016; Hernandez et al., 2016). In addition, anti-VEGF can have systemic complications if the drug reaches the systemic circulation, potentially causing hypertension and cardiovascular defects (Simo and Hernandez, 2008). Therefore, although anti-VEGF may be effective in counteracting DR progression, the wide range of side effects suggests that anti-VEGF does not represent the optimal therapeutic agent for DR. On the other hand, some anti-inflammatory agents are partially applied in clinics to counteract the upstream mechanisms occurring in DR. However, although there is evidence of the protective effects after the treatment with these drugs, the necessity of multiple reinjections and the high risk of side effects as infection, glaucoma, cataract formation as well as heart attacks and strokes, strongly limit their extensive application (Mohamed, Gillies and Wong, 2007; Cunningham, Edelman and Kaushal, 2008; Kim, Flach and Jampol, 2010). Hence, the current strategies for treating DR allow the intervention on the advanced stages, where retinal dysfunction and damage have already been established, with a wide range of side effects for the patients. In this context, there is the necessity to find alternative therapeutic strategies targeting early stages of DR whilst providing a non-invasive administration route and a restricted number of complications.

1.3.2 Retinal light damage and glaucoma: reduced mitochondrial activity impairs retinal bioenergetic and oxidative balance

The alteration of oxidative and bioenergetic balance can also result when mitochondrial function is negatively affected. The decreased mitochondrial activity characterized by reduced electron flow through the ETC increments electron leakage to O_2, leading to reduced ATP synthesis and augmented

ROS production (see paragraph 1.2). Many stressors could induce metabolic disturbances by reducing mitochondrial activity, impairing retinal cell function and survival. In this context, retinal damage induced by excessive light and elevated intraocular pressure (IOP), characterizing retinal disorders as retinal light damage (LD) and glaucoma, respectively, are pathological examples of reduced retinal functionality following the alteration of oxidative and bioenergetic balances induced by mitochondrial hypoactivity.

1.3.2.1 Retinal light damage

Light may represent a double-edged sword for the retina, inducing irreversible damage if the exposure is excessive and/or prolonged. Indeed, the excessive exposure to light can trigger a series of pathophysiological events leading to altered retinal function and viability, especially in photoreceptors which are the most photosensitive retinal cell type (Contín et al., 2016). The altered redox balance induced by excessive light seems to play a predominant role in damaging photoreceptors and reducing their viability (Organisciak and Vaughan, 2010).

Clinical manifestations and pathophysiology

The clinical manifestations resulting from LD are associated to visual impairment with structural changes that sometimes may not be detected by ophthalmoscopic analysis. When detectable, morphological signs of damage manifest as outer retinal whitening, mild pigmentary changes with a subsequent formation of a yellowish plaque-like lesion as the remaining evidence of LD (Youssef, Sheibani and Albert, 2011). At microscopic level, retinal histology of photic damaged retina shows areas of retinal edema, RPE pigment disorganization, macrophage infiltration and formation of a pathologic plaque at the outer retina (Youssef, Sheibani and Albert, 2011). The visual impairment occurring under LD is mainly due to retinal cell dysfunction occurring mainly in photoreceptors, where excessive light triggers a series of morpho functional alterations initially causing functional deficits and ultimately resulting in reduced neuronal viability (Organisciak and Vaughan, 2010). In particular, excessive exposure to light induces an initial shortening of the OS and mislocalization of visual pigments, followed by altered cell viability due to the activation of cell death mechanisms (Marc et al., 2008; Organisciak and Vaughan, 2010; Françon and Torriglia, 2023). The initial damage to photoreceptors triggers a series of retinal remodeling events involving the entire structure of the

retina and all its cell types, further modifying the retinal circuits and reducing the function of this organ (Marc et al., 2008).

The pathophysiology of photochemical damage seems to be predominantly related to an alteration of the redox balance in photoreceptors promoted by increased oxidative stress after excessive ROS production following light stimulation (Contín et al., 2016). In this respect, the retina is full of light-sensitive chromophores that form a transient triplet state with highly reactive properties following light stimulation (Boulton, Rózanowska and Rózanowski, 2001). The excited chromophores return to their ground state, but their state of excitation is long enough to interact directly or indirectly with O_2 in redox reactions. In particular, excited chromophores can either reduce the O_2 or interact with a substrate whose reduction to a free radical in turn reacts with O_2, thus leading to the overall production of ROS (Wielgus and Roberts, 2012; Figure 4). The increased ROS production under excessive light exposure overcomes the antioxidant capacity of the cell, leading to oxidative stress (Contín et al., 2016). The oxidative damage triggers an inflammatory response, thus increasing the production of pro-inflammatory factors and inducing the recruitments of microglia to phagocytize and clear dying photoreceptors (Kohno et al., 2013). The concurrence of oxidative stress and inflammation, which reverberates cell damage through further ROS production, induces retinal gliosis and the activation of retinal cell death mechanisms, hence altering the viability of retinal cells and reducing retinal function (Françon and Torriglia, 2023).

The high susceptibility of photoreceptors to LD is mainly due to their high abundance of light sensitive chromophores, including phototransduction pigments and their byproducts, which are excessively excited by the prolonged exposure to light (Rózanowska and Sarna, 2005; Maeda et al., 2008; Maeda et al., 2009; Lee et al., 2016). In addition, the high susceptibility of photoreceptors to LD is likely to be due to the abundance in the OS membranes of polyunsaturated fatty acids, which are the primarily target of lipoperoxidation reactions triggering the chain of ROS production (Organisciak and Vaughan, 2010). Moreover, photoreceptors may be highly vulnerable to LD giving the highly activated metabolism and the abundance of mitochondria, which may be a considerable source of light-promoted ROS (see next paragraph).

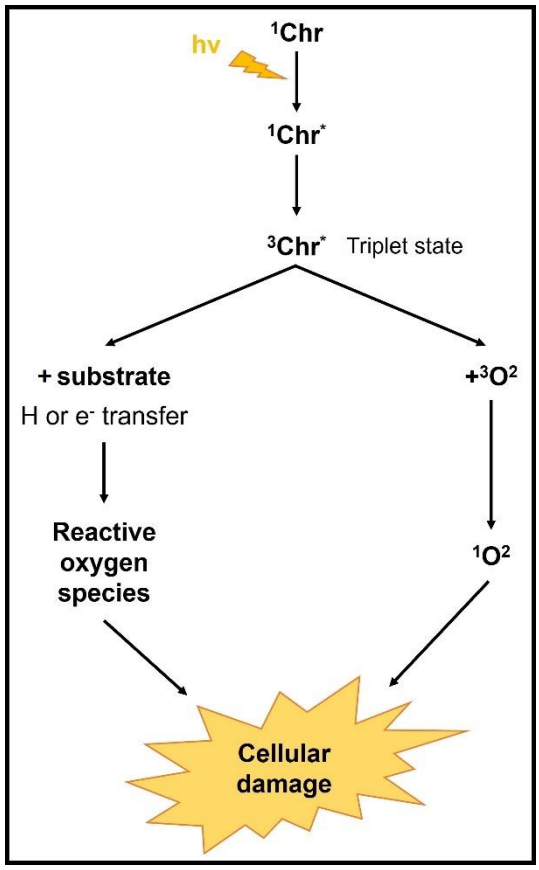

Figure 4. Formation of ROS following chromophore activation by light. The chromophore (Chr) is excited by the light (hv) absorption to reach the triplet state ($^3Chr^*$). On one hand, the excited chromophore in triplet state can reduce a substrate by the transfer of a hydrogen (H) molecule or an electron (e−). The reduced substrate can in turn react with the O_2 to form ROS. On the other hand, the excited chromophore can react directly with O_2 to produce a reactive ROS. Both these mechanisms lead to ROS increase, which damage cells. Modified from Françon and Torriglia, 2023.

Light damage and mitochondrial dysfunction

A considerable contribution to the variation of the oxidative balance occurring during LD may be attributed to mitochondria, whose activity and ROS producing capacity seem to be altered by LD, especially by some specific light wavelengths (Tao, Zhou and Zhu, 2019). Mitochondria contain chromophores that can absorb light and induce photochemical damage to mitochondrial complexes, contributing to ROS production. Indeed, the mitochondrial respiratory complexes of the ETC contains two major chromophores, flavin and porphyrin, which can absorb light, particularly in the blue wavelength (Tao, Zhou and Zhu, 2019). The excited forms of such chromophores induced by light absorption reduce the abundant O_2 in mitochondria and produce ROS that interact with unsaturated lipids, amino acid residues, and nucleic acids, causing mitochondrial damage and reducing mitochondrial activity (Aggarwal et al., 1978; Bonnett et al., 1980; Hockberger et al., 1999; Paoli, Marles-Wright and Smith, 2002). In particular, CI and CII contain many flavoproteins having FMN or FAD as a prosthetic group, which absorb light with a peak of approximately 450-520 nm (Hockberger et al., 1999). On the other hand, CIII and CIV include many porphyrin-containing cytochromes having an absorption peak at shorter wavelengths (Bell and Hall, 1981). Thus, the ETC has a huge potential of being excited by light, due to the abundance of chromophores, and increasing ROS production. On one hand, porphyrin and flavins may be molecularly excited by light absorption

and reach the triplet state. The triplet state of these excited chromophores may in turn interact with the O_2 in mitochondria, either directly or indirectly, and lead to ROS production with the potential mechanisms described in the previous paragraph. On the other hand, ROS production can oxidize the ETC protein components, thus impairing their structure and resulting in reduced electron transport capacity. As a result, the reduced complex activity promoted by ROS may further amplify the electron leakage and superoxide production, thus contributing to exacerbate oxidative stress (Guo et al., 2013). In addition, the reduced electron transport and the ROS-mediated oxidation and inactivation of mitochondrial ATP synthase may result in the overall decrease in ATP synthesis, inducing bioenergetic insufficiency (Tao, Zhou and Zhu, 2019; Ebanks and Chakrabarti, 2022). Numerous studies have indicated that ETC activity may be reduced following the absorption of blue light, which alters the bioenergetic and oxidative balance of the retina. For instance, the expression of CIV proteins in the rat retina was reduced after exposure to blue light and resulted in retinal damage (Chen, 1993). In addition, *ex vivo* studies reported altered mitochondrial complex activity, reduced ATP synthesis and increased ROS production in purified rod IS and OS isolated from whole mouse eyeball cultures irradiated with blue light (Calzia et al., 2016). Moreover, oxidative stress resulting from mitochondrial disruption may be further amplified by non-mitochondrial chromophores (e.g., phototransduction pigments and their byproducts), which have been demonstrated to impinge on mitochondrial function by uncoupling OXPHOS and reducing ETC activity once activated by light (Shaban, Gazzotti and Richter, 2001; Vives-Bauza et al., 2008; Maeda et al., 2009). Taken together, these studies suggest an involvement of mitochondria as potential initiators of retinal light-triggered oxidative stress, which alters both the oxidative and bioenergetic balance of retinal neurons.

Associated diseases and current therapies

Although forms of retinopathies caused by excessive light exposure exist (e.g. from exposure to direct sunlight or excessive bright light), LD acts more frequently as an important risk factor contributing, together with other pathophysiological events, to alter the viability of retinal cells under stress. In this respect, light may act as a risk factor worsening retinal cell damage occurring in many neurodegenerative retinopathies involving the outer retina, such as retinal inherited degenerations (e.g., retinitis pigmentosa; RP) and the dry form of age-related macular degeneration (AMD), which share photoreceptor damage and death as common features of disease (Contín et al., 2016). Although the etiologies of these disorders are different (e.g., genetic mutations for RP; genetic and environmental factors for dry AMD), oxidative stress has been reported to be a common mechanism

impinging on photoreceptor health in both contexts (Kutsyr et al., 2020; Wang et al., 2022; Kushwah et al., 2023; Schick et al., 2016). Here, light may accelerate the production of ROS and concur to exacerbate photoreceptor degeneration.

There are almost no current therapies available in the clinics for RP and dry AMD. In effect, the only approved therapy for RP is Luxturna®, a gene therapy only approved for a small sub-population of patients that carries a specific mutation representing a small percentage of the total cases (Cross et al., 2022). Regarding dry AMD, the only available therapy in the USA is the complement inhibitor Avacincaptad pegol, which has been recently received the approval from the FDA for intravitreal administration (Girgis and Lee, 2023). Similar to therapies for DR, also in the case of intravitreal injections to treat AMD, side effects such as inflammation, hemorrhages and eye pain may appear (Cross et al., 2022; Girgis and Lee, 2023). Besides the therapeutical strategies specific for each disease, the management of LD is not based onto pharmacological or surgical treatments, given the prevalent role of light as a mere risk factor. In effect, the management of LD is predominantly focused on prevention by reducing the frequency or the intensity of light exposure through the use of protective eyeglasses/lenses or the adoption of practices that reduce exposure to light-emitting devices (Cougnard-Gregoire et al., 2023). Although these strategies may reduce the light damage, they are not effective *per se* in completely buffering the detrimental effects induced by continuous exposure to light sources.

1.3.2.2 Glaucoma

Glaucoma is an RGC-related vision threatening disease estimated to affect 80 million patients worldwide with a putative increase to 111.8 million by 2040 (Tham et al., 2014; Weinreb, Aung and Medeiros, 2014). Despite its high prevalence, the multiple factors concurring to determine disease progression still need to be well characterized, being its pathophysiology a complex interplay of different genetic, metabolic and environmental factors (Weinreb et al., 2016). As considered above (paragraph 1.1.2), RGCs live on metabolic knife-edge; therefore glaucoma-induced alterations of RGC bioenergetic and oxidative balance resulting from mitochondrial dysfunction may play a key role in this pathology.

Clinical manifestations and pathophysiology

Glaucoma comprises a group of optic neuropathies characterized by morpho functional deficits causing RGC degeneration. A common clinical symptom associated to glaucoma is represented by detectable changes at the ONH, characterized by focal or extended thinning of neuroretinal rim accompanied by enlargement and excavation of the optic nerve cup, indicative of reduced numbers of RGC axons and deformation of the lamina cribrosa (Casson et al., 2012; Weinreb et al., 2016). In addition, functional deficits are reported in glaucoma patients as progressive visual dysfunction, with an initial deterioration of the mid-peripheral visual field and a further progression in a centripetal manner until severe visual compromise (Weinreb, Aung and Medeiros 2014). RGC dysfunction and degeneration occur in all the forms of glaucoma and they appear to affect all RGCs independent from the specific subtype. The main risk factors associated to glaucoma are the advanced age, genetics, and an elevated IOP (Weinreb et al., 2016).

The increase in IOP is considered as a strong risk factor for glaucoma and characterizes the most frequent forms of glaucoma occurring worldwide, collectively defined as hypertensive glaucoma (as compared to the normotensive forms, where RGC degeneration occurs without IOP elevation; Weinreb et al., 2016). In hypertensive glaucoma, the increase in IOP occurs as a consequence of the unbalance between aqueous humor secretion by the ciliary body and outflow from the anterior chamber through the trabecular meshwork. In hypertensive glaucoma, the outflow of the aqueous humor is inhibited by occlusion or increased resistance at the trabecular meshwork, leading to the accumulation of fluid in the anterior chamber and to increased pressure in all the compartments of the eye (Tamm et al., 2015; Figure 5). The increased IOP can cause mechanical stress to the posterior part of the eye and damage ONH and RGCs, likely due to compression, deformation and remodeling of lamina cribrosa with axonal damage and reduced retrograde transport of cell components and molecules, including factors promoting neural trophism such as brain derived neurotrophic factor (BDNF) and nerve growth factor (NGF) (Fechtner and Weinreb, 1994; Burgoyne et al., 2005). Under stress, RGCs undergo a series of morpho functional degenerative processes, which initially reduce their activity and ultimately influence their survival, such as dendritic atrophy, reduced axonal transport, axon degeneration and cell death (Williams et al. 2013; Dengler-Crish et al., 2014; Syc-Mazurek and Libby, 2019). The exact pathophysiology and the overall nature of RGC stress in glaucoma still need to be established, although a complex interplay of concurring mechanisms including vascular dysfunction, glial activation, dysmetabolism, mitochondrial dysfunction, oxidative stress and inflammation, together with reduced neurotrophin transport and IOP elevation, may result in altered RGC viability (Weinreb et al., 2016).

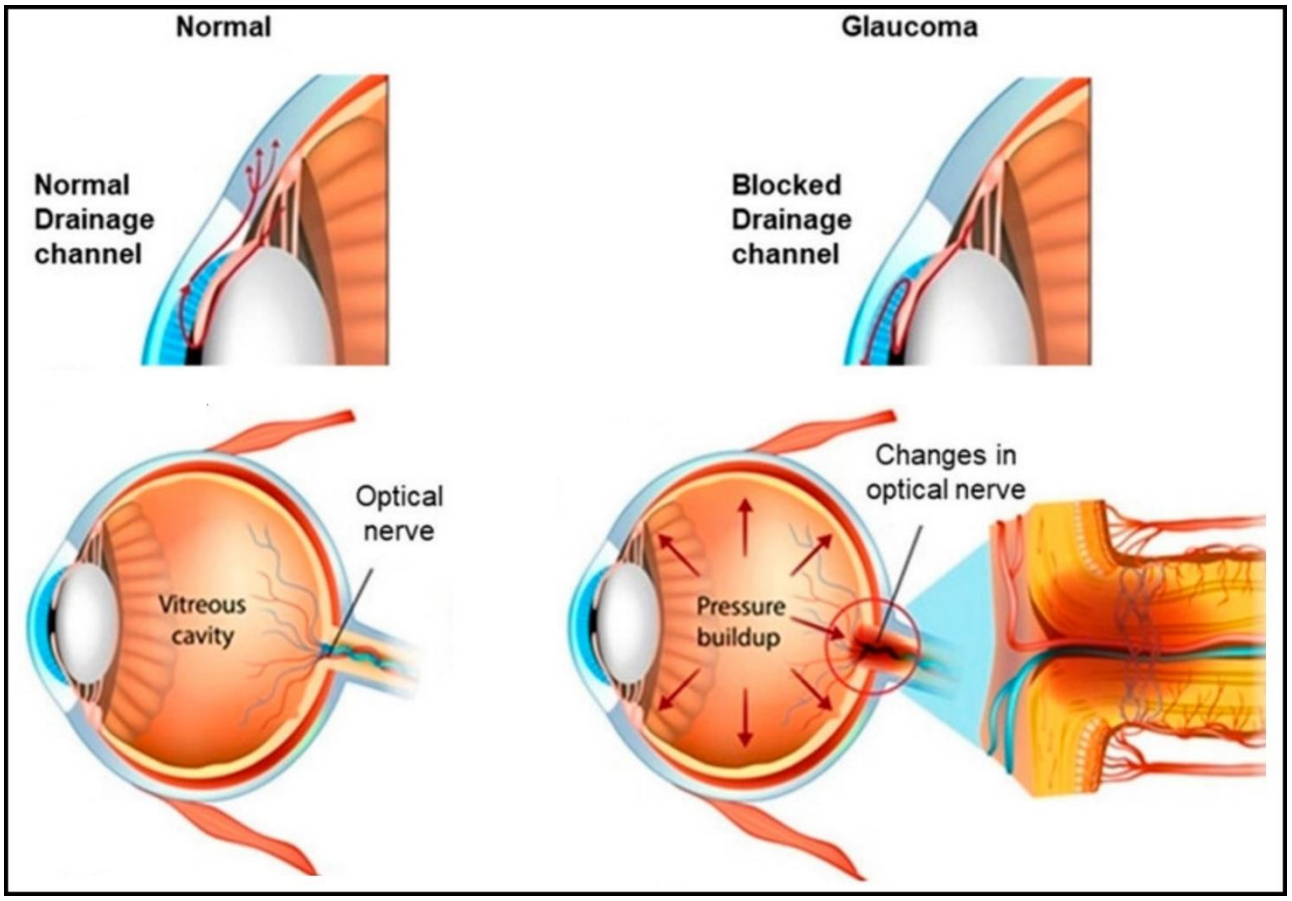

Figure 5. Schematic illustration showing the different dynamics of IOP establishment in hypertensive glaucoma compared to normal eyes. In healthy patients, the IOP is maintained at physiological levels by the balanced aqueous humor secretion from the ciliary body and its reabsorption at the trabecular meshwork. With normal IOP, the pressure on the posterior part of the eye is adequate and the optic nerve is not damaged. In hypertensive glaucoma, the blockage or the resistance of aqueous humor drainage at the trabecular meshwork induces the accumulation of this liquid into the anterior chamber, increasing the IOP. The augmented IOP exerts additional pressure to the posterior tissues of the eye, damaging the optic nerve. Modified from Albarqi et al., 2023.

Glaucoma and mitochondrial dysfunction

Considering their metabolic knife-edge (see Paragraph 1.1.2), it is not surprising that RGCs are particularly vulnerable to metabolic stress induced by dysfunction of metabolism and mitochondria. In this respect, many IOP-dependent alterations in RGC metabolism have been described in animal models of glaucoma, such as disturbed glucose metabolism, reduced pyruvate levels, reduced glucose and pyruvate transporters and NAD decline, before an evident optic nerve degeneration (Williams et al., 2017; Harun-Or-Rashid et al., 2018; Harder et al., 2020). These metabolic disturbances are accompanied by mitochondrial deficits, which further amplify the metabolic stress and decrease RGC viability. In DBA/2J (D2) mice, an inherited inbred strain developing glaucoma over time, RNA-sequencing demonstrated altered RGC gene expression of OXPHOS proteins at 9 months of age,

where RGC degeneration is still undetectable but IOP has started to increase (Williams et al., 2017). In addition, these transcriptional changes are accompanied by mitochondrial morphological alterations with reduced cristae volume in RGC somal and dendritic mitochondria, confirming mitochondrial dysfunction occurring prior to evident ON degeneration and RGC loss (Williams et al., 2017). Morphological alterations of RGC mitochondria have been further documented in the myelinated portion of the ON in D2 mice at 10 months of age, where mitochondria have small surface area, low density and disrupted cristae (Coughlin et al., 2015). Concomitantly, there is an IOP-dependent decline of ATP levels the ON, further evidencing RGC metabolic stress under glaucomatous disease (Baltan et al., 2010). Importantly, metabolic and mitochondrial dysfunctions have been confirmed in glaucoma patients. For instance, reduced plasma levels of nicotinamide, a precursor of NAD, and citrate, a metabolite of the TCA cycle, have been reported in glaucoma patients, suggesting systemic metabolic susceptibility in glaucoma (Fraenkl et al., 2011; Kouassi Nzoughet et al., 2019). Moreover, signs of dysfunctional mitochondria, such as reduced CI activity, mtDNA mutations, morphological remodeling and abnormal distribution have been reported in lymphoblasts from glaucoma patients and in post-mortem human retinal tissue with early glaucoma (Lee et al., 2012; Van Bergen et al., 2015; Sundaresan et al., 2015; Tribble et al., 2019). Taken together, these data suggest the involvement of dysmetabolism and mitochondrial dysfunction in the pathogenesis of glaucoma, which would reduce ATP supply to RGCs and induce a bioenergetic insufficiency altering RGC function and viability.

Dysfunctional mitochondria could increase the production of ROS, leading to an augmented oxidative stress that may amplify RGC damage under glaucomatous stress (Chrysostomou et al., 2013). In this respect, oxidative stress seems to occur in retinas of several models where ocular hypertension is artificially induced by surgical techniques, regardless of the mechanism of induction and the duration of the insult. In these models, the IOP elevation resulted in the early ROS increase and retinal lipid and protein oxidation, whilst reducing endogenous antioxidants and precociously activating Nrf2 pathway as a likely compensatory response to the increased oxidative stress (Moreno et al., 2004; Ko et al., 2005; Tezel, Yang and Cai, 2005; Ferreira et al., 2010; Naguib et al., 2021). Notably, all these changes occurred before detectable visual deficits and RGC degeneration, suggesting that the oxidative stress may concur in inducing RGC degeneration in these models. The altered redox balance characterized by increased ROS production and reduced antioxidant capacity have also been confirmed in retinas and ONs from 10-month-old D2 mice, where the IOP elevation occurs spontaneously (Jassim et al., 2021). This evidence suggests that oxidative stress is likely to be involved in the pathogenesis of glaucoma and that metabolic stress induced by dysmetabolism and

mitochondrial dysfunction may alter the bioenergetic and redox balance of RGCs, thus promoting RGC dysfunction and degeneration.

Current therapies

Since IOP is the most controllable risk factor, current therapies for glaucoma are mainly focused on IOP reduction using different pharmacological and surgical strategies. Topical treatments with pharmacological agents are the first-line strategy to treat hypertensive glaucoma by using drugs aiming at either reducing aqueous humor secretion (e.g., β-adrenergic receptor blockers, agonists of α-adrenergic receptors and inhibitors of carbonic anhydrase) or favoring aqueous humor outflow (e.g., prostaglandin analogues and cholinergic agonists) to lower IOP (Zhang, Zhang and Weinreb, 2011). Although the efficacy of these agents is well documented, some of them requires repeated administrations and cause some side effects ranging from darkening of periocular skin to respiratory and cardiovascular defects (Weinreb et al., 2016). Alternatively, the increase in IOP can be treated surgically by either laser trabeculoplasty, which induces the remodeling of extracellular matrix in the trabecular meshwork favoring aqueous humor outflow, or by trabeculectomy. However, these surgical strategies are associated to risk of complications as anterior chamber inflammation, ocular discomfort, infection, suprachoroidal hemorrhage and transient alterations in IOP (Weinreb et al., 2016). These drawbacks set some limits in the managing of IOP as a therapeutic strategy for treating glaucoma. In addition, many glaucoma patients are refractory to IOP lowering treatments and others loose visual function even in the presence of stabilized IOP, suggesting that adjuvant therapies independent from IOP are needed to effectively delay the progression of the disease. Moreover, RGCs in patients suffering from normotensive glaucoma degenerate under normal IOP range, requiring different strategies for this type of disease (Mozaffarieh and Flammer, 2007). Thus, the available evidence suggests the necessity to study the mechanisms behind the alteration of RGC viability in glaucomatous diseases to provide new therapeutic strategies to directly target RGC neurodegeneration.

1.4 Aims of the thesis

The current therapies for many retinopathies often target the late stages of the disease or, alternatively, the most common risk factors. Although effective in treating the pathological features of the disease, these current strategies require repetitive drug administrations and are often associated with side

effects affecting homeostatic mechanisms. Moreover, the targeting of disease-associated risk factors may limit the management of some retinal disorders to a restricted subtype of patients, where the risk factor is present and exerts relevant pathologic effects. In addition, it must be considered that the treatment, although beneficial, may not lead to complete resolution of the pathology due to the multifactorial nature of the vast majority of retinal diseases. Therefore, these limitations dictate the necessity to further investigate the mechanisms regulating the viability of retinal neurons in health and disease and to provide new complementary strategies to prevent or retard the progression of the disease from the early stages and in a specifically neuron-targeted manner.

Given the high metabolic demand of the retina, alterations in metabolic mechanisms and their related downstream effects may play a key role as determinants of retinal cell viability and function. Many retinal neurodegenerative diseases with different etiologies are characterized by early mitochondrial dysfunction causing bioenergetic insufficiency and downstream ROS production triggering oxidative stress. The dysregulation of the bioenergetic and oxidative balance seems to be a common target of many stressors impairing neuronal viability, thus suggesting key mechanisms fundamental for regulating retinal health. In this respect, the retinal neurodegenerative diseases are suitable contexts where the role of bioenergetic and oxidative balance in determining neuronal viability can be studied.

According to the state of the art, the aims of this thesis are: (i) to prove further insights into the role of the oxidative balance in regulating retinal neuron viability under different stress contexts, where mitochondrial activity has been reported to be altered (paragraphs 3.1-3.3); (ii) to confirm the role of the neuronal bioenergetic balance in determining the viability of retinal neurons using RGCs as a model (paragraph 3.4); (iii) to suggest novel non-invasive complementary strategies for the management of neurodegenerative retinopathies characterized by metabolic stress.

Chapter 2

Materials and methods

2.1 Animals

Animals were managed in accordance with the Association for Research in Vision and Ophthalmology statement for the Use of Animals in Ophthalmic and Vision Research. All the studies are also in agreement with the European Communities Council Directive (2010/63/UE) and the Italian guidelines for animal care (DL 26/14). The experimental protocols were authorized by the Commission for Animal Wellbeing of the University of Pisa (protocols no. 133/2019-PR, February 14, 2019 (paragraphs 3.1 and 3.2); 4/2022 (paragraph 3.3)), by the Ministry of Health (protocol no. 307/2022-PR; paragraph 3.3) and by the Stockholm's Committee for Ethical Animal Research (10389-2018; paragraph 3.4). The principles of the 3Rs (replacement, reduction, and refinement) for ethical use of animals in scientific research were applied to reduce both the number and suffering of the animals. Animals were housed in a regulated environment (23 ± 1°C, 50 ± 5% humidity) with 12 h light/dark cycles and fed with a standard diet and water ad libitum. Both rats and mice were used depending on the experimental model used in the different studies. Male Sprague Dawley rats (SD; 8 weeks old, about 300 g; purchased from Envigo Italy, San Pietro al Natisone, Italy) were used for the experiments shown in paragraphs 3.1-3.3, whereas C57BL/6J (B6) and MitoV mouse strains were bred and used at 12–20 weeks of age for the study in paragraph 3.4. The MitoV mouse strain is on a B6 background and expresses YFP under a rat neuron-specific Eno2 promoter. YFP is localized to mitochondria through a Cox8a gene-targeting signal fused to the YFP N-terminus. This line was selected due to its specificity in inner retinal expression, specifically restricted to RGCs (Tribble et al., 2021). The strain has been further characterized in previous reports (Tribble et al., 2021).

2.2 Experimental models

2.2.1 STZ-induced model of DR

The experimental model of DR used in the study reported in paragraph 3.1 was performed by using a rat model of streptozotocin (STZ)-induced model of diabetes. STZ (Sigma-Aldrich, St. Louis, MO, United States) diluted in citrate buffer, pH 4.5, was intraperitoneally injected at 65 mg/kg. Age-

matched rats treated with vehicle were considered as the control group. Blood glucose was measured 3 days after the injection by tail sampling using a OneTouch Ultra glucometer (LifeScan Inc, Milpitas, CA, United States) to confirm the diabetic induction. Animals were considered diabetic if glycemia was ≥250 mg/dl. Blood glucose level was then regularly checked once a week for the entire experimental period.

2.2.2 Light-induced damage

The experimental model of LD related to the experiments described in paragraph 3.2 was obtained in male SD rats following protocols in line with that reported in a previous study (Riccitelli et al., 2021). In particular, rats were dark-adapted overnight and then their pupils were dilated by 1% tropicamide eye drops (Allergan S.p.A.) immediately before the light exposure. Each animal was kept separately in a small cage and placed in the middle of a custom-made light box apparatus (dimensions 72 × 61 × 52 cm). Light intensity was measured through a digital illuminance meter (Dr. Meter, Ahern Ave, Union City, CA, USA). Rats were exposed to diffused 1000 lux cool-white light continuatively for 24 h emitted from six light-emitting diode bulbs. The temperature of the apparatus was controlled by a cooling aeration system based on a small air fan and maintained at (25 ± 1.5 °C). After light exposure, the rats were returned to the dim cyclic light environment. Two days later, rats underwent to further analyses.

2.2.3 Rat model of hypertensive glaucoma

The experimental model of hypertensive glaucoma in the study presented in paragraph 3.3 was performed in male SD rats where ocular hypertension was artificially induced by the administration of methylcellulose (MCE) in agreement with published procedures (Dal Monte et al., 2020a; Dal Monte et al., 2020b). Briefly, 2% MCE w/v in sterile saline was prepared to obtain a solution viscosity ranging from 3500 to 5600 cps. Rats were anesthetized with an intraperitoneal injection of sodium pentobarbital (30 mg/kg) and injected into the anterior chamber with 15 µL of the MCE solution in both eyes using a Hamilton syringe equipped with an 18-gauge needle. The needle was inserted in the iridocorneal angle at about 1 mm from the ora serrata and oriented parallel to the iris surface. After the slow injection of MCE (1-minute duration), the needle was kept in place for 1 minute to avoid MCE outpours. Immediately after the injection of MCE, antibiotic eyedrops were instilled in order to prevent the occurrence of endophthalmitis.

2.2.4 Retina axotomy explant model

The retinal axotomy model used in the study in paragraph 3.4 was performed as previously reported (Tribble et al., 2021). Briefly, B6 mice were euthanized by cervical dislocation, retinas immediately dissected in ice-cold HBSS and flat mounted on inserts for cell culture (Millicell 0.4 µm pore; Merck) with GCL up. Retinas were cultured (37 °C, 5% CO_2) in media composed of Neurobasal-A supplemented with 2 mM L-glutamate (GlutaMAX, Gibco), 2% B27, 1% N2, and 1% penicillin/streptomycin (Gibco) in 6-well culture plates. After 2 days, half of the media volume was replaced. Retinas were removed from culture to be further processed after 3 days ex vivo (DEV). For controls (0 DEV), eyes were enucleated, and retinas directly fixed and processed for immunofluorescent labelling.

2.2.5 Intravitreal rotenone model

Rotenone-induced retinal degeneration model was performed in B6 mice following established protocols (Tribble et al., 2021). B6 mice underwent anesthesia by an intraperitoneal injection of mixed ketamine (37.5 mg/kg) and medetomidine hydrochloride (1.25 mg/kg). Two µl of 10 mM rotenone diluted in DMSO (Sigma-Aldrich, St. Louis, MO, United States) or DMSO only (control) was bilaterally injected into the vitreous using a 33G tri-beveled needle on a 10 µl glass syringe (WPI). Mice were euthanized by cervical dislocation 24 h after rotenone injection and eyes were immediately isolated for further analyses.

2.3 Measurement of IOP

A time dependent IOP profile was performed on animals in the study presented in the paragraph 3.3. IOP was non-invasively assessed daily using rebound tonometry (Tonolab; iCare Finland Oy, Helsinki, Finland) before and after MCE injections in every group for the period under investigation (28 days; see paragraph 3.3). Multiple sampling procedures (5–10 readings) were performed at the same range of time during the day.

2.4 Electroretinogram

Retinal function was evaluated by different type of electroretinogram (ERG). In particular, scotopic, photopic and pattern ERG (PERG) were performed to assess the activity of different retinal circuits and cell types. The ERG recording was performed at the endpoint of the studies described in paragraphs 3.1-3.3 using commercially available setups (Biomedica Mangoni, Pisa, Italy; Retimax Advanced; CSO, Firenze, Italy). For scotopic ERG, animals were dark-adapted overnight and anesthetized by intraperitoneal injection of 30 mg/kg sodium pentobarbital. Pupils were dilated with a topical drop of 1% tropicamide (Allergan S.p.A., Rome, Italy) and the body temperature was kept constantly at 37.5°C by a heating pad. The electrophysiological signals were recorded using silver/silver chloride corneal ring electrodes inserted under the lower eyelids to avoid visual field obstruction. In order to prevent dryness and clouding of the ocular surface, saline solution drops were intermittently instilled. Each corneal electrode was referred to a needle electrode inserted subcutaneously at the level of the corresponding frontal region, and the ground electrode was inserted subcutaneously at the tail root. Scotopic ERG, which primarily measures rod function, was evoked by flashes of 1 log cd-s/m^2 light intensity over a dark background delivered by a Ganzfeld stimulator. For photopic ERG, after the scotopic stimulation the animals underwent light adaptation to 30-cd·s/m^2 rod-saturating background light for 10 minutes before photopic cone-mediated responses were recorded using a 3-cd·s/m^2 stimulus delivered over the same background light. The average of 20 consecutive responses was considered for the photopic ERG analyses. The interval between light flashes was adjusted to appropriate times that allowed response recovering (20 s for scotopic responses, 3 s for photopic responses). PERG recordings were then performed by delivering pattern stimuli consisting of 0.05-c/° black and white bars reversing at 1 Hz presented at 98% contrast. The pattern stimuli were administered through a light-emitting diode display with a mean luminance of 50 cd/m^2 aligned at about 20 cm from the corneal surface. A total of 200 signals were averaged. ERG responses were collected simultaneously from both eyes, amplified at 1000x gain, filtered with a 0.2–500 Hz bandpass and digitized at 5 kHz rate with a data acquisition device. ERG waveforms were analyzed using customized programs (Biomedica Mangoni; Retimax Scientific 7.0.4 software (CSO)). In compliance with the International Society for Clinical Electrophysiology guidelines, the b-wave amplitude was measured from the trough of the a-wave to the peak of the b-wave or, if no a-wave was detectable, from the pre-stimulus baseline. In the photopic ERG waveforms, the photopic negative response (PhNR) was identified as the first negative deflection after the b-wave. The PERG waveforms were analyzed using to retrieve the amplitude of positive (N35–P50) and negative (P50–N95) components.

2.5 Detection of vascular leakage by Evans blue dye perfusion

Animals were anesthetized with an intraperitoneal injection of 30 mg/kg sodium pentobarbital and perfused through the left ventricle with 0.5% Evans blue dye (Sigma-Aldrich) in phosphate-buffer saline (PBS) that was allowed to circulate for 10 min. The animals were then sacrificed, and retinas were dissected and flat mounted onto microscope slides. Retinas were then examined by an epifluorescence microscope (Ni-E; Nikon Europe, Amsterdam, Netherlands) and the images were acquired using a 10x plan apochromat objective and a digital camera (DS-Fi1c camera; Nikon-Europe).

2.6 Western blot

Animals were euthanized and eyes enucleated. Retinas were isolated from the other ocular tissues by microsurgical procedures. The optic nerves were isolated from the brain by cutting right before the optic chiasm. Two retinas or optic nerves were pooled together in a single sample. All the samples were then snap frozen in dry ice and stored at − 80 °C until further processing. Samples were lysed by radioimmunoprecipitation assay (RIPA) lysis buffer (Santa Cruz Biotechnology, Dallas, TX, United States) implemented with phosphatase and proteinase inhibitor cocktails (Roche Applied Science, Indianapolis, IN, United States). Protein content was evaluated by Micro BCA protein assay (Thermo Fisher Scientific, Waltham, MA, United States). Equal amounts of proteins per sample were separated by SDS-PAGE (4–20%; Bio-Rad Laboratories, Inc., Hercules, CA, United States) and gels were subsequently transblotted onto nitrocellulose membranes (Bio-Rad Laboratories, Inc.). Membranes were blocked with either 5% skim milk or 4% bovine serum albumin (BSA; Sigma-Aldrich) in TBS/Tween for 1 h at room temperature. Afterwards, the membranes were incubated overnight at 4 °C with the primary antibodies targeting the markers of interest in each study (for information on the specific markers and antibodies see chapter 3). Thereafter, blots were incubated for 2 h at room temperature with appropriate HRP-conjugated anti-rabbit, anti-mouse, anti-hamster, or anti-goat secondary antibodies, diluted 1:5000 (Santa Cruz Biotechnology). Blots were developed using the Clarity western enhanced chemiluminescence substrate (Bio-Rad Laboratories, Inc.) and the images were acquired by the ChemiDoc™ Imaging System (Bio-Rad Laboratories, Inc.). Membranes were stripped and reprobed with either rabbit polyclonal anti-NF-kB p65 (ab16502, Abcam; 1:1000) or mouse monoclonal anti-β-actin (A2228, Sigma-Aldrich; 1:2500) antibodies to visualize the bands related to the loading control (β-actin) or normalizers (NF-kB p65). The optical

density (OD) relative to the target bands (Image Lab 6.0 software; Bio-Rad Laboratories, Inc.) was normalized to the corresponding OD of β-actin as loading control or NF-kB p65 as appropriate.

2.7 Immunofluorescence

Enucleated eyes were immersion-fixed in 4% paraformaldehyde (PFA) in 0.1 M PBS for 2 h at room temperature. Fixed eyes were transferred to 25% sucrose in 0.1 M PBS and stored at 4°C. Following the inclusion in cryo-gel medium, fixed samples were cut into 10 μm thick coronal sections and mounted onto glass slides. Mounted sections were then incubated with the solutions of appropriate primary antibodies diluted in 0.1 M PBS containing 0.1% v/v Triton X-100, overnight at 4°C (see chapter 3 for markers and antibodies). After being rinsed, mounted sections were incubated with appropriate secondary antibodies conjugated with either Alexa-Fluor 555 (ab150078, Abcam; 1:200) or Alexa-Fluor 488 (ab150077, Abcam; 1:200) diluted in 0.1 M PBS containing 0.1% v/v Triton X-100 for 2 h at room temperature. Retinal sections were coverslipped with Fluoroshield mounting medium containing 4′, 6-diamidino-2-phenylindole (DAPI; Abcam).

Retinal explants at 3 DEV (paragraph 3.4) were fixed for 30 min, detached from the cell culture insets, and transferred on slides. On the other hand, retinal flat-mounts and RPE-choroid complexes were isolated from fixed eyes. Tissues were incubated with appropriate solutions of primary antibodies at 4 °C (see chapter 3). After rising in 0.1 M PBS, tissues were then incubated in appropriate secondary antibodies conjugated with either fluorescein, Alexa-Fluor 568 or Alexa-Fluor 488 as further indicated in chapter 3. Four radial incisions were made in the retinal whole-mounts and RPE-choroid complexes that were mounted on gelatin-coated glass slides. Images were acquired through an epifluorescence microscope (Ni-E, Nikon Europe, paragraphs 3.1-3.3; Leica DMi8, Leica, paragraph 3.4) at 20x or 40x using a digital camera (DS-Fi1c camera, Nikon Europe, paragraphs 3.1-3.3; Leica DFC7000 T camera, Leica, paragraph 3.4). Levels of the immunohistochemical signal on immunolabelled retinal sections were quantified by averaging the fluorescence intensity of five coronal sections randomly chosen from each retina. Four images per section were quantified by using the analysis tool of Adobe Photoshop. Images were then turned into grayscale, normalized for the background and analyzed for the mean gray levels to quantify the immunofluorescence intensity for each marker.

2.8 Mitochondrial morphological analyses

The analysis of mitochondrial morphology was performed in retinal and optic nerve sections from MitoV mice processed for high resolution confocal microscopy. Mice were euthanized and eyes enucleated. The brain was isolated with the attached optic nerves. Tissues were fixed in 3.7% PFA for 24 h and cryo-protected by immersion in 30% sucrose solution. Eyes were directly frozen in optimal cutting temperature medium (Sakura) on dry ice, whereas optic nerves were separated from the brain and then included in the same medium. Eyes and optic nerves were cryo-sectioned in 20 µm-thick coronal and longitudinal sections respectively using a cryostat (Cryostar NX70, Thermo Scientific). Sections were immunolabelled with chicken polyclonal anti-GFP primary antibody (ab13970, Abcam; 1:500) at 4 °C overnight. Anti-GFP primary antibody was used to limit loss of signal from potential bleaching of YFP. Thereafter, sections were stained with Alexa Fluor 488 conjugated goat anti-chicken secondary antibody (A11039, Invitrogen; 1:500) for 4 h at room temperature. Tissue was counterstained with DAPI (1 µg/mL in 1 M PBS) for 10 min and mounted using Fluoromount-G and glass coverslips (Invitrogen). The image acquisition was performed using confocal imaging on a Zeiss LSM-980 Airy (63×, 1.5 × optical zoom, image size 89.8 × 89.8 µm, 0.07 µm pixel size, z-stacks with 0.23 µm optimal interval). Images from retinal sections were acquired from central retina at ~ 500 µm lateral to the optic nerve head. Images from optic nerve sections were acquired from areas around the optic chiasm used for reference. DAPI channel was also imaged for reference purposes in retinal samples. Retinal images encompassed NFL, GCL and IPL. Mitochondrial particles were reconstructed in 3D using Imaris software (version 9.3.1). NFL/GCL and IPL were cropped for the analyses and reconstructed separately with different settings. Volume reconstructions were performed using the surface tool and volumes under 125 voxels were filtered and discarded from subsequent analysis to reduce noise. Volume and sphericity of each mitochondrial particle were calculated by the software and plotted as an average per retina or optic nerve. For the measurement of the volume, both the mean and the sum were calculated. Volume mean and volume sum in each retina were normalized to the number of GFP positive cells and then to the volume crop in NFL/GCL, or to only volume crop in IPL. The same parameters were normalized to the volume crop in the optic nerve images.

2.9 Measurement of ROS levels

ROS levels were measured using the general oxidative stress probe 2′,7′-dichlorodihydrofluorescein diacetate (DCFH-DA) (Invitrogen). DCFH-DA, a nonfluorescent dye, is cleaved by esterase activity to yield dichlorodihydrofluorescein (DCFH), which is subsequently oxidized by ROS to form fluorescent dichlorofluorescein (DCF). Retinal samples containing 20 µg proteins were incubated with 50 µM DCFHDA in 96-well plates. After 60 min at 37°C, fluorescence intensity was detected over 60 min using a microplate reader (FLUOstar Omega, BMG Labtech, Ortenberg, Germany) at excitation 488 nm and emission 525 nm. The relative ROS levels were expressed as arbitrary fluorescence units per µg of protein.

2.10 Measurement of oxidative stress markers

Oxidative stress in the retina was measured by evaluating the levels of common markers associated to lipid peroxidation (malondialdehyde (MDA) and 4-hydroxynonenal (4-HNE)), oxidative damage to DNA (8-hydroxy-deoxyguanosine (8-OH-dG)) and endogenous antioxidants (GSH). The levels of MDA, 4-HNE, 8-OH-dG, and GSH were evaluated using commercially available kits: Lipid Peroxidation (MDA) Assay Kit (ab118970, Abcam), Lipid Peroxidation (4-HNE) Assay Kit (ab238538, Abcam), 8-Hydroxy 2 Deoxyguanosine ELISA Kit (ab201734, Abcam), and GSH+GSSG/GSH Assay Kit (Colorimetric) (ab239709, Abcam), according to the manufacturer's instructions.

2.11 Luminometry-based ATP and NAD assays

ATP or NAD content was analyzed *in vitro* and *in vivo* following a similar protocol. Brain hemispheres were harvested from the whole cortex of B6 mice. Each hemisphere was transferred to 800 µl of dispase (5000 U; Corning) and incubated on a Thermomixer C heating block (Eppendorf) at 37 °C, 350 rpm for 30 min before being dissociated by gentle trituration. Cell concentration was calculated by cell counting on a C-Chip hemocytometer (NanoEntek) and each cell suspension was diluted to 2 million cells/mL. Aliquots of each cell suspension for each sample were incubated with different concentrations of pyrroloquinoline quinone (PQQ; see paragraph 3.4.2) for 2 h at 37 °C, 5% CO_2. Cells maintained in Hank's balanced salt solution (HBSS) for the same time were used as controls. Samples were then homogenized for 15 s at 30,000 min^{-1} (VDI 12, VWR) and ATP or NAD

content was measured using a luminometry-based assay (CellTiter-Glo® Luminescent Cell Viability Assay for ATP, NAD/NADH Glo-™ for NAD; Promega). Reagents of the kit were prepared according to the manufacturer's instructions. Equal volumes (50 µl) of sample (reaching a concentration of 100,000 cells/well) and working reagent were combined in a 96-well plate (Nunc™ F96 MicroWell™ White Polystyrene plate, Thermo Fisher Scientific). Luminescence was measured using a Tecan Infinite 200 at approximately 10 min for ATP and 1 h for NAD from initial mixing according to the manufacturer's instructions. To measure the *in vitro* ATP content on retina, optic nerve and superior colliculus (see paragraph 3.4), B6 mice were euthanized by cervical dislocation, whole eyes enucleated, and retinas dissected in HBSS. The brain was removed, and the superior colliculus was isolated. Optic nerves were cut at 3 mm from the end proximal to the eye, left and right segments were collected in two different samples and stored at 4 °C in HBSS until further processing. Retinas from left and right eyes were pooled to form a single sample. Retinas and superior colliculi were dissociated in 500 and 800 µl of dispase respectively and processed as described above. Cells from dissociated retinas and superior colliculi, as well as isolated optic nerve segments, were incubated with PQQ for the same time and in the same conditions as above. The bioluminescent assay was then conducted as previously described. The assessment of ATP *in vivo* was performed on B6 mice. Retinas, optic nerves, and superior colliculi were collected and processed as described above. A direct homogenization after the cell dilution was performed and the luminescent assay was run with the same procedure previously indicated.

2.12 JC-1 staining

JC-1 staining was performed according to previous protocols with some variations (Sivandzade, Bhalerao and Cucullo, 2019). Briefly, hemispheres from whole brain cortexes of B6 mice were harvested and brain cortical cells were obtained as described in paragraph 2.11. Cell suspensions were diluted at a concentration of 1 million cells/mL, then aliquots from each sample were incubated with solutions of PQQ at different concentrations (see paragraph 3.4) for 2 h. At the last 30 min of incubation, JC-1 (Thermo Fisher Scientific, dissolved in DMSO) was added at a final concentration of 2 µM and cells were kept in the dye until the end of PQQ incubation. Cells were washed from the dye, resuspended in HBSS and 50 µl of sample was loaded on a 96-well plate (Nunc™ F96 MicroWell™ White Polystyrene plate, Thermo Fisher Scientific) in an alternate manner to avoid interference between adjacent wells. Fluorescence at 535 nm (green; monomer) and 590 nm (red; aggregate) was measured using a Tecan Infinite 200 and $\Delta\Psi$ levels were expressed as the ratio of red

to green fluorescence. To measure ΔΨ levels in treated retina, optic nerve and superior colliculus, B6 mice were euthanized and the tissues collected as described in the previous section. Cells from retinas and superior colliculi were diluted at a concentration of 1 million cells/mL and incubated with PQQ for 2 h. JC-1 was administered at the same concentration and times used for cortical cells. Optic nerves were incubated with PQQ for 1 h, homogenized in PQQ at 8000 min^{-1} speed (VDI 12, VWR) and incubated with 2 μM JC-1 for 30 min at 37 °C for a total of 2 h of incubation in PQQ. Fluorescence was measured as previously described.

2.13 Quantitative real-time PCR

B6 mice were euthanized by cervical dislocation and eyes were enucleated and retinas dissected in ice-cold HBSS. A second operator isolated the optic nerves from the brain and cut around the optic chiasm. A single retina comprised of a sample, whereas left and right optic nerve segments were pooled together to make a unique sample. All the samples were then snap frozen in dry ice and stored at − 80 °C until further processing. A total RNA extraction was performed homogenizing retinas and optic nerves in buffer RLT (Qiagen) with 1% β-mercaptoethanol (Fisher Scientific) and using a QIAshredder kit (Qiagen) according to the manufacturer's instructions. A column-based kit (RNeasy Mini Kits, Qiagen) was used to extract RNA according to the manufacturer's instructions. Isolated RNA was suspended in nuclease-free water and RNA concentration was quantified using a NanoDrop™ One (Thermo Fisher Scientific). cDNA was generated starting from 1 μg of input RNA through an iScript™ cDNA Synthesis Kit and a MyIQ thermocycler (both Bio-Rad). Quantitative real-time PCR was performed at the CFX96 Touch Real-Time PCR Detection System thermocycler (Bio-Rad) using SsoAdvanced Universal SYBR Green Supermix (Bio-Rad), cDNA (15 ng for retina; 3 ng for optic nerve) and the appropriate DNA templates (Prime PCR Assay, *mus musculus*, Bio-Rad): *mt-Co2*, *Rsp18*, *Pgc-1α*, *Tfam*, *Ndufb8*, *Sdhb*, *Uqcrc2*, *mt-Co1*, *Atp5a1*. The expression levels were calculated by the ΔΔCt method. The mtRNA/nuRNA ratio was calculated using *mt-Co2* and *Rsp18* as the reference mitochondrial and nuclear gene, respectively, as previously described (Quiros et al., 2017). *Rsp18* was used as housekeeping gene when the expression of the other genes was calculated.

2.14 Metabolomics

B6 mice were euthanized by cervical dislocation. Eyes were enucleated and retinas were immediately dissected in ice cold HBSS, wiped dry, weighed and frozen on dry ice. A second investigator isolated the optic nerves. Optic nerves were cut at 3 mm from the end proximal to the eye and frozen as for retinas. Each sample comprised a single retina or an isolated optic nerve segment. Tissue was stored at − 80 °C and shipped kept in dry ice to the Swedish Metabolomics Centre for sample processing. 200 µl of extraction buffer (80:20 v/v MeOH:H_2O) including internal standards were added to the tubes together with 1 tungsten bead. Tissues were shaken at 30 Hz for 3 min in a mixer mill and samples were then centrifuged at 4 °C, 18620 g for 10 min. Afterwards, 200 µl of the supernatant was transferred to micro vials and evaporated to dryness in a speed-vac concentrator. Samples were stored at − 80 °C and small aliquots of the remaining supernatants were pooled and used to create quality control (QC) samples. Prior to the analysis, samples were re-suspended in 10 + 10 µl methanol and elution solvent A. The samples were analyzed in batches according to a randomized run order. Each batch of samples was first analyzed in positive mode. After all samples within a batch had been analyzed, the instrument was switched to negative mode and a second injection of each sample was performed. The chromatographic separation was performed on an Agilent 1290 Infinity UHPLC-system (Agilent Technologies, Waldbronn, Germany). 2 µl of each sample were injected onto an Atlantis Premier BEH-Z-HILIC VanGuard FIT (1.7 µm, 2.1 × 50 mm) column (Waters Corporation, Milford, MA, USA) held at 40 °C. The HILIC gradient elution solvents were (A) 10 mM ammonium formate, 5 µM Medronic acid in H_2O, pH 9 and (B) 90:10 Acetonitrile: [10 mM ammonium formate in H_2O], pH 9. Chromatographic separation was achieved using a linear gradient (flow rate of 0.4 mL/ min): min 0 = 90% B, min 6 = 80% B, min 9.5 = 20% B, min 11 = 90% B. The flow rate was then increased to 0.7 mL/min for 2 min, held at this rate for 0.5 min, and further reduced to 0.4 mL/min for 0.5 min before the next injection. Compounds were detected with an Agilent 6546 Q-TOF mass spectrometer equipped with a jet stream electrospray ion source operating in positive or negative ion mode. MSMS analysis was run on the QC samples for identification purposes. All data pre-processing was performed using the Agilent MassHunter Profinder version B.10.0 SP1 (Agilent Technologies Inc., Santa Clara, CA, USA). Sixty-three (retina) or seventy-three (optic nerves) low molecular weight metabolites that could be certified with standards were detected. The quantification of the metabolites was calculated as area under the curve of the mass spectrometry peak and normalized first to an internal standard for negative and positive runs, then for the weight of the tissue for retinal samples. Data were analyzed and graphs were made using MetaboAnalyst (version 5.0) and R. All data were subject to Pareto scaling (van den Berg et al., 2006). Hierarchical clustering (HC)

(Spearman, Average) was used to create the dendrograms. Principal component analysis (PCA) was performed in R (4.1.0) using the factoextra package. Comparisons between groups were analyzed by two-sample t-tests with an adjusted p value (false discovery rate, FDR), using a cutoff of 0.05 considered significant. Quantitative pathway analysis was performed using the *Mus musculus* KEGG library in MetaboAnalyst and a background metabolome of all detected metabolites.

2.15 Statistical analyses

Graph Pad Prism 8.0.2 software (Graph-Pad Software, Inc., San Diego, CA, United States) and R were used for the statistical analyses. A Shapiro Wilk test was used to verify the normality of the data. A Student's t-test, one-way or two-way ANOVA (followed by multiple comparison post hoc tests as indicated below) were applied as appropriate to analyze normally distributed data. A Mann–Whitney test was used to analyze non-normally distributed data. Differences with $p < 0.05$ were considered significant. All data are expressed as means ± SEM or SD of the indicated n values as indicated. The box plots related to the data of paragraph 3.3 are shown with minimum to maximum whiskers. On the other hand, in the box plots shown in paragraph 3.4, the median is represented by the center hinge with upper and lower hinges indicating the first and third quartiles, whereas whiskers denote 1.5 times the interquartile range. The graphs in paragraphs 3.1-3.3 were made in Graph Pad Prism 8.0.2, whereas R or MetaboAnalyst 5.0 (for dendrograms) were used for the creation of graphs shown in paragraph 3.4.

Chapter 3

Results

3.1 The positive modulation of the oxidative balance by an antioxidant compound improves neurovascular function under hyperglycemic stress

3.1.1 Background

Elevated blood glucose mediates the overactivation of mitochondrial activity, resulting in the onset of oxidative stress and activating the early cascade of damaging events both in retinal neurons and blood vessels characteristic of DR (see chapter 1). The use of dietary compounds with antioxidant/anti-inflammatory properties may be a good strategy to positively modulate the oxidative status in DR and protect retinal cells from damage, given their extensive bioactivity and limited risk of side effects (Rossino and Casini, 2019). Among natural compounds exerting antioxidant/anti-inflammatory properties, anthocyanin subcomponents, and in particular cyanidins as cyanidin-3-glucoside (C3G), have been shown to display a good uptake rate, a low decay and a predominant antioxidant capacity observed in several diabetic complications including DR, thus resulting one of the most pharmaceutically promising class of nutrients regulating the oxidative balance under hyperglycemia (Khoo et al., 2017; Sasaki et al., 2007; Wang et al., 2016; Li et al., 2018; Qin et al., 2018). Additional antioxidant/anti-inflammatory compounds belong to the extensive family of plant-derived polyphenols, among which verbascoside exerts an anti-inflammatory role due to its ROS scavenging, antioxidant and iron chelating properties (Perron and Brumaghim, 2009; Burgos et al., 2020). In addition to plant-derived antioxidant compounds, the activation of enzymes involved in antioxidant defenses has been related to the activity of zinc, which indirectly reduces the rate of ROS generation (Kamińska et al., 2021).

In this study, the efficacy of a compound including C3G, verbascoside and zinc was investigated with the aim of counteracting the oxidative stress due to hyperglycemia-driven ROS generation using the STZ rat model of diabetes, where hyperglycemia occurs after the STZ-induced acute disruption of pancreatic beta cells and the drastic interruption of insulin production. This model mimics the early

stages of DR occurring in humans, being characterized by an increased expression of oxidative stress and inflammation markers resulting in vascular alterations and retinal dysfunction (Naderi et al., 2019).

3.1.2 Treatments and experimental design

Thirty-two rats were divided in four groups of eight animals each: control, STZ untreated, STZ-treated with the low dose of the mixture and STZ-treated with the high dose. Among diabetic rats, 16 animals were treated with a compound including *Oryza sativa L.* seeds (C3G titrated at 20%), *Verbascum thapsus L.* (verbascoside titrated at 10%) and zinc gluconate (zinc titrated at 13.23%) with a content ratio of 60:30:10, respectively. The compound was diluted in water at 84 mg/mL and administered at low dose (100 µL containing 1.0 mg of C3G, 0.25 mg of verbascoside and 0.125 mg of zinc) or high dose (300 µL containing 3.0 mg of C3G, 0.75 mg of verbascoside and 0.375 mg of zinc). Rats were treated once daily by oral gavage for 30 days after STZ administration. Thirty days after STZ injection, the animals underwent to ERG analyses to evaluate retinal function. Afterwards, 2 rats per group were used for Evans blue dye analyses, whereas the remaining 6 animals in each group were used for immunofluorescence, biochemical and molecular analyses.

3.1.3 Findings

The compound does not affect body weight and glycemia

To assess whether the administration of the compound has some effects on systemic parameters, weight and blood glucose levels were measured over the entire experimental period. As shown in Figure 6A, control rats displayed a significant age-dependent gain of weight. Conversely, STZ injection resulted in markedly lower body weight as compared to controls. Following STZ administration, blood glucose levels were significantly increased and remained higher than in controls until the animals underwent to ERG recordings and were subsequently sacrificed (Figure 6B). Blood glucose levels did not significantly differ between STZ rats either untreated or treated with the compound at both doses. Taken together, all these data suggest that the treatment with the compound does not affect the STZ-induced body weight loss and hyperglycemia.

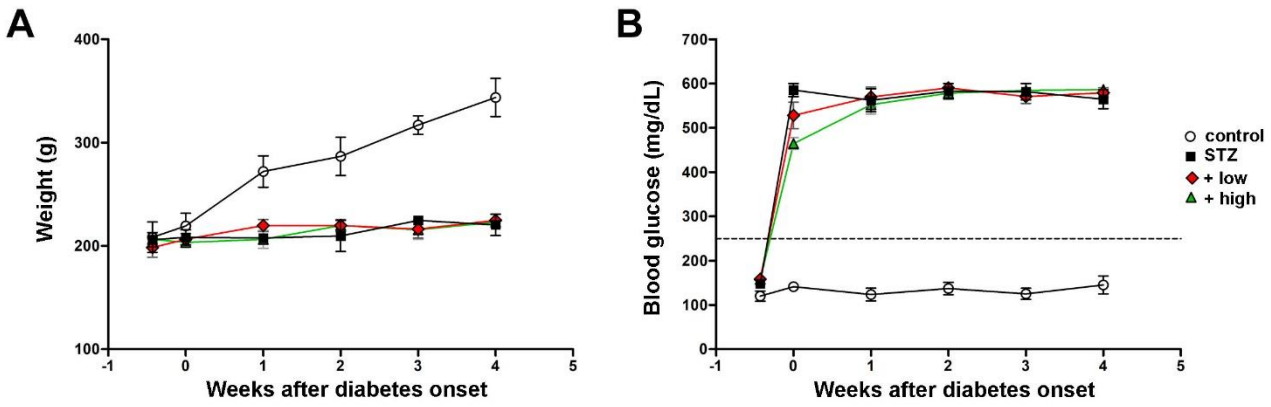

Figure 6. Longitudinal evaluation of (A) body weight and (B) blood glucose in controls, STZ-untreated rats or STZ rats treated with either the low dose or the high dose of the compound. Data are expressed as mean ± SEM. Statistical significance was assessed by two-ways ANOVA followed by Bonferroni's multiple comparison post-hoc test (n = 8).

The compound protects the retina from oxidative stress and inflammation

The preventive efficacy of the compound was first tested on ROS generation by measuring ROS levels. As shown in Figure 7A, STZ rats displayed a significant increase in ROS generation as compared to controls. STZ rats treated with the compound at low dose showed lower levels of ROS as compared to untreated STZ, although still resulting significantly higher than in controls. In STZ rats treated with the compound at high dose, ROS levels were comparable to those measured in controls. Oxidative stress was also evaluated by analyzing the protein levels of markers of the antioxidant response. In particular, the protein levels of Nrf2 and HO-1 were evaluated by Western blot using rabbit polyclonal anti-Nrf2 (ab92946, Abcam; 1:1000) and rabbit polyclonal anti-HO-1 (ab13243, Abcam; 1:500) as primary antibodies. As shown in Figures 7B and C, the densitometric analysis of immunoblots revealed a significant increment in both Nrf2 and HO-1 in STZ rats as compared to controls. This increment was partially attenuated by the compound at low dose, but completely prevented by the high dose. The expression pattern of HO-1 was also evaluated by immunofluorescence by the same primary antibody used in Western blot. As shown in Figure 7D, immunofluorescence analysis revealed a faint HO-1 immunoreactivity in control retinas mainly confined to the GCL. In retinas of STZ rats, HO-1 immunoreactivity was significantly increased in the GCL and expanded toward the outer retina, clearly depicting vertical processes in the IPL and cellular profiles localized in the inner nuclear layer (INL). Retinas of rats treated with compound at low dose displayed a less evident HO-1 immunostaining as compared to untreated STZ rats, with rare spots in the GCL and residual labeling in the IPL and INL. HO-1 immunostaining was not detectable

in the IPL and INL following the treatment with high dose, while a basal labeling was observed in the GCL similarly to what found in the control retina.

Since the inflammatory mechanisms can be activated following oxidative stress (see chapter 1), the effects of the compound administration on inflammatory markers were assessed by Western blot. In particular, the protein levels of the phosphorylated form of the p65 subunit of NF-kB and IL-6 were measured using the solutions of rabbit polyclonal anti-pNF-kB p65 (Ser 536) (sc-33020, Santa Cruz Biotechnology; 1:100) and mouse monoclonal anti-IL-6 (sc-57315, Santa Cruz Biotechnology; 1:100) primary antibodies. As shown in Figures 7E and F, STZ rats displayed a marked increase in pNF-KB and IL-6 as compared to controls. STZ rats treated with the compound at low dose showed lower levels of both markers as compared to untreated STZ, although still resulting significantly higher than in controls. On the other hand, in STZ rats treated with the high dose, the levels of pNF-kB and IL-6 were comparable to those measured in controls.

The reactive phenotype of glial cells triggered by the activation of inflammatory mechanisms was analyzed by immunostaining with GFAP (Figure 7G), a well-established marker of gliosis, using the rabbit monoclonal anti-GFAP (ab207165, Abcam; 1:400) as primary antibody. In control retinas, basal GFAP labeling was confined to the GCL. In contrast, STZ retinas showed an evident increment of GFAP immunoreactivity in the GCL together with densely immunopositive processes spreading across retinal layers as a typical hallmark of Müller cell reactivity. Comparable immunostaining could be detected in retinas of low dose-treated rats, although GFAP immunoreactivity was less prominent both in the GCL and in Müller cell processes. On the other hand, retinas of rats treated with the high dose displayed a GFAP immunostaining almost similar to that of controls, with the usual basal staining and barely detectable immunoreactive vertical processes. As shown in Figure 7H, quantitative analysis of fluorescence intensity showed a marked increment in GFAP immunoreactivity in STZ rats as compared to controls. In STZ rats treated with the low dose, GFAP immunoreactivity was significantly lower than in untreated STZ rats, while STZ rats treated with the high dose displayed GFAP immunofluorescence intensity comparable to that of controls. Taken together, these data support the antioxidant and anti-inflammatory effects exerted by the compound in STZ rats.

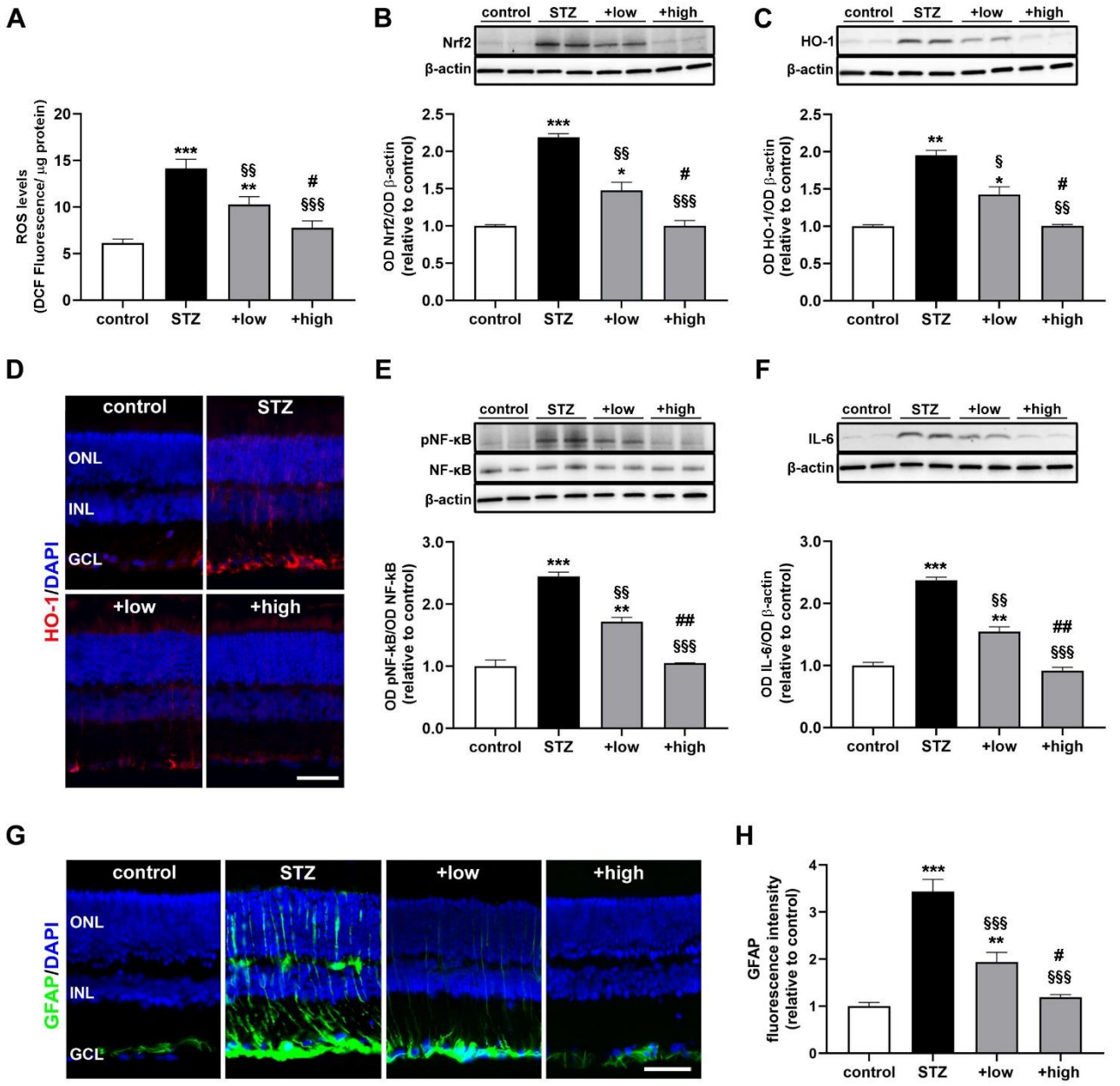

Figure 7. Effects of the compound on markers of oxidative stress and inflammation. (A) ROS levels in controls, STZ untreated or STZ treated with either the low dose or the high dose of the compound. (B, C) Representative Western blots and densitometric analysis of (B) Nrf2 and (C) HO-1. β-actin was used as loading control. (D) Representative images of retinal cross sections immunolabeled for HO-1 (red) and counterstained with DAPI (blue). Scale bar, 50 µm. GCL, ganglion cell layer; INL, inner nuclear layer; ONL, outer nuclear layer. (E, F) Western blots and densitometric analysis of levels of (E) pNF-kB and (F) IL-6. Levels of pNF-kB were normalized to NF-kB levels, while IL-6 was normalized to the loading control β-actin. (G) Representative images of retinal cross sections immunolabeled for GFAP (green) and counterstained with DAPI (blue). Scale bar, 50 µm. GCL, ganglion cell layer; INL, inner nuclear layer; ONL, outer nuclear layer. (H) Quantitative analysis of GFAP immunofluorescence intensity. Data are expressed as mean ± SEM. Statistical significance was assessed by one-way ANOVA followed by Tukey's multiple comparison post-hoc test (n = 6). * $p < 0.05$, ** $p < 0.01$ and *** $p < 0.001$ vs control; § $p < 0.05$, §§ $p < 0.01$ and §§§ $p < 0.001$ vs STZ; $^{\#}$ $p < 0.05$ and $^{\#\#}$ $p < 0.01$ vs low dose treated STZ.

Vascular homeostasis and BRB breakdown are prevented by the compound

Oxidative and inflammatory processes have a direct impact on molecular mechanisms regulating the vascular homeostasis and BRB dysfunction through the alteration of the HIF-1-dependent pathway and the consequent dysregulation of angiogenic factors such as VEGF (see chapter 1). For this reason, the levels of HIF-1α and VEGF were evaluated by Western blot using primary antibodies directed against these targets, such as rabbit monoclonal anti-HIF-1α (ab179483, Abcam; 1:1000) and rabbit polyclonal anti-VEGF (sc-507, Santa Cruz Biotechnology; 1:100). As shown in Figure 8A, HIF-1α levels were significantly increased in STZ rats as compared to controls. The increment in HIF-1α was significantly attenuated by the compound in a dose-dependent fashion, with the high dose maintaining HIF-1α to control levels (Figure 8A). Similarly, STZ rats displayed a marked increase in VEGF levels as compared to controls. The administration of the compound dose-dependently prevented VEGF accumulation with increased efficacy of the high dose, although VEGF levels were still higher than in controls (Figure 8B).

BRB dysfunction was evaluated by analyzing the levels of ZO-1 and claudin 5 as components of the inter-endothelial tight junctions using rabbit polyclonal anti-ZO-1 (40-2200, Invitrogen; 1:500) and mouse monoclonal anti-claudin 5 (35-2500, Invitrogen; 1:500) as primary antibodies. In addition, the BRB integrity was also assessed with the Evans Blue dye perfusion of retinal vessels (for inner BRB) and with ZO-1 immunostaining in RPE-choroid flatmounts (for outer BRB). For the latter, RPE-choroid flatmounts were incubated with the same anti-ZO-1 antibody used for Western blot (1:100 in 0.1 M PBS containing 1% Triton X-100) with an incubation for 72 h at 4°C followed by the incubation for 48 h at 4 °C in anti-rabbit secondary antibody conjugated with Alexa-Fluor 488 (Abcam; 1:200). As shown in Figures 8C and D, the levels of ZO-1 and claudin 5 were drastically decreased in STZ retinas. The treatment with the compound was found to prevent protein loss with dose-dependent efficacy, with the high dose displaying ZO-1 and claudin 5 levels comparable to those of controls. As shown in Figure 8E, in STZ rats, the dysregulation of BRB markers was correlated with inner BRB breakdown. In fact, Evans blue, a dye that binds to plasma proteins, was restricted to the vascular lumen in control retinas. Contrariwise, several focal points of extravasation were visible in STZ retinas. The vascular leakage was still evident in STZ rats treated with the compound at low dose, while the extravasation appeared more contained or even absent in retinas of rats treated with the high dose. ZO-1 immunostaining in RPE-choroid flatmounts from STZ rats revealed the presence of large holes between RPE cells indicating a significant loss of tight junctions leading to outer BRB breakdown (Figure 8F). Supplementation with the compound dose-dependently prevented tight junction loss with no apparent differences between controls and STZ rats treated with the high dose.

Taken together, these results indicate that the administration of the compound can prevent the vascular alterations resulting from hyperglycemia-induced oxidative stress.

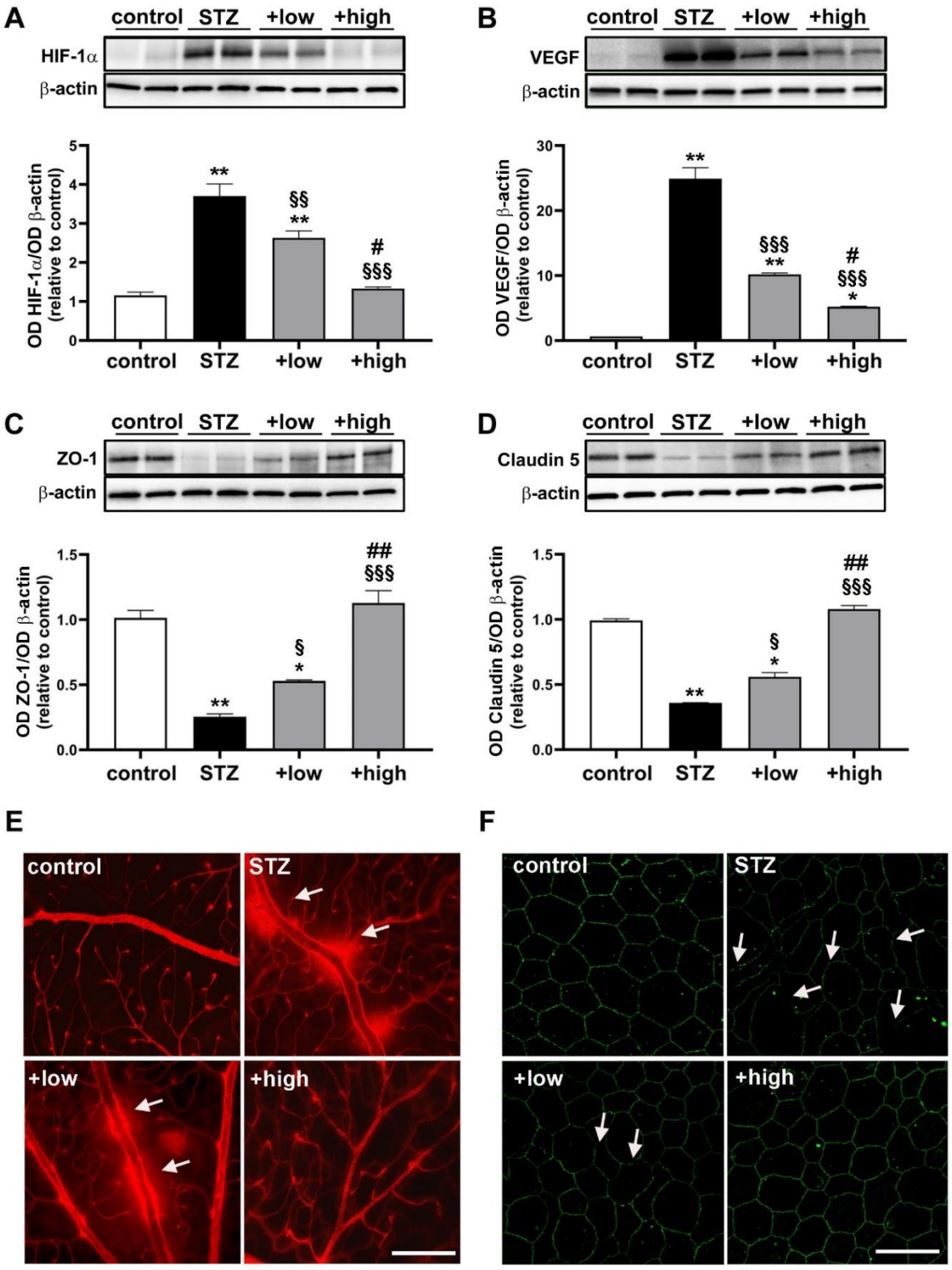

Figure 8. Effects of the compound on vascular-related markers and vascular leakage. (A, B) Representative Western blots and densitometric analysis of (A) HIF-1α and (B) VEGF in controls, STZ untreated or STZ rats treated with either the

low dose or the high dose of the compound. β-actin was used as loading control. (C, D) Representative Western blots and densitometric analysis of (C) ZO-1 and (D) claudin 5. β-actin was used as loading control. Data are expressed as mean ± SEM. Statistical significance was assessed by one-way ANOVA followed by Tukey's multiple comparison post-hoc test (n = 6). * $p < 0.05$ and ** $p < 0.001$ vs control; § $p < 0.05$, §§ $p < 0.01$ and §§§ $p < 0.001$ vs STZ; $^{\#}$ $p < 0.01$ and $^{\#\#}$ $p < 0.001$ vs low dose treated STZ (E) Representative images of whole-mounted retinas after Evans blue dye perfusion. Vascular leakage is indicated by the white arrows. Scale bar, 200 μm (F) Representative images of RPE-choroid flatmounts stained with ZO-1. White arrows indicate large holes appeared between the RPE cells. Scale bar, 20 μm.

.

The compound protects the retina from apoptosis and ERG dysfunction

To test whether the compound might influence the retinal viability by counteracting the hyperglycemia-induced apoptotic mechanisms, levels of proapoptotic markers were assessed by evaluating the ratio of pro-apoptotic Bax to anti-apoptotic Bcl-2 proteins, as a major checkpoint in the apoptotic pathway, as well as the levels of downstream activated caspase 3, as the major effector protease driving the programmed cell death. In order to evaluate the protein levels of these markers, Western blot analyses were performed by using rabbit monoclonal anti-Bax (ab182733, Abcam; 1:500), rabbit polyclonal anti-Bcl-2 (ab194583, Abcam; 1:500) and rabbit anti-cleaved caspase 3 (ab2302, Abcam; 1:500) primary antibody solutions. As shown by the representative blots and the densitometric analysis in Figures 9A and B, the Bax/Bcl-2 ratio and the levels of caspase 3 were significantly increased in STZ rats as compared to controls. Treatment with the compound dose-dependently prevented the STZ-induced increase in Bax/Bcl-2 ratio and caspase 3, with a partial efficacy of the low dose, while their increase was completely prevented by the high dose. The evidence of attenuated levels of caspase 3 was further supported by immunofluorescence analysis (Figure 9C), where retinal coronal sections were labelled with rabbit monoclonal anti-cleaved caspase 3 (9664S, Cell Signaling Technology, Danvers, MA, United States; 1:400) antibody. In STZ rats, increased caspase 3 was localized to cellular profiles in the GCL and INL as compared to controls in which caspase 3 immunostaining was absent. After the low dose, caspase 3-immunopositive cells were less evident and faintly stained, although some cellular profiles localized to the GCL and INL were still visible. Conversely, no caspase 3-immunopositive cell profiles could be observed after the high dose.

To evaluate whether the protective efficacy of the compound on retinal viability might be reflected on counteracting STZ-induced visual dysfunction, we analyzed the outer and inner retinal activity using scotopic ERG recordings. Under scotopic condition, a-wave reflects the activity of rods, while b-wave reflects the activity of bipolar cells and Müller glia. Figure 9D shows representative mixed a- and b-waves recorded at light intensity of 1 log cd-s/m^2. As shown in Figures 9E and F, in STZ rats treated with the low dose, ERG responses were partially preserved. In fact, the a-wave amplitude,

although not significantly different from that measured in STZ rats, showed a tendency toward an increase, while the b-wave amplitude was significantly higher than in STZ rats. After treatment with the high dose, a-and b-wave amplitudes were significantly higher than in STZ rats and in low dose-treated rats, but still lower than in controls. These data support the protective efficacy of the compound in counteracting the activation of retinal cell death and reducing the hyperglycemia-induced visual impairment.

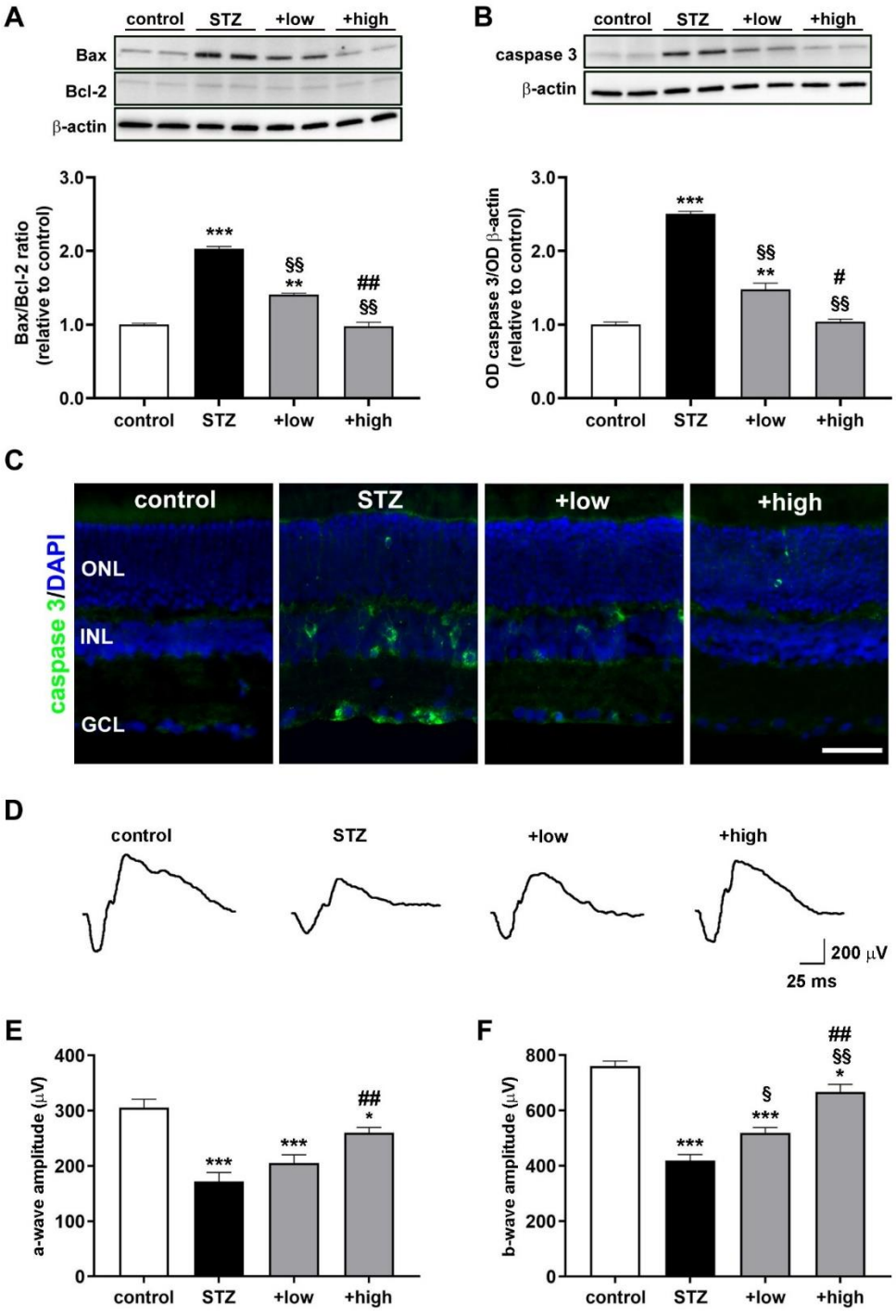

Figure 9. Effects of the compound on apoptotic mechanisms and retinal function. (A, B) Representative Western blots and densitometric analysis of (A) Bax/Bcl-2 ratio and (B) cleaved caspase 3 in controls, STZ untreated or STZ rats treated

with either the low dose or the high dose of the compound. The levels of cleaved caspase 3 were normalized to the loading control β-actin. Data are expressed as mean ± SEM. Statistical significance was assessed by one-way ANOVA followed by Tukey's multiple comparison post-hoc test (n = 6). (C) Representative images of retinal cross sections immunolabeled for cleaved caspase 3 (green) and counterstained with DAPI (blue). Scale bar, 50 μm. GCL, ganglion cell layer; INL, inner nuclear layer; ONL, outer nuclear layer. (D) Representative scotopic ERG waveforms recorded at 1 log cd-s/m^2 light intensity. (E, F) Quantitative analysis of the (E) scotopic a- and (F) b-wave amplitudes. Data are expressed as mean ± SEM. Statistical significance was assessed by one-way ANOVA followed by Tukey's multiple comparison post-hoc test (n = 8). * $p < 0.05$, ** $p < 0.01$ and *** $p < 0.001$ vs control; § $p < 0.01$ and §§ $p < 0.001$ vs STZ; $^{\#}$ $p < 0.05$ and $^{\#\#}$ $p < 0.01$ vs low dose treated STZ.

All these findings are collected in our published paper entitled "Preventive Efficacy of an Antioxidant Compound on Blood Retinal Barrier Breakdown and Visual Dysfunction in Streptozotocin-Induced Diabetic Rats", whose original pdf version is included in the Appendix.

3.2 The positive modulation of the oxidative balance by antioxidant formulations improves retinal function and photoreceptor viability under light damage

3.2.1 Background

The excessive exposure to light can reduce mitochondrial activity and amplify the production of ROS, resulting in the onset of oxidative stress which alters the viability of photoreceptors (see chapter 1). The positive modulation of photoreceptor oxidative balance by several promising compounds with antioxidant and anti-inflammatory properties may reduce photoreceptor damage induced by the LD-driven oxidative stress through a low invasive administration (Ikonne, Ikpeazu and Ugbogu, 2020). In particular, molecules belonging to carotenoid family, such as lutein, have been recognized among the most promising substances capable to prevent/counteract oxidative stress through an antioxidant direct free radical scavenging effect (Li et al., 2020). In addition, lutein accumulates in the human retina at the macular level, filtering the blue light and protecting photoreceptors from LD with additional mechanisms beyond anti-oxidative and anti-inflammatory properties (Bernstein et al., 2016; Mares, 2016; Eisenhauer et al., 2017; Liu et al., 2017b; Chang et al., 2018). Another promising molecule with antioxidant and anti-inflammatory properties potentially effective in counteracting oxidative stress in LD might be C3G (see paragraph 3.1.1). Considering the putative beneficial effects of these molecules, their possible administration in a coupled formulation or in the context of a multicomponent antioxidant mixture with other molecules, such as verbascoside and zinc (see

paragraph 3.1.1), would represent an interesting treatment proposal to protect photoreceptors from LD-mediated degeneration for a possible synergistic effect.
In this study, the efficacy of a positive modulation in the oxidative balance using lutein and C3G administered either in combination or in the context of a pre-formulated multicomponent mixture was investigated in a rat model of LD, which mimics reduced photoreceptor viability induced by oxidative stress and its related inflammation triggered by the excessive exposure to light (Kohno et al., 2013; Rashid, Wolf and Langmann, 2018).

3.2.2 Treatments and experimental design

Lutein oil from *Tagetes erecta* titrated at 20% lutein was obtained from Procemsa (Torino, Italy). Black rice extract titrated at 20% in C3G and verbascoside from *Verbascum thapsus* titrated at 10% were obtained from "La sorgente del Benessere" (Fiuggi, Italy). Treatments were performed by oral gavage once daily for 7 days before undergoing the LD protocol (see paragraph 2.2.2). Once a day, lutein and C3G, either individually or combined were freshly prepared by dissolving each compound in wheat germ oil to obtain the desired final dose 5.2 mg/kg lutein and 4.0 mg/kg C3G administered individually or in combination. In a second set of experiments, based on different commercial formulations for humans, a nutraceutical blend containing lutein, C3G, verbascoside and zinc (hereinafter referred to as mixture) was obtained by Sooft, SpA, Montegiorgio, Italy. The mixture was administered at two dosages in mg/kg: 1.08 lutein, 3.6 C3G; 0.36 verbascoside and 0.88 zinc (low dose) or 3.24 lutein, 10.8 C3G, 1.08 verbascoside and 2.64 zinc (high dose). Forty-two rats were used. Of them, six were used as control group. The remaining 36 rats underwent to LD protocol and were divided in six experimental groups (six rats in each experimental group): LD untreated group, lutein group (+Lut), C3G group (+C3G), lutein/C3G group (+Lut/C3G), low dose mixture group (+low dose) and high dose mixture group (+high dose). After two days of recovery in dim light following LD, rats underwent ERG and subsequent euthanasia. Afterwards, eyes and retinas were collected for immunofluorescence and molecular analyses.

3.2.3 Findings

Combined efficacy of lutein and C3G on oxidative stress, inflammatory response, glial activation

To evaluate whether the administration of lutein and C3G either alone or in combination was effective in counteracting LD-driven oxidative stress, protein levels of Nrf2 and HO-1 were assessed by Western blot using the same antibodies indicated in paragraph 3.1.3. As shown in Figures 10A and B, in untreated LD rats, protein levels of Nrf2 were upregulated in response to light stimulation. As a consequence of Nrf2 upregulation, HO-1 was increased, as compared to control rats. Compared to untreated LD rats, pretreatment with either lutein or C3G decreased the protein levels of Nrf2 and HO-1, which still remained higher than in controls. The pretreatment with lutein in combination with C3G resulted in a much stronger decrease in Nrf2 and HO-1 levels which returned to levels similar to those measured in control rats.

To test if the lutein and C3G-mediated counteraction of oxidative stress may result in reduced activation of inflammatory mechanisms, protein levels of inflammatory markers were evaluated by Western blot. In particular, pro-inflammatory (as the phosphorylated form of NF-kB and IL-6) and anti-inflammatory (e.g. IL-10) markers were analyzed using the primary antibodies anti-pNF-kB p65 (Ser 536) (see paragraph 3.1.3), anti-IL-6 (see paragraph 3.1.3) and goat polyclonal anti-IL-10 (sc-1783, Santa Cruz Biotechnology; 1:100). As depicted in Figures 10C-F, LD rats displayed upregulated levels of pro-inflammatory markers including the phosphorylated form of NF-kB and IL-6, while the anti-inflammatory cytokine IL-10 was downregulated. Pretreatment with either lutein or C3G reduced both phosphorylated NF-kB and IL-6 in concomitance with an increase in IL-10 levels as compared to untreated LD rats. After pretreatment with lutein and C3G, the levels of pNF-kB, IL-6 and IL-10 did not differ from those measured in controls.

Since the oxidative stress and inflammation promote Müller cell gliosis and microglial activation (see chapter 1), the reactive phenotype of these cell types following lutein/C3G treatment was assessed by immunofluorescence. In particular, retinal cross sections were immunolabeled for GFAP or ionized calcium-binding adapter molecule 1 (Iba-1) as markers of activated Müller cells and microglia, respectively, by using primary antibodies anti-GFAP (see paragraph 3.1.3) and rabbit monoclonal anti-Iba-1 (ab178846, Abcam; 1:200). As shown in Figure 10G, in control retinas, GFAP immunoreactivity was confined to the GCL while in untreated LD rats, Müller cells showed extensive GFAP immunolabeling along their processes spreading across retinal layers. GFAP-positive processes were less evident, but still detectable in retinas of lutein- or C3G-treated rats. On the

contrary, in retinas of rats pretreated with lutein and C3G in combination, GFAP immunoreactivity in vertical processes was undetectable resulting confined to the GCL, similarly to controls. Quantitative analysis of fluorescence intensity showed that in untreated LD rats, GFAP immunoreactivity was increased as compared to controls. Individual administration of lutein or C3G reduced GFAP intensity with no difference among single compounds. In contrast, the pretreatment with their combination resulted in a further decrease of GFAP immunofluorescence with no statistical difference from control rats (Figure 10H). As shown in Figure 5G, Iba-1 immunolabeling was weakly represented in the inner retinal layers of control retinas, with arborizing processes likely associated to inactive microglia. In contrast, Iba1 immunoreactivity was more prominent in the retina of untreated LD rats with enlarged amoeboid-shaped immunopositive cells localized in INL, ONL and subretinal space. Pretreatment with either lutein or C3G partially prevented microglial activation as determined by decreased Iba1-immunolabeled cells, while no evidence of activated microglia was observed when the compounds were given in combination. As shown by the quantitative analysis of fluorescence intensity, in untreated LD rats, Iba-1 was increased compared to controls. Iba1 immunofluorescence was reduced after the administration of either lutein or C3G compared to LD rats, while their combination preserved Iba1 immunoreactivity to control levels (Figure 10H). Taken together, these findings support a positive modulation of the oxidative balance exerted by the treatment with lutein/C3G, thus reducing LD-driven oxidative stress and inflammation.

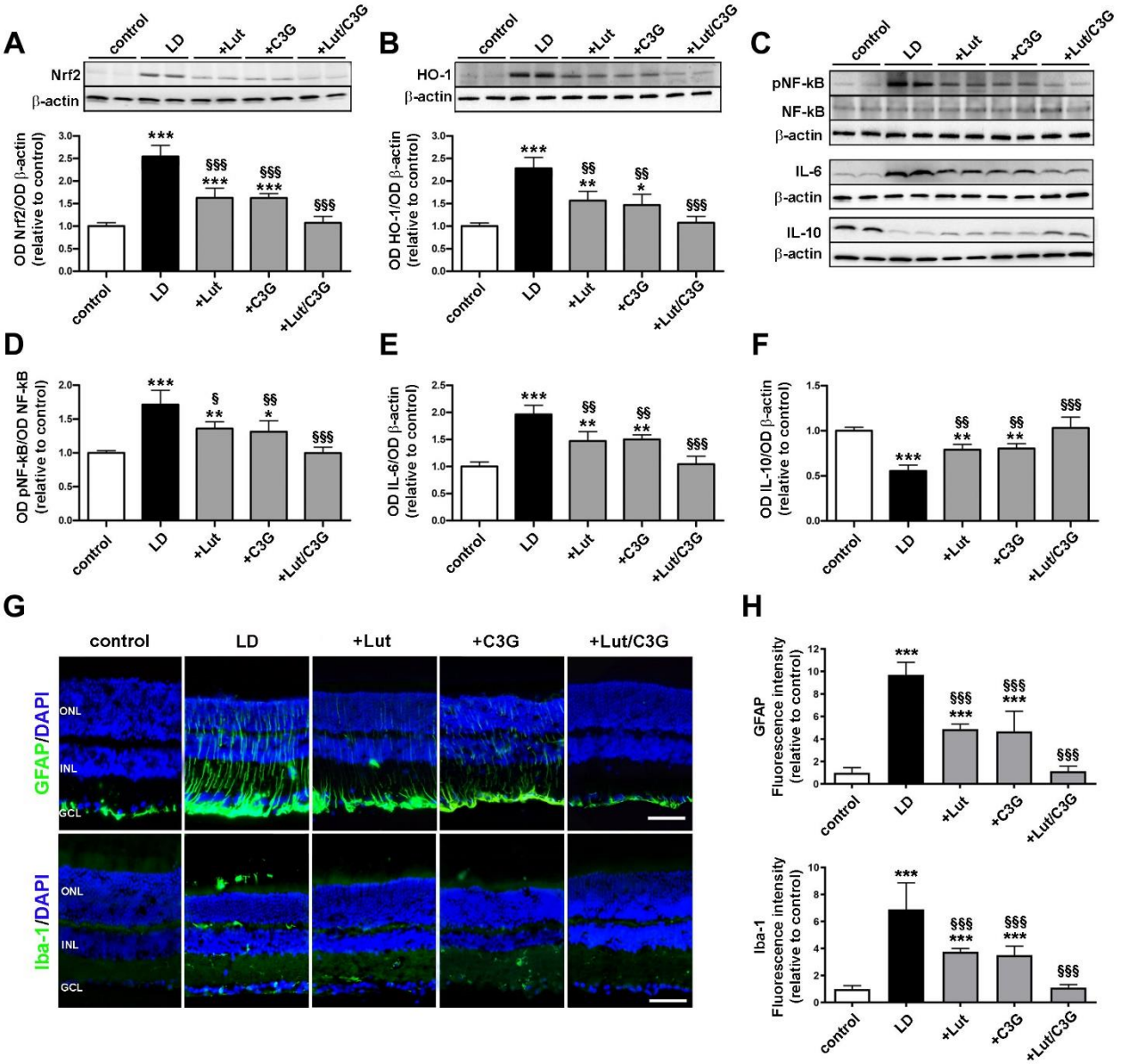

Figure 10. Individual and combined effects of lutein and C3G on oxidative stress, inflammation and glial activation. (A, B) Representative Western blots and relative densitometric analyses of (A) Nrf2 and (B) HO-1 immunoblots from retinal homogenates of control and LD rats untreated or pretreated with either lutein, C3G or their combination. The expression of Nrf2 and HO-1 was normalized to the loading control β-actin. (C) Representative Western blots of phosphorylated and total NF-kB, IL-6 and IL-10. (D-F) Densitometric analyses of the (D) phosphorylation levels of NF-kB, (E) IL-6 and (F) IL-10. The expression of pNF-kB was normalized to the level of NF-kB, while the expression of IL-6 and IL-10 was relative to the loading control β-actin. (G) Representative images of retinal sections from control and LD rats untreated or pretreated with either lutein, C3G or their combination immunolabeled for GFAP and Iba-1 (green). Sections are counterstained with DAPI to highlight retinal nuclear layers. (H) Quantitative analysis of GFAP and Iba1 fluorescence intensity. GCL, ganglion cell layer; INL, inner nuclear layer; ONL, outer nuclear layer. Scale bar, 50 µm. Data are expressed as mean ± SD. Differences between groups were tested for statistical significance using one-way ANOVA followed by the Newman–Keuls multiple comparison post hoc test (n = 6 retinal homogenates (Western blot) or retinas (immunofluorescence) per group). * $p < 0.05$; ** $p < 0.01$; *** $p < 0.001$ versus control; § $p < 0.05$; §§ $p < 0.01$; §§§ $p < 0.001$ versus LD.

Combined efficacy of lutein and C3G on photoreceptor degeneration

To evaluate whether the reduction of oxidative and inflammatory mechanisms by lutein/C3G administration results in improved photoreceptor viability, immunofluorescence of rod- and cone-specific markers was performed. In particular, retinal sections were immunolabeled for rhodopsin (rods) and cone-arrestin (cones) by utilizing mouse monoclonal anti-rhodopsin (ab5417, Abcam; 1:200) and rabbit polyclonal anti-cone arrestin (AB15282, Sigma-Aldrich; 1:200) primary antibodies. Representative images of retinal sections immunolabeled with rhodopsin or cone-arrestin and counterstained with DAPI are shown in Figure 11A. The outer nuclear layer (ONL) thickness (extending from the interface between the outer plexiform layer and the inner segment layer) was measured in five sections for each retina (six retinas per group) and four images in each section were sampled. Retinas of untreated LD rats showed a prominent decrease of ONL thickness compared to control (Figure 11B), as a consequence of photoreceptor loss. Photoreceptors were partially protected following individual pretreatment with lutein or C3G compared to LD. No evidence of photoreceptor loss was observed after combined pretreatment. Untreated LD rats showed a similar residual expression of rhodopsin and cone-arrestin compared to control. After individual treatments with lutein or C3G, the immunofluorescence levels of both rhodopsin and cone-arrestin were partially preserved compared to those in LD rats. In contrast, retinas of light-exposed rats treated with lutein and C3G in combination displayed a well-organized and abundant expression of rhodopsin and cone-arrestin at levels similar to control (Figure 11C and D).

Since the treatment with lutein/C3G resulted in photoreceptor protection, an effect of the dietary combination of lutein and C3G in affecting the activation of selected components in the apoptotic pathway was assessed. In particular, the ratio of Bax to Bcl-2, as well as the downstream activation of caspase 3, were evaluated by Western blot (see paragraph 3.1.3). As shown by the representative blots in Figure 11E and the densitometric analysis in Figure 11F and G, the Bax/Bcl-2 ratio was increased in untreated LD rats compared to control with upregulated levels of the pro-apoptotic Bax and stable levels of the anti-apoptotic Bcl-2 (Figure 11F). Downstream to the increased Bax/Bcl-2 ratio, levels of caspase 3 increased in LD rats compared to control (Figure 11G). Treatment with lutein or C3G attenuated the increase in Bax/Bcl-2 ratio and the caspase level compared to LD untreated rats. The combined treatment further reduced the levels of Bax/Bcl-2 ratio and caspase 3 compared to LD rats, reaching values that were comparable to those measured in controls. These findings support the efficacy of combined lutein and C3G in improving photoreceptor viability under LD.

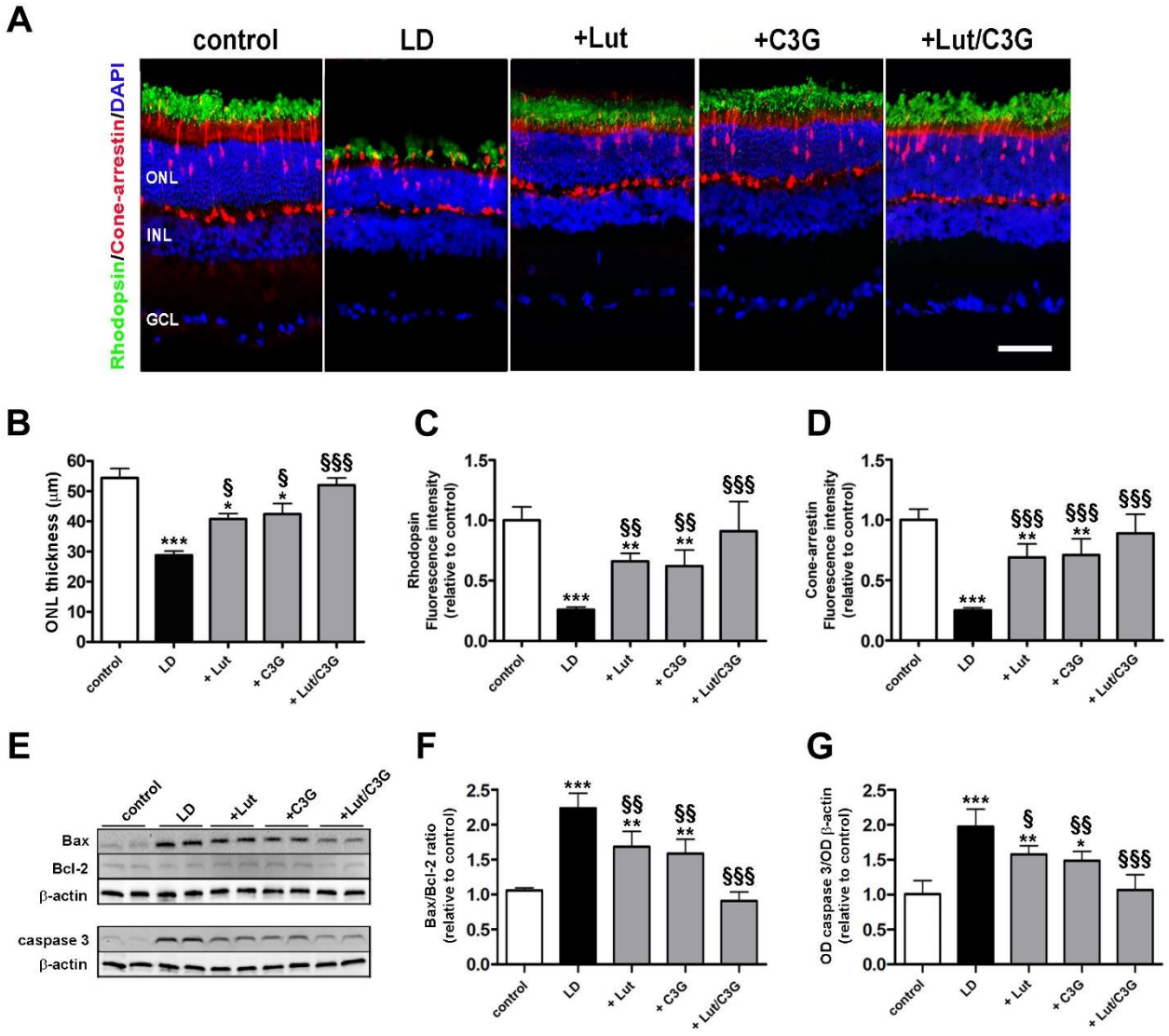

Figure 11. Individual and combined effects of lutein and C3G on photoreceptor degeneration. (A) Representative images of retinal sections from control and LD rats untreated or pretreated with either lutein, C3G or their combination immunolabeled for rhodopsin (green) and cone-arrestin (red). Retinal nuclear layers are highlighted by the DAPI counterstaining. (B) Quantitative analysis of ONL thickness. (C, D) Quantitative analysis of (C) rhodopsin and (D) cone-arrestin immunofluorescence intensity. GCL, ganglion cell layer; INL, inner nuclear layer; ONL, outer nuclear layer. Scale bar, 50 µm. (E) Representative Western blots of Bax, Bcl-2 and active caspase 3 from each experimental group. (F, G) Densitometric analysis of the (F) Bax/Bcl-2 ratio and (G) active caspase 3. The expression of active caspase 3 was relative to the loading control β-actin. Data are expressed as mean ± SD. Differences between groups were tested for statistical significance using one-way ANOVA followed by the Newman-Keuls multiple comparison post-hoc test (n = 6 retinal homogenates (Western blot) or retinas (immunofluorescence) per group). * $p < 0.05$; ** $p < 0.01$; *** $p < 0.001$ versus control; § $p < 0.05$; §§ $p < 0.01$; §§§ $p < 0.001$ versus LD.

Combined efficacy of lutein and C3G on retinal function

In additional experiments aimed at evaluating whether protective efficacy of dietary combination on photoreceptor loss were accompanied by ameliorated visual function, LD rats treated with lutein and

C3G either alone or in combination were subjected to comprehensive ERG analyses to assess outer and inner retinal function. Under scotopic conditions, the a-wave reflects the activity of rods while the b-wave reflects the activity of inner retina. As shown by scotopic ERG responses in Figure 12A and quantitative analysis of both a- and b-wave amplitudes in Figures 12B and C, untreated LD rats displayed a reduced amplitude of a-wave and b-wave compared to those measured in controls. The pretreatment with either lutein or C3G administered alone partially preserved the a-wave and b-wave amplitudes compared with untreated LD rats. Lutein in combination with C3G completely preserved the a-wave and b-wave amplitudes, resulting in amplitudes similar to those of controls.

Under photopic conditions, additional measurements included the b-wave, which indirectly reflects the cone activity since the a-wave cannot be measured reliably, and the PhNR, a negative-going wave following the b-wave that originates in the inner retinal layer and is correlated with RGC activity (Marmoy and Viswanathan, 2021). As shown by photopic ERG responses in Figure 12D and quantitative analysis of b-wave and PhNR amplitudes in Figures 12E and F, in untreated LD rats the photopic b-wave and the PhNR were both reduced in amplitude compared to control. Lutein or C3G administered alone partially prevented the photopic ERG dysfunction, with both b-wave and PhNR amplitudes higher than those in untreated LD rats. The lutein and C3G combination completely preserved the photopic ERG responses in both b-wave and PhNR amplitudes to control levels. Taken together, these data suggest the capacity of lutein/C3G to improve retinal function under LD.

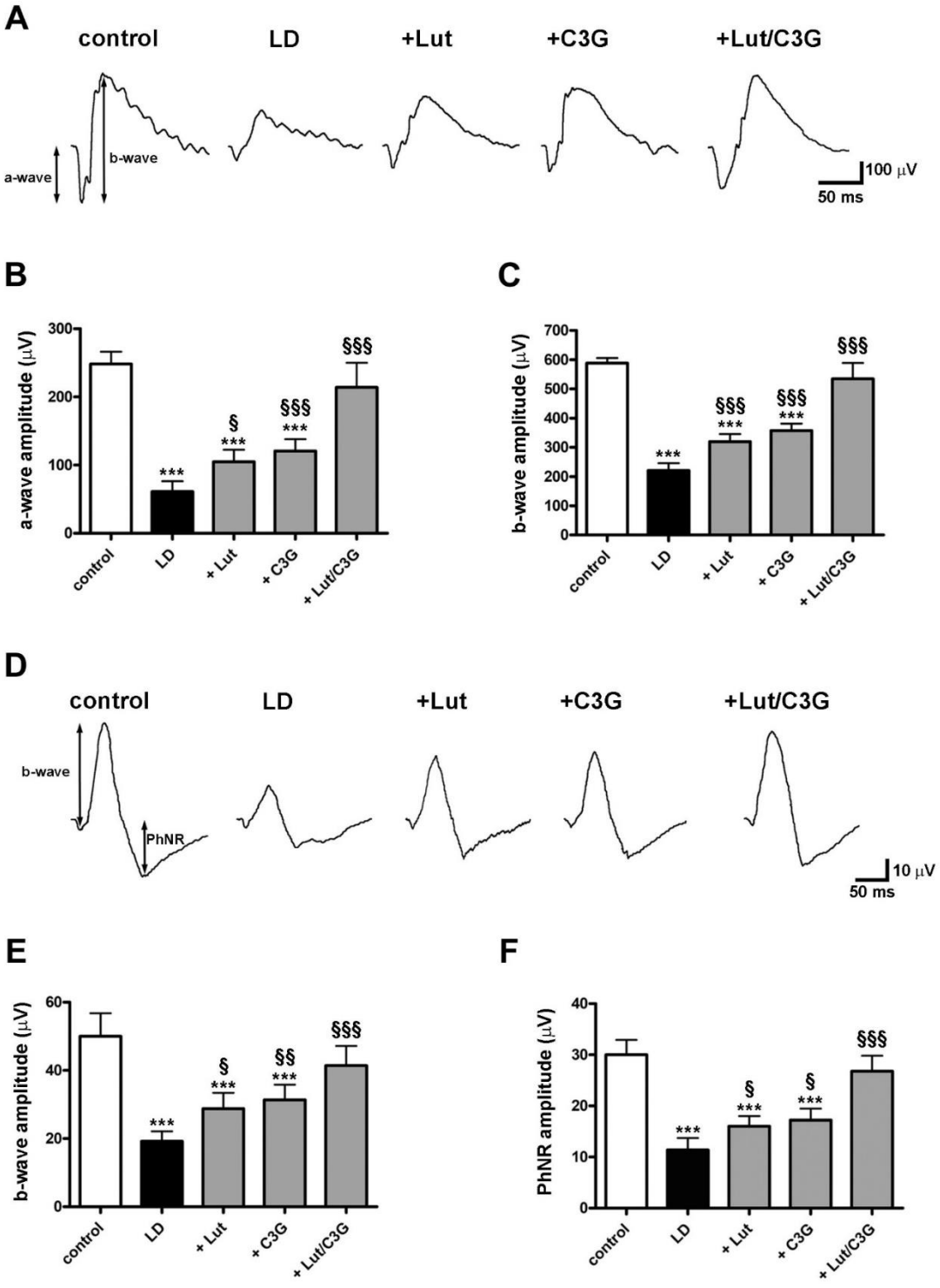

Figure 12. Individual and combined effects of lutein and C3G on scotopic and photopic full field ERG. (A) Representative ERG waveforms showing scotopic a- and b-waves from control and LD rats untreated or pretreated with either lutein, C3G or their combination. (B, C) Quantitative analysis of scotopic (B) a- and (C) b-wave amplitudes. (D) Representative ERG waveforms showing photopic b-waves and PhNR. (E, F) Quantitative analysis of (E) photopic b-wave and (F) PhNR amplitudes. Data are expressed as mean ± SD. Differences between groups were tested for statistical significance using one-way ANOVA followed by the Newman–Keuls multiple comparison post hoc test (n = 6 animals per group). *** $p < 0.001$ versus control; § $p < 0.05$; §§ $p < 0.01$; §§§ $p < 0.001$ versus LD.

Efficacy of a pre-formulated mixture on light-induced retinal damage

After having established the efficacy of the combined treatment of lutein and C3G, whether their effects could be modulated in a more sophisticated blend of functional nutrients was investigated. In particular, the efficacy of a mixture including lutein and C3G together with verbascoside and zinc was evaluated at two different doses performing Western blot, immunofluorescence and ERG analyses. As shown in Figures 13A and B, rats pretreated with a low dose of the mixture showed a significant reduction in upregulated levels of Nrf2 and HO-1 as compared to untreated LD rats. After pretreatment with a high dose of the mixture, the levels of Nrf2 and HO-1 did not differ from those measured in controls.

Representative images of retinal sections immunolabeled with GFAP and Iba-1 are shown in Figure 13C, while the quantitative analysis of immunostaining is shown in Figures 13D–E. After low dose of the mixture, the ONL thickness was greater than in untreated LD rats, while the high dose of the mixture completely prevented the light-induced ONL decrease as compared to control (Figure 13D). As shown in Figures 13E and F, the pretreatment at low dose partially prevented the increase in GFAP and Iba-1 immunostaining compared to untreated LD rats. After high dose pretreatment, GFAP and Iba-1 immunostaining was not different from control rats.

Figures 13G-L show how light exposure led to a decrease in the amplitude of both scotopic a-wave and b-wave, and photopic b-wave and PhNR as compared to control. The mixture at low dose attenuated the reduction in the amplitude of scotopic and photopic waves as compared to LD rats. The pretreatment with the mixture at high dose prevented such amplitude reduction maintaining both scotopic and photopic ERG responses to control levels suggesting preservation of photoreceptors from death. Taken together, the present findings demonstrate the ability of combined administration of antioxidants as lutein, C3G, verbascoside and zinc to improve visual function under LD-driven imbalanced oxidative status by ameliorating retinal cell viability through a major antioxidant and anti-inflammatory action.

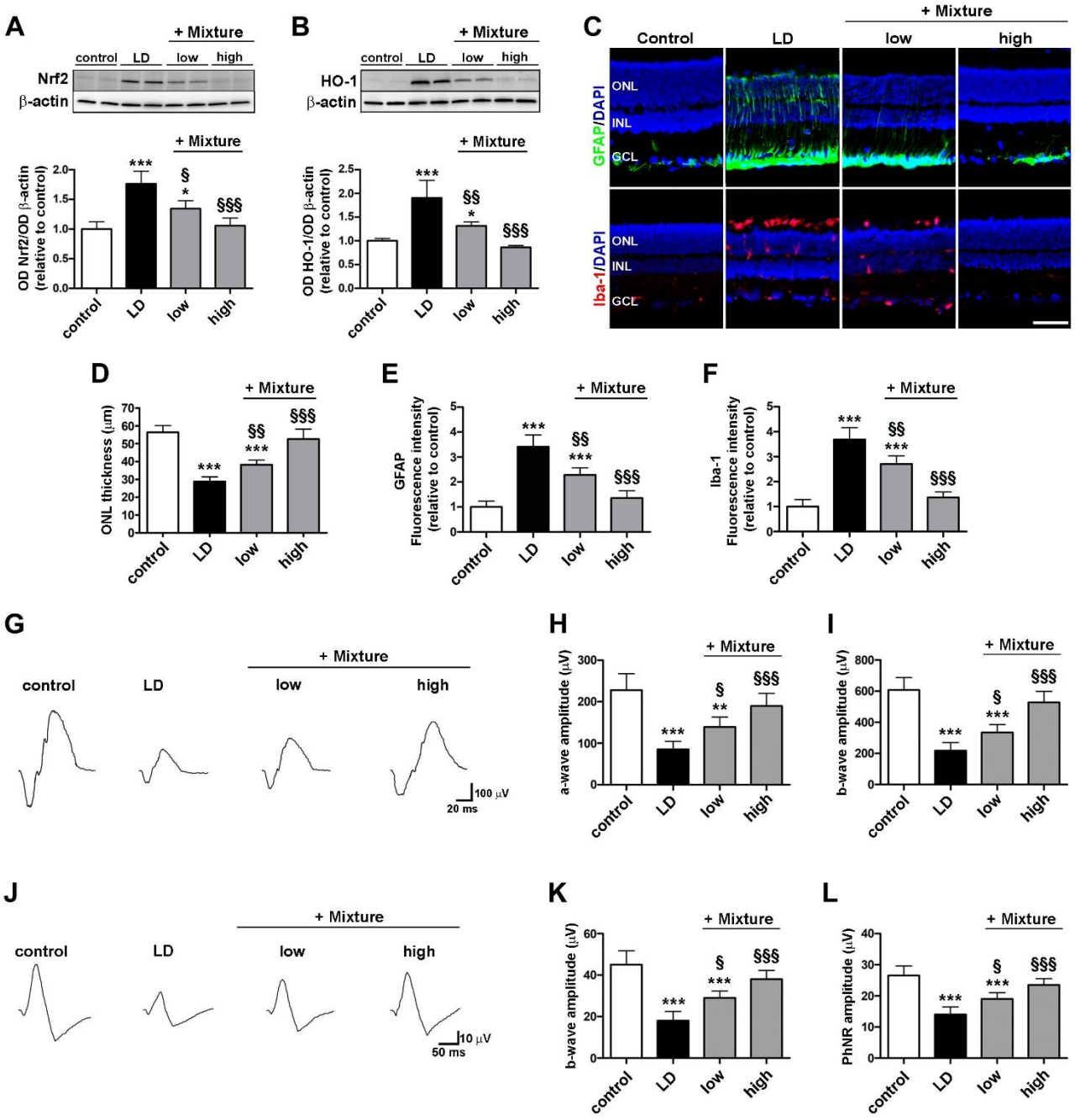

Figure 13. Effects of pre-formulated mixture on oxidative markers, glial activation and retinal function. (A, B) Western blots and densitometric analysis of (A) Nrf2 and (B) HO-1 in retinal homogenates of control and LD rats untreated or pretreated with the mixture at low or high dosage. (C) Representative images of retinal sections immunolabeled for GFAP (green) and Iba-1 (red) and counterstained with DAPI (blue). Scale bar, 50 µm. (D) Quantitative analysis of ONL thickness. (E, F) Quantitative analysis of (E) GFAP and (F) Iba1 immunofluorescence intensity. (G) Representative ERG waveforms showing scotopic a- and b-waves. (H, I) Quantitative analysis of scotopic (H) a- and (I) b-wave amplitudes. (J) Representative ERG waveforms showing photopic b-waves with PhNR. (K, L) Quantitative analysis of photopic (K) b-wave and (L) PhNR amplitudes. Data are expressed as mean ± SD. Differences between groups were tested for statistical significance using one-way ANOVA followed by the Newman–Keuls multiple comparison post hoc test. (n = 6 retinal homogenates (Western blot), retinas (immunofluorescence) or animals (ERG) per group). * $p < 0.05$, ** $p < 0.01$ and *** $p < 0.001$ versus control; § $p < 0.05$; §§ $p < 0.01$; §§§ $p < 0.001$ versus LD.

The findings shown in this study account for a part of the data set contained in our published paper entitled “Dietary Supplementation of Antioxidant Compounds Prevents Light-Induced Retinal Damage in a Rat Model” (see Appendix for the original pdf version).

3.3 The modulation of the oxidative stress by spearmint extract: improving retinal ganglion cell viability under ocular hypertension

3.3.1 Background

In various forms of glaucoma, the IOP elevation contributes to alter RGC viability by the establishment of several detrimental pathophysiological mechanisms, among which early mitochondrial dysfunction seems to play a key role. The reduced mitochondrial activity occurring in RGCs results in increased production of ROS, thus triggering the onset of oxidative stress which contributes with other pathophysiological events (e.g. reduced neurotrophic support) to damage RGCs (see chapter 1). The use of compounds regulating the oxidative balance by antioxidant, anti-inflammatory, and/or neurotrophic properties may reduce RGC degeneration under glaucomatous stress. The polyphenol-rich spearmint extract (SPE), derived from patented lines of spearmint (*Mentha spicata L.*) plants (Cirlini et al., 2016), may be a promising treatment strategy to reduce RGC degeneration given its potential antioxidant, anti-inflammatory and neurotrophic properties. In effect, SPE contains a powerful assortment of phenolic compounds including, but not limited to, rosmarinic acid (RA), salvianolic acid, caffeic acid, caftaric acid, quinic acid, and lithospermic acid, all displaying antioxidant and anti-inflammatory properties (Cirlini et al., 2016). As a support of its potential efficacy, multiple preclinical studies with SPE have demonstrated its capacity of reducing oxidative stress, inflammation and modulate brain neurotransmitters in mouse neuronal districts, thus promoting neuroprotection in neural tissue (Bian et al., 2020; Taira et al., 2020; Zhang et al., 2021). In addition, recent animal models of glaucomatous conditions induced by optic nerve crush or MCE-induced ocular hypertension indicate that dietary interventions including SPE counteract the inflammatory processes and morpho-functional alterations of glaucoma (Locri et al., 2019; Cammalleri et al., 2020). These studies suggest that SPE could be a potential candidate for providing nutritional support for ocular neural tissues.

Hence, the objective of this study was to investigate the efficacy of the SPE oral supplementation in reducing RGC degeneration following IOP elevation in a rat model of MCE-induced hypertensive glaucoma. In this model, the increase in IOP results in a sudden elevation of inflammatory and oxidative stress markers, resulting in impaired RGC function and viability.

3.3.2 Treatments and experimental design

SPE (provided by Kemin Foods, L.C., Des Moines, IA) was tested at low (SPE-low) and high (SPE-high) doses corresponding to half or full dosages found to exert cognitive benefits in clinical trials (Nieman et al., 2015; Herrlinger et al., 2018; Falcone et al., 2019; Tubbs et al., 2021), taking into account the difference in the metabolism of the two species (man and rat; Reagan-Shaw, Nihal and Ahmad, 2008) and the dose used in previous preclinical studies (Bian et al., 2020; Taira et al., 2020; Zhang et al., 2021). SPE-low and SPE-high were administered at 46.5 mg/kg and 93.0 mg/kg body weight per day respectively. High- and low-dose solutions of SPE were freshly prepared every day in distilled water immediately before the treatment. In particular, SPE was dissolved at 93 mg/mL in distilled water (vehicle) in order to obtain the stock solution to be administered for the high dose. Hence, the low-dose solution containing SPE at 46.5 mg/mL was prepared by performing 1:2 dilution of the high-dose solution. Equal amounts of low- and high-dose solutions (volume administered 300 µL) were administered daily by oral gavage for 14 days before and 14 days after the MCE injection (see paragraph 2.2.3). Rats were randomly divided into four groups as follows: one group (10 rats) of healthy controls (control, rats receiving no MCE injection and no supplementation; group 1), and three groups of glaucomatous rats (10 rats/group) receiving MCE injection and randomized to oral supplementation with vehicle (MCE + vehicle; group 2); low-dose SPE (MCE + SPE-low; group 3); and high-dose SPE (MCE + SPE-high; group 4). Retinal function was evaluated by scotopic, photopic and PERG analyses at the end of the experimental period. Immediately after ERG recordings, the rats were euthanized and retinas were dissected from other ocular tissues by microsurgical procedures. One retina from each rat was used for immunofluorescence to assess RGC density, the other was divided into four quadrants for molecular analyses. In particular, for each retina, the four quadrants were randomly used for: (i) Western blot and 4-HNE levels, (ii) MDA levels, (iii) 8-OH-dG levels and (iv) GSH levels.

3.3.3 Findings

Spearmint extract does not affect MCE-induced ocular hypertension

To evaluate if SPE administration might counteract the MCE-induced ocular hypertension, the IOP of control and MCE-treated rats fed either with vehicle or with SPE-low or high was measured over the entire experimental period. As shown in Figure 14, the IOP profiles in all of the MCE-treated rats, assessed by rebound tonometry, revealed a significant increment in IOP levels, reaching a peak of about 34 mmHg within 24 hours after the MCE injection. Hereinafter, IOP gradually decreased over time, although it maintained higher levels as compared to healthy controls, thus confirming the reliability of the model in reproducing a glaucomatous-like ocular hypertension throughout the time window under analysis. Glaucomatous rats treated with either low- or high-dose SPE displayed IOP profiles comparable to those of vehicle-treated glaucomatous controls, without any significant difference in either the early IOP peak or its following gradual decrement. These findings suggest that the administration of SPE does not have any hypotensive effects.

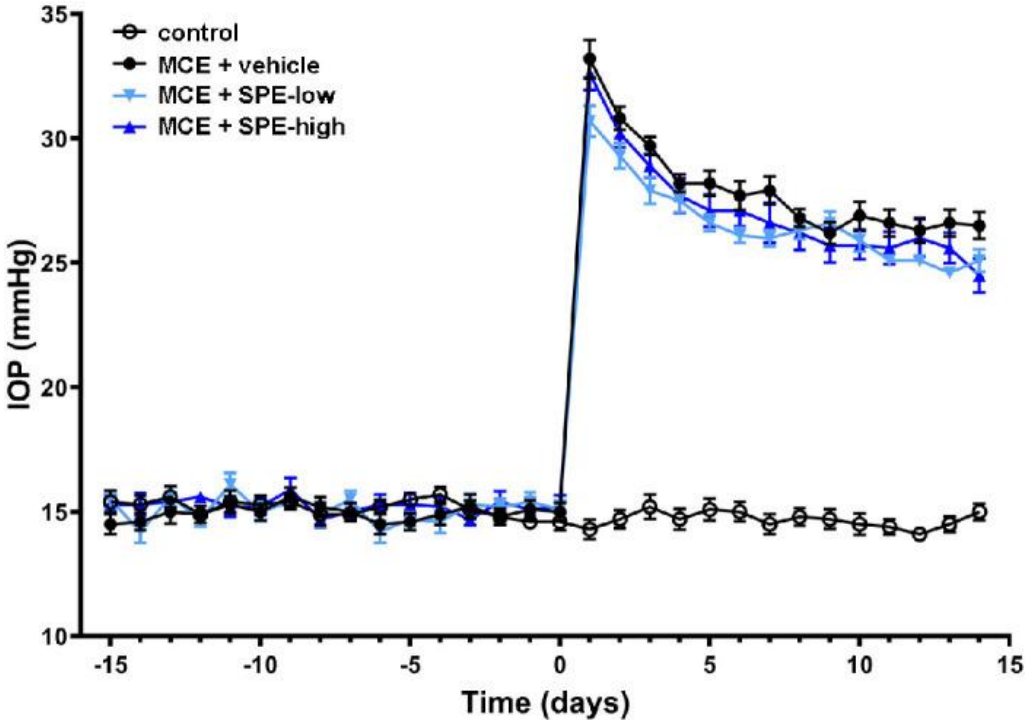

Figure 14. Values of intraocular pressure in control rats and in rats injected with MCE fed with either vehicle or SPE. Data are shown as mean ± SEM (n = 10 for each group). Day 0 corresponds to the day of MCE intraocular injection. Healthy controls did not receive an MCE injection.

Spearmint extract exerts a dose-dependent beneficial effect in RGC-related ERG parameters

In order to evaluate any SPE-mediated effects on retinal function, scotopic ERG was performed to assess the overall photoreceptor activity, reflected by the scotopic a-wave, and the overall post-receptor activity, reflected by the scotopic b-wave, at the end of the study. As expected, neither scotopic ERG parameters were significantly affected following either the MCE injection or the supplementation regimens (Figure 15A–C). Similarly, the photopic b-wave, reflecting the cone-specific overall post-receptor activity, displayed no alterations in amplitude in any experimental group (Figure 15D and E). In contrast, the PhNR amplitude, which is considered as a parameter reflecting RGC-specific activity (see paragraph 3.2.3), was significantly decreased in vehicle-treated MCE rats as compared to the healthy controls (Figure 15D and F). The loss in PhNR amplitude was dose-dependently attenuated following SPE intervention. To further assess RGC functional alterations in glaucomatous rats and putative protection of SPE, another RGC-specific functional measurement as PERG was performed. In vehicle-treated MCE rats, amplitudes in both N35–P50 and P50–N95 components were halved compared to the healthy controls (Figure 15G-I). SPE administration resulted in significant dose-dependent protection of the amplitude of both N35–P50 and P50–N95 components of the PERG response. Taken together, these results demonstrate the capacity of SPE to reduce impairment of RGC activity induced by MCE-driven ocular hypertension.

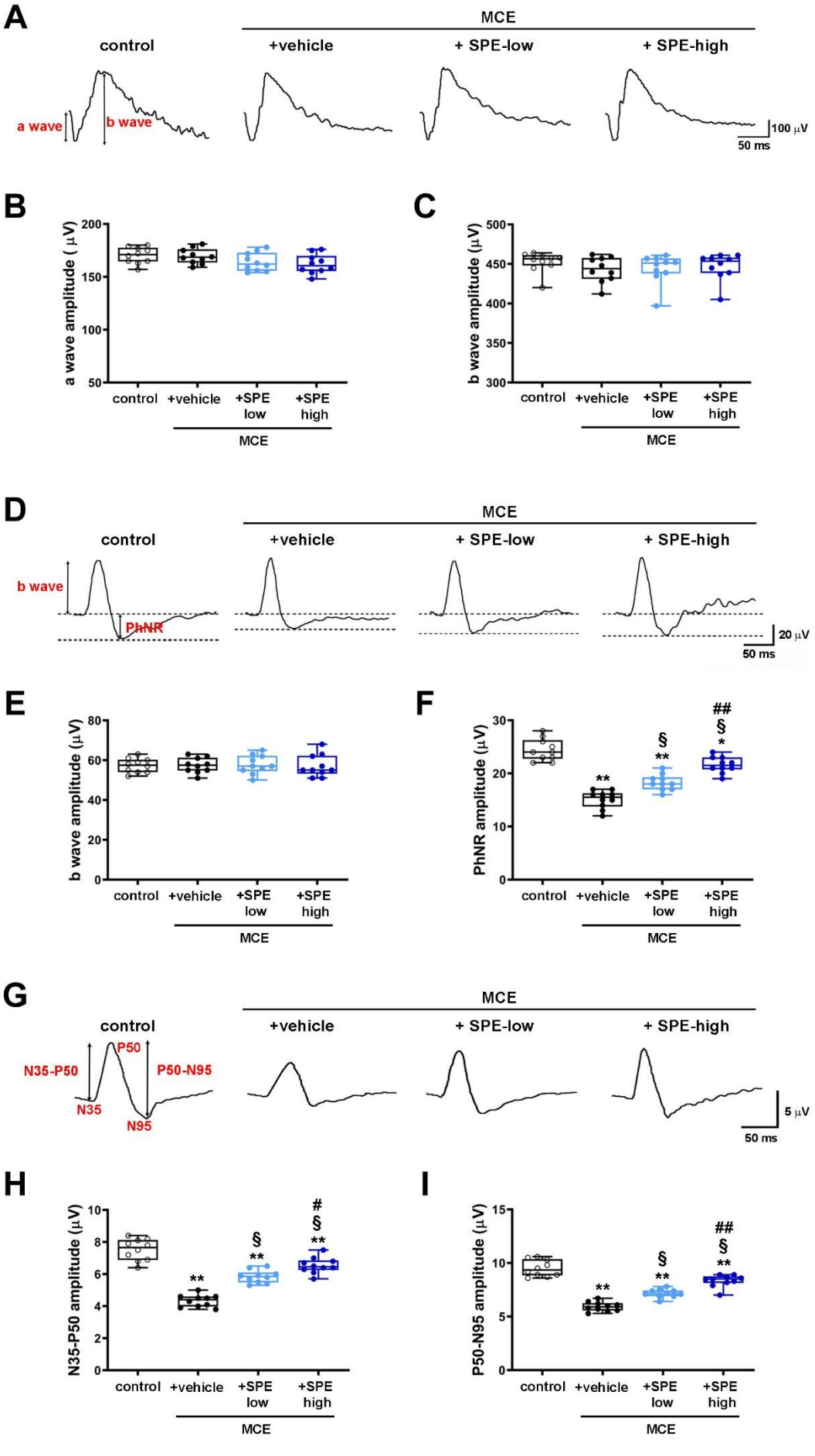
A
MCE
control
+vehicle
+ SPE-low
+ SPE-high
a wave
b wave
100 μV
50 ms
B
a wave amplitude (μV)
200
150
100
50
control
+vehicle
+SPE low
+SPE high
MCE
C
b wave amplitude (μV)
500
450
400
350
300
control
+vehicle
+SPE low
+SPE high
MCE
D
MCE
control
+vehicle
+ SPE-low
+ SPE-high
b wave
PhNR
20 μV
50 ms
E
b wave amplitude (μV)
80
60
40
20
0
control
+vehicle
+SPE low
+SPE high
MCE
F
PhNR amplitude (μV)
30
20
10
0
**
§
**
##
§
*
control
+vehicle
+SPE low
+SPE high
MCE
G
MCE
control
+vehicle
+ SPE-low
+ SPE-high
N35-P50
P50
P50-N95
N35
N95
5 μV
50 ms
H
N35-P50 amplitude (μV)
10
8
6
4
2
0
**
§
**
#
§
**
control
+vehicle
+SPE low
+SPE high
MCE
I
P50-N95 amplitude (μV)
15
10
5
0
**
§
**
##
§
**
control
+vehicle
+SPE low
+SPE high
MCE

Figure 15. Effects of SPE administration on RGC-related ERG parameters. (A) Representative scotopic ERG waveforms recorded at a light intensity of 10 cd·s/m^2 in control rats and in rats injected with MCE fed with either vehicle or SPE. (B, C) Scotopic (B) a-wave and (C) b-wave amplitudes. (D) Representative photopic ERG waveforms recorded using a 3 cd·s/m^2 stimulus on a 30 cd·s/m^2 rod-saturating background light. (E) Photopic b-wave amplitude. (F) PhNR amplitude. (G) Representative PERG traces showing the two negative peaks (N35 and N95) and the positive peak P50. (H, I) Mean amplitudes of the (H) N35–P50 and (I) P50–N95 waves. Data are shown as box plots with minimum to maximum whiskers (n = 10 for each group). *$p < 0.01$ and **$p < 0.001$ versus control; $^{§}p < 0.001$ versus MCE; $^{\#}p < 0.05$ and $^{\#\#}p < 0.001$ versus SPE-low (one-way ANOVA followed by the multiple-comparison Tukey's test).

Spearmint extract improves RGC density and trophism following MCE-induced IOP elevation in a dose-dependent manner

To assess whether SPE-mediated improvement in RGC function might be correlated with the increased RGC viability, RGC density was evaluated by immunofluorescence. In particular, RGC density was measured on retinal whole mounts labelled for RNA-binding protein with multiple splicing (RBPMS), a selective RGC marker in the mammalian retina (Rodriguez, Pérez de Sevilla Müller and Brecha, 2014), using a guinea pig polyclonal antibody (ABN1376, Merck KGaA, Darmstadt, Germany) at 1:100 dilution. Whole mount retinas were incubated with the primary antibody solution for 72 hours, followed by 48-hour incubation with a fluorescein-conjugated donkey anti-guinea pig secondary antibody (AP193F, Merck KGaA) at 1:80 dilution. The RGC density was calculated analyzing the images for RBPMS-positive cell density following the sampling of four radially opposite images at two different radial eccentricities (center = 0.5 mm, periphery = 4 mm from the optic disc) in order to determine the average density of RGCs in peripheral and central retina. As shown in Figure 16A and B, the immunostaining of RBPMS in whole-mount retinas revealed the typical difference in RGC density between the peripheral and central portion of the retina. The intracameral injection of MCE produced a proportional loss of RGC density in both central and peripheral retina. Oral supplementation with SPE resulted in a significant dose-dependent preservation of RGC density at both central and peripheral retinal locations. Furthermore, in glaucomatous rats supplemented with high-dose SPE, RGC density in the central retina was not statistically different from that in healthy controls.

Since RGC survival is strictly related to neuronal trophism exerted by several factors as BDNF and NGF, the protein levels of these neurotrophins were assessed as a further support of improved RGC viability. In particular, BDNF and NGF protein levels were measured by Western blot using rabbit monoclonal anti-BDNF (ab108319, Abcam, Cambridge, UK; 1:1000) or anti-NGF (ab52918, Abcam; 1:1000) as primary antibodies. As demonstrated by the Western blot analysis shown in Figure 16C and D, retinal levels of both BDNF and NGF significantly decreased after the intracameral injection

of MCE compared to levels observed in healthy control rats. As compared to vehicle-treated MCE rats, animals receiving SPE at both doses displayed a significant dose-dependent increase in neurotrophin supply. Taken together, these findings identified the capacity of SPE to improve RGC viability under MCE-induced ocular hypertension.

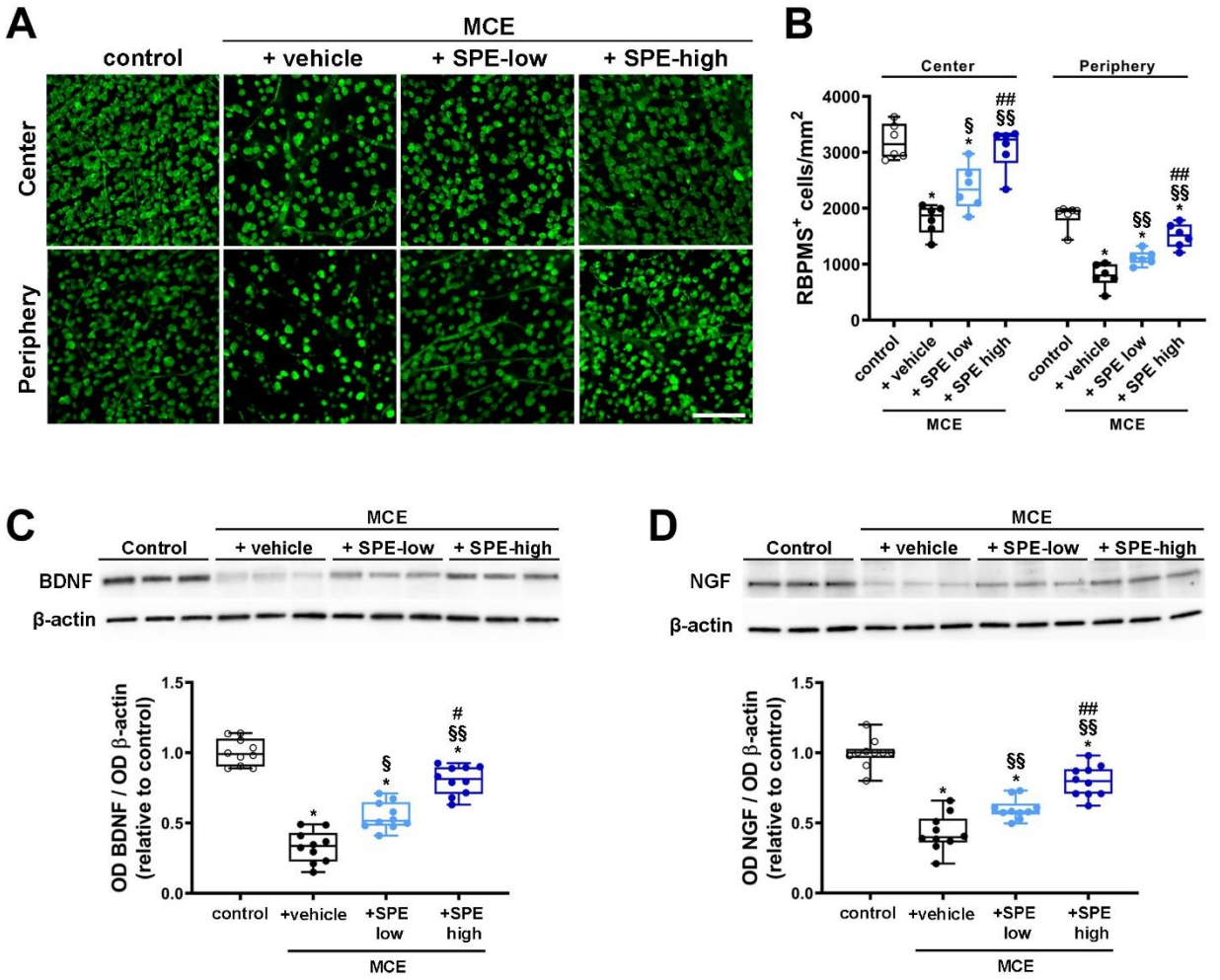

Figure 16. Effects of SPE administration on MCE-induced reduction of RGC density and neurotrophin levels. (A) Representative images of RBPMS staining (green) in central and peripheral areas of retinas from control rats and rats injected with MCE which were fed with either vehicle or SPE. Scale bar: 100 µm. (B) Analysis of RBPMS-positive cell density, differentially sampled from the peripheral and central areas of the retina. (C-D) Representative Western blots and relative densitometric analysis of (C) BDNF and (D) NGF in retinal homogenates of control rats or rats that received MCE which were fed with either vehicle or SPE. The OD of the target bands were normalized to the OD of β-actin used as loading control. Data are shown as box plots with minimum to maximum whiskers (n = 10 for each group). *$p < 0.001$ versus control; $^{\S}p < 0.01$ and $^{\S\S}p < 0.001$ versus MCE; $^{\#}p < 0.01$ and $^{\#\#}p < 0.001$ versus SPE-low (one-way ANOVA followed by the multiple-comparison Tukey's test).

Spearmint extract counteracts the MCE-induced oxidative stress and inflammation in a dose-dependent manner

To assess whether SPE-mediated amelioration of RGC viability under elevated IOP was accompanied by SPE-related antioxidant activity, markers of oxidative stress were measured. The effect of SPE in counteracting MCE-induced oxidative stress was analyzed by colorimetric analyses and Western blot. In particular, the colorimetric analysis was performed to evaluate the levels of oxidation-deriving products including MDA, 8-OH-dG, and 4-HNE, as well as depletion of the endogenous antioxidant GSH. On the other hand, Western blot was used to assess the levels of Nrf2 and HO-1 using the same primary antibodies of paragraphs 3.1.3-3.2.3 (Figure 17A-G). Retinal levels of MDA (Figure 17A), 8-OH-dG (Figure 17B), and 4-HNE (Figure 17C) were significantly increased in rats receiving the intracameral injection of MCE, paralleled by a significant depletion of GSH (Figure 17D). SPE resulted in a statistically significant dose-dependent inhibition of oxidative stress-related phenomena, with the high SPE dose able to restore 4-HNE and GSH to healthy control levels. The MCE-induced increase in oxidative products was reflected in the induction of the cellular antioxidant response as demonstrated by the rise in Nrf2 (Figure 17E and F) and subsequent increase in HO-1 (Figure 17E and G) protein levels. The effect of SPE in counteracting MCE-induced oxidative stress status was also supported by the related dose-dependent attenuation of the cellular antioxidant response. MCE-induced increments of HO-1 levels were substantially attenuated by low- and high-dose SPE. Furthermore, high-dose SPE completely restored Nrf2 to the levels observed in healthy control animals.

In order to evaluate whether the antioxidant activity of SPE was correlated with the inhibition of MCE-promoted inflammatory mechanisms, levels of the active (phosphorylated) form of NF-κB and the related levels of pro- and anti-inflammatory cytokines were evaluated by Western blot using primary antibodies anti-pNF-kB p65 (Ser 536) (see paragraph 3.1.3), anti-IL-6 (see paragraph 3.1.3), anti-IL-10 (see paragraph 3.2.3) or hamster monoclonal anti-IL-1β (sc-12742, Santa Cruz Biotechnology; 1:100). The Western blot shown in Figure 17H revealed that the intracameral injection of MCE resulted in an incremental increase in pNF-κB (Figure 17H and I), which was paralleled by an increase in pro-inflammatory cytokines IL-6 (Figure 17H and J) and IL-1β (Figure 17H and K) and a significant decrease in the anti-inflammatory cytokine IL-10 (Figure 17H and L). Oral supplementation with SPE exerted a significant dose-dependent inhibition of the pro-inflammatory processes, as demonstrated by the significant decrease in pNF-κB with subsequent reduced levels of IL-6 and IL-1β, and the increase in IL-10 compared to vehicle-treated MCE rats. In

this context, the high dose of SPE returned pNF-κB, IL-1β, and IL-10 to healthy control levels. Taken together, these findings demonstrate the antioxidant and anti-inflammatory activity of SPE.

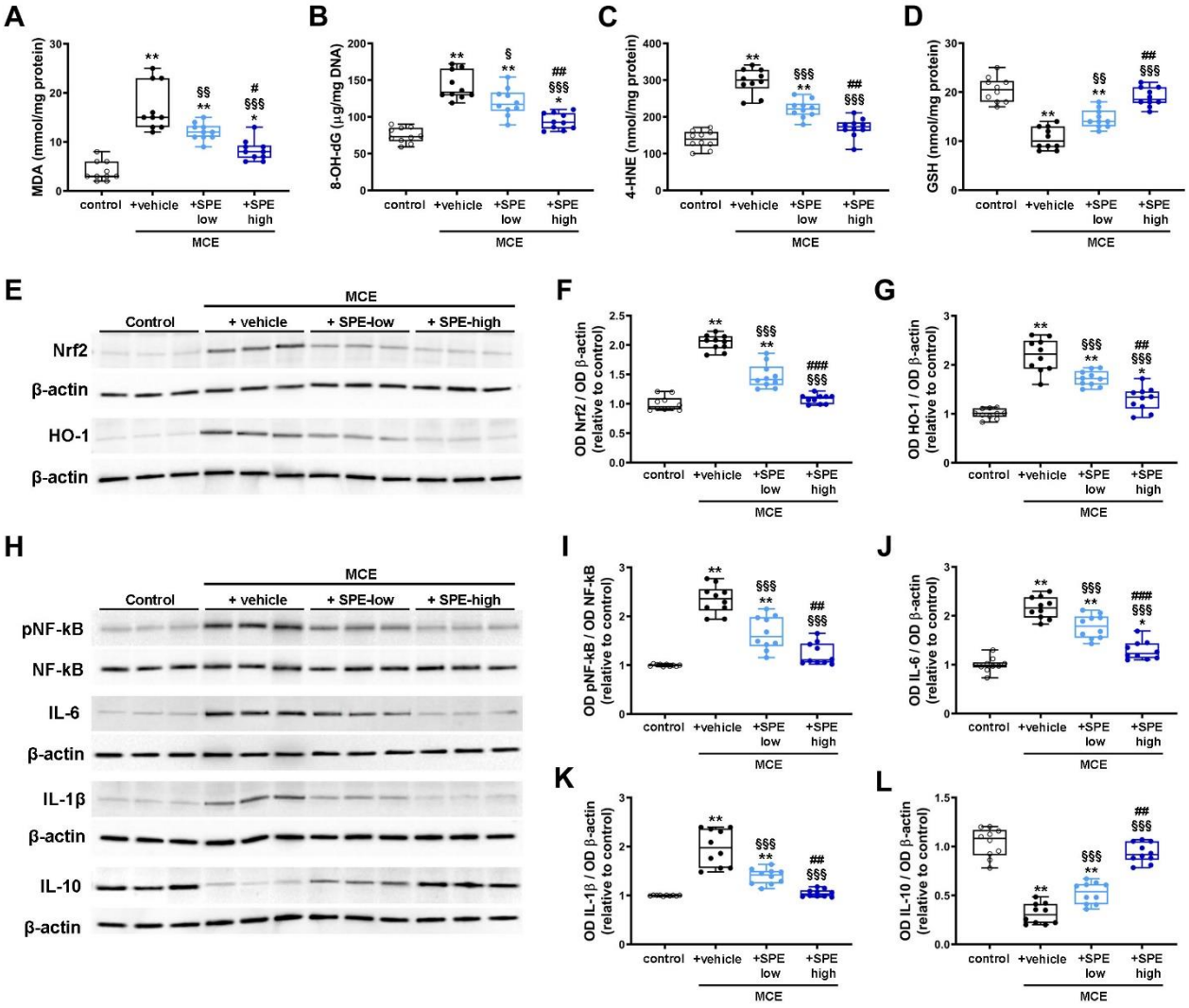

Figure 17. Effects of SPE on MCE-induced oxidative stress and the subsequent inflammatory response. (A–D) Levels of oxidative stress biomarkers of (A) MDA, (B) 8-OH-dG, (C) 4-HNE and (D) GSH in in control rats or rats that received MCE fed with either vehicle or SPE. (E) Representative Western blots from retinal homogenates of control rats or rats that received MCE fed with either vehicle or SPE. (F, G) Densitometric analysis of the levels of (F) Nrf2 and (G) HO-1. (H) Representative Western blots of pNF-κB, IL-6, IL-1β, and IL-10. (I-L) Densitometric analysis of the levels of (I) pNF-κB, (J) IL-6, (K) IL-1β, and (L) IL-10. The OD of the target bands were normalized for the OD of β-actin used as loading control, except for pNF-kB normalized to total NF-kB levels. Data are shown as box plots with minimum to maximum whiskers (n = 10 for each group). *$p < 0.05$ and **$p < 0.001$ versus control; $^{§}p < 0.05$, $^{§§}p < 0.01$ and $^{§§§}p < 0.001$ versus MCE; $^{\#}p < 0.05$, $^{\#\#}p < 0.01$, and $^{\#\#\#}p < 0.001$ versus SPE-low (one-way ANOVA followed by the multiple-comparison Tukey's test).

The datasets shown in this paragraph are collected in our published paper entitled “Efficacy of a Spearmint (*Mentha spicata L.*) Extract as Nutritional Support in a Rat Model of Hypertensive Glaucoma”, included as an original pdf version in the Appendix.

3.4 Providing retinal bioenergetic support: the positive modulation of retinal ganglion cell metabolism exerted by pyrroloquinoline quinone

3.4.1 Background

The oxidative stress mediating RGC degeneration in glaucoma occurs downstream to a reduced mitochondrial activity and bioenergetic insufficiency, which renders RGCs highly susceptible to damage for ATP depletion (see chapter 1). Given their high metabolic rate and their strict dependence on OXPHOS, RGCs may hence be a suitable cell type to study the effects associated with the regulation of the upstream mitochondrial mechanisms and metabolic processes to restore the RGC bioenergetic balance and counteract neuronal death under metabolic stress. The use of natural compounds bolstering metabolism and improving ATP production may be a promising strategy to modulate metabolic processes and increase RGC resilience with low risk of side effects.

Among the various bioenergetic compounds regulating cell metabolism, PQQ may have a strong potential as a metabolic promoter. PQQ is a quinone cofactor considered as a ‘new vitamin’ for its importance on mammalian growth, reproduction, and development (Steinberg et al., 1994; Steinberg et al., 2003). PQQ is not synthetized de novo in mammals, but is instead present in several foods, such as parsley, green pepper, spinach, kiwi, and soybeans, thus giving the possibility to consume PQQ through dietary supplementation (Kumazawa et al., 1995). Several studies have suggested the capacity of PQQ to modulate the cell bioenergetic balance, acting as an enzyme cofactor (Akagawa et al., 2016), regulating NAD content (Jonscher, Chowanadisai and Rucker, 2021), increasing OXPHOS and ATP production (Ebeling et al., 2020), and altering mitochondrial dynamics and content through the regulation of pathways particularly involved in mitochondrial biogenesis (Chowanadisai et al., 2010; Saihara et al., 2017). However, such effects are highly context-dependent and heterogeneous, dictating the necessity to study the metabolic properties of PQQ in specific systems. Although there is some evidence suggesting its protective effects in models of acute damage

in the CNS (Zhang, Feustel and Kimelberg, 2006; Zhang et al., 2012; Zhang et al., 2016; Sawmiller et al., 2017), its role in metabolic processes has not been extensively investigated in a retinal context. In this study, the role of PQQ as neuroprotective compound was assessed in models of RGC degeneration, such as retinal *ex vivo* axotomy and *in vivo* model of rotenone-induced retinal degeneration, where bioenergetic capacity is compromised. Given the reported ability of PQQ to provide bioenergetic support in non-retinal systems, the role of PQQ as metabolic promoter was assessed in *in vitro* and *in vivo* RGC-related models.

3.4.2 Treatments and experimental design

PQQ disodium salt (Mitsubishi Gas Chemical Company Inc., Tokyo, Japan) was dissolved in DMSO and diluted in either HBSS (without $CaCl_2$, $MgCl_2$ and phenol red) (Gibco) for *in vitro* and *in vivo* administration, or in culture media for *ex vivo* studies. For *in vitro* experiments, PQQ was tested at several concentrations ranging from 0.1 to 50 μM (see below). In addition, PQQ was administered *in vivo* at 20 mg/kg i.p. with different routes as further indicated. In *ex vivo* experiments PQQ was tested at 50 and 100 μM.

The experimental design accounts for two main phases where different experimental models have been used. The evaluation of PQQ neuroprotection was tested in the *ex vivo* model of retinal axotomy and in *in vivo* model of rotenone-induced retinal degeneration. For the *ex vivo* model of retinal axotomy, retinas from B6 mice were cultured as indicated in the paragraph 2.2.4. On the other hand, PQQ neuroprotection *in vivo* was assessed in B6 mice injected bilaterally with an intravitreal injection of rotenone (see paragraph 2.2.5). At the end of the experimental procedures for both the *ex vivo* and the *in vivo* models, retinas were processed for assessing RGC density by immunofluorescence.

In another phase of the study, the evaluation of the metabolic capacity of PQQ was analyzed both *in vitro* and *in vivo* models. In particular, the assessment of PQQ effects *in vitro* were performed by biochemical assays in cells from dissociated brain cortex, retina, superior colliculus and optic nerve segments isolated from B6 mice as described in paragraphs 2.11-2.12. Conversely, the investigation of PQQ-mediated metabolic processes *in vivo* was performed by immunofluorescence, molecular and metabolomic analyses in healthy B6 or MitoV mice (see below).

3.4.3 Findings

PQQ positively modulates RGC viability in different models of metabolic stress

Since RGCs strictly rely on a perfectly controlled metabolism and PQQ has been demonstrated to regulate the cell bioenergetic balance in non-retinal systems (see paragraph 3.4.1), it was hypothesized that PQQ could protect RGCs under stressors which compromise bioenergetic capacity. PQQ neuroprotection was first evaluated in an *ex vivo* model of axotomy, which reproduces an axon-specific insult to RGCs by separating the retina from the optic nerve and resulting in Wallerian degeneration and loss of ATP (Tribble et al., 2021; Enz, Tribble and Williams, 2021). Retinas from B6 mice were cultured as indicated in the paragraph 2.2.4 and treated with PQQ at a concentration of either 50 or 100 μM. After culture, retinas were processed for counting RGC density by immunolabelling of RBPMS using the rabbit polyclonal anti-RBPMS (NBP2-20112, Novusbio; 1:500) as primary antibody with an incubation at 4 °C overnight. Retinas were subsequently incubated with anti-rabbit secondary antibody conjugated with Alexa-Fluor 568 (A11011, Invitrogen, Waltham MA, United States; 1:500) for 4 h. RGC density was calculated by acquiring six images per retina (40× magnification) equidistantly at 0, 2, 4, 6, 8, and 10 o'clock from a superior to inferior line through the optic nerve head at an eccentricity of around 1000 μm. Images were cropped to 100 μm × 100 μm squares and the cell counter plugin in Fiji was used to count RBPMS + cells. The mean of cell counts per retina was measured across the 6 images and expressed as a density per 0.01 mm^2. As shown in Figures 18A and B, significant RGC loss was detected after 3 DEV. Administration of PQQ via the culture media at both 50 and 100 μM provided a significant preservation of RGC density under stress condition (Figure 18A and B).

To further explore PQQ neuroprotection, the ability of PQQ to protect RGC was tested *in vivo* in a mouse model of RGC degeneration induced by rotenone. In this model, retinal cell death is induced by the rotenone-mediated inhibition of mitochondrial Complex I, resulting in a rapid degeneration of RGCs for ATP depletion and oxidative stress (Zhang, Jones and Gonzalez-Lima, 2006; Tribble et al., 2021). Mice were treated with either vehicle (HBSS) or 20 mg/kg PQQ i.p. 24 h prior to and immediately after rotenone (or DMSO as control) injection. Immunolabelling and measurement of RGC density was performed as above. A significant RGC loss was identified after 24 h from the rotenone injection, which was prevented by PQQ administration (Figure 18C and D). Taken together, these data support a neuroprotective role of PQQ against a range of different stressors impairing RGC bioenergetic balance, such as RGC axonal damage and severe mitochondrial dysfunction.

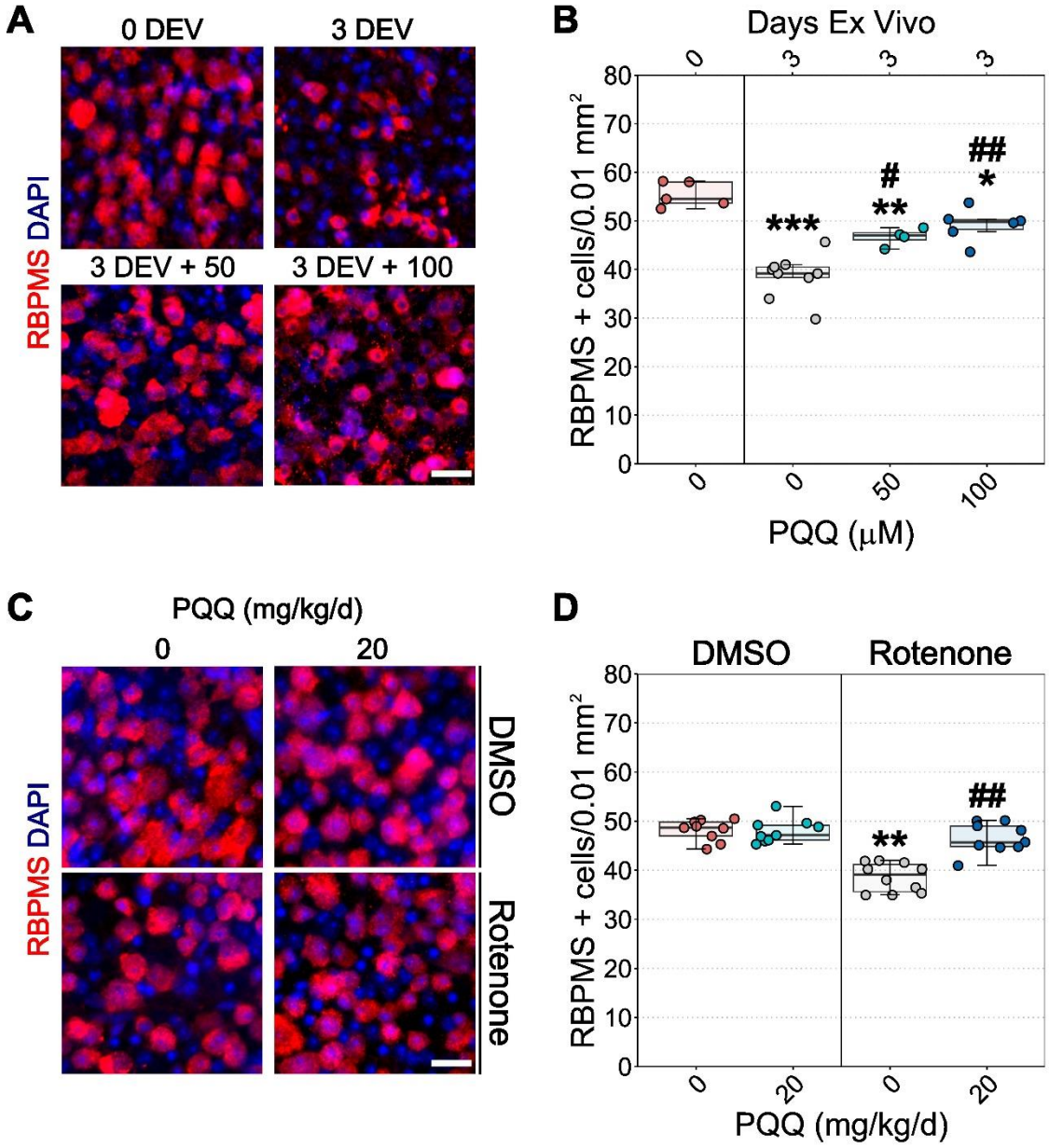

Figure 18. Effects of PQQ administration on RGC survival in *ex vivo* and *in vivo* models of RGC stress. (A) Representative image of retinas cultured *ex vivo*, immunolabeled for RBPMS (red) and counterstained with DAPI (blue). Retinal explants were cultured in either basic or supplemented media with either 50 or 100 µM PQQ for 3 days ex vivo (DEV). Control retinas (0 DEV) were directly fixed and processed after the dissection. (B) Quantification of RBPMS positive cell density per 0.01 mm^2. n = 5 (0 DEV), 9 (3 DEV), 4 (3 DEV + 50 µM PQQ), 6 (3 DEV + 100 µM PQQ) retinas. (C) Representative images of retinas from mice injected with either DMSO or rotenone and treated with either vehicle or 20 mg/kg PQQ. Flat mount retinas were immunolabeled for RBPMS (red) and counterstained with DAPI (blue). (D) Quantification of RBPMS positive cell density per 0.01 mm^2. n = 9 DMSO, 9 DMSO + PQQ, 10 rotenone and 9 rotenone + PQQ retinas. Scale bar = 20 µm. *$p < 0.05$, **$p < 0.01$ and ***$p < 0.001$ versus 0 DEV (explants) or DMSO (rotenone model); $^{\#}p < 0.01$ and $^{\#\#}p < 0.001$ versus 3 DEV (explants) or rotenone (rotenone model).

PQQ increases ATP content in vitro and in visual system tissues in vivo

As PQQ has been reported to influence metabolism and regulate the bioenergetic balance in several non-neuronal systems (Chowanadisai et al., 2010; Akagawa et al., 2016; Saihara et al., 2017; Ebeling et al., 2020; Jonscher, Chowanadisai and Rucker, 2021), the metabolic effect of PQQ in promoting neuronal ATP production was investigated. The initial assessment of whether PQQ was rapidly utilized *in vitro* was performed by measuring the ATP content in dissociated brain cortical cells incubated with PQQ as a high throughput screening. In particular, cortical cells were incubated with increasing concentrations of PQQ (0.1, 0.5, 1, 5, 10, 50 μM) for 2 h and ATP levels assessed by luminometry. A significant dose-dependent increase in ATP content was demonstrated in cortical cells from concentrations at 0.5 μM, reaching > 50-fold the untreated control at the highest dose tested (Figure 19A). As NAD is a key cofactor involved in metabolism and ATP synthesis, the capacity of short-term incubation with PQQ to promote NAD synthesis was assessed. However, PQQ effect on generating ATP *in vitro* appeared not predominantly dependent on NAD synthesis, since NAD content was not significantly influenced following the incubation with PQQ (Figure 19B). To support these findings in an RGC specific context, a similar ATP-boosting activity of PQQ was assessed in cells from dissociated RGC-related tissues. In particular, ATP content was measured in cells from dissociated retinas and superior colliculi (a major target for RGC axons in the brain), as well as isolated optic nerve segments, incubated with PQQ at 50 μM (where the highest ATP increase in cortical cells was demonstrated) for 2 h. Notably, dissociated retinal cells and optic nerve confirmed the increase in ATP as seen in cortical neurons (Figure 19C).

To further investigate the mechanisms behind PQQ's rapid ATP increase *in vitro*, ΔΨ levels in cortical cells incubated with PQQ was assessed as a dose-response curve. Cortical cells were incubated with increasing concentrations of PQQ (0.5, 5, 50 μM) for 2 h and ΔΨ level was subsequently measured by JC-1 staining. The levels of ΔΨ dose-dependently reduced in PQQ-incubated cells, decreasing to 47% of the control at 50 μM (Figure 19D). To assess a similar ΔΨ variation in RGC-related tissues, cells from retinas, optic nerves and superior colliculi were incubated with 50 μM PQQ for the same time of cortical cells. The decline in ΔΨ levels was further confirmed in dissociated retina, optic nerve, or superior colliculus incubated at a dose of 50 μM (Figure 19E), suggesting that, together with a concomitant increase in ATP levels, mitochondrial potential may be dissipated to produce ATP (Sivandzade, Bhalerao and Cucullo, 2019). Taken together, these data suggest that cells from CNS and RGC-related tissues can quickly use PQQ and increase their ATP content.

To further confirm the PQQ-mediated ATP-boosting activity in visual system tissues *in vivo*, ATP assays were performed on B6 mice treated with a single intraperitoneal injection of either vehicle or 20 mg/kg PQQ. A significant increase in ATP levels in retina, optic nerve, and superior colliculus from PQQ-treated animals was identified after 24 h following the injection. Higher levels of ATP in PQQ-treated mice were also detected in retinas and superior colliculi after 48 and 72 h (Figure 19F). Taken together, these results confirm the *in vitro* findings previously identified, further suggesting the capacity of PQQ to promote the increased ATP content in retinal districts.

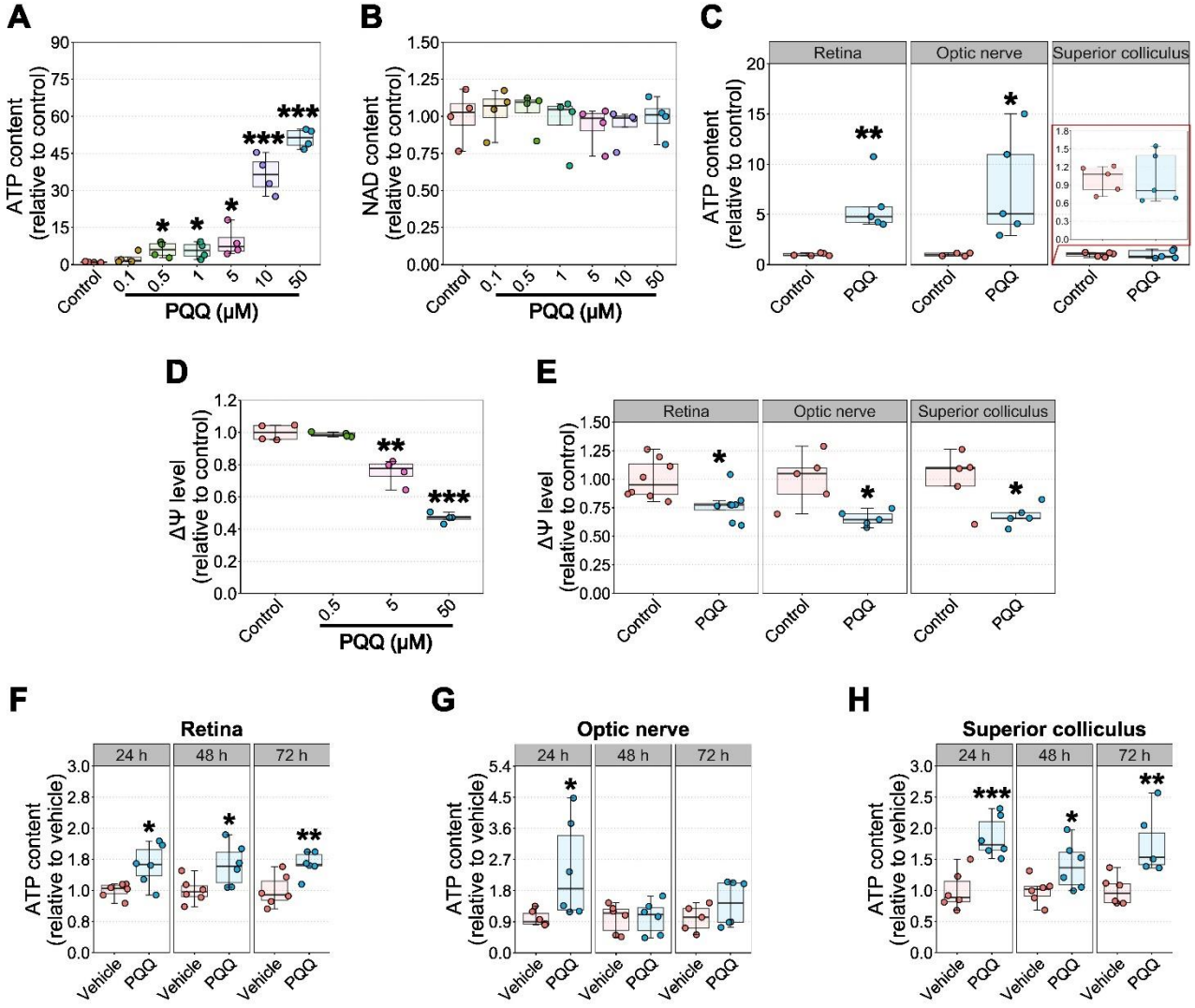

Figure 19. Effects of PQQ administration on levels of ATP, NAD and mitochondrial membrane potential *in vitro* and *in vivo*. (A) ATP and (B) NAD content in dissociated mouse brain cortical cells incubated with different doses of PQQ (0.1, 0.5, 1, 5, 10, 50 μM) for 2 h. n = 4 different cell suspensions from different hemispheres. (C) ATP content in dissociated retinal and superior colliculus cells and in isolated optic nerves incubated with 50 μM PQQ for 2 h. The red inset shows a zoom of the graph related to the ATP content in superior colliculus. n = 5 retinal replicates made by 2 pooled retinas, 5 optic nerve replicates made of isolated segments cut to 3 mm length, 5 superior colliculus replicates. (D) ΔΨ levels in dissociated brain cortical cells incubated with several concentrations of PQQ (0.5, 5, 50 μM) for 2 h. n = 4 different cell suspensions from different hemispheres. (E) ΔΨ levels in dissociated retinal and superior colliculus cells and in isolated optic nerves incubated with 50 μM PQQ for 2 h. n = 8 retinal replicates made by 2 pooled retinas, 5 optic nerve replicates

made of isolated segments cut to 3 mm length, 5 superior colliculus replicates. *p < 0.05, **p < 0.01 and ***p < 0.001 versus control. (F) ATP content in retina, optic nerve and superior colliculus from animals treated with either vehicle or a single injection of 20 mg/kg PQQ assessed after 24, 48 or 72 h from the treatment. n = 6 animals per group for each time point. *p < 0.05, **p < 0.01 and ***p < 0.001 versus vehicle.

PQQ exerts a mild effect on mitochondrial content and morphology in RGCs

ATP production is strictly dependent on mitochondrial activity and content, and PQQ has been previously reported to induce mitochondrial biogenesis through the activation of peroxisome proliferator-activated receptor-gamma coactivator alpha (PGC-1α) and the expression of mitochondrial transcription factor A (TFAM) (Chowanadisai et al., 2010; Saihara et al., 2017). Therefore, the PQQ-promoted transcriptional activation of mitochondrial biogenesis and the regulation of mitochondrial content was evaluated after a chronic administration of PQQ. B6 mice were treated long-term with 20 mg/kg PQQ i.p. every 48 h for 2 weeks and retinas/optic nerves collected for molecular analyses. Quantitative real-time PCR was performed to assess the mtRNA:nuRNA ratio, which provides an estimate of the number of mitochondrial genome copies, an early hallmark of mitochondrial biogenesis and an indicator of the number of mitochondria (Quiros et al., 2017). The expression of *Pgc-1α* and *Tfam* were also assessed. In addition to *Pgc-1α*, *Tfam*, and the mtRNA:nuRNA ratio, the expression of individual mitochondrial complexes-related genes was quantified to further assess an influence of PQQ on mitochondrial content. In particular, mRNA levels of *Ndufb8* (CI), *Sdhb* (CII), *Uqcrc2* (CIII), *mt-Co1* (CIV), *Atp5a1* (CV; ATP synthase) were evaluated. Chronic administration of PQQ had no effect on either retinal mtRNA:nuRNA ratio or *Pgc-1α* and *Tfam* mRNA, suggesting that PQQ is not effective in triggering mitochondrial biogenesis transcriptionally long-term (Figure 20A and B). However, PQQ-treated retinas displayed a significant increase in *Ndufb8* mRNA levels, without a change in other mitochondrial markers (Figure 20C). Since whole retinas contain different mixed cell populations, we next assessed if PQQ could induce a similar response in the optic nerve, which is an RGC enriched tissue (RGC axons). A significant decrease in mtRNA:nuRNA ratio, as well as *Ndufb8* and *mt-Co1* mRNA levels, was identified in optic nerves from PQQ-injected mice (Figure 20D–F). To further confirm these molecular regulations, the protein levels of these mitochondrial complex markers were analyzed to assess if the observed transcriptional changes were strictly correlated with variations in protein levels. In particular, protein levels of mitochondrial complexes were quantified by Western blot, using the mouse monoclonal total OXPHOS rodent WB antibody cocktail (ab110413, Abcam; 1:250, recognizing 5 different targets: NDUFB8, SDHB, UQCRC2, mt-CO1, ATP5a) as primary antibodies solution. A significant increase in NDUFB8 protein levels was demonstrated in retinas from PQQ-

treated animals, suggesting that its transcriptional regulation consequently results in its protein translation (Figure 20G). However, no changes in the levels of mitochondrial complexes were identified in the optic nerve after PQQ treatment (Figure 20H).

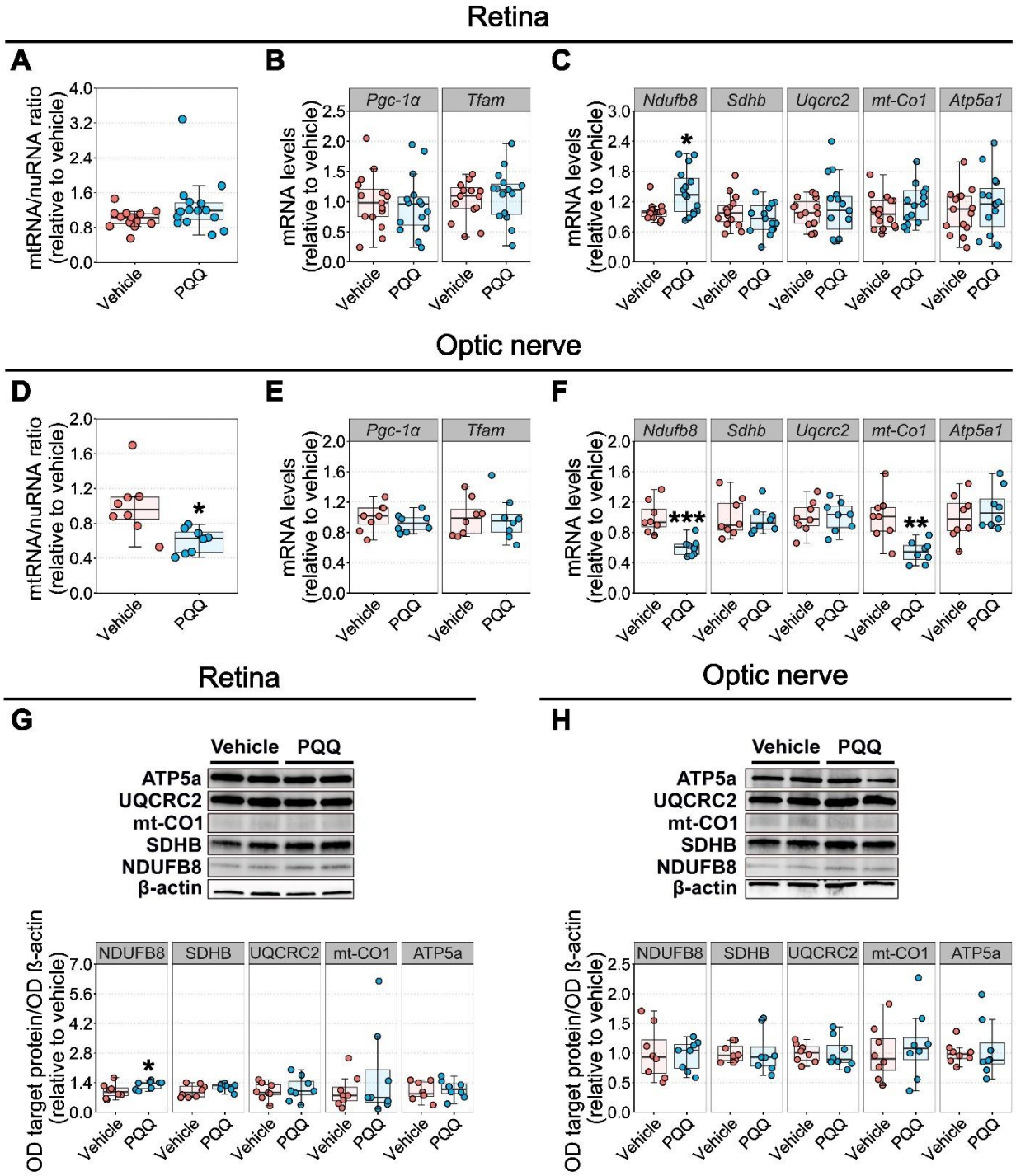

Figure 20. Effects of PQQ administration on molecular regulation of mitochondrial content *in vivo*. (A) mtRNA/nuRNA ratio in retinal samples from animals treated with either vehicle or 20 mg/kg PQQ long-term, calculated using the expression of *mt-Co2* and *Rsp18* as mitochondrial and nuclear reference gene, respectively. (B, C) *Pgc-1α*, *Tfam* (B) and *Ndufb8*, *Sdhb*, *Uqcrc2*, *mt-Co1* and *Atp5a1* (C) mRNA levels in whole retinas from vehicle and PQQ treated animals. *Rsp18* was used as housekeeping gene. n = 15 retinas per group. (D) mtRNA/nuRNA ratio in optic nerve samples from

vehicle and PQQ treated animals, calculated using the same genes described in A as mitochondrial and nuclear reference genes. (E, F) *Pgc-1α*, *Tfam* (E) and *Ndufb8*, *Sdhb*, *Uqcrc2*, *mt-Co1* and *Atp5a1* (F) mRNA levels in optic nerves from vehicle and PQQ treated animals. *Rsp18* was used as housekeeping gene. n = 8 optic nerves per group. (G, H) Representative blots and densitometric analysis of NDUFB8, SDHB, UQCRC2, mt-CO1 and ATP5a protein levels in retinas (G) and optic nerves (H) from vehicle and PQQ treated animals. Protein levels were expressed as the OD of the target normalized for the respective OD of β-actin used as loading control. n = 8 samples per group. *$p < 0.05$, **$p < 0.01$ and ***$p < 0.001$ versus vehicle.

To assess whether molecular changes of mitochondrial markers were accompanied by RGC-specific mitochondrial morphological remodeling, immunofluorescence analyses were performed on retinal and optic nerve sections from the mitochondrial reporter mouse MitoV, which specifically expresses YFP in RGC mitochondria (see chapter 2). Mice were administered either vehicle or 20 mg/kg PQQ long term and then euthanized and their tissue processed for high resolution confocal microscopy. Mitochondrial particles represented by GFP-positive particles were reconstructed and the morphology calculated in retinal GCL/NFL, IPL and optic nerves (see paragraph 2.8). All the morphological parameters were similar between retinas of vehicle- and PQQ- treated mice in both the GCL/NFL and IPL (Figure 21A-D). Conversely, the normalized mean volume and normalized volume sum were significantly increased in the optic nerve after the administration of PQQ (Figure 21E-H). Taken together, all the changes identified both at the molecular and morphological level may reflect some heterogeneity and variability across tissues and within conditions, suggesting that the overall effect of PQQ administration results in only a mild effect on mitochondrial content.

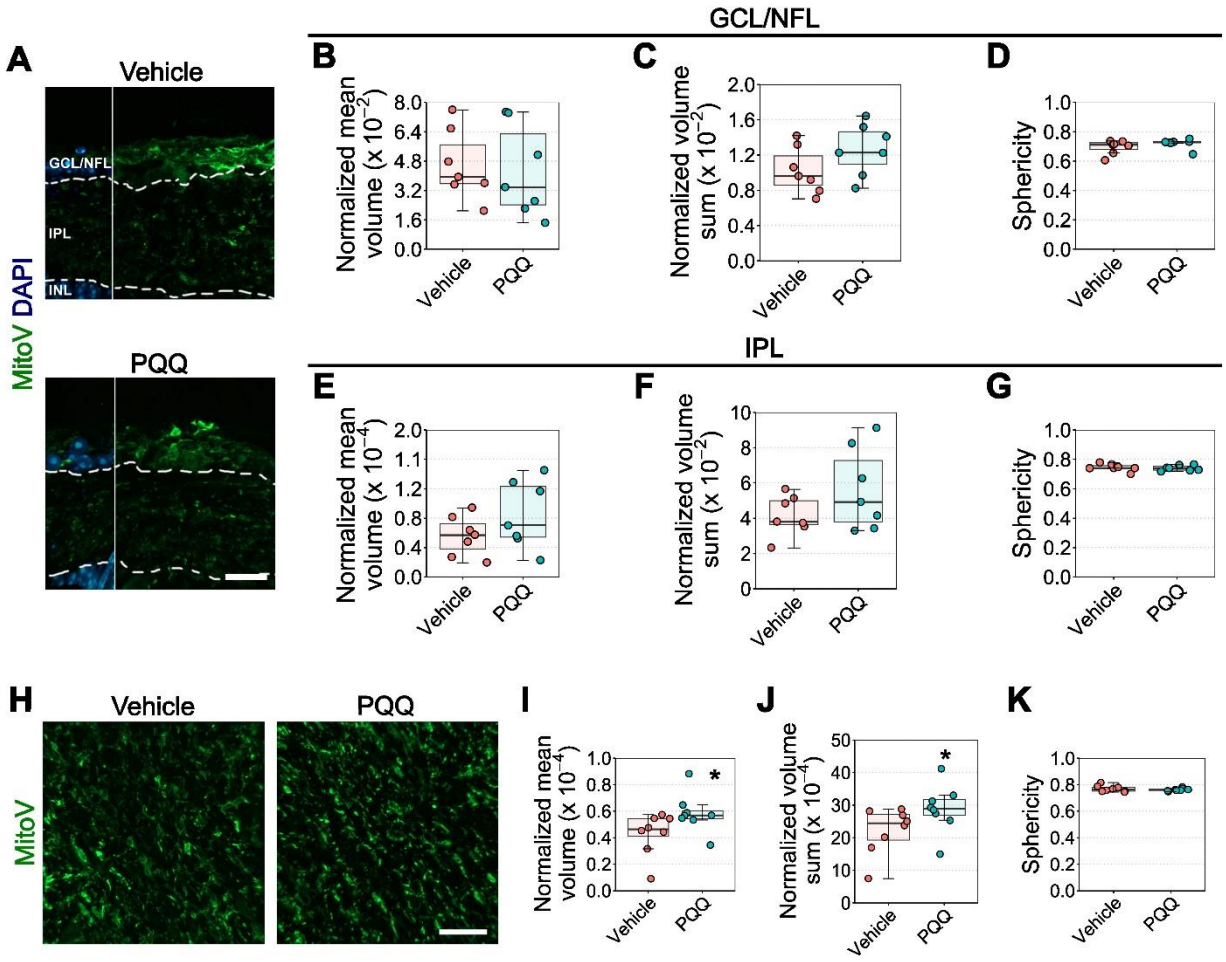

Figure 21. Effects of PQQ administration on RGC-specific mitochondrial morphology in retina and optic nerve *in vivo*. (A) Representative image of retinal cross sections from MitoV animals treated long-term with either vehicle or 20 mg/kg PQQ immunolabeled for YFP (the staining is indicated here as MitoV; green) and counterstained with DAPI (blue). The DAPI was used for reference to crop GCL/NFL from IPL. Dashed lines demark the boundaries between GCL/NFL, IPL and INL on retinal sections. (B–D) Normalized volume mean (B), normalized volume sum (C) and sphericity (D) of MitoV-positive mitochondrial particles in GCL/NFL. (E-G) Normalized volume mean (E), normalized volume sum (F) and sphericity (G) of MitoV-positive mitochondrial particles in IPL. (H) Representative images of optic nerve longitudinal sections from MitoV animals treated with either vehicle or PQQ immunolabeled for YFP (MitoV; green). (I-K) Normalized volume mean (I), normalized volume sum (J) and sphericity (K) of MitoV-positive particles in the optic nerve. n = 7 retinas and 8 optic nerves per group. Scale bar = 20 µm. GCL, ganglion cell layer; INL, inner nuclear layer; IPL, inner plexiform layer; NFL, nerve fiber layer. *p < 0.05 versus vehicle.

PQQ modifies the metabolic profiles in non-diseased RGCs

Since an only mild effect of PQQ was identified on mitochondrial content, complementary metabolic mechanisms involved in ATP-boosting effects of PQQ were determined by assessing whether PQQ administration altered the metabolic profile of RGCs under basal conditions. To achieve this, low molecular weight metabolomics was performed across retinas and optic nerves collected from mice

treated with a single injection of either vehicle or PQQ after 24 h from the treatment. HC of samples and the relative dendrograms in Figure 22A identified some heterogeneity across and within conditions in retinal samples, overall suggesting similarities between retinas from vehicle- and PQQ-treated mice. However, the division between samples in optic nerve was largely distinguished (Figure 22A). PCA confirmed a complete overlap between groups in retina, whilst identifying a clear separation of samples in the optic nerve (Figure 22B). This suggests that PQQ exerts differing effects on the two tissues studied. Administration of PQQ resulted in 5 changed metabolites in the retina (2 increased, 3 decreased) and 18 in the optic nerve (12 increased, 6 decreased) (Figure 22C and D). Comparison of changed metabolites across tissues identified AMP as a commonly changed metabolite, although demonstrating an increase in the retina and a decrease in the optic nerve (Figure 22E). Pathway analysis revealed that PQQ-induced metabolite modifications are predicted to have a minimal impact on retinal pathways, whilst significantly affecting phenylalanine metabolism, and arginine, phenylalanine, tyrosine, and tryptophan biosynthesis in the optic nerve (Figure 22F). Taken together, these data suggest the capacity of PQQ to alter the metabolic profile of non-diseased RGC-related tissues.

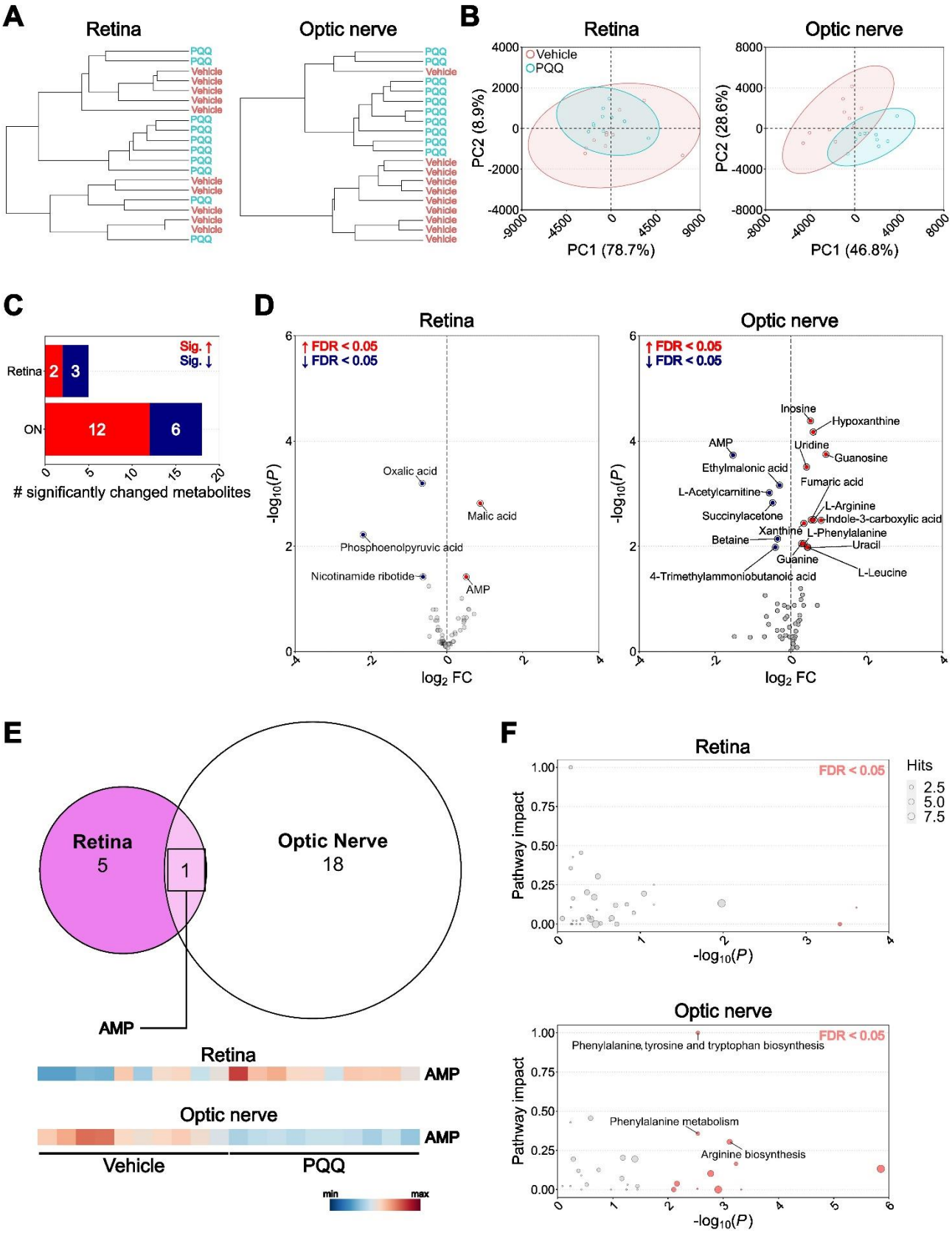
A
Retina
Optic nerve
PQQ
Vehicle
B
Retina
Optic nerve
Vehicle
PQQ
PC2 (8.9%)
PC1 (78.7%)
PC2 (28.6%)
PC1 (46.8%)
C
Sig. ↑
Sig. ↓
Retina
ON
2
3
12
6
significantly changed metabolites
D
Retina
Optic nerve
↑ FDR < 0.05
↓ FDR < 0.05
-log10(P)
log2 FC
Oxalic acid
Malic acid
Phosphoenolpyruvic acid
Nicotinamide ribotide
AMP
Inosine
Hypoxanthine
Uridine
Guanosine
Ethylmalonic acid
Fumaric acid
L-Acetylcarnitine
L-Arginine
Succinylacetone
Indole-3-carboxylic acid
Xanthine
L-Phenylalanine
Betaine
Uracil
Guanine
L-Leucine
4-Trimethylammoniobutanoic acid
E
Retina
5
1
Optic Nerve
18
AMP
Retina
AMP
Optic nerve
AMP
Vehicle
PQQ
min
max
F
Retina
Optic nerve
FDR < 0.05
Hits
2.5
5.0
7.5
Pathway impact
-log10(P)
Phenylalanine, tyrosine and tryptophan biosynthesis
Phenylalanine metabolism
Arginine biosynthesis

Figure 22. Effects of PQQ administration on metabolic profile of non-diseased RGC- related tissues *in vivo*. (A, B) Dendrograms (A) and PCA (B) of retinal and optic nerve samples collected from mice treated with either vehicle or a single injection of 20 mg/kg PQQ after 24 h. (C, D) Bar chart (C) and volcano plots (D) indicating respectively the number and the increase/decrease of significantly changed metabolites in retinas and optic nerves from PQQ-treated animals compared to their vehicle-injected controls (FDR < 0.05; red = increased in PQQ, blue = decreased). (E) Euler plot and heatmaps showing commonly changed metabolites across tissues. The red and the blue in the heatmaps indicates respectively the highest and the lowest value by row. (F) KEGG pathway analysis indicating the predicted affected pathways based on the detected changed metabolites in retinas and optic nerves from PQQ-treated mice. Pathways were highlighted in red when FDR < 0.05 and annotated when the impact was high. The size of the points indicates the pathways hits, underlining the number of the metabolites detected within the pathway. n = 10 retinas or optic nerves per group.

All these findings represent a part of the entire dataset published in our paper entitled "Pyrroloquinoline quinone drives ATP synthesis in vitro and in vivo and provides retinal ganglion cell neuroprotection" (see Appendix for the original pdf version).

Chapter 4

Discussion and final considerations

The study of the mechanisms regulating retinal neuron viability can unravel the role of key determinants for neuronal survival potentially suitable as therapeutic targets, acting early on the disease and effectively counteracting neurodegeneration. The elevated metabolism of the retina may render retinal neurons susceptible to metabolic stressors, which can alter the mitochondrial activity and create an imbalance in bioenergetic and oxidative mechanisms, thus resulting in neuronal energy depletion and damage. In this respect, several findings report an early dysregulation of bioenergetic and oxidative mechanisms prior to cell degeneration in the pathogenesis of many retinopathies induced by different type of stressors (see chapter 1), suggesting the key role of the maintenance of metabolic and oxidative processes as a general mechanism for retinal survival and a potential target for new therapies.

The data reported in this thesis provide further insights on the role of the bioenergetic and oxidative balance as determinants of retinal neuron viability and suggest possible novel approaches for neuroprotection in different retinal disorders. In particular, the studies shown in paragraphs 3.1-3.3 demonstrated a beneficial effect of a restored oxidative balance promoted by the administration of antioxidant molecules in models of hyperglycemia, LD and ocular hypertension, where oxidative stress plays a key role in retinal damage. On the other hand, the study described in paragraph 3.4 showed the efficacy of PQQ in regulating RGC bioenergetic balance and improving neuronal viability in models of metabolic stress. These studies suggest the beneficial effects of these compounds in modulating retinal oxidative and bioenergetic status under stressors, thus providing potential therapeutical implications for the management of retinal disorders.

4.1 Counteracting oxidative stress in DR

Chronic hyperglycemia can precociously induce an imbalance in metabolic and oxidative mechanisms, driving the onset of pathological events impinging on cell viability. In effect, the excess in glucose hyperactivates mitochondrial ETC reaching the maximum threshold, thus forcing the electron transfer to molecular O_2 hence generating ROS and inducing oxidative stress (see chapter 1). The susceptibility of retinal cells to metabolic stress and altered oxidative balance induced by hyperglycemic conditions is clearly evident in models of DR, where the diabetic milieu determines

the disruption of metabolic cascades sharing the oxidative stress as common downstream event altering neuronal viability (Al-Kharashi, 2018). Therefore, the administration of molecules with antioxidant activity may counteract the damaging effects of hyperglycemia-induced oxidative stress, resulting in improved retinal viability. In this context, the administration of a compound including C3G, verbascoside and zinc shown in paragraph 3.1 reduced retinal damage induced by hyperglycemia possibly through the modulation of the oxidative balance exerted by the antioxidant and anti-inflammatory properties of these molecules. C3G is a potent inhibitor of oxidative stress and its antioxidant properties include the activation of endogenous antioxidant enzymes, inhibition of ROS-promoting enzymes, and ROS scavenger activity (Tena et al., 2020). ROS scavenging activates a downstream anti-inflammatory cascade leading to the inhibition of the NF-kB activity and to the reduced release of pro-inflammatory cytokines (Min et al., 2010; Jin et al., 2018). Verbascoside has been reported to exert a major anti-inflammatory activity through the inhibition of NF-kB signaling pathway, thus resulting in decreased inflammatory response (Wu et al., 2020). In diabetic condition, verbascoside has been established to inhibit AGE formation, thus reducing one of the sources of ROS production (Liu et al., 2013; Galli et al., 2020). Zinc is known as a fundamental trace element potentiating the endogenous antioxidant response by increasing the activity of antioxidant proteins and enzymes that are transcribed by Nrf2 (Jarosz et al., 2017). The boundary line between the activity and the contribution of these hypothetical classes of natural molecules is complicated by the fact that many of the properties of each molecule are shared with the others, suggesting the possibility of interactions which may amplify the effects exerted by the individual molecules. Therefore, although a theoretical classification of the molecules could be done based on their individual bioactivity, an actual discrimination of each component activity in the context of a compound is difficult to retrieve. Nonetheless, the overall antioxidant and anti-inflammatory effect of their combination significantly prevented the establishment of vascular and neuronal alterations as BRB disruption, retinal cell death and functional impairment occurring under hyperglycemic stress. Notably, at least in the model used here, these effects act independently from hyperglycemic control, suggesting that the compound supplementation has a downstream effect in inhibiting oxidative stress- and inflammation-related mechanisms.

4.2 Rebalancing oxidative status in LD

The excessive exposure to light represents another context where the oxidative stress plays a key role in damaging retinal cells. In effect, prolonged exposures to high light intensities may cause injury to the eye, causing chemical changes in photoreceptors and reducing their viability mainly through the

onset of oxidative stress (see chapter 1). Although the LD is responsible of a reduced mitochondrial activity, unlike the hyperglycemia where ETC is oppositely overactivated, the oxidative stress seems to be a common outcome for both stressors. Therefore, the modulation of the oxidative balance by similar strategies and molecules used in the paragraph 3.1 may be effective also in reducing retinal damage in these models. In this regard, in the study described in paragraph 3.2 we demonstrated that the positive modulation of retinal oxidative balance by antioxidant and anti-inflammatory compounds including lutein or C3G improves photoreceptor viability, actively counteracting the effects of LD. The rebalance of the oxidative status by the antioxidant and anti-inflammatory properties of lutein or C3G results in a similar effective but incomplete preservation of both rods and cones that is reflected in ameliorated visual function, in line with previous findings (Sasaki et al., 2012; Wang et al., 2016). In contrast, their combined administration provides synergistic efficacy to improve photoreceptor viability under light damage. In particular, lutein and C3G may exert a multitarget role by hampering major retinal events activated by light, as demonstrated by the general reduction in upregulated levels of oxidative and pro-inflammatory markers associated with improved retinal cell viability and visual function. The synergistic effects of antioxidant mixtures may increase the bioactivity of each individual component that acts on different levels of the same signaling cascade or activates different pathways thus leading to multi-target and multifunctional effects (Leena et al., 2020). The protective capacity of lutein and C3G was also confirmed in a more complex multicomponent formula with zinc and verbascoside, confirming the capacity of these antioxidant molecules to counteract LD-driven oxidative stress and preserve retinal function.

4.3 Inhibiting oxidative stress in glaucoma

Reduced mitochondrial activity and its related oxidative stress have also been reported as early alterations occurring in RGCs during the progression of glaucoma (see chapter 1). Here, the alteration of RGC redox balance is included in a complex multifactorial context, where many other pathophysiological events concur in deteriorating RGC viability. For this reason, we investigated whether the modulation of the oxidative balance by antioxidant compounds included in SPE might be sufficient to counteract the progression of RGC degeneration. As demonstrated by the study in paragraph 3.3, the administration of SPE dose-dependently improves RGC density and activity under IOP elevation in a model of MCE-induced ocular hypertension, possibly by rebalancing the altered oxidative status. SPE has already displayed significant beneficial effects on conditions sharing increased oxidative stress and inflammation as common denominators, such as age-related cognitive decline in healthy subjects, as well as in a mouse model of stroke (Bian et al., 2020; Taira et al., 2020;

Zhang et al., 2021). The capacity of SPE in regulating the redox balance of RGCs is suggested by its richness in RA and other polyphenol compounds such as salvianolic and lithospermic acid, which are known for their anti-inflammatory and antioxidant properties (Nadeem et al., 2019; Luo et al., 2020). In addition, the finding that GSH levels are completely preserved by SPE further supports the capacity of SPE to counteract oxidative stress, indicating that this polyphenol-rich ingredient may restore the non-enzymatic antioxidant endogenous defenses acting as rapid inactivators of radicals and oxidants. Nevertheless, the novel finding that SPE may attenuate the reduced production or availability of neurotrophins seen in the glaucomatous condition is of particular importance and may provide another mechanism for the positive regulation of the redox balance. In fact, neurotrophins mediates the neuronal cell survival in the optical system and may further improve RGC oxidative balance by promoting neuronal metabolism and potentiating antioxidant defenses (Colardo et a., 2021). Of note, the administration of SPE improves RGC health independently from any hypotensive effect, suggesting that SPE acts on downstream effectors that are affected by an increase in IOP or that may partially act independently from IOP elevation.

4.4 Ameliorating bioenergetic insufficiency in RGCs

The protective effect associated with the positive regulation of RGC redox balance under glaucomatous stress suggests the potential to target the upstream mitochondrial and metabolic mechanisms to improve RGC viability. RGCs were hence used in the study reported in paragraph 3.4 to investigate whether the positive modulation of the bioenergetic balance improves RGC health under metabolic stress by using PQQ, which has been identified as metabolic regulator in non-neuronal systems (Chowanadisai et al., 2010; Akagawa et al., 2016; Saihara et al., 2017; Ebeling et al., 2020; Jonscher, Chowanadisai and Rucker, 2021). The metabolic capacity of PQQ was confirmed in our study by assessing the increase in ATP production in a retinal context. As demonstrated by the *in vitro* findings reported in paragraph 3.4, PQQ promoted the increase in ATP content in cells isolated from both cortical neurons and RGC-relevant tissues, suggesting that PQQ may be rapidly utilized to enhance the concentration of ATP. The ATP-boosting effect of PQQ was consistently obtained in visual system tissues *in vivo*, with a sustained elevation of ATP over 3 days after administration. The potential role of PQQ as a potent inducer of ATP synthesis with durable effects was identified over the whole RGC-trajectory through the visual system including retina containing RGC soma and dendrites, optic nerve containing RGC axons, and superior colliculus containing RGC terminals. Noteworthy, variation in ATP content may not undoubtedly attributed to changes in RGC energetic balance but rather be the result of the integration of neural, glial and vascular cell types in

each of the visual system tissues, whose different composition might explain the variability in response and time identified across these tissues.

The capacity of PQQ to increase ATP may be promoted by the regulation of different metabolic aspects. For instance, the short-term ATP-boosting activity of PQQ was associated with a significant variation in mitochondrial membrane potential. On the other hand, the long-term administration of PQQ resulted in a mild but significant influence on transcription and translation of mitochondrial complex-related markers together with a subtle variation in RGC mitochondrial morphology. However, the treatment with PQQ does not seem to affect the expression of mitochondrial biogenesis machinery, suggesting that the ATP-boosting effect of PQQ in the healthy retina is likely independent on mitochondrial biogenesis mechanisms. Taken together, these results suggest that the ATP-boosting activity of PQQ only partially consists in a direct effect on mitochondrial content, at least in healthy conditions. Moreover, the present findings demonstrated a clear distinction between untreated and PQQ-treated optic nerve, suggesting a PQQ-mediated change in metabolic profile. Pathway analysis predicted impact on phenylalanine metabolism, and arginine, phenylalanine, tyrosine, and tryptophan biosynthesis, similarly to nicotinamide, another relevant ATP-boosting compound providing strong neuroprotection via a metabolic mechanism (Tribble et al., 2021). Most of the metabolites displaying a significant increment following PQQ administration may be strictly involved in anaplerotic mechanisms providing substrates to improve local ATP generation by fueling glycolysis or TCA cycle and OXPHOS (Owen, Kalhan and Hanson, 2021). In particular, the PQQ-dependent increase of L-arginine and fumarate can be derived from the metabolization of argininosuccinate in a reaction catalyzed by the argininosuccinate lyase (Morris, 2002). Fumarate supports the activity of the TCA cycle and could contribute to the increased PQQ-mediated ATP content. In addition, low molecular weight metabolomics also revealed a PQQ-driven increment in L-leucine, which has been reported to induce ATP synthesis alone or in combination with other branched-chain amino acids, suggesting a potential metabolic substrate involved in the bioenergetic support of RGCs (Murín and Hamprecht, 2008; Hasegawa et al., 2018). All these mechanisms may act singularly or in concert to govern the ATP-boosting activity of PQQ, although the regulation of other potential metabolic mechanisms cannot be excluded.

Given its ability to increase local ATP content, PQQ might be a promising compound supplying RGCs with substrates counteracting stress-deriving bioenergetic insufficiency and the resultant neurodegeneration. For this reason, its neuroprotective efficacy was tested in different models of RGC stress where bioenergetic capacity has been compromised. PQQ neuroprotection was initially evaluated using an *ex vivo* model of retinal axotomy, which results in Wallerian degeneration and loss of ATP causing significant RGC degeneration (Howell et al., 2007; Maddineni et al., 2020;

Tribble et al., 2021; Enz, Tribble and Williams, 2021). The findings shown in this thesis demonstrated that the administration of PQQ moderately reduced RGC loss in this model. The moderate PQQ neuroprotection reflects the complexity of factors regulating RGC degeneration in this context and might suggest that PQQ protection may act only on some of the neurodegenerative mechanisms in this model (e.g. supplementing ATP but not addressing neuroinflammation or caspase activity) (Tribble et al., 2021; Enz, Tribble and Williams, 2021; Tribble et al., 2022). Considering the ATP-boosting capacity of PQQ demonstrated in healthy conditions, a possible mechanism of PQQ neuroprotection may be ascribed, at least in part, to a likely counteraction of bioenergetic insufficiency through an increased ATP reservoir. To isolate and further investigate the potential contribution of PQQ in reducing RGC stress by regulating neuronal bioenergetic balance, we used PQQ in a model where impaired bioenergetic capacity represents the principal insult driving RGC death. To test this, we used an *in vivo* model of bioenergetic injury initiated by the inhibition of mitochondrial Complex I following intravitreal injection of rotenone (Zhang, Jones and Gonzalez-Lima, 2006; Sasaoka et al., 2020). Rotenone injection induces acute mitochondrial damage, resulting in ATP depletion and oxidative stress which in turn impairs RGC viability. The preservation of RGC density resulting from PQQ administration supports the efficacy of PQQ in ameliorating RGC vitality under inhibition of mitochondrial activity. Since in this model RGC viability is strongly related to altered ATP reservoirs and PQQ has an ATP-boosting activity, the PQQ-promoted RGC viability is likely due to an improvement of cell bioenergetic capacity by supporting ATP levels. Therefore, the findings reported in paragraph 3.4 suggest that the prominent efficacy of PQQ against RGC damage under metabolic stress is possibly related to its ATP boosting activity, although a clear correlation would need further investigations.

4.5 Therapeutic implications

The data shown in this thesis support the role of many different molecules as potential modulators of the oxidative and bioenergetic balance to provide neuroprotection in context of retinal disorders. Notably, these molecules can be administered without invasive routes and with a relative safe profile, being naturally derived compounds which can be easily consumed by diet supplementation. The possibility of treatment without the risk of side effects suggests the potential use of these compounds as complementary strategies to those already available, especially when the latter are not sufficiently effective. For instance, the glycemic control is the milestone for the management of diabetes and its related complications including DR, although a significant number of diabetic patients undergoing glycemic control still develop DR symptoms. Here, the supplementation of combined C3G,

verbascoside and zinc may be an adjuvant strategy to the hypoglycemic drugs for the treatment of DR by acting on the oxidative events independently from any effect on blood glycemia. Moreover, the IOP-independent effects of SPE in reducing oxidative stress and protecting RGCs highlights the possibility of its application as a complementary approach in support of hypotensive treatments aimed at optimizing the management of glaucoma. This might be important for glaucoma patients where the exclusive lowering of IOP is not completely resolutive or where the RGC degeneration occurs in presence of normal IOP values (Weinreb, Aung and Medeiros, 2014).

Despite the therapeutic potential of the molecules tested in this thesis, the direct translation into the clinic is not straightforward, as there are some potential limitations. For instance, the animal models used in the experiments showed in this thesis develop pathological signs of disease in a short period of time, whereas the same damage in humans can require years to manifest. In addition, these models do not recapitulate all the clinical features of disease (e.g. proliferative retinopathy does not occur in STZ rats) or models only a subgroup of diseases (e.g. MCE-induced glaucoma mimics only hypertensive forms). In some cases, the comprehensive view of the mechanisms influenced by these molecules needs to be fully elucidated and the exact administration route is still under optimization. For instance, further studies are needed to identify the optimal dose and delivery system for PQQ to achieve similar effects in promoting ATP content by the dietary supplementation before PQQ could be considered ready for clinical use.

In conclusion, the data included in the body of this thesis provide further insights on the key role of retinal bioenergetic and oxidative balance as key determinants in neuron viability, thus suggesting possible common therapeutic targets for many different retinal disorders. In addition, the present findings suggest the potential role of antioxidant and ATP-boosting molecules as novel adjuvant strategies for the management of retinal disorders characterized by metabolic and oxidative stress.

.

Acknowledgements

Karolinska Institutet

S:T ERIKS ÖGON SJUKHUS

University of Pisa,

Department of Biology,

General Physiology unit

Massimo Dal Monte, PhD

Maurizio Cammalleri, PhD

Paola Bagnoli, PhD

Giovanni Casini, PhD

Rosario Amato, PhD

Alberto Melecchi, MS

Division of Eye and Vision,

Department of Clinical Neuroscience,

St. Erik Eye Hospital,

Karolinska Institutet

Pete A. Williams, PhD

James R. Tribble, PhD

Melissa Jöe, MS

Daniela Y. Westerlund, BS

CENTRE FOR
Eye Research
Australia

Department of Surgery,

Centre for Eye Research Australia,

Royal Victorian Eye and Ear Hospital,

Ophthalmology,

University of Melbourne

Ian A. Trounce, PhD

Swedish Metabolomics Centre

Annika Johansson, PhD

Elin Maria Näsström, PhD

References

Aggarwal BB, Quintanilha AT, Cammack R, Packer L. Damage to mitochondrial electron transport and energy coupling by visible light. Biochim Biophys Acta. 1978;502(2):367-82.

Akagawa M, Minematsu K, Shibata T, Kondo T, Ishii T, Uchida K. Identification of lactate dehydrogenase as a mammalian pyrroloquinoline quinone (PQQ)-binding protein. Sci Rep. 2016;6:26723.

Albarqi HA, Garg A, Ahmad MZ, Alqahtani AA, Walbi IA, Ahmad J. Recent Progress in Chitosan-Based Nanomedicine for Its Ocular Application in Glaucoma. Pharmaceutics. 2023;15(2):681.

Al-Kharashi AS. Role of Oxidative Stress, Inflammation, Hypoxia and Angiogenesis in the Development of Diabetic Retinopathy. Saudi J. Ophthalmol. 2018;32 (4), 318–323.

Amato R, Biagioni M, Cammalleri M, Dal Monte M, Casini G. VEGF as a Survival Factor in Ex Vivo Models of Early Diabetic Retinopathy. Invest Ophthalmol Vis Sci. 2016;57(7):3066-76.

Amato R, Catalani E, Dal Monte M, Cammalleri M, Cervia D, Casini G. Morpho-functional analysis of the early changes induced in retinal ganglion cells by the onset of diabetic retinopathy: The effects of a neuroprotective strategy. Pharmacol Res. 2022;185:106516.

Anger WH Jr. Blood Pressure Control for Diabetic Retinopathy. Am J Nurs. 2016;116(1):56.

Arjamaa O, Nikinmaa M. Oxygen-dependent diseases in the retina: role of hypoxia-inducible factors. Exp Eye Res. 2006;83(3):473-83.

Balaban RS, Nemoto S, Finkel T. Mitochondria, oxidants, and aging. Cell. 2005;120(4):483-95.

Baltan S, Inman DM, Danilov CA, Morrison RS, Calkins DJ, Horner PJ. Metabolic vulnerability disposes retinal ganglion cell axons to dysfunction in a model of glaucomatous degeneration. J Neurosci. 2010;30(16):5644-52.

Barber AJ, Baccouche B. Neurodegeneration in diabetic retinopathy: Potential for novel therapies. Vision Res. 2017;139:82-92.

Barot M, Gokulgandhi MR, Mitra AK. Mitochondrial dysfunction in retinal diseases. Curr Eye Res. 2011;36(12):1069-77.

Behl T, Kaur I, Kotwani A. Implication of oxidative stress in progression of diabetic retinopathy. Surv Ophthalmol. 2016;61(2):187-96.

Bell J. E., Hall C. Hemoproteins. In: Roberts G. C. K., Bell J. E., editors. Encyclopedia of Biophysics. Berlin, Heidelberg: Springer; 1981. pp. 42–46.

Bernstein PS, Li B, Vachali PP, Gorusupudi A, Shyam R, Henriksen BS, Nolan JM. Lutein, zeaxanthin, and meso-zeaxanthin: The basic and clinical science underlying carotenoid-based nutritional interventions against ocular disease. Prog. Retin. Eye Res. 2016;50:34–66.

Bian Y, Yamashita T, Taira Y, Shang J, Tsunoda K, Feng T, Sasaki R, Liu X, Shi X, Tadokoro K, Nomura E, Matsumoto N, Osakada Y, Omote Y, Takemoto M, Hishikawa N, Ohta Y, Abe K. A Polyphenolic Complex Attenuates Inflammatory Response and Blood- Brain Barrier Disruption. Curr Neurovasc Res. 2020;17(3):286-293.

Birben E, Sahiner UM, Sackesen C, Erzurum S, Kalayci O. Oxidative stress and antioxidant defense. World Allergy Organ J. 2012;5(1):9-19.

Bonnett R, Charlambides AA, Land EJ, Sinclair RS, Tait D, Truscott TG. Triplet states of porphyrin esters. Journal of the Chemical Society, Faraday Transactions 1: Physical Chemistry in Condensed Phases. 1980;76:852–859.

Boulton M, Rózanowska M, Rózanowski B. Retinal photodamage. J Photochem Photobiol B. 2001;64(2-3):144-61.

Brownlee M. Biochemistry and molecular cell biology of diabetic complications. Nature. 2001;414(6865):813-20.

Burgos C, Muñoz-Mingarro D, Navarro I, Martín-Cordero C, Acero N. Neuroprotective Potential of Verbascoside Isolated from Acanthus mollis L. Leaves through Its Enzymatic Inhibition and Free Radical Scavenging Ability. Antioxidants (Basel). 2020;9(12):1207.

Burgoyne CF, Downs JC, Bellezza AJ, Suh JK, Hart RT. The optic nerve head as a biomechanical structure: a new paradigm for understanding the role of IOP-related stress and strain in the pathophysiology of glaucomatous optic nerve head damage. Prog Retin Eye Res. 2005;24(1):39-73.

Calzia D, Panfoli I, Heinig N, Schumann U, Ader M, Traverso CE, Funk RH, Roehlecke C. Impairment of extramitochondrial oxidative phosphorylation in mouse rod outer segments by blue light irradiation. Biochimie. 2016;125:171-8.

Cammalleri M, Dal Monte M, Amato R, Bagnoli P, Rusciano D. A dietary combination of forskolin with homotaurine, spearmint and B vitamins protects injured retinal ganglion cells in a rodent model of hypertensive glaucoma. Nutrients. 2020; 12: 1189.

Casson RJ, Chidlow G, Crowston JG, Williams PA, Wood JPM. Retinal energy metabolism in health and glaucoma. Prog Retin Eye Res. 2021;81:100881.

Casson RJ, Chidlow G, Wood JP, Crowston JG, Goldberg I. Definition of glaucoma: clinical and experimental concepts. Clin Exp Ophthalmol. 2012;40(4):341-9.

Cervantes-Villagrana AR, Garcia-Román J, González-Espinosa C, Lamas M. Pharmacological inhibition of N-methyl d-aspartate receptor promotes secretion of vascular endothelial growth factor in müller cells: effects of hyperglycemia and hypoxia. Curr Eye Res. 2010;35(8):733-41.

Cervia D, Catalani E, Dal Monte M, Casini G. Vascular endothelial growth factor in the ischemic retina and its regulation by somatostatin. J Neurochem. 2012;120(5):818-29.

Chang J, Zhang Y, Li Y, Lu K, Shen Y, Guo Y, Qi Q, Wang M, Zhang S. NrF2/ARE and NF-κB pathway regulation may be the mechanism for lutein inhibition of human breast cancer cell. Future Oncol. 2018;14:719–726.

Chatziralli IP. The Role of Glycemic Control and Variability in Diabetic Retinopathy. Diabetes Ther. 2018;9(1):431-434.

Chen E. Inhibition of cytochrome oxidase and blue-light damage in rat retina. Graefes Arch Clin Exp Ophthalmol. 1993;231(7):416-23.

Cheung N, Wong IY, Wong TY. Ocular anti-VEGF therapy for diabetic retinopathy: overview of clinical efficacy and evolving applications. Diabetes Care. 2014;37(4):900-5.

Chidlow G, Wood JPM, Sia PI, Casson RJ. Distribution and Activity of Mitochondrial Proteins in Vascular and Avascular Retinas: Implications for Retinal Metabolism. Invest Ophthalmol Vis Sci. 2019;60(1):331-344.

Choi YK, Park JH, Yun JA, Cha JH, Kim Y, Won MH, Kim KW, Ha KS, Kwon YG, Kim YM. Heme oxygenase metabolites improve astrocytic mitochondrial function via a Ca2+-dependent HIF-1α/ERRα circuit. PLoS One. 2018;13(8):e0202039.

Chowanadisai W, Bauerly KA, Tchaparian E, Wong A, Cortopassi GA, Rucker RB. Pyrroloquinoline quinone stimulates mitochondrial biogenesis through cAMP response element-binding protein phosphorylation and increased PGC-1alpha expression. J Biol Chem. 2010;285(1):142–152.

Chrysostomou V, Rezania F, Trounce IA, Crowston JG. Oxidative stress and mitochondrial dysfunction in glaucoma. Curr Opin Pharmacol. 2013;13(1):12-5.

Chun YS, Kim MS, Park JW. Oxygen-dependent and -independent regulation of HIF-1alpha. J Korean Med Sci. 2002;17(5):581-8.

Cirlini M, Mena P, Tassotti M, Herrlinger KA, Nieman KM, Dall'Asta C, Del Rio D. Phenolic and Volatile Composition of a Dry Spearmint (Mentha spicata L.) Extract. Molecules. 2016;21(8):1007.

Colardo M, Martella N, Pensabene D, Siteni S, Di Bartolomeo S, Pallottini V, Segatto M. Neurotrophins as Key Regulators of Cell Metabolism: Implications for Cholesterol Homeostasis. Int J Mol Sci. 2021;22(11):5692.

Contín MA, Benedetto MM, Quinteros-Quintana ML, Guido ME. Light pollution: the possible consequences of excessive illumination on retina. Eye (Lond). 2016;30(2):255-63.

Coucha M, Elshaer SL, Eldahshan WS, Mysona BA, El-Remessy AB. Molecular mechanisms of diabetic retinopathy: potential therapeutic targets. Middle East Afr J Ophthalmol. 2015;22(2):135-44.

Coughlin L, Morrison RS, Horner PJ, Inman DM. Mitochondrial morphology differences and mitophagy deficit in murine glaucomatous optic nerve. Invest Ophthalmol Vis Sci. 2015;56(3):1437-46.

Cougnard-Gregoire A, Merle BMJ, Aslam T, Seddon JM, Aknin I, Klaver CCW, Garhöfer G, Layana AG, Minnella AM, Silva R, Delcourt C. Blue Light Exposure: Ocular Hazards and Prevention-A Narrative Review. Ophthalmol Ther. 2023;12(2):755-788.

Cringle SJ, Yu DY, Yu PK, Su EN. Intraretinal oxygen consumption in the rat in vivo. Invest Ophthalmol Vis Sci. 2002;43(6):1922-7. Erratum in: Invest Ophthalmol Vis Sci 2003;44(1):9.

Cross N, van Steen C, Zegaoui Y, Satherley A, Angelillo L. Current and Future Treatment of Retinitis Pigmentosa. Clin Ophthalmol. 2022;16:2909-2921.

Cunningham MA, Edelman JL, Kaushal S. Intravitreal steroids for macular edema: the past, the present, and the future. Surv Ophthalmol. 2008;53(2):139-49.

Curcio CA, Allen KA. Topography of ganglion cells in human retina. J Comp Neurol. 1990;300(1):5-25.

Dal Monte M, Cammalleri M, Amato R, Pezzino S, Corsaro R, Bagnoli P, Rusciano D. A Topical Formulation of Melatoninergic Compounds Exerts Strong Hypotensive and Neuroprotective Effects in a Rat Model of Hypertensive Glaucoma. Int J Mol Sci. 2020b;21(23):9267.

Dal Monte M, Cammalleri M, Pezzino S, Corsaro R, Pescosolido N, Bagnoli P, Rusciano D. Hypotensive Effect of Nanomicellar Formulation of Melatonin and Agomelatine in a Rat Model: Significance for Glaucoma Therapy. Diagnostics (Basel). 2020a;10(3):138.

Dengler-Crish CM, Smith MA, Inman DM, Wilson GN, Young JW, Crish SD. Anterograde transport blockade precedes deficits in retrograde transport in the visual projection of the DBA/2J mouse model of glaucoma. Front Neurosci. 2014;8:290.

Duh EJ, Sun JK, Stitt AW. Diabetic retinopathy: current understanding, mechanisms, and treatment strategies. JCI Insight. 2017;2(14):e93751.

Ebanks B, Chakrabarti L. Mitochondrial ATP Synthase is a Target of Oxidative Stress in Neurodegenerative Diseases. Front Mol Biosci. 2022;9:854321.

Ebeling MC, Polanco JR, Qu J, Tu C, Montezuma SR, Ferrington DA. Improving retinal mitochondrial function as a treatment for age-related macular degeneration. Redox Biol. 2020;34:101552.

Eisenhauer B, Natoli S, Liew G, Flood VM. Lutein and Zeaxanthin-Food Sources, Bioavailability and Dietary Variety in Age-Related Macular Degeneration Protection. Nutrients. 2017;9:120.

Enz TJ, Tribble JR, Williams PA. Comparison of glaucoma-relevant transcriptomic datasets identifies novel drug targets for retinal ganglion cell neuroprotection. J Clin Med. 2021;10(17):3938.

Falcone PH, Nieman KM, Tribby AC, Vogel RM, Joy JM, Moon JR, Slayton CA, Henigman MM, Lasrado JA, Lewis BJ, Fonseca BA, Herrlinger KA. The attention-enhancing effects of spearmint extract supplementation in healthy men and women: a randomized, double-blind, placebo-controlled, parallel trial. Nutr Res. 2019;64:24-38.

Fechtner RD, Weinreb RN. Mechanisms of optic nerve damage in primary open angle glaucoma. Surv Ophthalmol. 1994;39(1):23-42.

Fernandez-Vizarra E, Zeviani M. Mitochondrial disorders of the OXPHOS system. FEBS Lett. 2021;595(8):1062-1106.

Ferreira SM, Lerner SF, Brunzini R, Reides CG, Evelson PA, Llesuy SF. Time course changes of oxidative stress markers in a rat experimental glaucoma model. Invest Ophthalmol Vis Sci. 2010;51(9):4635-40.

Foxton RH, Finkelstein A, Vijay S, Dahlmann-Noor A, Khaw PT, Morgan JE, Shima DT, Ng YS. VEGF-A is necessary and sufficient for retinal neuroprotection in models of experimental glaucoma. Am J Pathol. 2013;182(4):1379-90.

Fraenkl SA, Muser J, Groell R, Reinhard G, Orgul S, Flammer J, Goldblum D. Plasma citrate levels as a potential biomarker for glaucoma. J Ocul Pharmacol Ther. 2011;27(6):577-80.

Françon A, Torriglia A. Cell death mechanisms in retinal phototoxicity. Journal of Photochemistry and Photobiology. 2023;15:100185.

Frey T, Antonetti DA. Alterations to the blood-retinal barrier in diabetes: cytokines and reactive oxygen species. Antioxid Redox Signal. 2011;15(5):1271-84.

Galli A, Marciani P, Marku A, Ghislanzoni S, Bertuzzi F, Rossi R, Di Giancamillo A, Castagna M, Perego C. Verbascoside Protects Pancreatic β-Cells against ER-Stress. Biomedicines 2020;8(12):582.

Girgis S, Lee LR. Treatment of dry age-related macular degeneration: A review. Clin Exp Ophthalmol. 2023;51(8):835-852.

Guo C, Sun L, Chen X, Zhang D. Oxidative stress, mitochondrial damage and neurodegenerative diseases. Neural Regen Res. 2013;8(21):2003-14.

Han WH, Gotzmann J, Kuny S, Huang H, Chan CB, Lemieux H, Sauvé Y. Modifications in Retinal Mitochondrial Respiration Precede Type 2 Diabetes and Protracted Microvascular Retinopathy. Invest Ophthalmol Vis Sci. 2017;58(10):3826-3839.

Harder JM, Guymer C, Wood JPM, Daskalaki E, Chidlow G, Zhang C, Balasubramanian R, Cardozo BH, Foxworth NE, Deering KE, Ouellette TB, Montgomery C, Wheelock CE, Casson RJ, Williams PA, John SWM. Disturbed glucose and pyruvate metabolism in glaucoma with neuroprotection by pyruvate or rapamycin. Proc Natl Acad Sci U S A. 2020;117(52):33619-33627.

Harun-Or-Rashid M, Pappenhagen N, Palmer PG, Smith MA, Gevorgyan V, Wilson GN, Crish SD, Inman DM. Structural and Functional Rescue of Chronic Metabolically Stressed Optic Nerves through Respiration. J Neurosci. 2018;38(22):5122-5139.

Hasegawa T, Ikeda HO, Iwai S, Muraoka Y, Tsuruyama T, Okamoto-Furuta K, Kohda H, Kakizuka A, Yoshimura N. Branched chain amino acids attenuate major pathologies in mouse models of retinal degeneration and glaucoma. Heliyon. 2018;4(2):e00544.

Hernández C, Dal Monte M, Simó R, Casini G. Neuroprotection as a Therapeutic Target for Diabetic Retinopathy. J Diabetes Res. 2016;2016:9508541.

Herrlinger KA, Nieman KM, Sanoshy KD, Fonseca BA, Lasrado JA, Schild AL, Maki KC, Wesnes KA, Ceddia MA. Spearmint Extract Improves Working Memory in Men and Women with Age-Associated Memory Impairment. J Altern Complement Med. 2018;24(1):37-47.

Hoang QV, Linsenmeier RA, Chung CK, Curcio CA. Photoreceptor inner segments in monkey and human retina: mitochondrial density, optics, and regional variation. Vis Neurosci. 2002;19(4):395-407.

Hockberger PE, Skimina TA, Centonze VE, Lavin C, Chu S, Dadras S, Reddy JK, White JG. Activation of flavin-containing oxidases underlies light-induced production of H2O2 in mammalian cells. Proc Natl Acad Sci U S A. 1999;96(11):6255-60.

Howell GR, Libby RT, Jakobs TC, Smith RS, Phalan FC, Barter JW, Barbay JM, Marchant JK, Mahesh N, Porciatti V, Whitmore AV, Masland RH, John SW. Axons of retinal ganglion cells are insulted in the optic nerve early in DBA/2J glaucoma. J Cell Biol. 2007;179(7):1523–1537.

Huang LE, Arany Z, Livingston DM, Bunn HF. Activation of hypoxia-inducible transcription factor depends primarily upon redox-sensitive stabilization of its alpha subunit. J Biol Chem. 1996;271(50):32253-9.

Iacobini C, Vitale M, Pesce C, Pugliese G, Menini S. Diabetic Complications and Oxidative Stress: A 20-Year Voyage Back in Time and Back to the Future. Antioxidants (Basel). 2021;10(5):727.

Ikonne EU, Ikpeazu VO, Ugbogu EA. The potential health benefits of dietary natural plant products in age related eye diseases. Heliyon. 2020;6:e04408.

Ito YA, Di Polo A. Mitochondrial dynamics, transport, and quality control: A bottleneck for retinal ganglion cell viability in optic neuropathies. Mitochondrion. 2017;36:186-192.

Ivan M, Kondo K, Yang H, Kim W, Valiando J, Ohh M, Salic A, Asara JM, Lane WS, Kaelin WG Jr. HIFalpha targeted for VHL-mediated destruction by proline hydroxylation: implications for O2 sensing. Science. 2001;292(5516):464-8.

Jarosz M, Olbert M, Wyszogrodzka G, Młyniec K, Librowski T. Antioxidant and Anti-inflammatory Effects of Zinc. Zinc-dependent NF-κB Signaling. Inflammopharmacology 2017;25(1):11–24.

Jassim AH, Fan Y, Pappenhagen N, Nsiah NY, Inman DM. Oxidative Stress and Hypoxia Modify Mitochondrial Homeostasis During Glaucoma. Antioxid Redox Signal. 2021;35(16):1341-1357.

Jin X, Wang C, Wu W, Liu T, Ji B, Zhou F. Cyanidin-3-glucoside Alleviates 4-Hydroxyhexenal-Induced NLRP3 Inflammasome Activation via JNK-C-Jun/AP-1 Pathway in Human Retinal Pigment Epithelial Cells. J. Immunol. Res. 2018;5604610.

Jonscher KR, Chowanadisai W, Rucker RB. Pyrroloquinoline-quinone is more than an antioxidant: a vitamin-like accessory factor important in health and disease prevention. Biomolecules. 2021;11(10):1441.

Joyal JS, Gantner ML, Smith LEH. Retinal energy demands control vascular supply of the retina in development and disease: The role of neuronal lipid and glucose metabolism. Prog Retin Eye Res. 2018;64:131-156.

Juan CA, Pérez de la Lastra JM, Plou FJ, Pérez-Lebeña E. The Chemistry of Reactive Oxygen Species (ROS) Revisited: Outlining Their Role in Biological Macromolecules (DNA, Lipids and Proteins) and Induced Pathologies. Int J Mol Sci. 2021;22(9):4642.

Kamińska A, Romano GL, Rejdak R, Zweifel S, Fiedorowicz M, Rejdak M, Bajka A, Amato R, Bucolo C, Avitabile T, Drago F, Toro MD. Influence of Trace Elements on Neurodegenerative Diseases of The Eye-The Glaucoma Model. Int J Mol Sci. 2021;22(9):4323.

Kang Q, Yang C. Oxidative stress and diabetic retinopathy: Molecular mechanisms, pathogenetic role and therapeutic implications. Redox Biol. 2020;37:101799.

Kanwar M, Chan PS, Kern TS, Kowluru RA. Oxidative damage in the retinal mitochondria of diabetic mice: possible protection by superoxide dismutase. Invest Ophthalmol Vis Sci. 2007;48(8):3805-11.

Khoo HE, Azlan A, Tang ST, Lim SM. Anthocyanidins and Anthocyanins: Colored Pigments as Food, Pharmaceutical Ingredients, and the Potential Health Benefits. Food Nutr. Res. 2017;61(1):1361779.

Kim JH, Kim JH, Jun HO, Yu YS, Kim KW. Inhibition of protein kinase C delta attenuates blood-retinal barrier breakdown in diabetic retinopathy. Am J Pathol. 2010a;176(3):1517-24.

Kim SJ, Flach AJ, Jampol LM. Nonsteroidal anti-inflammatory drugs in ophthalmology. Surv Ophthalmol. 2010b;55(2):108-33.

Ko ML, Peng PH, Ma MC, Ritch R, Chen CF. Dynamic changes in reactive oxygen species and antioxidant levels in retinas in experimental glaucoma. Free Radic Biol Med. 2005;39(3):365-73.

Kohno H, Chen Y, Kevany BM, Pearlman E, Miyagi M, Maeda T, Palczewski K, Maeda A. Photoreceptor proteins initiate microglial activation via Toll-like receptor 4 in retinal degeneration mediated by all-trans-retinal. J. Biol. Chem. 2013;288:15326–15341.

Kouassi Nzoughet J, Chao de la Barca JM, Guehlouz K, Leruez S, Coulbault L, Allouche S, Bocca C, Muller J, Amati-Bonneau P, Gohier P, Bonneau D, Simard G, Milea D, Lenaers G, Procaccio V, Reynier P. Nicotinamide Deficiency in Primary Open-Angle Glaucoma. Invest Ophthalmol Vis Sci. 2019;60(7):2509-2514.

Kowluru RA. Diabetes-induced elevations in retinal oxidative stress, protein kinase C and nitric oxide are interrelated. Acta Diabetol. 2001;38(4):179-85.

Kumazawa T, Sato K, Seno H, Ishii A, Suzuki O. Levels of pyrroloquinoline quinone in various foods. Biochem J. 1995;307 (Pt 2)(Pt 2):331-3.

Kushwah N, Bora K, Maurya M, Pavlovich MC, Chen J. Oxidative Stress and Antioxidants in Age-Related Macular Degeneration. Antioxidants (Basel). 2023;12(7):1379.

Kutsyr O, Sánchez-Sáez X, Martínez-Gil N, de Juan E, Lax P, Maneu V, Cuenca N. Gradual Increase in Environmental Light Intensity Induces Oxidative Stress and Inflammation and Accelerates Retinal Neurodegeneration. Invest Ophthalmol Vis Sci. 2020;61(10):1.

Lee M, Li S, Sato K, Jin M. Interphotoreceptor Retinoid-Binding Protein Mitigates Cellular Oxidative Stress and Mitochondrial Dysfunction Induced by All-trans-Retinal. Invest Ophthalmol Vis Sci. 2016;57(4):1553-62.

Lee S, Sheck L, Crowston JG, Van Bergen NJ, O'Neill EC, O'Hare F, Kong YX, Chrysostomou V, Vincent AL, Trounce IA. Impaired complex-I-linked respiration and ATP synthesis in primary open-angle glaucoma patient lymphoblasts. Invest Ophthalmol Vis Sci. 2012;53(4):2431-7.

Leena MM, Silvia MG, Vinitha K, Moses JA, Anandharamakrishnan C. Synergistic potential of nutraceuticals: Mechanisms and prospects for futuristic medicine. Food Funct. 2020;11:9317–9337.

Léveillard T, Sahel JA. Metabolic and redox signaling in the retina. Cell Mol Life Sci. 2017;74(20):3649-3665.

Li LH, Lee JC, Leung HH, Lam WC, Fu Z, Lo A. Lutein Supplementation for Eye Diseases. Nutrients. 2020;12:1721.

Li W, Chen S, Zhou G, Li H, Zhong L, Liu S. Potential Role of Cyanidin 3-glucoside (C3G) in Diabetic Cardiomyopathy in Diabetic Rats: An In Vivo Approach. Saudi J. Biol. Sci. 2018;25(3):500–506.

Li YH, Zhuo YH, Lü L, Chen LY, Huang XH, Zhang JL, Li SY, Wang XG. Caspase-dependent retinal ganglion cell apoptosis in the rat model of acute diabetes. Chin Med J (Engl). 2008;121(24):2566-71.

Liu H, Prokosch V. Energy Metabolism in the Inner Retina in Health and Glaucoma. Int J Mol Sci. 2021;22(7):3689.

Liu T, Liu WH, Zhao JS, Meng FZ, Wang H. Lutein protects against β-amyloid peptide-induced oxidative stress in cerebrovascular endothelial cells through modulation of Nrf-2 and NF-κb. Cell Biol. Toxicol. 2017b;33:57–67.

Liu T, Zhang L, Joo D, Sun SC. NF-κB signaling in inflammation. Signal Transduct Target Ther. 2017a;2:17023.

Liu YH, Lu YL, Han CH, Hou WC. Inhibitory Activities of Acteoside, Isoacteoside, and its Structural Constituents against Protein Glycation In Vitro. Bot. Stud. 2013;54(1):6.

Locri F, Cammalleri M, Dal Monte M, Rusciano D, Bagnoli P. Protective efficacy of a dietary supplement based on forskolin, homotaurine, spearmint extract, and group B vitamins in a mouse model of optic nerve injury. Nutrients. 2019; 11: 2931.

Lorenzi M. The polyol pathway as a mechanism for diabetic retinopathy: attractive, elusive, and resilient. Exp Diabetes Res. 2007;2007:61038.

Luo C, Zou L, Sun H, Peng J, Gao C, Bao L, Ji R, Jin Y, Sun S. A Review of the Anti-Inflammatory Effects of Rosmarinic Acid on Inflammatory Diseases. Front Pharmacol. 2020;11:153.

Ma Q. Role of nrf2 in oxidative stress and toxicity. Annu Rev Pharmacol Toxicol. 2013;53:401-26.

Maddineni P, Kasetti RB, Patel PD, Millar JC, Kiehlbauch C, Clark AF, Zode GS. CNS axonal degeneration and transport deficits at the optic nerve head precede structural and functional loss of retinal ganglion cells in a mouse model of glaucoma. Mol Neurodegener. 2020;15(1):48.

Maeda A, Maeda T, Golczak M, Chou S, Desai A, Hoppel CL, Matsuyama S, Palczewski K. Involvement of all-trans-retinal in acute light-induced retinopathy of mice. J Biol Chem. 2009;284(22):15173-83.

Maeda A, Maeda T, Golczak M, Palczewski K. Retinopathy in mice induced by disrupted all-trans-retinal clearance. J Biol Chem. 2008;283(39):26684-93.

Mailloux RJ. An Update on Mitochondrial Reactive Oxygen Species Production. Antioxidants (Basel). 2020;9(6):472.

Marc RE, Jones BW, Watt CB, Vazquez-Chona F, Vaughan DK, Organisciak DT. Extreme retinal remodeling triggered by light damage: implications for age related macular degeneration. Mol Vis. 2008;14:782-806.

Mares J. Lutein and Zeaxanthin Isomers in Eye Health and Disease. Annu. Rev. Nutr. 2016;36:571–602.

Marmoy OR, Viswanathan S. Clinical electrophysiology of the optic nerve and retinal ganglion cells. Eye Lond. 2021

Masser DR, Otalora L, Clark NW, Kinter MT, Elliott MH, Freeman WM. Functional changes in the neural retina occur in the absence of mitochondrial dysfunction in a rodent model of diabetic retinopathy. J Neurochem. 2017;143(5):595-608.

McDonald HR, Schatz H. Visual loss following panretinal photocoagulation for proliferative diabetic retinopathy. Ophthalmology. 1985;92(3):388-93.

Metea MR, Newman EA. Signalling within the neurovascular unit in the mammalian retina. Exp Physiol. 2007;92(4):635-40.

Miller DJ, Cascio MA, Rosca MG. Diabetic Retinopathy: The Role of Mitochondria in the Neural Retina and Microvascular Disease. Antioxidants (Basel). 2020;9(10):905.

Min SW, Ryu SN, Kim D. HAnti-inflammatory Effects of Black rice, Cyanidin-3-O-Beta-D-Glycoside, and its Metabolites, Cyanidin and Protocatechuic Acid. Int. Immunopharmacol. 2010;10(8):959–966.

Mittal M, Siddiqui MR, Tran K, Reddy SP, Malik AB. Reactive oxygen species in inflammation and tissue injury. Antioxid Redox Signal. 2014;20(7):1126-67.

Mohamed Q, Gillies MC, Wong TY. Management of diabetic retinopathy: a systematic review. JAMA. 2007;298(8):902-16.

Moreno MC, Campanelli J, Sande P, Sánez DA, Keller Sarmiento MI, Rosenstein RE. Retinal oxidative stress induced by high intraocular pressure. Free Radic Biol Med. 2004;37(6):803-12.

Morgan JE. Circulation and axonal transport in the optic nerve. Eye (Lond). 2004;18(11):1089-95.

Morris SM., Jr Regulation of enzymes of the urea cycle and arginine metabolism. Annu Rev Nutr. 2002;22:87–105.

Mozaffarieh M, Flammer J. Is there more to glaucoma treatment than lowering IOP? Surv Ophthalmol. 2007;52 Suppl 2:S174-9.

Muoio V, Persson PB, Sendeski MM. The neurovascular unit - concept review. Acta Physiol (Oxf). 2014;210(4):790-8.

Murín R, Hamprecht B. Metabolic and regulatory roles of leucine in neural cells. Neurochem Res. 2008;33(2):279–284.

Nadeem M, Imran M, Aslam Gondal T, Imran A, Shahbaz M, Muhammad Amir R, Wasim Sajid M, Batool Qaisrani T, Atif M, Hussain G, Salehi B, Ostrander EA, Martorell M, Sharifi-Rad J, Cho WC, Martins N. Therapeutic potential of rosmarinic acid: a comprehensive review. Appl Sci. 2019; 9: 3139.

Naderi A, Zahed R, Aghajanpour L, Amoli FA, Lashay A. Long term features of diabetic retinopathy in streptozotocin-induced diabetic Wistar rats. Exp Eye Res. 2019;184:213-220.

Naguib S, Backstrom JR, Gil M, Calkins DJ, Rex TS. Retinal oxidative stress activates the NRF2/ARE pathway: An early endogenous protective response to ocular hypertension. Redox Biol. 2021;42:101883.

Narayan DS, Chidlow G, Wood JP, Casson RJ. Glucose metabolism in mammalian photoreceptor inner and outer segments. Clin Exp Ophthalmol. 2017;45(7):730-741.

Neupane P, Bhuju S, Thapa N, Bhattarai HK. ATP Synthase: Structure, Function and Inhibition. Biomol Concepts. 2019;10(1):1-10.

Nieman KM, Sanoshy KD, Bresciani L, Schild AL, Kelley KM, Lawless AL, Ceddia MA, Maki KC, Del Rio D, Herrlinger KA. Tolerance, bioavailability, and potential cognitive health implications of a distinct aqueous spearmint extract. J Funct Food Health Dis. 2015; 5: 165–187.

Okawa H, Sampath AP, Laughlin SB, Fain GL. ATP consumption by mammalian rod photoreceptors in darkness and in light. Curr Biol. 2008;18(24):1917-21.

O'Leary F, Campbell M. The blood-retina barrier in health and disease. FEBS J. 2023;290(4):878-891.

Organisciak DT, Vaughan DK. Retinal light damage: mechanisms and protection. Prog Retin Eye Res. 2010;29(2):113-34.

Osorio-Paz I, Uribe-Carvajal S, Salceda R. In the Early Stages of Diabetes, Rat Retinal Mitochondria Undergo Mild Uncoupling due to UCP2 Activity. PLoS One. 2015;10(5):e0122727.

Otterbein LE, Choi AM. Heme oxygenase: colors of defense against cellular stress. Am J Physiol Lung Cell Mol Physiol. 2000;279(6):L1029-37.

Owen OE, Kalhan SC, Hanson RW. The key role of anaplerosis and cataplerosis for citric acid cycle function. J Biol Chem. 2002;277(34):30409–30412.

Paoli M, Marles-Wright J, Smith A. Structure-function relationships in heme-proteins. DNA Cell Biol. 2002;21(4):271-80.

Perron NR, Brumaghim JL. A review of the antioxidant mechanisms of polyphenol compounds related to iron binding. Cell Biochem Biophys. 2009;53(2):75-100.

Qin Y, Zhai Q, Li Y, Cao M, Xu Y, Zhao K., Wang T. Cyanidin-3-O-glucoside Ameliorates Diabetic Nephropathy through Regulation of Glutathione Pool. Biomed. Pharmacother. 2018;103:1223–1230.

Quigley HA, Dunkelberger GR, Green WR. Chronic human glaucoma causing selectively greater loss of large optic nerve fibers. Ophthalmology. 1988;95(3):357-63.

Quiros PM, Goyal A, Jha P, Auwerx J. Analysis of mtDNA/nDNA ratio in mice. Curr Protoc Mouse Biol. 2017;7(1):47–54.

Raman R, Gupta A, Kulothungan V, Sharma T. Prevalence and risk factors of diabetic retinopathy in subjects with suboptimal glycemic, blood pressure and lipid control. Sankara Nethralaya Diabetic Retinopathy Epidemiology and Molecular Genetic Study (SN-DREAMS, Report 33). Curr Eye Res. 2012;37(6):513-23.

Rashid K, Wolf A, Langmann T. Microglia Activation and Immunomodulatory Therapies for Retinal Degenerations. Front. Cell. Neurosci. 2018;12:176.

Reagan-Shaw S, Nihal M, Ahmad N. Dose translation from animal to human studies revisited. FASEB J. 2008; 22: 659–661.

Riccitelli S, Di Paolo M, Ashley J, Bisti S, Di Marco S. The Time courses of Functional, Morphological, and Molecular Changes Triggered by Light Exposure in Sprague-Dawley Rat Retinas. Cells. 2021;10:1561.

Rodriguez AR, Pérez de Sevilla Müller L, Brecha NC. The RNA binding protein RBPMS is a selective marker of ganglion cells in the mammalian retina. J Comp Neurol. 2014; 522: 1411–1443.

Rossino MG, Casini G. Nutraceuticals for the Treatment of Diabetic Retinopathy. Nutrients 2019;11(4):771.

Rossino MG, Lulli M, Amato R, Cammalleri M, Monte MD, Casini G. Oxidative Stress Induces a VEGF Autocrine Loop in the Retina: Relevance for Diabetic Retinopathy. Cells. 2020;9(6):1452.

Rózanowska M, Sarna T. Light-induced damage to the retina: role of rhodopsin chromophore revisited. Photochem Photobiol. 2005;81(6):1305-30.

Saihara K, Kamikubo R, Ikemoto K, Uchida K, Akagawa M. Pyrroloquinoline quinone, a redox-active o-Quinone, stimulates mitochondrial biogenesis by activating the SIRT1/PGC-1α signaling pathway. Biochemistry. 2017;56(50):6615–6625.

Sasaki M, Yuki K, Kurihara T, Miyake S, Noda K, Kobayashi S, Ishida S, Tsubota K, Ozawa Y. Biological role of lutein in the light-induced retinal degeneration. J. Nutr. Biochem. 2012;23:423–429.

Sasaki R, Nishimura N, Hoshino H, Isa Y, Kadowaki M, Ichi T, Tanaka A, Nishiumi S, Fukuda I, Ashida H, Horio F, Tsuda T. Cyanidin 3-glucoside Ameliorates Hyperglycemia and Insulin Sensitivity Due to Downregulation of Retinol Binding Protein 4 Expression in Diabetic Mice. Biochem. Pharmacol. 2007;74(11):1619–1627.

Sasaoka M, Ota T, Kageyama M. Rotenone-induced inner retinal degeneration via presynaptic activation of voltage-dependent sodium and L-type calcium channels in rats. Sci Rep. 2020;10(1):969.

Sawmiller D, Li S, Mori T, Habib A, Rongo D, Delic V, Bradshaw PC, Shytle RD, Sanberg C, Bickford P, Tan J. Beneficial effects of a pyrroloquinolinequinone-containing dietary formulation on motor deficiency, cognitive decline and mitochondrial dysfunction in a mouse model of Alzheimer's disease. Heliyon. 2017;3(4):e00279.

Schellini SA, Gregório EA, Spadella CT, Machado JL, de-Moraes-Silva MA. Müller cells and diabetic retinopathy. Braz J Med Biol Res. 1995;28(9):977-80.

Schick T, Ersoy L, Lechanteur YT, Saksens NT, Hoyng CB, den Hollander AI, Kirchhof B, Fauser S. HISTORY OF SUNLIGHT EXPOSURE IS A RISK FACTOR FOR AGE-RELATED MACULAR DEGENERATION. Retina. 2016;36(4):787-90.

Semeraro F, Cancarini A, dell'Omo R, Rezzola S, Romano MR, Costagliola C. Diabetic Retinopathy: Vascular and Inflammatory Disease. J Diabetes Res. 2015;2015:582060.

Shaban H, Gazzotti P, Richter C. Cytochrome c oxidase inhibition by N-retinyl-N-retinylidene ethanolamine, a compound suspected to cause age-related macula degeneration. Arch Biochem Biophys. 2001;394(1):111-6.

Simó R, Hernández C. Advances in the medical treatment of diabetic retinopathy. Diabetes Care. 2009;32(8):1556-62.

Simó R, Hernández C. Intravitreous anti-VEGF for diabetic retinopathy: hopes and fears for a new therapeutic strategy. Diabetologia. 2008;51(9):1574-80.

Simó R, Stitt AW, Gardner TW. Neurodegeneration in diabetic retinopathy: does it really matter? Diabetologia. 2018;61(9):1902-1912.

Sivandzade F, Bhalerao A, Cucullo L. Analysis of the mitochondrial membrane potential using the cationic JC-1 dye as a sensitive fluorescent probe. Bio Protoc. 2019;9(1):e3128.

Steinberg F, Stites TE, Anderson P, Storms D, Chan I, Eghbali S, Rucker R. Pyrroloquinoline quinone improves growth and reproductive performance in mice fed chemically defined diets. Exp Biol Med (Maywood) 2003;228(2):160–166.

Steinberg FM, Gershwin ME, Rucker RB. Dietary pyrroloquinoline quinone: growth and immune response in BALB/c mice. J Nutr. 1994;124(5):744–753.

Stitt AW, Curtis TM, Chen M, Medina RJ, McKay GJ, Jenkins A, Gardiner TA, Lyons TJ, Hammes HP, Simó R, Lois N. The progress in understanding and treatment of diabetic retinopathy. Prog Retin Eye Res. 2016;51:156-86.

Sundaresan P, Simpson DA, Sambare C, Duffy S, Lechner J, Dastane A, Dervan EW, Vallabh N, Chelerkar V, Deshpande M, O'Brien C, McKnight AJ, Willoughby CE. Whole-mitochondrial genome sequencing in primary open-angle glaucoma using massively parallel sequencing identifies novel and known pathogenic variants. Genet Med. 2015;17(4):279-84.

Syc-Mazurek SB, Libby RT. Axon injury signaling and compartmentalized injury response in glaucoma. Prog Retin Eye Res. 2019;73:100769.

Taira Y, Yamashita T, Bian Y, Shang J, Matsumoto N, Sasaki R, Tadokoro K, Nomura E, Tsunoda K, Omote Y, Takemoto M, Hishikawa N, Ohta Y, Abe K. Antioxidative effects of a novel dietary supplement Neumentix in a mouse stroke model. J Stroke Cerebrovasc Dis. 2020;29(8):104818.

Tamm ER, Braunger BM, Fuchshofer R. Intraocular Pressure and the Mechanisms Involved in Resistance of the Aqueous Humor Flow in the Trabecular Meshwork Outflow Pathways. Prog Mol Biol Transl Sci. 2015;134:301-14.

Tao JX, Zhou WC, Zhu XG. Mitochondria as Potential Targets and Initiators of the Blue Light Hazard to the Retina. Oxid Med Cell Longev. 2019;2019:6435364.

Tena N, Martín J, Asuero AG. State of the Art of Anthocyanins: Antioxidant Activity, Sources, Bioavailability, and Therapeutic Effect in Human Health. Antioxidants (Basel) 2020;9(5): 451.

Tezel G, Yang X, Cai J. Proteomic identification of oxidatively modified retinal proteins in a chronic pressure-induced rat model of glaucoma. Invest Ophthalmol Vis Sci. 2005;46(9):3177-87.

Tham YC, Li X, Wong TY, Quigley HA, Aung T, Cheng CY. Global prevalence of glaucoma and projections of glaucoma burden through 2040: a systematic review and meta-analysis. Ophthalmology. 2014;121(11):2081-90.

Tribble JR, Kastanaki E, Uslular AB, Rutigliani C, Enz TJ, Williams PA. Valproic acid reduces neuroinflammation to provide retinal ganglion cell neuroprotection in the retina axotomy model. Front Cell Dev Biol. 2022;10:903436.

Tribble JR, Otmani A, Sun S, Ellis SA, Cimaglia G, Vohra R, Jöe M, Lardner E, Venkataraman AP, Domínguez-Vicent A, Kokkali E, Rho S, Jóhannesson G, Burgess RW, Fuerst PG, Brautaset R, Kolko M, Morgan JE, Crowston JG, Votruba M, Williams PA. Nicotinamide provides neuroprotection in glaucoma by protecting against mitochondrial and metabolic dysfunction. Redox Biol. 2021;43:101988

Tribble JR, Vasalauskaite A, Redmond T, Young RD, Hassan S, Fautsch MP, Sengpiel F, Williams PA, Morgan JE. Midget retinal ganglion cell dendritic and mitochondrial degeneration is an early feature of human glaucoma. Brain Commun. 2019;1(1):fcz035.

Tubbs AS, Kennedy KER, Alfonso-Miller P, Wills CCA, Grandner MA. A randomized, double-blind, placebo-controlled trial of a polyphenol botanical blend on sleep and daytime functioning. Int J Environ Res Public Health. 2021; 18: 3044.

Van Bergen NJ, Crowston JG, Craig JE, Burdon KP, Kearns LS, Sharma S, Hewitt AW, Mackey DA, Trounce IA. Measurement of Systemic Mitochondrial Function in Advanced Primary Open-Angle Glaucoma and Leber Hereditary Optic Neuropathy. PLoS One. 2015;10(10):e0140919.

van den Berg RA, Hoefsloot HC, Westerhuis JA, Smilde AK, van der Werf MJ. Centering, scaling, and transformations: improving the biological information content of metabolomics data. BMC Genom. 2006;7:142.

Vives-Bauza C, Anand M, Shiraz AK, Magrane J, Gao J, Vollmer-Snarr HR, Manfredi G, Finnemann SC. The age lipid A2E and mitochondrial dysfunction synergistically impair phagocytosis by retinal pigment epithelial cells. J Biol Chem. 2008;283(36):24770-80. Erratum in: J Biol Chem. 2013 Nov 8;288(45):32639. Shirazi, Arash K [corrected to Shiraz, Ashton K].

Wang GL, Jiang BH, Rue EA, Semenza GL. Hypoxia-inducible factor 1 is a basic-helix-loop-helix-PAS heterodimer regulated by cellular O2 tension. Proc Natl Acad Sci U S A. 1995;92(12):5510-4.

Wang J, Li M, Geng Z, Khattak S, Ji X, Wu D, Dang Y. Role of Oxidative Stress in Retinal Disease and the Early Intervention Strategies: A Review. Oxid Med Cell Longev. 2022;2022:7836828.

Wang L, Dong J, Cull G, Fortune B, Cioffi GA. Varicosities of intraretinal ganglion cell axons in human and nonhuman primates. Invest Ophthalmol Vis Sci. 2003;44(1):2-9.

Wang Y., Huo Y., Zhao L., Lu F., Wang O., Yang X., Ji B., Zhou F. Cyanidin-3-glucoside and its phenolic acid metabolites attenuate visible light-induced retinal degeneration in vivo via activation of Nrf2/HO-1 pathway and NF-κB suppression. Mol. Nutr. Food Res. 2016;60:1564–1577.

Weinreb RN, Aung T, Medeiros FA. The pathophysiology and treatment of glaucoma: a review. JAMA. 2014; 311: 1901–1911.

Weinreb RN, Leung CK, Crowston JG, Medeiros FA, Friedman DS, Wiggs JL, Martin KR. Primary open-angle glaucoma. Nat Rev Dis Primers. 2016;2:16067.

Wielgus AR, Roberts JE. Retinal photodamage by endogenous and xenobiotic agents. Photochem Photobiol. 2012;88(6):1320-45.

Wilkinson CP, Ferris FL 3rd, Klein RE, Lee PP, Agardh CD, Davis M, Dills D, Kampik A, Pararajasegaram R, Verdaguer JT; Global Diabetic Retinopathy Project Group. Proposed international clinical diabetic retinopathy and diabetic macular edema disease severity scales. Ophthalmology. 2003;110(9):1677-82.

Williams PA, Harder JM, Foxworth NE, Cochran KE, Philip VM, Porciatti V, Smithies O, John SW. Vitamin B3 modulates mitochondrial vulnerability and prevents glaucoma in aged mice. Science. 2017;355(6326):756-760.

Williams PA, Howell GR, Barbay JM, Braine CE, Sousa GL, John SW, Morgan JE. Retinal ganglion cell dendritic atrophy in DBA/2J glaucoma. PLoS One. 2013;8(8):e72282.

Wong TY, Cheung CM, Larsen M, Sharma S, Simó R. Diabetic retinopathy. Nat Rev Dis Primers. 2016;2:16012.

Wong-Riley MT. Energy metabolism of the visual system. Eye Brain. 2010;2:99-116.

Woodburn SC, Bollinger JL, Wohleb ES. The semantics of microglia activation: neuroinflammation, homeostasis, and stress. J Neuroinflammation. 2021;18(1):258.

Wu L, Georgiev MI, Cao H, Nahar L, El-Seedi HR, Sarker SD, Xiao J, Lu B. Therapeutic Potential of Phenylethanoid Glycosides: A Systematic Review. Med. Res. Rev. 2020;40(6): 2605–2649.

Wu Y, Tang L, Chen B. Oxidative stress: implications for the development of diabetic retinopathy and antioxidant therapeutic perspectives. Oxid Med Cell Longev. 2014;2014:752387.

Wu Y, Zou H. Research Progress on Mitochondrial Dysfunction in Diabetic Retinopathy. Antioxidants (Basel). 2022;11(11):2250.

Yang X, Yu XW, Zhang DD, Fan ZG. Blood-retinal barrier as a converging pivot in understanding the initiation and development of retinal diseases. Chin Med J (Engl). 2020;133(21):2586-2594.

Yang Y, Jiang G, Zhang P, Fan J. Programmed cell death and its role in inflammation. Mil Med Res. 2015;2:12.

Youssef PN, Sheibani N, Albert DM. Retinal light toxicity. Eye (Lond). 2011;25(1):1-14.

Yuan Q, Zeng ZL, Yang S, Li A, Zu X, Liu J. Mitochondrial Stress in Metabolic Inflammation: Modest Benefits and Full Losses. Oxid Med Cell Longev. 2022;2022:8803404.

Zhang K, Zhang L, Weinreb RN. Ophthalmic drug discovery: novel targets and mechanisms for retinal diseases and glaucoma. Nat Rev Drug Discov. 2012;11(7):541-59.

Zhang L, Liu J, Cheng C, Yuan Y, Yu B, Shen A, Yan M. The neuroprotective effect of pyrroloquinoline quinone on traumatic brain injury. J Neurotrauma. 2012;29(5):851–864.

Zhang Q, Chen S, Yu S, Qin J, Zhang J, Cheng Q, Ke K, Ding F. Neuroprotective effects of pyrroloquinoline quinone against rotenone injury in primary cultured midbrain neurons and in a rat model of Parkinson's disease. Neuropharmacology. 2016;108:238–251.

Zhang X, Jones D, Gonzalez-Lima F. Neurodegeneration produced by rotenone in the mouse retina: a potential model to investigate environmental pesticide contributions to neurodegenerative diseases. J Toxicol Environ Health A. 2006;69(18):1681–1697.

Zhang X, Zeng H, Bao S, Wang N, Gillies MC. Diabetic macular edema: new concepts in patho-physiology and treatment. Cell Biosci. 2014;4:27.

Zhang Y, Feustel PJ, Kimelberg HK. Neuroprotection by pyrroloquinoline quinone (PQQ) in reversible middle cerebral artery occlusion in the adult rat. Brain Res. 2006;1094(1):200–206.

Zhang Y, Jia X, Chen X, Liu Y, Zhao Z, Hao J, Wu R, Feng H, Ren X. L-theanine and Neumentix mixture improves sleep quality and modulates brain neurotransmitter levels in mice. Ann Palliat Med. 2021;10(4):4572-4581.

Zhao RZ, Jiang S, Zhang L, Yu ZB. Mitochondrial electron transport chain, ROS generation and uncoupling (Review). Int J Mol Med. 2019;44(1):3-15.

Appendix:

Below are reported the original pdf versions of the manuscripts relative to the data presented in this thesis. During the whole PhD, other papers have been published but not included in this thesis:

- Pesce NA, **Canovai A**, Lardner E, Cammalleri M, Kvanta A, André H, Dal Monte M. Autophagy Involvement in the Postnatal Development of the Rat Retina. Cells. 2021;10(1):177. doi:10.3390/cells10010177.
- Pesce NA*, **Canovai A***, Plastino F, Lardner E, Kvanta A, Cammalleri M, André H, Dal Monte M. An imbalance in autophagy contributes to retinal damage in a rat model of oxygen-induced retinopathy. J Cell Mol Med. 2021;25(22):10480-10493. doi: 10.1111/jcmm.16977.
  * Co-first authorship.
- Cantarini M, Rusciano D, Amato R, **Canovai A**, Cammalleri M, Monte MD, Minnelli C, Laudadio E, Mobbili G, Giorgini G, Galeazzi R. Structural Basis for Agonistic Activity and Selectivity toward Melatonin Receptors hMT1 and hMT2. Int J Mol Sci. 2023;24(3):2863. doi: 10.3390/ijms24032863.
- Amato R, Melecchi A, Pucci L, **Canovai A**, Marracci S, Cammalleri M, Dal Monte M, Caddeo C, Casini G. Liposome-Mediated Delivery Improves the Efficacy of Lisosan G against Retinopathy in Diabetic Mice. Cells. 2023;12(20):2448. doi: 10.3390/cells12202448.

frontiers in Pharmacology

ORIGINAL RESEARCH
published: 03 January 2022
doi: 10.3389/fphar.2021.811818

Preventive Efficacy of an Antioxidant Compound on Blood Retinal Barrier Breakdown and Visual Dysfunction in Streptozotocin-Induced Diabetic Rats

Alessio Canovai[1], Rosario Amato[1], Alberto Melecchi[1], Massimo Dal Monte[1,2], Dario Rusciano[3], Paola Bagnoli[1] and Maurizio Cammalleri[1,2]**

[1]Department of Biology, University of Pisa, Pisa, Italy, [2]Interdepartmental Research Center Nutrafood "Nutraceuticals and Food for Health", University of Pisa, Pisa, Italy, [3]Research Center, Sooft Italia SpA, Catania, Italy

In diabetic retinopathy (DR), high blood glucose drives chronic oxidative stress and inflammation that trigger alterations of the neurovascular balance finally resulting in vascular abnormalities and retinal cell death, which converge towards altered electroretinogram (ERG). In the last years, a growing body of preclinical evidence has suggested that nutrients with anti-inflammatory/antioxidant properties can be able to hamper DR progression since its very early stages. In the present study, we used a streptozotocin-induced rat model of DR, which mimics most aspects of the early stages of human DR, to test the preventive efficacy of a novel compound containing cyanidin-3-glucoside (C3G), verbascoside and zinc as nutrients with antioxidant and anti-inflammatory properties. Western blot, immunofluorescence and electroretinographic analyses demonstrated a dose-dependent inhibition of oxidative stress- and inflammation-related mechanisms, with a significant counterpart in preventing molecular mechanisms leading to DR-associated vasculopathy and its related retinal damage. Preventive efficacy of the compound on dysfunctional a- and b-waves was also demonstrated by electroretinography. The present demonstration that natural compounds, possibly as a consequence of vascular rescue following ameliorated oxidative stress and inflammation, may prevent the apoptotic cascade leading to ERG dysfunction, adds further relevance to the potential application of antioxidants as a preventive therapy to counteract DR progression.

Keywords: oxidative stress, inflammation, gliosis, vasopermeability, apoptosis, electroretinogram

OPEN ACCESS

Edited by:
Claudio Bucolo, University of Catania, Italy

Reviewed by:
Sebastiano Alfio Torrisi, University of Catania, Italy
Yvette Wooff, Australian National University, Australia

****Correspondence:***
Rosario Amato
rosario.amato@biologia.unipi.it ;
Maurizio Cammalleri
maurizio.cammalleri@unipi.it

Specialty section:
This article was submitted to Inflammation Pharmacology, a section of the journal Frontiers in Pharmacology

Received: *09 November 2021*
Accepted: *06 December 2021*
Published: *03 January 2022*

Citation:
Canovai A, Amato R, Melecchi A, Dal Monte M, Rusciano D, Bagnoli P and Cammalleri M (2022) Preventive Efficacy of an Antioxidant Compound on Blood Retinal Barrier Breakdown and Visual Dysfunction in Streptozotocin-Induced Diabetic Rats. Front. Pharmacol. 12:811818. doi: 10.3389/fphar.2021.811818

INTRODUCTION

Diabetic retinopathy (DR) is a leading cause of acquired visual impairment in developed countries. DR is characterized by a chronic progression, which might result asymptomatic for several years before the occurrence of overt clinical evidence (Al-Kharashi, 2018). Major signs of DR are morpho functional alterations of retinal vascularization, primarily manifested as a significant increase in vascular leakage, and macular oedema deriving from the blood retinal barrier (BRB) breakdown (Klaassen et al., 2013). Noteworthy, the onset of relevant clinical signs of DR corresponds to advanced stages of the disease that marks a point of no return (Sinclair and Schwartz, 2019). These aspects render the clinical management of DR a challenging topic

and feeds the research of treatment approaches to intervene on the early stages of the disease in order to prevent or delay DR progression.

Although the clinical symptoms of DR are almost exclusively attributed to dysfunctional vascularization, DR consists in a complex interplay of pathological processes affecting the integrity of the neurovascular unit since its early stages (Simó et al., 2018; Rossino et al., 2019). In fact, prolonged exposure to high glucose leads to metabolic stress that affects the BRB and the highly specialized neural connections, responsible for vision processes (Feng et al., 2012; Mi et al., 2014). In particular, hyperglycemia initiates an early increase of reactive oxygen species (ROS), which triggers the activation of endogenous antioxidant response through increased levels of nuclear factor erythroid 2-related factor 2 (Nrf2) leading to the transcription of antioxidant enzymes such as heme oxygenase-1 (HO-1) (Kang and Yang, 2020). However, antioxidant defenses are overwhelmed by ROS accumulation thus producing the onset of oxidative stress (Kowluru and Chan, 2007).

Oxidative stress activates inflammation that exacerbates ROS production, both events converging on retinal cell degeneration and altered vascularization (Tang and Kern 2011). Among the several players that participate to the early vascular pathology that characterizes DR, vascular endothelial growth factor (VEGF) and its regulatory transcription factor hypoxia inducible factor-1 (HIF-1) play an important role and their increase takes place in response to hyperglycemia-induced hypoxic environment (Gu et al., 2019). VEGF overexpression induces the loss of tight-junction proteins and subsequent alterations in the BRB integrity (Qaum et al., 2001). Therefore, the early neurovascular dysfunction appears to be strictly related to a series of metabolic unbalances deriving from the hyperglycemic condition of which common denominators are oxidative stress and inflammation (Al-Kharashi, 2018). Their importance along the progression of DR is further corroborated by the fact that strategies already approved for the management of advanced DR, such as treatments with anti-VEGF drugs and the use of steroids, have been found to interfere on inflammatory pathways (Giurdanella et al., 2015; Bucolo et al., 2018). On the other hand, the efficacy of dietary compounds with antioxidant/anti-inflammatory properties has been largely studied for their extensive bioactivity and limited risk of side effects (Rossino and Casini, 2019). However, clinical trials using antioxidants in DR have provided controversial results and much preclinical evidence is still needed to demonstrate the efficacy of antioxidant compounds to counteract the multifactorial nature of DR (Garcia-Medina et al., 2020). In this respect, the use of a multicomponent formula may further improve antioxidant efficacy as the different compounds contained in the mixture may exert multi-target and multifunctional effects by acting at different levels of the same signaling cascade or by modulating different cascades (Leena et al., 2020).

Among natural compounds exerting antioxidant/anti-inflammatory properties, anthocyanin subcomponents, and in particular cyanidins, have been shown to display a good uptake rate, a low decay and a significant clinical relevance, thus resulting one of the most pharmaceutically promising class of nutrients (Khoo et al., 2017). Among cyanidins, cyanidin-3-glucoside (C3G), the most abundant anthocyanin, has a predominant antioxidant capacity that has been reported in several diabetic complications including DR (Sasaki et al., 2007; Wang et al., 2016; Li et al., 2018; Qin et al., 2018).

Additional antioxidant/anti-inflammatory compounds belong to the extensive family of phenylpropanoids, a class of plant-derived polyphenols, which are biosynthesized from the amino acid phenylalanine (Alipieva et al., 2014). Of them verbascoside exerts an anti-inflammatory role due to its ROS scavenging, antioxidant and iron chelating properties (Perron and Brumaghim, 2009; Burgos et al., 2020) although its potential role in DR remains to be established. In addition to plant-derived antioxidant compounds, the activation of enzymes involved in antioxidant defenses has been related to the activity of zinc (Kamińska et al., 2021). Zinc itself is not redox active but is a cofactor that exerts an indirect redox activity by regulating mitochondrial function and, therefore, the rate of ROS generation (Marreiro et al., 2017).

The individual antioxidant efficacy of C3G, verbascoside and zinc has been demonstrated in several experimental models of ocular diseases including DR, glaucoma and age-related macular degeneration (Miao et al., 2013; Chen et al., 2019; Nomi et al., 2019; Oliveira et al., 2020), but information is lacking about their combined efficacy in preventing the early signs of experimental DR.

In the present study, we investigated the efficacy of a compound including C3G, verbascoside and zinc using the chemically induced streptozotocin (STZ) rat model of diabetes, which has been routinely used in preclinical studies and therapeutic drug investigations. This model that mimics the early stages of DR in humans, is characterized by an increased expression of oxidative stress and inflammation markers resulting in VEGF-induced retinal vasopermeability that causes BRB breakdown and retinal dysfunction (Naderi et al., 2019). In STZ rats, we evaluated the preventive efficacy of the compound on oxidative stress, inflammation, gliotic responses and apoptotic markers. In addition, its preventive efficacy on neuroretinal components responsible for vision processes was also assessed by electroretinography.

MATERIALS AND METHODS

Reagents

Rabbit polyclonal anti-NRF2 (catalog n. ab92946), rabbit polyclonal anti-HO-1 (catalog n. ab13243), rabbit polyclonal anti-NF-kB p65 (catalog n. ab16502), rabbit monoclonal anti-HIF-1α (catalog n. ab179483), rabbit monoclonal anti-Bax (catalog n. ab182733), rabbit polyclonal anti-Bcl-2 (catalog n. ab194583), rabbit polyclonal anti-cleaved caspase 3 (catalog n. ab2302), rabbit monoclonal anti-GFAP (catalog n. ab207165), goat polyclonal anti-rabbit conjugated with either Alexa-Fluor 555 (catalog n. ab150078) or Alexa-Fluor 488 (catalog n. ab150077) antibodies were purchased from Abcam (Cambridge, United Kingdom). Rabbit polyclonal anti-pNF-kB p65 (Ser 536) (catalog n. sc-33020), mouse monoclonal anti-IL-6

(catalog n. sc-57315), rabbit polyclonal anti-VEGF (catalog n. sc-507) antibodies were purchased from Santa Cruz Biotechnology, Inc (Dallas, TX, United States). Rabbit polyclonal anti-ZO-1 (catalog n. 40-2200), mouse monoclonal anti-Claudin 5 (catalog n. 35-2500) antibodies were purchased from Invitrogen (Waltham MA, United States). Mouse monoclonal anti-β-actin (catalog n. A2228), rabbit polyclonal anti-mouse HRP-conjugated (catalog n. A9044) antibody were purchased from Sigma-Aldrich (St. Louis, MO, United States). Rabbit monoclonal anti-cleaved caspase 3 (catalog n. 9664S) antibody used for immunofluorescence was purchased from Cell Signaling Technology (Danvers, MA, United States). Goat polyclonal anti-rabbit HRP-conjugated (catalog n. 170-6515) antibody was purchased from Bio-Rad Laboratories, Inc (Hercules, CA, United States).

Animals

Animals were managed in accordance with the Association for Research in Vision and Ophthalmology statement for the Use of Animals in Ophthalmic and Vision Research. The present study is also in agreement with the European Communities Council Directive (2010/63/UE) and the Italian guidelines for animal care (DL 26/14). The experimental protocol was authorized by the Commission for Animal Wellbeing of the University of Pisa (protocol no. 133/2019-PR, February 14, 2019). Efforts to reduce both the number and suffering of the animals were made in accordance with the 3Rs principles for ethical use of animals in scientific research. Male Sprague Dawley rats (8 weeks old, about 200 g weight) were purchased from Envigo Italy (San Pietro al Natisone, Italy). Animals were housed in a regulated environment (23 ± 1°C, 50 ± 5% humidity) with 12 h light/dark cycles (lights on at 08:00 a.m.) and fed with a standard diet and water ad libitum. Thirty-two rats were used. They were divided in four groups of eight rats each: control, STZ untreated, STZ-treated with the low dose of the mixture and STZ-treated with the high dose (see below). To evaluate the effect of the compound on weight, glycemia and visual function of healthy rats, additional six rats were supplemented with the compound.

STZ-Induced Model of Diabetes and Treatments

STZ (Sigma-Aldrich, St. Louis, MO, United States) diluted in citrate buffer, pH 4.5, was intraperitoneally injected at 65 mg/kg. Age-matched rats treated with vehicle were considered as the control group. Blood glucose was measured 3 days after the injection by tail sampling using a OneTouch Ultra glucometer (LifeScan Inc, Milpitas, CA, United States) to confirm the diabetic induction. Animals were considered diabetic if glycemia was ≥250 mg/dl. Blood glucose level was then regularly checked once a week for the entire experimental period. Among diabetic rats, 16 animals for each group were treated with a compound including *Oryza sativa* L. seeds (C3G titrated at 20%), *Verbascum thapsus* L (verbascoside titrated at 10%) and zinc gluconate (zinc titrated at 13.23%) with a content ratio of 60:30:10, respectively. The compound was diluted in water at 84 mg/ml and administered at low dose (100 µL containing 1.0 mg of C3G, 0.25 mg of verbascoside and 0.125 mg of zinc) or high dose (300 µL containing 3.0 mg of C3G, 0.75 mg of verbascoside and 0.375 mg of zinc). Dosage range corresponds to that recommended in humans, normalized by the body surface area for interspecies drug dosage translation (Nair and Jacob, 2016). Rats were treated once daily by oral gavage for 30 days after STZ administration. Thirty days after STZ administration, the animals underwent to electroretinography. In **Table 1**, the experimental groups, the schedule of treatment, the amount of daily administered components and the number of rats for each experimental group are shown.

Electroretinogram

In the four groups, retinal function was examined with scotopic full-field electroretinogram (ERG). Before ERG, rats underwent overnight dark-adaptation and subsequent anesthesia with intraperitoneal injection of 30 mg/kg sodium pentobarbital. Pupils were dilated with a topical drop of 1% tropicamide (Allergan S.p.A.) and the body temperature was kept constantly at 37.5°C by a heating pad. The electrophysiological signals were recorded using silver/silver chloride corneal ring electrodes inserted under the lower eyelids to avoid visual field obstruction. In order to prevent dryness and clouding of the ocular surface, saline solution drops were intermittently instilled. Each corneal electrode was referred to a needle electrode inserted subcutaneously at the level of the corresponding frontal region, and the ground electrode was inserted subcutaneously at the tail root. Scotopic ERG, which primarily measures rod function, was evoked by flashes of increasing light intensities ranging from −3.4 to one log cd-s/m^2 generated through a Ganzfeld stimulator (Biomedica Mangoni, Pisa, Italy). An interval of 20 s between light flashes was adjusted to allow response recovery. Scotopic responses were collected simultaneously from both eyes, amplified at 10000x gain, filtered with a 0.2–500 Hz bandpass and digitized at 5 kHz rate with a data acquisition device (Biomedica Mangoni). ERG waveforms were analyzed using a customized program (Biomedica Mangoni). In the absence of light stimulation, the electrical activity was measured to evaluate noise amplitude. In accordance with the International Society for Clinical Electrophysiology guidelines, the a-wave amplitude was measured from the pre-stimulus baseline to the negative through of the a-wave while the b-wave amplitude was retrieved from the through of the a-wave to the peak of the b-wave. Data were pooled and reported as mean amplitude ±SEM (in µV). Intensity-response function of the b-wave was fitted to the following modified Naka-Rushton function (Naka and Rushton, 1966):

$$V(I) = V0 + \frac{Vmax \times In}{In + kn}$$

In this equation, V is the amplitude of the b-wave (in µV), I is the stimulus intensity (in log cd-s/m^2), V0 is the nonzero baseline effect, Vmax is the saturated amplitude of the b-wave (in µV) and k is the stimulus intensity that evokes b-waves of half-maximum amplitude (in log cd-s/m^2); n, which was constrained to unity, is a dimensionless constant that controls the slope of the function and represents the degree of heterogeneity of retinal sensitivity.

TABLE 1 | Experimental groups and schedule of treatments.

Group	N	Treatment	Daily amount	Days of treatment
Control	8	None	—	—
	3	+ low dose	C3G (1.0 mg), verbascoside (0.25 mg), zinc (0.125 mg)	30
	3	+ high dose	C3G (3.0 mg), verbascoside (0.75 mg), zinc (0.375 mg)	30
STZ	8	None	—	—
	8	+ low dose	C3G (1.0 mg), verbascoside (0.25 mg), zinc (0.125 mg)	30
	8	+ high dose	C3G (3.0 mg), verbascoside (0.75 mg), zinc (0.375 mg)	30

Detection of Vascular Leakage by Evans Blue Dye Perfusion

After electroretinography, two rats per group were anesthetized with an intraperitoneal injection of 30 mg/kg sodium pentobarbital and perfused through the left ventricle with 0.5% Evans blue dye (Sigma-Aldrich) in phosphate-buffer saline (PBS) that was allowed to circulate for 10 min. The animals were then sacrificed, and retinas were dissected and flat mounted onto microscope slides. Retinas were then examined by an epifluorescence microscope (Ni-E; Nikon Europe, Amsterdam, Netherlands) and the images were acquired using a 10x plan apochromat objective and a digital camera (DS-Fi1c camera; Nikon-Europe).

Western Blot

In six rats per group, eyes were enucleated and alternatively used for Western blot analysis in explanted retinas or immunohistochemistry (see below). For Western blot, retinas were lysed with RIPA lysis buffer (Santa Cruz Biotechnology, Dallas, TX, United States) implemented with phosphatase and proteinase inhibitor cocktails (Roche Applied Science, Indianapolis, IN, United States). Protein content was evaluated by Micro BCA protein assay (Thermo Fisher Scientific, Waltham, MA, United States). Fourty micrograms of proteins per sample were separated by SDS-PAGE (4–20%; Bio-Rad Laboratories, Inc., Hercules, CA, United States) and gels were subsequently transblotted onto nitrocellulose membranes (Bio-Rad Laboratories, Inc.). Membranes were blocked with 5% skim milk for 1 h at room temperature and then incubated overnight at 4°C with the solutions of primary anti-NRF2 (1:1,000), anti-HO-1 (1:500), anti-pNF-kB p65 (Ser 536) (1:100), anti-NF-kB p65 (1:1,000), anti-IL-6 (1:100), anti-HIF-1α (1:1,000), anti-VEGF (1:100), anti-ZO-1 (1:500), anti-Claudin 5 (1:500), anti-Bax (1:500), anti-Bcl-2 (1:500), anti-cleaved caspase 3 (1:500), anti-β-actin (1:2500) antibodies. Thereafter, membranes were incubated for 2 h at room temperature with appropriate HRP-conjugated secondary anti-mouse or anti-rabbit (1:5,000) antibodies. Blots were developed using the Clarity western enhanced chemiluminescence substrate (Bio-Rad Laboratories, Inc.) and the images were acquired by the ChemiDoc XRS+ (Bio-Rad Laboratories, Inc.). The optical density (OD) relative to the target bands (Image Lab 3.0 software; Bio-Rad Laboratories, Inc.) was normalized to the corresponding OD of β-actin as loading control or nuclear factor kappa-light-chain-enhancer of activated B cells (NF-kB) p65 as appropriate.

Measurement of ROS Levels

ROS levels were measured using the general oxidative stress probe 2′,7′-dichlorodihydrofluorescein diacetate (DCFH-DA) (Invitrogen, CA, United States). DCFH-DA, a nonfluorescent dye, is cleaved by esterase activity to yield dichlorodihydrofluorescein (DCFH), which is subsequently oxidized by ROS to form fluorescent dichlorofluorescein (DCF). Retinal samples containing 20 μg proteins were incubated with 50 μM DCFHDA in 96-well plates. After 60 min at 37°C, fluorescence intensity was detected over 60 min using a microplate reader (FLUOstar Omega, BMG Labtech, Ortenberg, Germany) at excitation 488 nm and emission 525 nm. The relative ROS levels were expressed as arbitrary fluorescence units per μg of protein.

Immunofluorescence

Enucleated eyes were immersion-fixed in 4% paraformaldehyde in 0.1 M PBS for 2 h at room temperature. Fixed eyes were transferred to 25% sucrose in 0.1 M PBS and stored at 4°C. Following the inclusion in cryo-gel medium, fixed samples were cut into 10 μm thick coronal sections and mounted onto glass slides. Mounted sections were then incubated with the solutions of primary anti-HO-1 (1:500), anti-GFAP (1:400) or anti-cleaved caspase 3 (1:400) antibodies diluted in 0.1 M PBS containing 0.1% v/v Triton X-100, overnight at 4°C. Mounted sections were incubated with goat polyclonal anti-rabbit secondary antibodies conjugated with Alexa-Fluor 555 (ab150078, Abcam, Cambridge, United Kingdom; dilution: 1: 200) or Alexa-Fluor 488 (ab150077, Abcam; dilution: 1:200) diluted in 0.1 M PBS containing 0.1% v/v Triton X-100 for 2 h at room temperature. Finally, retinal sections were coverslipped with Fluoroshield mounting medium containing 4′, 6-diamidino-2-phenylindole (DAPI; Abcam). In order to analyze the outer BRB, the retinal pigmented epithelium (RPE)-choroid complexes were isolated from fixed eyes and incubated for 72 h at 4°C in anti-ZO-1 antibody (1:100 in 0.1 M PB containing 1.0% Triton X-100). Subsequently, they were incubated for 48 h at 4 °C in anti-rabbit secondary antibody conjugated with Alexa-Fluor 488 (1: 200) followed by 0.1 M PB rinsing. Four radial incisions were made in the RPE-choroid complexes that were flat-mounted on gelatin-coated glass slides. Images of retinal sections or RPE-choroid flatmounts were acquired through an epifluorescence microscope (Nikon-Europe) at 20× and 40x,

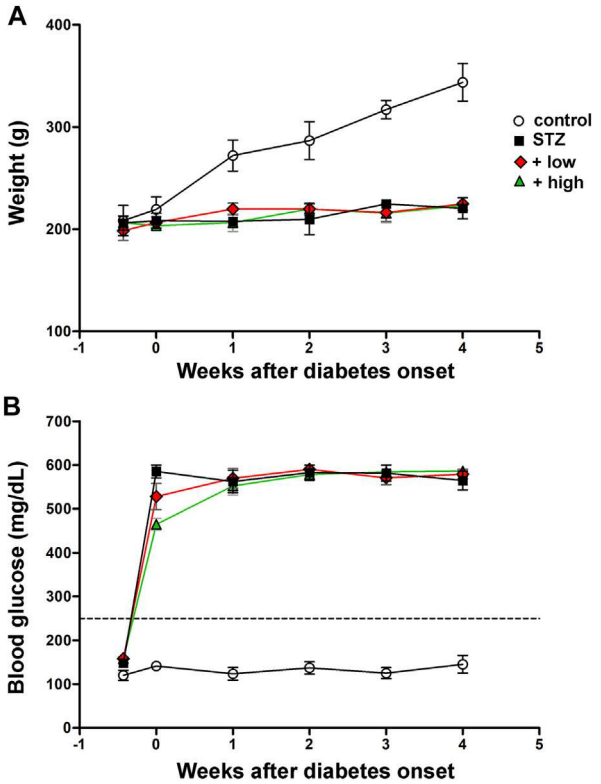

FIGURE 1 | Longitudinal evaluation of body weight **(A)** and blood glucose **(B)** in controls, STZ-untreated rats or STZ rats treated with either the low dose (C3G, 1.0 mg; verbascoside, 0.25 mg and zinc, 0.125 mg) or the high dose (C3G, 3.0 mg; verbascoside, 0.75 mg and zinc, 0.375 mg) of the compound. Data are expressed as mean ± SEM. Statistical significance was assessed by two-ways ANOVA followed by Bonferroni's multiple comparison post-hoc test (N = 8).

respectively using a digital camera (Nikon-Europe). The quantification of the GFAP immunostaining was performed by averaging the fluorescence intensity of five coronal sections (4 images per section) randomly chosen from each retina (6 retinas per group). Fluorescence intensity was calculated on grayscale images normalized for the background by measuring the mean gray level using the analysis tool of Adobe Photoshop. The thickness of the outer nuclear layer (ONL) was measured as the interface between the outer plexiform layer and photoreceptor inner segment, while the thickness of the inner nuclear layer (INL) was measured as the interface between the outer plexiform layer and the inner plexiform layer. The quantification of ONL and INL thickness was performed by averaging measurements from five coronal sections (4 images per section) randomly chosen from each retina (6 retinas per group).

Statistical Analysis

Graph Pad Prism 8.0.2 software (Graph-Pad Software, Inc., San Diego, CA, United States) was used for the statistical analyses. Differences among groups were assessed through one-way or two-ways ANOVA followed by Tukey's or Bonferroni's multiple comparison post hoc test, respectively. Differences with $p < 0.05$ were considered significant. All data are expressed as means ± SEM of the indicated n values.

RESULTS

The Compound Does Not Affect Body Weight and Glycemia

Control rats displayed a significant age-dependent gain of weight. In line with previous findings (Furman, 2015), STZ injection resulted in markedly lower body weight as compared to controls ($p < 0.01$, **Figure 1A**). Following STZ administration, blood glucose levels were significantly increased and remained higher than in controls until the animals underwent to ERG recordings and were subsequently sacrificed ($p < 0.0001$ vs control, **Figure 1B**). Blood glucose levels did not significantly differ between STZ rats either untreated or treated with the compound at both doses. Control rats treated with the compound displayed an age-dependent gain of weight and blood glucose levels comparable to those of untreated controls (**Supplementary Figure S1**).

The Compound Protects the Retina From Oxidative Stress and Inflammation

The preventive efficacy of the compound was tested on ROS generation. Levels of specific markers of oxidative stress and inflammation known to play a crucial role in the early progression of DR (Al-Kharashi, 2018) were also measured. As shown in **Figure 2A,,** STZ rats displayed a significant increase in ROS generation as compared to controls ($p < 0.001$ vs control). STZ rats treated with the compound at low dose showed lower levels of ROS as compared to untreated STZ ($p < 0.01$ vs STZ), although still resulting significantly higher than in controls ($p < 0.01$ vs control). In STZ rats treated with the compound at high dose, ROS levels were comparable to those measured in controls ($p > 0.05$ vs control). Oxidative stress was evaluated by analyzing the protein levels of NRF2, a ROS-sensitive transcriptional factor, and HO-1, one of the antioxidant enzymes involved in defensive responses to oxidative stress (Kang and Yang., 2020). As shown in **Figures 2B, C**, the densitometric analysis of immunoblots revealed a significant increment in both Nrf2 and HO-1 in STZ rats as compared to controls ($p < 0.01$ vs control). This increment was partially attenuated by the compound at low dose ($p < 0.05$ vs STZ), but completely prevented by the high dose ($p < 0.001$ vs STZ; $p < 0.05$ vs low dose). As shown in **Figure 2D**, immunofluorescence analysis revealed a faint HO-1 immunoreactivity in control retinas mainly confined to the ganglion cell layer (GCL). In retinas of STZ rats, HO-1 immunoreactivity was significantly increased in the GCL and expanded toward the outer retina, clearly depicting vertical processes in the inner plexiform layer (IPL) and cellular profiles localized in the inner nuclear layer (INL). Retinas of rats treated with compound at low dose displayed a less evident HO-1 immunostaining as compared to untreated STZ rats, with rare spots in the GCL and residual labeling in the IPL and INL. HO-1 immunostaining was not detectable in the IPL and INL

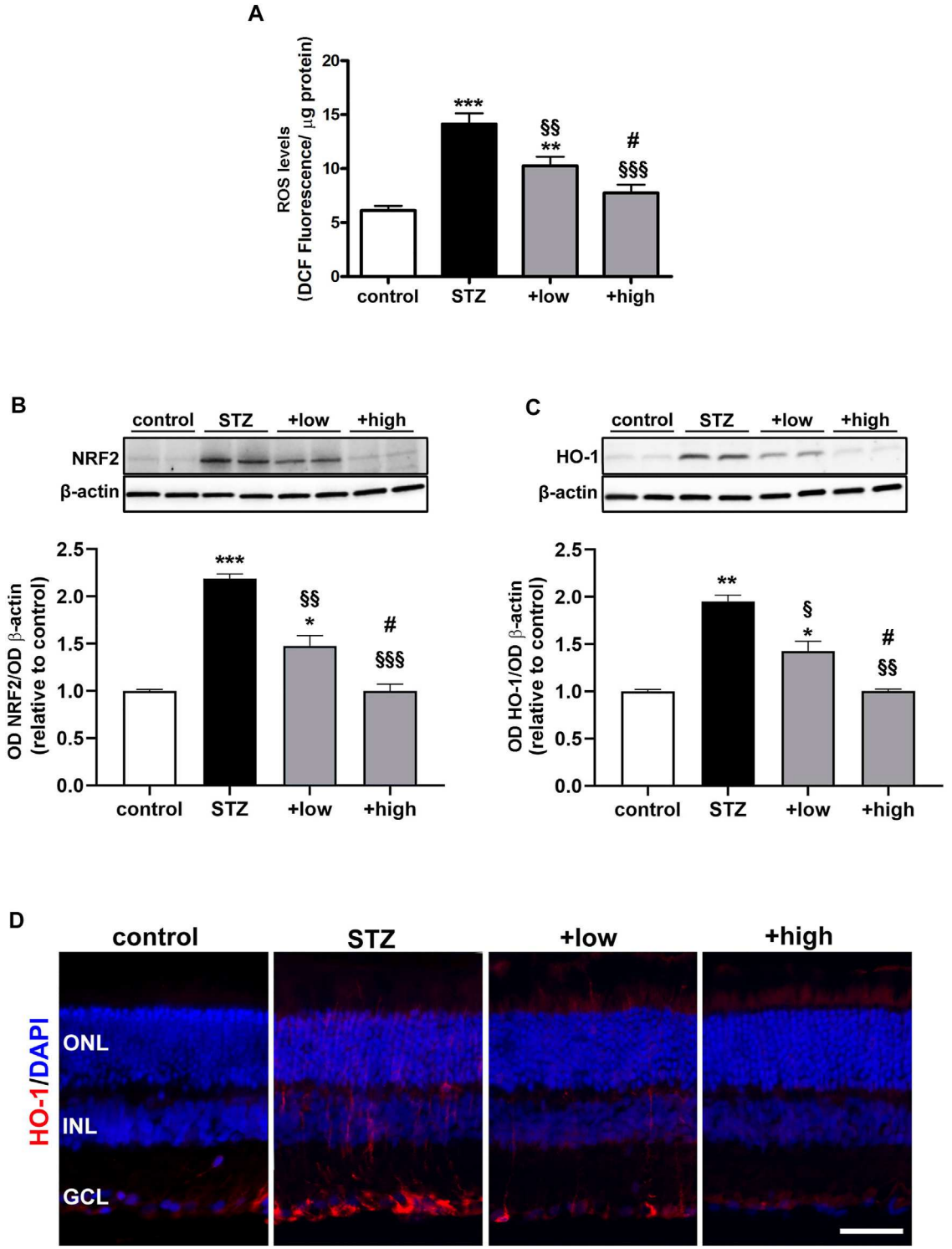

FIGURE 2 | Effects of the compound on ROS levels and markers of oxidative stress **(A)** ROS levels in controls, STZ untreated or STZ treated with either the low dose (C3G, 1.0 mg; verbascoside, 0.25 mg and zinc, 0.125 mg) or the high dose (C3G, 3.0 mg; verbascoside, 0.75 mg and zinc, 0.375 mg) of the compound. Representative Western blots and densitometric analysis of NRF2 **(B)** and HO-1 **(C)** in controls, STZ untreated or STZ rats treated with either the low dose or the high dose. β-actin was used as loading control. Data are expressed as mean ± SEM. Statistical significance was assessed by one-way ANOVA followed by Tukey's multiple comparison post-hoc test (N = 6). $^{*}p < 0.05$, $^{**}p < 0.01$ and $^{***}p < 0.001$ vs control; $^{\S}p < 0.05$, $^{\S\S}p < 0.01$ and $^{\S\S\S}p < 0.001$ vs STZ; $^{\#}p < 0.05$ vs low dose-treated STZ **(D)** Representative images of retinal cross sections immunolabeled for HO-1 (red) and counterstained with DAPI (blue). Scale bar, 50 µm. GCL, ganglion cell layer; INL, inner nuclear layer; ONL, outer nuclear layer.

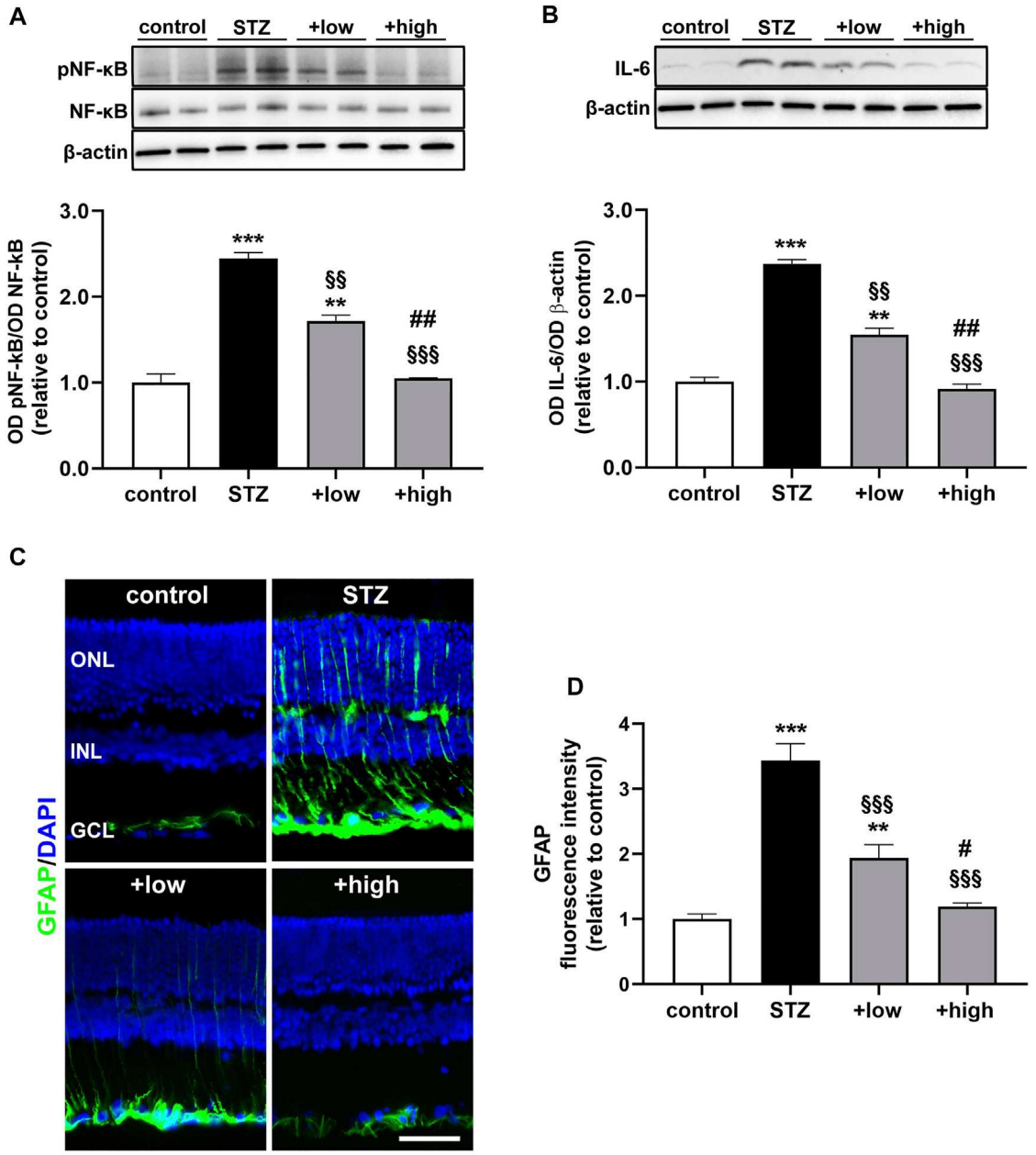

FIGURE 3 | Effects of the compound on inflammatory and gliosis markers. Representative Western blots and densitometric analysis of levels of pNF-kB **(A)** and IL-6 **(B)** in controls, STZ untreated or STZ rats treated with either the low dose (C3G, 1.0 mg; verbascoside, 0.25 mg and zinc, 0.125 mg) or the high dose (C3G, 3.0 mg; verbascoside, 0.75 mg and zinc, 0.375 mg) of the compound. Levels of pNF-kB were normalized to NF-kB levels, while IL-6 was normalized to the loading control β-actin. Data are expressed as mean ± SEM. Statistical significance was assessed by one-way ANOVA followed by Tukey's multiple comparison post-hoc test (N = 6). $^{**}p < 0.01$ and $^{***}p < 0.001$ vs control; $^{§§}p < 0.01$ and $^{§§§}p < 0.001$ vs STZ; $^{##}p < 0.01$ vs low dose treated STZ **(C)** Representative images of retinal cross sections immunolabeled for GFAP (green) and counterstained with DAPI (blue). Scale bar, 50 μm. GCL, ganglion cell layer; INL, inner nuclear layer; ONL, outer nuclear layer **(D)** Quantitative analysis of GFAP immunofluorescence intensity. Data are expressed as mean ± SEM. Statistical significance was assessed by one-way ANOVA followed by Tukey's multiple comparison post-hoc test (N = 6). $^{**}p < 0.01$ and $^{***}p < 0.001$ vs control; $^{§§}p < 0.01$ and $^{§§§}p < 0.001$ vs STZ; $^{#}p < 0.05$ and $^{##}p < 0.01$ vs low dose treated STZ.

following the treatment with high dose, while a basal labeling was observed in the GCL similarly to what found in the control retina.

The protein levels of the phosphorylated form of the p65 subunit of NF-kB, a master transcriptional regulator of pro-inflammatory factors and interleukin 6 (IL-6), a related pro-inflammatory cytokine (Liu et al., 2017), were also measured. As shown in **Figures 3A, B**, STZ rats displayed a marked increase in pNF-KB and IL-6 as compared to controls ($p < 0.001$ vs control). STZ rats treated with the compound at low dose showed lower levels of both markers as compared to untreated STZ ($p < 0.01$ vs

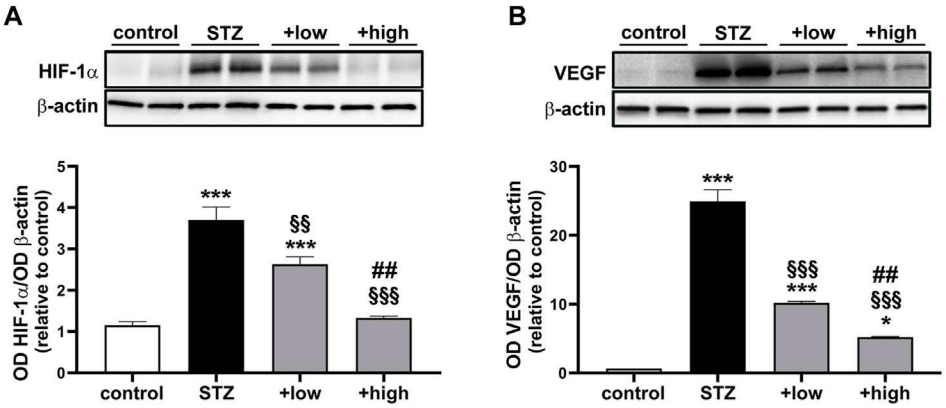

FIGURE 4 | Effects of the compound on vascular-related markers. Representative Western blots and densitometric analysis of HIF-1α **(A)** and VEGF **(B)** in controls, STZ untreated or STZ rats treated with either the low dose (C3G, 1.0 mg; verbascoside, 0.25 mg and zinc, 0.125 mg) or the high dose (C3G, 3.0 mg; verbascoside, 0.75 mg and zinc, 0.375 mg) of the compound. β-actin was used as loading control. Data are expressed as mean ± SEM. Statistical significance was assessed by one-way ANOVA followed by Tukey's multiple comparison post-hoc test (N = 6). $^{*}p < 0.05$ and $^{***}p < 0.001$ vs control; $^{§§}p < 0.01$ and $^{§§§}p < 0.001$ vs STZ; $^{##}p < 0.01$ vs low dose treated STZ.

STZ), although still resulting significantly higher than in controls ($p < 0.01$ vs control). On the other hand, in STZ rats treated with the high dose, the levels of pNF-kB and IL-6 were comparable to those measured in controls ($p > 0.05$ vs control). The activation of inflammatory processes triggers glial reactivity, which participates to the chronic inflammatory response (Rübsam et al., 2018). The reactive phenotype of glial cells was analyzed by immunostaining with glial fibrillary acidic protein (GFAP), a well-established marker of gliosis (**Figure 3C**). In control retinas, basal GFAP labeling was confined to the GCL. In contrast, STZ retinas showed an evident increment of GFAP immunoreactivity in the GCL together with densely immunopositive processes spreading across retinal layers as a typical hallmark of Müller cell reactivity. Comparable immunostaining could be detected in retinas of low dose-treated rats, although GFAP immunoreactivity was less prominent both in the GCL and in Müller cell processes. On the other hand, retinas of rats treated with the high dose displayed a GFAP immunostaining almost similar to that of controls, with the usual basal staining and barely detectable immunoreactive vertical processes. As shown in **Figure 3D**, quantitative analysis of fluorescence intensity showed a marked increment in GFAP immunoreactivity in STZ rat as compared to controls ($p < 0.001$). In STZ rats treated with the low dose, GFAP immunoreactivity was significantly lower than in untreated STZ rats ($p < 0.001$ vs STZ), while STZ rats treated with the high dose displayed GFAP immunofluorescence intensity comparable to that of controls ($p > 0.05$ vs control).

VEGF-Induced Vascular Permeability and BRB Breakdown Are Prevented by the Compound

Oxidative and inflammatory processes have a direct impact on molecular mechanisms regulating the vascular homeostasis through the alteration of the HIF-1-dependent pathway and the consequent dysregulation of angiogenic factors such as VEGF (Semeraro et al., 2015). As shown in **Figure 4**, HIF-1α levels were significantly increased in STZ rats as compared to controls ($p < 0.0001$). The increment in HIF-1α was significantly attenuated by the compound in a dose-dependent fashion (low dose $p < 0.001$ vs STZ; high dose $p < 0.0001$ vs STZ), with the high dose maintaining HIF-1α to control levels ($p > 0.05$ vs control; **Figure 4A**). Similarly, STZ rats displayed a marked increase in VEGF levels as compared to controls ($p < 0.0001$). The administration of the compound dose-dependently prevented VEGF accumulation with increased efficacy of the high dose ($p < 0.0001$ vs low dose), although VEGF levels were still higher than in controls (high dose $p < 0.05$ vs control; **Figure 4B**).

BRB dysfunction resulting from altered HIF-1α-VEGF axis was evaluated by analyzing the levels of zonula occludens 1 (ZO-1) and Claudin 5 as components of the inter-endothelial tight junctions. The BRB integrity was also assessed with the Evans Blue dye perfusion of retinal vessels (for inner BRB) and with ZO-1 immunostaining in RPE-choroid flatmounts (for outer BRB). As shown in **Figures 5A, B**, the levels of ZO-1 and Claudin five were drastically decreased in STZ retinas ($p < 0.0001$ vs control). The treatment with the compound was found to prevent protein loss with dose-dependent efficacy (low dose $p < 0.05$ vs STZ; high dose $p < 0.0001$ vs STZ), with the high dose displaying ZO-1 and Claudin five levels comparable to those of controls ($p > 0.05$ vs control). As shown in **Figure 5C**, in STZ rats, the dysregulation of BRB markers was correlated with inner BRB breakdown. In fact, Evans blue, a dye that binds to plasma proteins, was restricted to the vascular lumen in control retinas. Contrariwise, several focal points of extravasation were visible in STZ retinas. The vascular leakage was still evident in STZ rats treated with the compound at low dose, while the extravasation appeared more contained or even absent in retinas of rats treated with the high dose. ZO-1 immunostaining in RPE-choroid flatmounts from STZ rats revealed the presence of large holes between RPE cells indicating a significant loss of tight junctions leading to outer

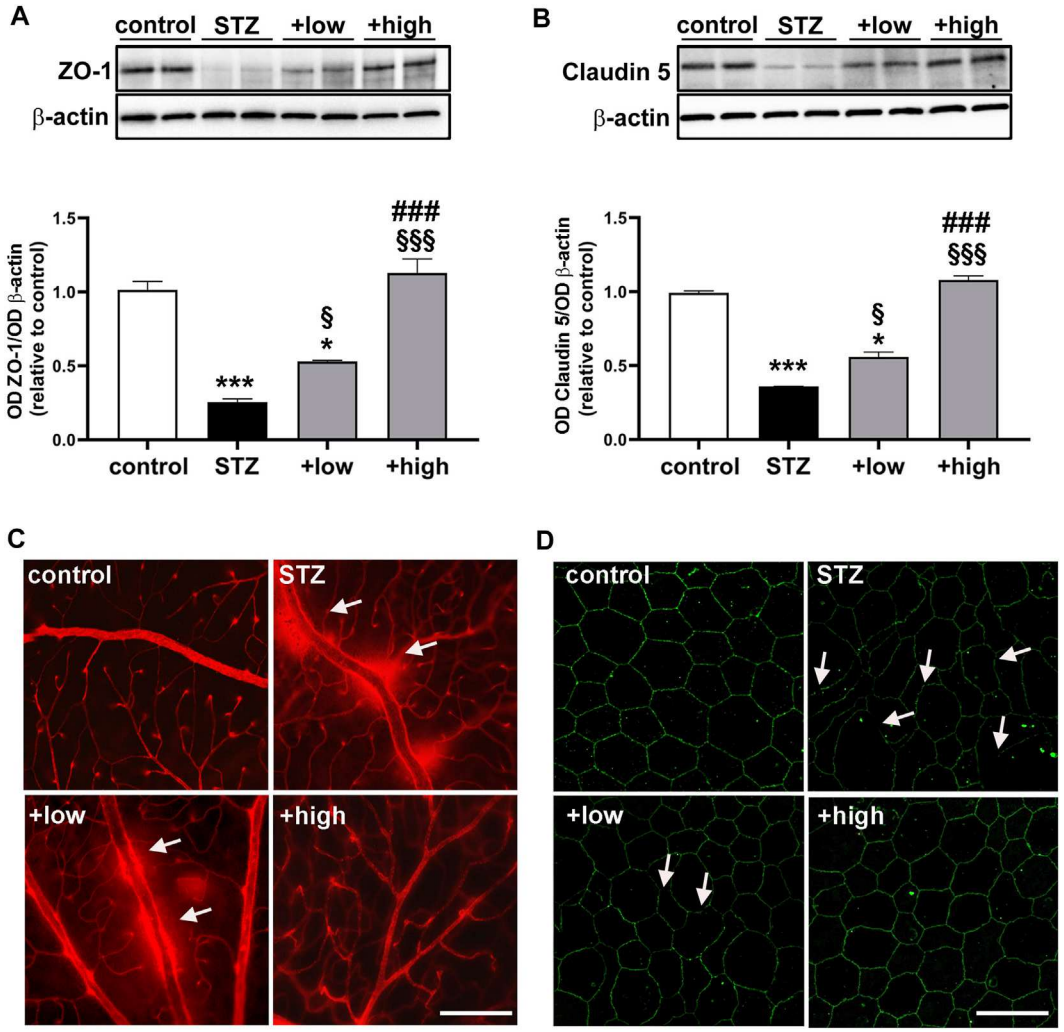

FIGURE 5 | Effects of the compound on BRB markers and vascular leakage. Representative Western blots and densitometric analysis of ZO-1 **(A)** and Claudin 5 **(B)** in controls, STZ untreated or STZ rats treated with either the low dose (C3G, 1.0 mg; verbascoside, 0.25 mg and zinc, 0.125 mg) or the high dose (C3G, 3.0 mg; verbascoside, 0.75 mg and zinc, 0.375 mg) of the compound. β-actin was used as loading control. Data are expressed as mean ± SEM. Statistical significance was assessed by one-way ANOVA followed by Tukey's multiple comparison post-hoc test (N = 6). $^{*}p < 0.05$ and $^{***}p < 0.001$ vs control; $^{§}p < 0.05$ and $^{§§§}p < 0.001$ vs STZ; $^{###}p < 0.001$ vs low dose treated STZ **(C)** Representative images of whole-mounted retinas after Evans blue dye perfusion. Vascular leakage is indicated by the white arrows. Scale bar, 200 μm **(D)** Representative images of RPE-choroid flatmounts stained with ZO-1. White arrows indicate large holes appeared between the RPE cells Scale bar, 20 μm.

BRB breakdown (**Figure 5D**). Supplementation with the compound dose-dependently prevented tight junction loss with no apparent differences between controls and STZ rats treated with the high dose.

The Compound Protects the Retina From Apoptosis and ERG Dysfunction

A growing body of evidence has underlined that early DR is characterized by apoptosis-related degenerative processes and vascular abnormalities that concur to ERG dysfunction (Barber and Baccouche, 2017). Whether the compound might influence the levels of proapoptotic markers was assessed by evaluating the ratio of pro-apoptotic Bax to anti-apoptotic Bcl-2 proteins as a major checkpoint in the apoptotic pathway. Downstream to the Bax/Bcl-2 ratio, levels of activated caspase 3 as the major effector protease driving the programmed cell death were also determined. As shown by the representative blots and the densitometric analysis in **Figures 6A, B**, the Bax/Bcl-2 ratio and the levels of caspase 3 were significantly increased in STZ rats as compared to controls ($p < 0.0001$). Treatment with the compound dose-dependently prevented the STZ-induced increase in Bax/Bcl-2 ratio and caspase 3, with a partial efficacy of the low dose ($p < 0.001$ vs STZ), while their increase was completely prevented by the high dose ($p < 0.0001$ vs STZ; $p > 0.05$ vs control). The evidence of attenuated levels of caspase 3 was further supported by immunofluorescence analysis (**Figure 6C**). In STZ rats,

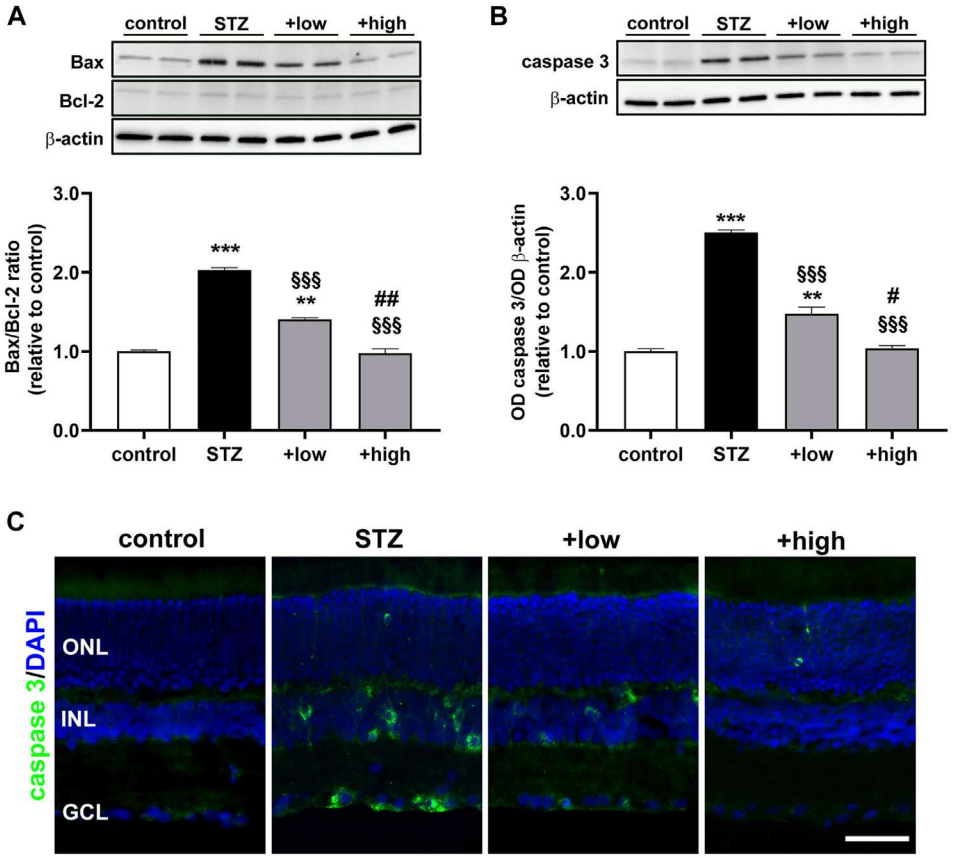

FIGURE 6 | Effects of the compound on apoptotic markers. Representative Western blots and densitometric analysis of Bax/Bcl-2 ratio **(A)** and cleaved caspase 3 **(B)** in controls, STZ untreated or STZ rats treated with either the low dose (C3G, 1.0 mg; verbascoside, 0.25 mg and zinc, 0.125 mg) or the high dose (C3G, 3.0 mg; verbascoside, 0.75 mg and zinc, 0.375 mg) of the compound. The levels of cleaved caspase 3 were normalized to the loading control β-actin. Data are expressed as mean ± SEM. Statistical significance was assessed by one-way ANOVA followed by Tukey's multiple comparison post-hoc test (N = 6). $^{**}p < 0.01$ and $^{***}p < 0.001$ vs control; $^{§§§}p < 0.001$ vs STZ; $^{\#}p < 0.05$ and $^{\#\#}p < 0.01$ vs low dose treated STZ **(C)** Representative images of retinal cross sections immunolabeled for cleaved caspase 3 (green) and counterstained with DAPI (blue). Scale bar, 50 μm. GCL, ganglion cell layer; INL, inner nuclear layer; ONL, outer nuclear layer.

increased caspase 3 was localized to cellular profiles in the GCL and INL as compared to controls in which caspase 3 immunostaining was absent. After the low dose, caspase 3-immunopositive cells were less evident and faintly stained, although some cellular profiles localized to the GCL and INL were still visible. Conversely, no caspase 3-immunopositive cell profiles could be observed after the high dose.

To evaluate whether protective efficacy of the compound might be reflected on preventing STZ-induced visual dysfunction, we analyzed the outer and inner retinal activity using scotopic ERG recordings. Under scotopic condition, a-wave reflects the activity of rods, while b-wave reflects the activity of bipolar cells and Müller glia. **Figure 7A** shows representative mixed a- and b-waves recorded at light intensities of one log cd-s/m^2. As shown in **Figures 7B, C**, In STZ rats treated with the low dose, ERG responses were partially preserved. In fact, at maximal stimulus intensity of 1 log cd-s/m^2, the a-wave amplitude, although not significantly different from that measured in STZ rats (196.5 ± 10.8, $p > 0.05$ vs STZ), showed a tendency toward an increase, while the b-wave amplitude was significantly higher than in STZ rats (518.2 ± 15.7, $p < 0.01$ vs STZ). After treatment with the high dose, a-and b-wave amplitudes were significantly higher than in STZ rats (a-wave 251.2 ± 12.8; b-wave 682.2 ± 24.8 $p < 0.001$ vs STZ) and in low dose-treated rats ($p < 0.01$ vs low dose), but still lower than in controls ($p < 0.05$). No significant effects on ERG responses were found in control rats treated with the compound either at low or high dose (**Supplementary Figure S2**). As shown in **Figures 7D, E**, a- and b-wave amplitude increased with increasing stimulus intensity. A clear a-wave developed at a light intensity of approximately −1.6 log cd-s/m^2. Compared to controls, STZ rats showed a reduction in the amplitude of both the a-wave and the b-wave at light intensities ranging from −1.6 to one log cd-s/m^2 ($p < 0.001$ vs control) although the thickness of both ONL and INL measured in untreated STZ rats did not differ from that measured in controls (**Supplementary Figure S3**). As shown in **Figure 7E**, b-wave amplitudes over increasing light intensities were fitted using the Naka-Rushton equation to evaluate the post-

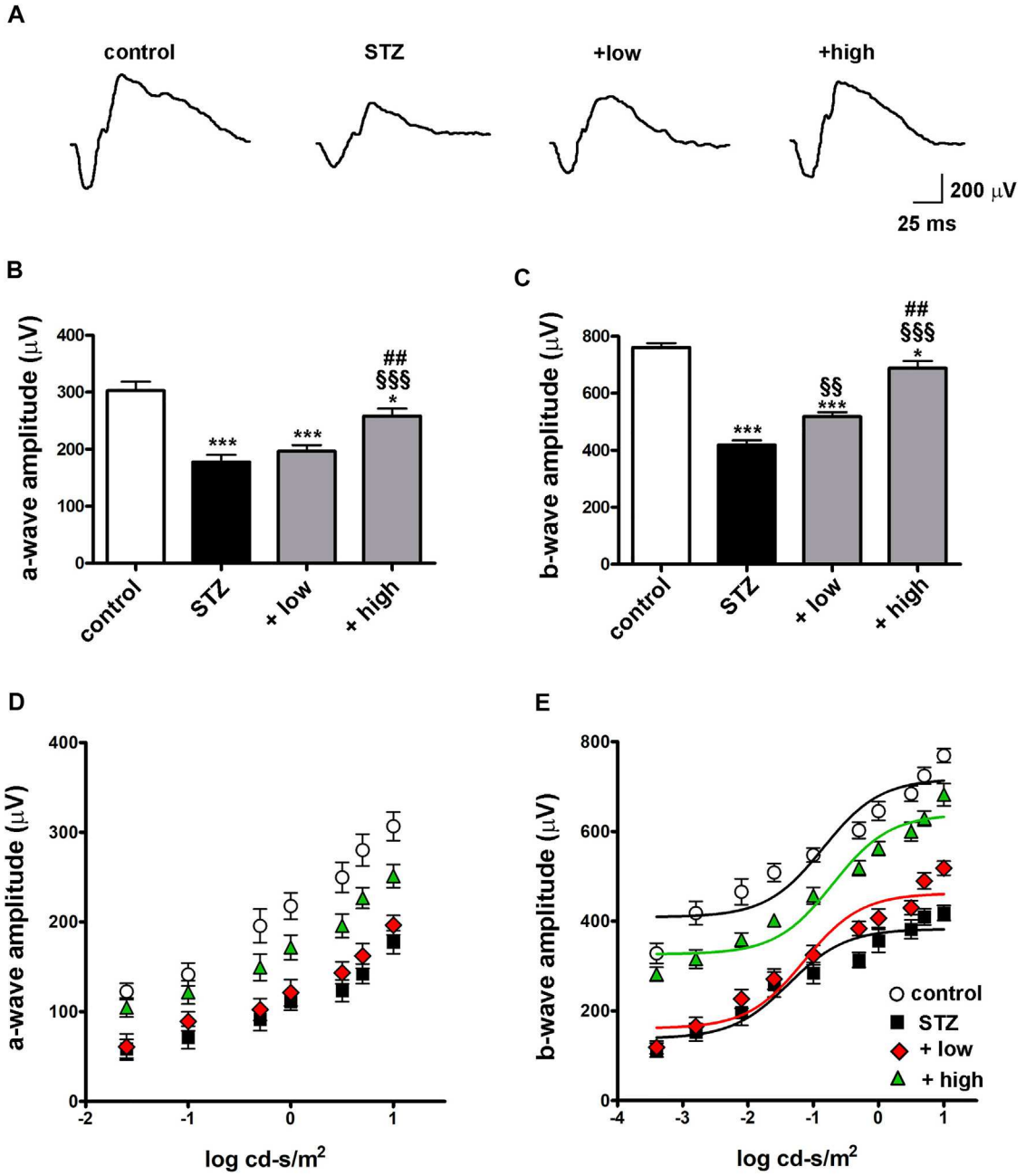

FIGURE 7 | Effects of the compound on scotopic ERG responses **(A)** Representative scotopic ERG waveforms recorded at one log cd-s/m^2 light intensity. Quantitative analysis of the scotopic a- **(B)** and b-wave **(C)** amplitudes recorded at one log cd-s/m^2 light intensity in controls, STZ-untreated rats or STZ rats treated with either the low dose (C3G, 1.0 mg; verbascoside, 0.25 mg and zinc, 0.125 mg) or the high dose (C3G, 3.0 mg; verbascoside, 0.75 mg and zinc, 0.375 mg) of the compound. Statistical significance was assessed by one-way ANOVA followed by Tukey's multiple comparison post-hoc test (N = 8). *$p < 0.05$ and ***$p < 0.001$ vs control; $^{§§}p < 0.01$ and $^{§§§}p < 0.001$ vs STZ; $^{##}p < 0.01$ vs low dose treated STZ. Quantitative analysis of the scotopic a- **(D)** and b-wave **(E)** amplitudes recorded at increasing light intensities. Lines indicate the Naka-Rushton fit of the variation of the b-wave amplitude depending on stimulus intensity. Statistical significance was assessed by two-ways ANOVA followed by Bonferroni's multiple comparison post-hoc test (N = 8).

receptor response amplitude (Vmax) and the retinal sensitivity (k). As shown in **Table 2**, in STZ rats, the values of Vmax and k were significantly lower than in controls ($p < 0.001$). In STZ rats treated with the low dose, Vmax values were significantly higher than those in untreated STZ rats, whereas k values were almost comparable. On the contrary, in STZ rats treated with the high dose, the values of both Vmax and k were significantly higher than in untreated STZ rats.

TABLE 2 | Parameters obtained from b-wave amplitude using the Naka-Rushton function.

	Control	STZ	+ Low	+ High
Vmax (μV)	717.5 ± 16.5	382.9 ± 11.7***	462.4 ± 12.5***,§	638.7 ± 14.2**,§§,##
k (log cd-s/m^2)	−0.87 ± 0.12	−1.40 ± 0.11**	−1.31 ± 0.12*	−0.75 ± 0.11§§,#

*$p < 0.05$, **$p < 0.0$, ***$p < 0.001$ vs control, §$p < 0.01$, §§$p < 0.001$ vs STZ, #$p < 0.01$, ##$p < 0.001$ vs low dose.

DISCUSSION

Recently, much effort has been devoted to preclinical studies in which preventive treatments have been tested in order to stop/delay DR progression. Here, preclinical data on the efficacy of antioxidant compounds in preventing the occurrence of pathological signs that characterize DR have been collected and discussed in light of their possible application to humans.

Currently, the recommended treatment for severe non-proliferative or proliferative DR is photocoagulation and intravitreal injections of anti-VEGF associated, or not, with focal laser for diabetic macular oedema (DME). Anti-VEGF therapy not only counteracts new vessel proliferation but also interferes with inflammatory processes that have a considerable role in the pathogenesis of DME. In particular, VEGF accumulation induced by high blood glucose triggers major inflammatory processes and several drugs are already approved in clinical practice to handle DME. Anti-VEGF agents act also with mechanisms that interfere with inflammatory pathways. In particular, inflammation-induced dropout of pericytes leads to the formation of aberrant capillaries through VEGF accumulation, which reverberates on inflammatory pathways thus contributing to further compromise pericyte viability (Giurdanella et al., 2015). The complex network of pro-inflammatory factors involved in DME represents the rationale for its treatment by intravitreal steroids. In particular, repeated dexamethasone implants have been found to correlate well with DME duration with a better efficacy than anti-VEGF treatments (Bucolo et al., 2018).

Among the major limitations of treatments against vascular complications that characterize DR, late beginning of therapy is the greatest obstacle to cure the disease. In fact, in a high percentage of diabetic patients, inadequate control of metabolic parameters is a major cause of chronic complications including progressive DR. Approximately 15% of patients may show some degree of DR at the time of diabetes first diagnosis although severe microvascular complications will develop many years later. Early diagnosis of DR is the best tool to prevent or delay vision loss, but DR has been long considered as an asymptomatic disease and its progression to advanced stages has reduced the effectiveness of treatments (Corcóstegui et al., 2017; Rodríguez et al., 2019). Current work using subtle analysis of ERG waveforms in diabetic patients has allowed ophthalmologists to reach early diagnosis of non-proliferative DR and to evaluate the possibility to intervene at early stages when the retinal neuro-vascular unit is not yet seriously compromised (Ahmadieh et al., 2021). In this respect, natural plant extracts or their naturally occurring components have been shown to be very proficient in the prevention and treatment of DR. In preclinical studies, treatments with protective compounds that inhibit oxidative stress and inflammation have been shown to counteract the pathological signs of DR although clinical trials dealing with the effect of antioxidants on human DR have provided limited results that are often controversial (Garcia-Medina et al., 2020).

At the preclinical level, the STZ model of diabetes is a well-established and useful tool to investigate complications of diabetes including DR, although its progression to visual dysfunction, which in humans take years to be established, in rodents occur early after STZ injection. However, some limitations need to be considered when approaching the translation to clinics. The induction of diabetes with STZ consists in the acute disruption of pancreatic beta cells and the drastic interruption of insulin production. Therefore, it results in an all-or-nothing phenomenon in which different predispositions or risks of diabetes and, subsequently, different risks of developing DR, are not reproducible.

After STZ injection, elevated blood glucose concentration induced by pancreatic β-cell disruption, initiates an early increase of ROS, which overwhelms endogenous antioxidant defences and leads to early inflammation, increased levels of both HIF-1α and VEGF, increased vascular permeability that causes BRB breakdown leading to decreased visual function (Rodríguez et al., 2019).

There is convincing evidence that throughout the pathologic process of DR, oxidative stress plays an important role. In fact, a series of metabolic pathways altered by the exposure to high glucose concurrently result in the increment of ROS production in the retina. The excess in glucose undergoing glycolysis and citric acid cycle compels the increment in mitochondrial electron transport reaching the maximum threshold, and thus forcing the electron transfer to molecular oxygen generating radical species. In addition, chronic exposure to hyperglycemia favors the nonenzymatic glycation of proteins and lipids leading to the accumulation of advanced glycation end products (AGEs). Besides causing the loss of protein structure and function, AGEs can bind their receptors driving the downstream activation of NADPH oxidases, thus enhancing ROS generation. ROS accumulation triggers the endogenous antioxidant response masterly regulated by the redox sensitive transcriptional factor NRF2, which in turn mediates the increment in antioxidant enzymes such as HO-1 (Kang and Yang, 2020). However, the high glucose-driven ROS accumulation overcomes the endogenous capacity of antioxidant enzymes, which is further hindered by the high-glucose mediated activation of metabolic pathways driving the depletion of enzymatic cofactors. Both the ROS increment and

the antioxidant depotentiation initiate a cascade of events leading to retinal damage (Kowluru and Chan, 2007).

ROS increase also reverberates on the stimulation of the inflammatory response that further promotes oxidative damage. Indeed, ROS accumulation triggers the activation of NF-kB, a transcription factor involved in the modulation of the inflammatory response, which in turn regulates the expression of pro-inflammatory cytokines, such as IL-6 (Liu et al., 2017). In particular, inflammatory cytokines contribute to further amplify retinal cell damage by recruiting and activating immune cells as well as by increasing the levels of mediators responsible for the BRB dysfunction (Semeraro et al., 2015).

Pro-inflammatory stimuli result in macroglia activation as identified by GFAP overexpression, which can be considered as a marker for gliosis. In the healthy retina, GFAP is expressed only in astrocytes and not in Müller cells, whereas in the diseased retina, Müller cells exhibit dense GFAP immunostaining that has been widely used as a cellular marker for retinal pathological injury (Vecino et al., 2016).

Inflammation and gliosis lead to cell injury both in the neuroretina and in retinal blood vessels, thus promoting neuronal and vascular dysfunction. In particular, capillary closure and non-perfusion that develop relatively early after the onset of diabetes participate to establish hypoxic condition in the retina. Hypoxia causes the upregulation of HIF-1α, although HIF-1α increase may also occur as a direct consequence of hyperglycaemia independently on hypoxia (Xiao et al., 2013). HIF-1α accumulation leads to an increased production of VEGF that is a target of HIF-1. Upregulation of the VEGF signalling pathway ultimately leads to the dysfunction of inner and outer BRB with the loss of tight junctions integrity between neighbouring endothelial cells of both retinal microvasculature endothelium and RPE cells (Antonetti et al., 1999). Tight junction proteins including Claudin five and ZO-1, play a pivotal role in maintaining the BRB function through the regulation of the transport of solutes and molecules (Eshaq et al., 2017). The BRB breakdown results in the leakage of blood contents from retinal and choroidal vessels to the surrounding tissue which reverberate on inflammatory and ischemic processes leading to neuroretinal cell damage and ERG dysfunction (Xu and Le, 2011; Klaassen et al., 2013).

Retinal cell death is driven by the activation of apoptotic cascade, as also confirmed here by the altered Bax/Bcl-2 ratio, ultimately leading to the activation of caspase 3, a critical enzyme involved in apoptosis execution. As shown by the present findings, active caspase 3 is mostly localized to the inner retina in agreement with previous results indicating a significant involvement of inner retinal cells in apoptotic processes that characterize DR (Li et al., 2008; Sasaki et al., 2010; Thounaojam et al., 2017; Amato et al., 2018) while the outer retina is rather preserved at least soon after blood glucose increase (Park et al., 2003).

As a consequence of retinal damage, ERG becomes dysfunctional as demonstrated by the decreased amplitude of the scotopic a-wave arising from photoreceptor hyperpolarization, and the b-wave that reflects bipolar cell depolarization leading to potassium outflux that is buffered by Muller cells, which produce a transretinal current participating to b-wave generation (Dong and Hare, 2000 PMID 10824262). ERG dysfunction occurs at 4 weeks after STZ injection in agreement with previous longitudinal studies demonstrating that in the STZ model, ERG responses are unaffected by hyperglycemia up to 3 weeks after diabetes onset (Li et al., 2002; Shinoda et al., 2007; Cammalleri et al., 2017; Amato et al., 2018).

Impairment of scotopic ERG components might be reconducted to alterations of the activity of both photoreceptors and inner retinal cells. In this respect, despite no evidence of reduced thickness of the outer retina in which no apoptotic activity was detected, decreased amplitude of the a-wave is indicative of early photoreceptor suffering in line with previous reports demonstrating early degenerative changes of photoreceptors and pigment epithelium prior to apoptotic events (Énzsöly et al., 2014; Liu et al., 2016). On the other hand, the increased apoptotic activity in the inner retina as demonstrated by the presence of caspase 3-positive cells together with Müller cell gliosis, correlates well with altered b-waves that are known to be early and extensively affected in DR as a sign of inner retina dysfunction (Li et al., 2002).

Ongoing apoptotic processes in the inner retina were not correlated with reduced thickness of the INL in line with previous findings demonstrating that apoptosis becomes manifest as early as 4 weeks after STZ injection to then progress over an extended period of time, eventually leading to a later reduction in the retinal layer thickness (Barber et al., 1998).

As shown by the present results hyperglycaemia-induced cascade leading to ERG dysfunction is prevented by diet administration with antioxidant compounds including C3G, verbascoside and zinc starting on the day of STZ injection and persisting until the fourth week after, when the rats have undergone to ERG recording.

Most chronic diseases including diabetes are worsened by a deficiency of essential antioxidant nutrients, a condition that is further impaired by deficits in their absorption and utilization (Shi et al., 2020). Although major efforts to support the clinical benefits of vitamin and antioxidant interventions to reduce the risk and severity of vision loss, nutraceutical therapy is still limited and more large scales studies in DR are needed to overcome the limitations of clinical trials. Large clinical trials such as the AREDS2 formulation was a major improvement, bringing together natural antioxidants for the treatment of macular degeneration (AREDS2 Research Group et al., 2012; Shi et al., 2020). In this respect, decreased incidence of blindness in patients with macular degeneration have been observed in the zinc supplemented elderly (Prasad and Bao, 2019). Results from clinical trials about the efficacy of natural antioxidants in DR patients are highly variable and, in some cases, controversial. However, a general tendency towards the efficacy of antioxidants in combination has been reported to match the need of counteracting the wide spectrum of pathogenic mechanisms characterizing DR (Garcia-Medina et al., 2020). For instance, the supplementation with lutein, alpha-tocopherol, niacin, beta-carotene, zinc and selenium has been found to delay DR progression in patients with type 2 diabetes, although no effects on visual acuity have been detected (Garcia-Medina

et al., 2011). In contrast, ameliorated visual acuity, but no efficacy on retinal thickness have been determined in patients with type 2 diabetes following the treatment with combined antioxidants including carotenoids, racemic compounds, vitamins and botanical extracts (Chous et al., 2016).

Still, major limitation to the conflicting results of clinical trials in DR depends on the fact that antioxidant efficacy of natural compounds is generally tested on patients who already experienced disorders of visual processing at various levels. Instead, the specific interest would be to test the antioxidant efficacy of nutraceutical compounds by intervening on the early stages of DR to prevent/delay its progression to proliferative DR. In this respect, there is an increasing body of evidence about the role of antioxidants in the control of DR in animal models.

The present results in the STZ model of DR demonstrate the preventive efficacy of a novel compound containing C3G, verbascoside and zinc as nutrients with antioxidant and anti-inflammatory properties. The PK profile of C3G has been characterized by de Ferrars et al. (2014) demonstrating C3G retention in the plasma up to 6 h post-oral administration. In a recent work, C3G has been detected in the plasma from which it reaches the ocular tissue following oral administration (Amato et al., 2021) also in line with previous findings (Matsumoto et al., 2006). Orally administered verbascoside appears to be distributed to most tissues including the brain suggesting its ability to cross the blood-brain barrier (Wen et al., 2016). In addition, verbascoside, has been found to protect ocular tissues and fluids from naturally occurring oxidation (Mosca et al., 2014). The PK profile and biodistribution of zinc have been established in previous studies (Nève et al., 1991; Gilbert et al., 2019). Recently, zinc, orally administered, has been found to accumulate in the retina where it acts as cofactor for antioxidant enzymes (Kamińska et al., 2021). C3G is a potent inhibitor of oxidative stress and its antioxidant properties include the activation of endogenous anti-oxidant enzymes, quenching singlet oxygen, chelation of trace metals involved in free radical production, inhibition of ROS-promoting enzymes, ROS scavenger properties (Tena et al., 2020). ROS scavenging activates a downstream anti-inflammatory cascade leading to the inhibition of the NF-kB activity, the reduced release of pro-inflammatory cytokines and the inhibition of inflammasome activity (Min et al., 2010; Jin et al., 2018). Additional efficacy of C3G includes its capacity to counteract pathological neoangiogenesis by contrasting VEGF overexpression in response to high glucose (Matsunaga et al., 2010; Oliveira et al., 2020). Verbascoside has been reported to exert a major anti-inflammatory activity through the inhibition of NF-kB signalling and nitric oxide pathway, thus resulting in decreased inflammatory response (Wu et al., 2020). Interestingly, verbascoside has also been shown to directly interact with cell survival mechanisms by inhibiting autophagy-induced apoptosis (Chen et al., 2019). In diabetic condition, verbascoside has been established to inhibit endoplasmic reticulum stress and advanced glycation end-product formation (Liu et al., 2013; Galli et al., 2020). Zinc is known as a fundamental trace element involved in the structure and function of numerous enzymes regulating cellular processes and signalling pathways. Zinc potentiates the endogenous antioxidant response by increasing the activity of antioxidant proteins and enzymes that are transcribed by NRF2 (Jarosz et al., 2017). Zinc deficiency has been shown to correlate with ocular abnormalities such as cataract and retinal diseases including age-related macular degeneration and DR (Miao et al., 2013). In line with the negative effects of zinc deficiency, the supplementation of zinc, in combination with additional functional nutrients, has provided promising results to establish its potential for counteracting retinal diseases (Miao et al., 2013; Vishwanathan et al., 2013). However, the boundary line between the activity and the contribution of these hypothetical classes of natural molecules is complicated by the fact that many of the properties of each molecule are shared with the others. For instance, C3G may also activate endogenous antioxidant defenses, as played by zinc. In addition, verbascoside may exert an anti-inflammatory activity leading to reduced ROS generation thus amplifying the effect of zinc and C3G. In this respect, although a theoretical classification of the molecules could be done based on their individual bioactivity, an actual discrimination of each component activity in the context of a compound is difficult to retrieve. The efficacy of C3G, verbascoside and zinc has already been established in a model of light induced retinal damage in which the combined formula has been shown to exert marked antioxidant and anti-inflammatory effects resulting in a significant protection of photoreceptor morpho-functional integrity (Amato et al., 2021). Its application to DR is further stressed by the hypoglycaemic properties of the compounds included in the formula (Sasaki et al., 2007; Xiong et al., 2013; Sadri et al., 2017). However, as shown by the present results, glycemia is not affected by the formula presumably because the serious destruction of islet function by STZ renders the blood glucose difficult to control (Pang et al., 2020). Although the efficacy of the compound supplementation on pathological signs of DR is independent on glycemia control, oxidative stress- and inflammation-related mechanisms downstream hyperglycaemia are markedly counteracted with a significant counterpart in preventing BRB leakage, retinal cell death and retinal dysfunction.

CONCLUSION

One the major clinical problems of late stages of DR is irreversible visual loss due to the scarce availability of drugs restoring visual function once proliferative DR is established. Therefore, research work to investigate possible strategies to prevent DR progression should be accurately pursued. The fact that antioxidant/anti-inflammatory compounds, possibly through their protective efficacy on vascular damage may prevent the apoptotic cascade leading to ERG dysfunction, adds further relevance to their potential application as a preventive therapy to counteract DR progression. On the other hand, the glycemic control is the milestone for the management of diabetes and its related complications including DR. However, a significant number of diabetic patients undergoing glycemic control therapies still develop DR symptoms, thus highlighting the need of

complementary therapies, other than those dedicated to blood glucose lowering. The present study demonstrates that antioxidant supplementation could represent a non-invasive solution to prevent or delay DR signs. Therefore, the translational goal of the present approach consists in its potential complementary role in combination with hypoglycemic drugs in order to further reduce the risk of DR onset and progression. However, the extrapolation of these experimental findings to the clinic is not straightforward as animal models of DR may not faithfully recapitulate all the pathologic signs seen in human DR. In this respect, neither macular edema nor proliferative retinopathy ever develop in STZ-rats, indicating that they are a suitable model for the early phase of human DR.

DATA AVAILABILITY STATEMENT

The raw data supporting the conclusions of this article will be made available by the authors, without undue reservation.

ETHICS STATEMENT

The animal study was reviewed and approved by the Commission for Animal Wellbeing of the University of Pisa.

AUTHOR CONTRIBUTIONS

Conceptualization, DR, PB and MC; methodology, AC, RA and AM; validation, AC and AM; formal analysis, AC and RA; investigation, AC, RA and AM, resources, MD; data curation, RA and MC; writing-original draft preparation, RA, PB and MC.; writing-review and editing, RA, MD, DR, PB and MC; supervision, MC; project administration, DR, PB and MC; funding acquisition, MD. All authors have read and agreed to the published version of the manuscript.

FUNDING

This research was funded by grants from Sooft Italia, SpA (Montegiorgio, FM, Italy) to MDM.

ACKNOWLEDGMENTS

The authors wish to thank Prof. Giuseppe Guarnaccia, Director, ESASO, Switzerland and Prof. Giacomo Panozzo, board coordinator, ESASO Plus, Switzerland, for the critical reading of the manuscript and Marco Pellegrini (Ophthalmology Unit, S.Orsola-Malpighi University Hospital, University of Bologna) for his critical advise on the current state of the art about the use of natural antioxidant compounds in ophthalmology. The authors also wish to thank Tiziana Cintio for animal assistance.

SUPPLEMENTARY MATERIAL

The Supplementary Material for this article can be found online at: https://www.frontiersin.org/articles/10.3389/fphar.2021.811818/full#supplementary-material

REFERENCES

Ahmadieh, H., Behbahani, S., and Safi, S. (2021). Continuous Wavelet Transform Analysis of ERG in Patients with Diabetic Retinopathy. *Doc. Ophthalmol.* 142 (3), 305–314. doi:10.1007/s10633-020-09805-9

Al-Kharashi, A. S. (2018). Role of Oxidative Stress, Inflammation, Hypoxia and Angiogenesis in the Development of Diabetic Retinopathy. *Saudi J. Ophthalmol.* 32 (4), 318–323. doi:10.1016/j.sjopt.2018.05.002

Alipieva, K., Korkina, L., Orhan, I. E., and Georgiev, M. I. (2014). Verbascoside--a Review of its Occurrence, (Bio)synthesis and Pharmacological Significance. *Biotechnol. Adv.* 32 (6), 1065–1076. doi:10.1016/j.biotechadv.2014.07.001

Amato, R., Canovai, A., Melecchi, A., Pezzino, S., Corsaro, R., Dal Monte, M., et al. (2021). Dietary Supplementation of Antioxidant Compounds Prevents Light-Induced Retinal Damage in a Rat Model. *Biomedicines* 9 (9), 1177. doi:10.3390/biomedicines9091177

Amato, R., Rossino, M. G., Cammalleri, M., Locri, F., Pucci, L., Dal Monte, M., et al. (2018). Lisosan G Protects the Retina from Neurovascular Damage in Experimental Diabetic Retinopathy. *Nutrients* 10 (12), 1932. doi:10.3390/nu10121932

Antonetti, D. A., Barber, A. J., Hollinger, L. A., Wolpert, E. B., and Gardner, T. W. (1999). Vascular Endothelial Growth Factor Induces Rapid Phosphorylation of Tight junction Proteins Occludin and Zonula Occluden 1. A Potential Mechanism for Vascular Permeability in Diabetic Retinopathy and Tumors. *J. Biol. Chem.* 274 (33), 23463–23467. doi:10.1074/jbc.274.33.23463

AREDS2 Research GroupChew, E. Y., Chew, E. Y., Clemons, T., SanGiovanni, J. P., Danis, R., et al. (2012). The Age-Related Eye Disease Study 2 (AREDS2): Study Design and Baseline Characteristics (AREDS2 Report Number 1). *Ophthalmology* 119 (11), 2282–2289. doi:10.1016/j.ophtha.2012.05.027

Barber, A. J., and Baccouche, B. (2017). Neurodegeneration in Diabetic Retinopathy: Potential for Novel Therapies. *Vis. Res.* 139, 82–92. doi:10.1016/j.visres.2017.06.014

Barber, A. J., Lieth, E., Khin, S. A., Antonetti, D. A., Buchanan, A. G., and Gardner, T. W. (1998). Neural Apoptosis in the Retina during Experimental and Human Diabetes. Early Onset and Effect of Insulin. *J. Clin. Invest.* 102 (4), 783–791. doi:10.1172/JCI2425

Bucolo, C., Gozzo, L., Longo, L., Mansueto, S., Vitale, D. C., and Drago, F. (2018). Long-term Efficacy and Safety Profile of Multiple Injections of Intravitreal Dexamethasone Implant to Manage Diabetic Macular Edema: A Systematic Review of Real-World Studies. *J. Pharmacol. Sci.* 138 (4), 219–232. doi:10.1016/j.jphs.2018.11.001

Burgos, C., Muñoz-Mingarro, D., Navarro, I., Martín-Cordero, C., and Acero, N. (2020). Neuroprotective Potential of Verbascoside Isolated from Acanthus Mollis L. Leaves through its Enzymatic Inhibition and Free Radical Scavenging Ability. *Antioxidants (Basel)* 9 (12), 1207. doi:10.3390/antiox9121207

Cammalleri, M., Locri, F., Marsili, S., Dal Monte, M., Pisano, C., Mancinelli, A., et al. (2017). The Urokinase Receptor-Derived Peptide UPARANT Recovers Dysfunctional Electroretinogram and Blood-Retinal Barrier Leakage in a Rat Model of Diabetes. *Invest. Ophthalmol. Vis. Sci.* 58 (7), 3138–3148. doi:10.1167/iovs.17-21593

Chen, Q., Xi, X., Zeng, Y., He, Z., Zhao, J., and Li, Y. (2019). Acteoside Inhibits Autophagic Apoptosis of Retinal Ganglion Cells to rescue Glaucoma-Induced Optic Atrophy. *J. Cel Biochem.* 120 (8), 13133–13140. doi:10.1002/jcb.28586

Chous, A. P., Richer, S. P., Gerson, J. D., and Kowluru, R. A. (2016). The Diabetes Visual Function Supplement Study (DiVFuSS). *Br. J. Ophthalmol.* 100 (2), 227–234. doi:10.1136/bjophthalmol-2014-306534

Corcóstegui, B., Durán, S., González-Albarrán, M. O., Hernández, C., Ruiz-Moreno, J. M., Salvador, J., et al. (2017). Update on Diagnosis and Treatment of Diabetic Retinopathy: A Consensus Guideline of the Working Group of Ocular Health (Spanish Society of Diabetes and Spanish Vitreous and Retina Society). *J. Ophthalmol.* 2017, 8234186. doi:10.1155/2017/8234186

de Ferrars, R. M., Czank, C., Zhang, Q., Botting, N. P., Kroon, P. A., Cassidy, A., et al. (2014). The Pharmacokinetics of Anthocyanins and Their Metabolites in Humans. *Br. J. Pharmacol.* 171 (13), 3268–3282. doi:10.1111/bph.12676

Dong, C. J., and Hare, W. A. (2000). Contribution to the Kinetics and Amplitude of the Electroretinogram B-Wave by Third-Order Retinal Neurons in the Rabbit Retina. *Vis. Res.* 40 (6), 579–589. doi:10.1016/s0042-6989(99)00203-5

Énzsöly, A., Szabó, A., Kántor, O., Dávid, C., Szalay, P., Szabó, K., et al. (2014). Pathologic Alterations of the Outer Retina in Streptozotocin-Induced Diabetes. *Invest. Ophthalmol. Vis. Sci.* 55 (6), 3686–3699. doi:10.1167/iovs.13-13562

Eshaq, R. S., Aldalati, A. M. Z., Alexander, J. S., and Harris, N. R. (2017). Diabetic Retinopathy: Breaking the Barrier. *Pathophysiology* 24 (4), 229–241. doi:10.1016/j.pathophys.2017.07.001

Feng, Y., Busch, S., Gretz, N., Hoffmann, S., and Hammes, H. P. (2012). Crosstalk in the Retinal Neurovascular Unit - Lessons for the Diabetic Retina. *Exp. Clin. Endocrinol. Diabetes* 120 (4), 199–201. doi:10.1055/s-0032-1304571

Furman, B. L. (2015). Streptozotocin-Induced Diabetic Models in Mice and Rats. *Curr. Protoc. Pharmacol.* 70, 5.47.1–5.47.20. doi:10.1002/0471141755.ph0547s70

Galli, A., Marciani, P., Marku, A., Ghislanzoni, S., Bertuzzi, F., Rossi, R., et al. (2020). Verbascoside Protects Pancreatic β-Cells against ER-Stress. *Biomedicines* 8 (12), 582. doi:10.3390/biomedicines8120582

Garcia-Medina, J. J., Pinazo-Duran, M. D., Garcia-Medina, M., Zanon-Moreno, V., and Pons-Vazquez, S. (2011). A 5-year Follow-Up of Antioxidant Supplementation in Type 2 Diabetic Retinopathy. *Eur. J. Ophthalmol.* 21 (5), 637–643. doi:10.5301/EJO.2010.6212

Garcia-Medina, J. J., Rubio-Velazquez, E., Foulquie-Moreno, E., Casaroli-Marano, R. P., Pinazo-Duran, M. D., Zanon-Moreno, V., et al. (2020). Update on the Effects of Antioxidants on Diabetic Retinopathy: *In Vitro* Experiments, Animal Studies and Clinical Trials. *Antioxidants (Basel)* 9 (6), 561. doi:10.3390/antiox9060561

Gilbert, R., Peto, T., Lengyel, I., and Emri, E. (2019). Zinc Nutrition and Inflammation in the Aging Retina. *Mol. Nutr. Food Res.* 63 (15), e1801049. doi:10.1002/mnfr.201801049

Giurdanella, G., Anfuso, C. D., Olivieri, M., Lupo, G., Caporarello, N., Eandi, C. M., et al. (2015). Aflibercept, Bevacizumab and Ranibizumab Prevent Glucose-Induced Damage in Human Retinal Pericytes *In Vitro*, through a PLA2/COX-2/VEGF-A Pathway. *Biochem. Pharmacol.* 96 (3), 278–287. doi:10.1016/j.bcp.2015.05.017

Gu, L., Xu, H., Zhang, C., Yang, Q., Zhang, L., and Zhang, J. (2019). Time-dependent Changes in Hypoxia- and Gliosis-Related Factors in Experimental Diabetic Retinopathy. *Eye (Lond)* 33 (4), 600–609. doi:10.1038/s41433-018-0268-z

Jarosz, M., Olbert, M., Wyszogrodzka, G., Młyniec, K., and Librowski, T. (2017). Antioxidant and Anti-inflammatory Effects of Zinc. Zinc-dependent NF-κB Signaling. *Inflammopharmacology* 25 (1), 11–24. doi:10.1007/s10787-017-0309-4

Jin, X., Wang, C., Wu, W., Liu, T., Ji, B., and Zhou, F. (2018). Cyanidin-3-glucoside Alleviates 4-Hydroxyhexenal-Induced NLRP3 Inflammasome Activation via JNK-C-Jun/AP-1 Pathway in Human Retinal Pigment Epithelial Cells. *J. Immunol. Res.* 2018, 5604610. doi:10.1155/2018/5604610

Kamińska, A., Romano, G. L., Rejdak, R., Zweifel, S., Fiedorowicz, M., Rejdak, M., et al. (2021). Influence of Trace Elements on Neurodegenerative Diseases of the Eye-The Glaucoma Model. *Int. J. Mol. Sci.* 22 (9), 4323. doi:10.3390/ijms22094323

Kang, Q., and Yang, C. (2020). Oxidative Stress and Diabetic Retinopathy: Molecular Mechanisms, Pathogenetic Role and Therapeutic Implications. *Redox Biol.* 37, 101799. doi:10.1016/j.redox.2020.101799

Khoo, H. E., Azlan, A., Tang, S. T., and Lim, S. M. (2017). Anthocyanidins and Anthocyanins: Colored Pigments as Food, Pharmaceutical Ingredients, and the Potential Health Benefits. *Food Nutr. Res.* 61 (1), 1361779. doi:10.1080/16546628.2017.1361779

Klaassen, I., Van Noorden, C. J., and Schlingemann, R. O. (2013). Molecular Basis of the Inner Blood-Retinal Barrier and its Breakdown in Diabetic Macular Edema and Other Pathological Conditions. *Prog. Retin. Eye Res.* 34, 19–48. doi:10.1016/j.preteyeres.2013.02.001

Kowluru, R. A., and Chan, P. S. (2007). Oxidative Stress and Diabetic Retinopathy. *Exp. Diabetes Res.* 2007, 43603. doi:10.1155/2007/43603

Leena, M. M., Silvia, M. G., Vinitha, K., Moses, J. A., and Anandharamakrishnan, C. (2020). Synergistic Potential of Nutraceuticals: Mechanisms and Prospects for Futuristic Medicine. *Food Funct.* 11 (11), 9317–9337. doi:10.1039/d0fo02041a

Li, Q., Zemel, E., Miller, B., and Perlman, I. (2002). Early Retinal Damage in Experimental Diabetes: Electroretinographical and Morphological Observations. *Exp. Eye Res.* 74 (5), 615–625. doi:10.1006/exer.2002.1170

Li, W., Chen, S., Zhou, G., Li, H., Zhong, L., and Liu, S. (2018). Potential Role of Cyanidin 3-glucoside (C3G) in Diabetic Cardiomyopathy in Diabetic Rats: An *In Vivo* Approach. *Saudi J. Biol. Sci.* 25 (3), 500–506. doi:10.1016/j.sjbs.2016.11.007

Li, Y. H., Zhuo, Y. H., Lü, L., Chen, L. Y., Huang, X. H., Zhang, J. L., et al. (2008). Caspase-dependent Retinal Ganglion Cell Apoptosis in the Rat Model of Acute Diabetes. *Chin. Med. J. (Engl)* 121 (24), 2566–2571. doi:10.1097/00029330-200812020-00018

Liu, H., Tang, J., Du, Y., Saadane, A., Tonade, D., Samuels, I., et al. (2016). Photoreceptor Cells Influence Retinal Vascular Degeneration in Mouse Models of Retinal Degeneration and Diabetes. *Invest. Ophthalmol. Vis. Sci.* 57 (10), 4272–4281. doi:10.1167/iovs.16-19415

Liu, T., Zhang, L., Joo, D., and Sun, S. C. (2017). NF-κB Signaling in Inflammation. *Signal. Transduct. Target. Ther.* 2, 17023. doi:10.1038/sigtrans.2017.23

Liu, Y. H., Lu, Y. L., Han, C. H., and Hou, W. C. (2013). Inhibitory Activities of Acteoside, Isoacteoside, and its Structural Constituents against Protein Glycation *In Vitro*. *Bot. Stud.* 54 (1), 6. doi:10.1186/1999-3110-54-6

Marreiro, D. D., Cruz, K. J., Morais, J. B., Beserra, J. B., Severo, J. S., and de Oliveira, A. R. (2017). Zinc and Oxidative Stress: Current Mechanisms. *Antioxidants (Basel)* 6 (2), 24. doi:10.3390/antiox6020024

Matsumoto, H., Nakamura, Y., Iida, H., Ito, K., and Ohguro, H. (2006). Comparative Assessment of Distribution of Blackcurrant Anthocyanins in Rabbit and Rat Ocular Tissues. *Exp. Eye Res.* 83 (2), 348–356. doi:10.1016/j.exer.2005.12.019

Matsunaga, N., Tsuruma, K., Shimazawa, M., Yokota, S., and Hara, H. (2010). Inhibitory Actions of Bilberry Anthocyanidins on Angiogenesis. *Phytother Res.* 24 (Suppl. 1), S42–S47. doi:10.1002/ptr.2895

Mi, X. S., Yuan, T. F., Ding, Y., Zhong, J. X., and So, K. F. (2014). Choosing Preclinical Study Models of Diabetic Retinopathy: Key Problems for Consideration. *Drug Des. Devel. Ther.* 8, 2311–2319. doi:10.2147/DDDT.S72797

Miao, X., Sun, W., Miao, L., Fu, Y., Wang, Y., Su, G., et al. (2013). Zinc and Diabetic Retinopathy. *J. Diabetes Res.* 2013, 425854. doi:10.1155/2013/425854

Min, S. W., Ryu, S. N., and Kim, D. H. (2010). Anti-inflammatory Effects of Black rice, Cyanidin-3-O-Beta-D-Glycoside, and its Metabolites, Cyanidin and Protocatechuic Acid. *Int. Immunopharmacol.* 10 (8), 959–966. doi:10.1016/j.intimp.2010.05.009

Mosca, M., Ambrosone, L., Semeraro, F., Casamassima, D., Vizzarri, F., and Costagliola, C. (2014). Ocular Tissues and Fluids Oxidative Stress in Hares Fed on Verbascoside Supplement. *Int. J. Food Sci. Nutr.* 65 (2), 235–240. doi:10.3109/09637486.2013.836742

Naderi, A., Zahed, R., Aghajanpour, L., Amoli, F. A., and Lashay, A. (2019). Long Term Features of Diabetic Retinopathy in Streptozotocin-Induced Diabetic Wistar Rats. *Exp. Eye Res.* 184, 213–220. doi:10.1016/j.exer.2019.04.025

Nair, A. B., and Jacob, S. (2016). A Simple Practice Guide for Dose Conversion between Animals and Human. *J. Basic Clin. Pharm.* 7 (2), 27–31. doi:10.4103/0976-0105.177703

Naka, K. I., and Rushton, W. A. (1966). S-potentials from Colour Units in the Retina of Fish (Cyprinidae). *J. Physiol.* 185 (3), 536–555. doi:10.1113/jphysiol.1966.sp008001

Nève, J., Hanocq, M., Peretz, A., Abi Khalil, F., Pelen, F., Famaey, J. P., et al. (1991). Pharmacokinetic Study of Orally Administered Zinc in Humans: Evidence for an Enteral Recirculation. *Eur. J. Drug Metab. Pharmacokinet.* 16 (4), 315–323. doi:10.1007/BF03189977

Nomi, Y., Iwasaki-Kurashige, K., and Matsumoto, H. (2019). Therapeutic Effects of Anthocyanins for Vision and Eye Health. *Molecules* 24 (18), 3311. doi:10.3390/molecules24183311

Oliveira, H., Fernandes, A., F Brás, N., Mateus, N., de Freitas, V., and Fernandes, I. (2020). Anthocyanins as Antidiabetic Agents-In Vitro and In Silico Approaches of Preventive and Therapeutic Effects. *Molecules* 25 (17), 3813. doi:10.3390/molecules25173813

Pang, B., Ni, Q., Di, S., Du, L. J., Qin, Y. L., Li, Q. W., et al. (2020). Luo Tong Formula Alleviates Diabetic Retinopathy in Rats through Micro-200b Target. *Front. Pharmacol.* 11, 551766. doi:10.3389/fphar.2020.551766

Park, S. H., Park, J. W., Park, S. J., Kim, K. Y., Chung, J. W., Chun, M. H., et al. (2003). Apoptotic Death of Photoreceptors in the Streptozotocin-Induced Diabetic Rat Retina. *Diabetologia* 46 (9), 1260–1268. doi:10.1007/s00125-003-1177-6

Perron, N. R., and Brumaghim, J. L. (2009). A Review of the Antioxidant Mechanisms of Polyphenol Compounds Related to Iron Binding. *Cell Biochem. Biophys.* 53 (2), 75–100. doi:10.1007/s12013-009-9043-x

Prasad, A. S., and Bao, B. (2019). Molecular Mechanisms of Zinc as a Pro-antioxidant Mediator: Clinical Therapeutic Implications. *Antioxidants (Basel)* 8 (6), 164. doi:10.3390/antiox8060164

Qaum, T., Xu, Q., Joussen, A. M., Clemens, M. W., Qin, W., Miyamoto, K., et al. (2001). VEGF-initiated Blood-Retinal Barrier Breakdown in Early Diabetes. *Invest. Ophthalmol. Vis. Sci.* 42 (10), 2408–2413.

Qin, Y., Zhai, Q., Li, Y., Cao, M., Xu, Y., Zhao, K., et al. (2018). Cyanidin-3-O-glucoside Ameliorates Diabetic Nephropathy through Regulation of Glutathione Pool. *Biomed. Pharmacother.* 103, 1223–1230. doi:10.1016/j.biopha.2018.04.137

Rodríguez, M. L., Pérez, S., Mena-Mollá, S., Desco, M. C., and Ortega, Á. L. (2019). Oxidative Stress and Microvascular Alterations in Diabetic Retinopathy: Future Therapies. *Oxid. Med. Cel. Longev.* 2019, 4940825. doi:10.1155/2019/4940825

Rossino, M. G., and Casini, G. (2019). Nutraceuticals for the Treatment of Diabetic Retinopathy. *Nutrients* 11 (4), 771. doi:10.3390/nu11040771

Rossino, M. G., Dal Monte, M., and Casini, G. (2019). Relationships between Neurodegeneration and Vascular Damage in Diabetic Retinopathy. *Front. Neurosci.* 13, 1172. doi:10.3389/fnins.2019.01172

Rübsam, A., Parikh, S., and Fort, P. E. (2018). Role of Inflammation in Diabetic Retinopathy. *Int. J. Mol. Sci.* 19 (4), 942. doi:10.3390/ijms19040942

Sadri, H., Larki, N. N., and Kolahian, S. (2017). Hypoglycemic and Hypolipidemic Effects of Leucine, Zinc, and Chromium, Alone and in Combination, in Rats with Type 2 Diabetes. *Biol. Trace Elem. Res.* 180 (2), 246–254. doi:10.1007/s12011-017-1014-2

Sasaki, M., Ozawa, Y., Kurihara, T., Kubota, S., Yuki, K., Noda, K., et al. (2010). Neurodegenerative Influence of Oxidative Stress in the Retina of a Murine Model of Diabetes. *Diabetologia* 53 (5), 971–979. doi:10.1007/s00125-009-1655-6

Sasaki, R., Nishimura, N., Hoshino, H., Isa, Y., Kadowaki, M., Ichi, T., et al. (2007). Cyanidin 3-glucoside Ameliorates Hyperglycemia and Insulin Sensitivity Due to Downregulation of Retinol Binding Protein 4 Expression in Diabetic Mice. *Biochem. Pharmacol.* 74 (11), 1619–1627. doi:10.1016/j.bcp.2007.08.008

Semeraro, F., Cancarini, A., dell'Omo, R., Rezzola, S., Romano, M. R., and Costagliola, C. (2015). Diabetic Retinopathy: Vascular and Inflammatory Disease. *J. Diabetes Res.* 2015, 582060. doi:10.1155/2015/582060

Shi, C., Wang, P., Airen, S., Brown, C., Liu, Z., Townsend, J. H., et al. (2020). Nutritional and Medical Food Therapies for Diabetic Retinopathy. *Eye Vis. (Lond)* 7, 33. doi:10.1186/s40662-020-00199-y

Shinoda, K., Rejdak, R., Schuettauf, F., Blatsios, G., Völker, M., Tanimoto, N., et al. (2007). Early Electroretinographic Features of Streptozotocin-Induced Diabetic Retinopathy. *Clin. Exp. Ophthalmol.* 35 (9), 847–854. doi:10.1111/j.1442-9071.2007.01607.x

Simó, R., Stitt, A. W., and Gardner, T. W. (2018). Neurodegeneration in Diabetic Retinopathy: Does it Really Matter? *Diabetologia* 61 (9), 1902–1912. doi:10.1007/s00125-018-4692-1

Sinclair, S. H., and Schwartz, S. S. (2019). Diabetic Retinopathy-An Underdiagnosed and Undertreated Inflammatory, Neuro-Vascular Complication of Diabetes. *Front. Endocrinol. (Lausanne)* 10, 843. doi:10.3389/fendo.2019.00843

Tang, J., and Kern, T. S. (2011). Inflammation in Diabetic Retinopathy. *Prog. Retin. Eye Res.* 30 (5), 343–358. doi:10.1016/j.preteyeres.2011.05.002

Tena, N., Martín, J., and Asuero, A. G. (2020). State of the Art of Anthocyanins: Antioxidant Activity, Sources, Bioavailability, and Therapeutic Effect in Human Health. *Antioxidants (Basel)* 9 (5), 451. doi:10.3390/antiox9050451

Thounaojam, M. C., Powell, F. L., Patel, S., Gutsaeva, D. R., Tawfik, A., Smith, S. B., et al. (2017). Protective Effects of Agonists of Growth Hormone-Releasing Hormone (GHRH) in Early Experimental Diabetic Retinopathy. *Proc. Natl. Acad. Sci. U S A.* 114 (50), 13248–13253. doi:10.1073/pnas.1718592114

Vecino, E., Rodriguez, F. D., Ruzafa, N., Pereiro, X., and Sharma, S. C. (2016). Glia-neuron Interactions in the Mammalian Retina. *Prog. Retin. Eye Res.* 51, 1–40. doi:10.1016/j.preteyeres.2015.06.003

Vishwanathan, R., Chung, M., and Johnson, E. J. (2013). A Systematic Review on Zinc for the Prevention and Treatment of Age-Related Macular Degeneration. *Invest. Ophthalmol. Vis. Sci.* 54 (6), 3985. doi:10.1167/iovs.12-11552

Wang, Y., Huo, Y., Zhao, L., Lu, F., Wang, O., Yang, X., et al. (2016). Cyanidin-3-glucoside and its Phenolic Acid Metabolites Attenuate Visible Light-Induced Retinal Degeneration *In Vivo* via Activation of Nrf2/HO-1 Pathway and NF-κB Suppression. *Mol. Nutr. Food Res.* 60 (7), 1564–1577. doi:10.1002/mnfr.201501048

Wen, Y., Huo, S., Zhang, W., Xing, H., Qi, L., Zhao, D., et al. (2016). Pharmacokinetics, Biodistribution, Excretion and Plasma Protein Binding Studies of Acteoside in Rats. *Drug Res. (Stuttg)* 66 (3), 148–153. doi:10.1055/s-0035-1555896

Wu, L., Georgiev, M. I., Cao, H., Nahar, L., El-Seedi, H. R., Sarker, S. D., et al. (2020). Therapeutic Potential of Phenylethanoid Glycosides: A Systematic Review. *Med. Res. Rev.* 40 (6), 2605–2649. doi:10.1002/med.21717

Xiao, H., Gu, Z., Wang, G., and Zhao, T. (2013). The Possible Mechanisms Underlying the Impairment of HIF-1α Pathway Signaling in Hyperglycemia and the Beneficial Effects of Certain Therapies. *Int. J. Med. Sci.* 10 (10), 1412–1421. doi:10.7150/ijms.5630

Xiong, W. T., Gu, L., Wang, C., Sun, H. X., and Liu, X. (2013). Anti-hyperglycemic and Hypolipidemic Effects of Cistanche Tubulosa in Type 2 Diabetic Db/db Mice. *J. Ethnopharmacol.* 150 (3), 935–945. doi:10.1016/j.jep.2013.09.027

Xu, H. Z., and Le, Y. Z. (2011). Significance of Outer Blood-Retina Barrier Breakdown in Diabetes and Ischemia. *Invest. Ophthalmol. Vis. Sci.* 52 (5), 2160–2164. doi:10.1167/iovs.10-6518

Conflict of Interest: MM received a study grant from Sooft Italia SpA. DR is an employee of Sooft Italia SpA. Sooft Italia SpA had no direct role in the collection, analyses or interpretation of data or in the decision to publish the results.

The remaining authors declare that the research was conducted in the absence of any commercial or financial relationships that could be construed as a potential conflict of interest.

The reviewer ST declared a past collaboration with one of the authors MC to the handling editor.

biomedicines

MDPI

Article

Dietary Supplementation of Antioxidant Compounds Prevents Light-Induced Retinal Damage in a Rat Model

Rosario Amato [1,†], Alessio Canovai [1,†], Alberto Melecchi [1], Salvatore Pezzino [2], Roberta Corsaro [2], Massimo Dal Monte [1,3], Dario Rusciano [2], Paola Bagnoli [1] and Maurizio Cammalleri [1,3,*]

1 Department of Biology, University of Pisa, 56127 Pisa, Italy; rosario.amato@biologia.unipi.it (R.A.); a.canovai@student.unisi.it (A.C.); a.melecchi@studenti.unipi.it (A.M.); massimo.dalmonte@unipi.it (M.D.M.); paola.bagnoli@unipi.it (P.B.)
2 Research Center, Sooft Italia SpA, 95100 Catania, Italy; salvatore.pezzino@sooft.it (S.P.); roberta.corsaro@sooft.it (R.C.); dario.rusciano@sooft.it (D.R.)
3 Interdepartmental Research Center Nutrafood "Nutraceuticals and Food for Health", University of Pisa, 56124 Pisa, Italy
* Correspondence: maurizio.cammalleri@unipi.it; Tel.: +39-05-0221-1434
† These authors contributed equally to the present work.

Abstract: Light-induced retinal damage (LD) is characterized by the accumulation of reactive oxygen species leading to oxidative stress and photoreceptor cell death. The use of natural antioxidants has emerged as promising approach for the prevention of LD. Among them, lutein and cyanidin-3-glucoside (C3G) have been shown to be particularly effective due to their antioxidant and anti-inflammatory activity. However, less is known about the possible efficacy of combining them in a multicomponent mixture. In a rat model of LD, Western blot analysis, immunohistochemistry and electroretinography were used to demonstrate that lutein and C3G in combination or in a multicomponent mixture can prevent oxidative stress, inflammation, gliotic and apoptotic responses thus protecting photoreceptor cells from death with higher efficacy than each component alone. Combined efficacy on dysfunctional electroretinogram was also demonstrated by ameliorated rod and cone photoreceptor responses. These findings suggest the rationale to formulate multicomponent blends which may optimize the partnering compounds bioactivity and bioavailability.

Keywords: phototoxicity; oxidative stress; inflammation; neuroprotection; photoreceptor death; electroretinography; nutraceuticals

Citation: Amato, R.; Canovai, A.; Melecchi, A.; Pezzino, S.; Corsaro, R.; Dal Monte, M.; Rusciano, D.; Bagnoli, P.; Cammalleri, M. Dietary Supplementation of Antioxidant Compounds Prevents Light-Induced Retinal Damage in a Rat Model. *Biomedicines* **2021**, *9*, 1177. https://doi.org/10.3390/biomedicines9091177

Academic Editor: H. P. Vasantha Rupasinghe

Received: 27 July 2021
Accepted: 6 September 2021
Published: 7 September 2021

1. Introduction

Oxidative stress and exacerbated inflammatory response are key pathological mechanisms driving several high-incidence neurodegenerative disorders of the retina [1]. In particular, under excessive light irradiation and/or dysfunction of the visual cycle, photoreceptors accumulate toxic metabolites promoting the overproduction of reactive oxygen species (ROS) [2,3]. ROS overproduction triggers an endogenous antioxidant response mediated by the increase in nuclear factor erythroid 2-related factor 2 (Nrf2) with the consequent increment in the production of antioxidant enzymes such as heme oxygenase-1 (HO-1) [4]. In some cases, the accumulation of oxidative species overcomes the protective potential of antioxidant responses thus producing an oxidative imbalance and the onset of oxidative stress [5].

Several promising treatments preventively targeting oxidative stress-driven neurodegeneration have emerged in recent years [6]. Among them, the administration of natural substances by dietary supplementation has been increasingly considered for their potential antioxidant and anti-inflammatory efficacy attained with a low invasiveness [7]. Several studies have suggested that treatment with protective compounds that inhibit oxidative stress and inflammation could reduce the amount of photoreceptor cell death

in animal models of light-induced retinal damage (LD) [8–10]. In particular, exogenous compounds belonging to carotenoid or anthocyanin families, such as lutein and cyanidin-3-glucoside (C3G), have been recognized among the most promising substances capable to prevent/counteract oxidative stress through a direct free radical scavenging effect [11,12].

Lutein is a dietary carotenoid found in several fruits and vegetables that accumulates in the human retina at the macular level [13,14]. Besides having anti-oxidative and anti-inflammatory properties [15,16], lutein is also able to filter blue light thus protect photoreceptors from light-induced damage [17]. C3G is one of the most common anthocyanins naturally found in many edible parts of plants and appears to benefit vision through its potent antioxidant and anti-inflammatory activity [18,19]. Additional efficacy of C3G depends on its capability to stimulate rhodopsin regeneration in the outer retina [20]. In response to oxidative stress, the antioxidant and anti-inflammatory properties of lutein or C3G result in improved retinal function presumably through reduced photoreceptor death [11,12].

Considering the protective potential of lutein or C3G in models of photooxidative damage, their possible administration in a coupled formulation or in the context of a multicomponent antioxidant mixture would represent an interesting treatment proposal. In this respect, the combination of different antioxidants has been proven as a promising approach for the treatment of retinal neurodegenerative diseases [6]. The use of mixed natural compounds may exert a synergistic effect because of their ability to affect multiple targets [21]. This has been particularly evident in the treatment of photoreceptor degeneration in the rd1 model of retinitis pigmentosa in which the use of individual antioxidants had no significant rescue effect, while treatment with a combination drastically reduced rod degeneration [22].

In the present study, we address the antioxidant efficacy of lutein and C3G administered either in combination or in the context of a pre-formulated multicomponent mixture in a rat model of LD (LD rats) that mimics photoreceptor loss induced by oxidative stress. This model is characterized by an increased expression of proinflammatory chemokines, which further enhance oxidative stress and activate microglia to clear dying photoreceptors [23,24]. In LD rats, we evaluated the preventive efficacy of lutein and C3G administered either alone, in combination or in a multicomponent mixture on oxidative stress, inflammation, gliotic responses, apoptotic markers and photoreceptor cell death. In addition, preventive efficacy on dysfunctional electroretinogram (ERG) was also investigated with a particular focus on the relative contributions of rod and cone photoreceptors.

2. Materials and Methods

2.1. Animals

Animals were used in compliance with the Association for Research in Vision and Ophthalmology statement for the Use of Animals in Ophthalmic and Vision Research. The present study also adheres to the European Communities Council Directive (2010/63/UE) and the Italian guidelines for animal care (DL 26/14). The experimental protocol was approved by the Commission for Animal Wellbeing of the University of Pisa (protocol no. 133/2019-PR, 14 February 2019). According to the 3Rs principles for ethical use of animals in scientific research, all efforts were made to reduce both the number of animals and their suffering. Male Sprague Dawley rats (8 weeks old) were obtained from Envigo Italy (San Pietro al Natisone, Italy). Animals were maintained in a regulated environment (23 ± 1 °C, 50 ± 5% humidity) with 12 h light/dark cycles (lights on at 08:00 a.m.) and fed with a standard diet and water ad libitum. 50 rats were used. Of them, eight were used for lutein and C3G detection in the plasma and ocular tissues (see below) and six were used as control group. The remaining 36 rats underwent to LD protocol (see below) and were divided in six experimental groups (six rats in each experimental group): LD untreated group, lutein group (+Lut), C3G group (+C3G), lutein/C3G group (+Lut/C3G), low dose mixture group (+low dose) and high dose mixture group (+high dose).

2.2. Treatments

Lutein oil from *Tagetes erecta* titrated at 20% lutein was obtained from Procemsa (Torino, Italy). Black rice extract titrated at 20% in cyanidine-3-glucoside and verbascoside from *Verbascum Thapsus* titrated at 10% were obtained from "La sorgente del Benessere" (Fiuggi, Italy). Treatments were performed by oral gavage once daily for 7 days before undergoing the LD protocol. Once a day, the compounds, either individually or combined were freshly prepared by dissolving each compound in wheat germ oil to obtain the desired final dose 5.2 mg/Kg lutein and 4.0 mg/Kg C3G administered individually or in combination. In a second set of experiments, based on different commercial formulations for humans, a nutraceutical blend containing lutein, C3G, verbascoside and zinc (hereinafter referred to as mixture) was obtained by Sooft, SpA, Montegiorgio, Italy. The mixture was administered at two dosages in mg/Kg: 1.08 lutein, 3.6 C3G; 0.36 verbascoside and 0.88 zinc (low dose) or 3.24 lutein, 10.8 C3G, 1.08 verbascoside and 2.64 zinc (high dose). These doses correspond to the recommended in humans normalized by the body surface area method for interspecies' drug dosage translation [25].

2.3. Determination of Lutein and C3G

After 7 days of lutein or C3G administration, animals were euthanized, plasma samples were collected and choroid and retina were isolated from their eyes. Pooled tissue samples of either choroid or retina were homogenized with an Ultra-Turrax homogenizer for 3 min on ice at 4 °C in methanol as extraction solvent (1 µL per mg of tissue), then subjected to a 5-min ultrasonication in a cold-water bath. A volume of 100 µL of plasma was extracted with 100 µL of methanol and sonicated. All samples were finally centrifuged for 10 min at 10,000 rpm and the supernatants were stored frozen for further analysis. Lutein and cyanidin 3-glucoside were quantitated in tissue extracts by HPLC/MS/MS using the triple quadrupole instrument Agilent 6410-A equipped with a Phenomenex Gemini C18 column at 25 °C under isocratic conditions using 10% of Buffer A (water 0.5% formic acid) and 90% of methanol at a flow rate of 0.1 mL/min. The system is equipped with a positive ionizing mode ESI interface, such that the mass transition for lutein is 551 > 429 m/z and for C3G is 449 > 287 m/z. The operational MS parameters of the instrument were: gas temperature, 350 °C; gas flow, 6 L/min; nebulizer, 20 psi; capillary, 4000 V; collision energy, 15 V; dwell-time, 200 msec; fragmentor, 135 V. Calibration curves were constructed adding each pure compound to the respective blank tissue extract, devoid of detectable amounts of lutein and C3G.

2.4. Light-Induced Damage

The protocol used here for light-induced damage is in line with that reported in previous studies in which the duration and the intensity of light exposure needed to cause morphological and functional damage to the retina have been determined [26]. In particular, rats were dark-adapted overnight and then their pupils were dilated by 1% tropicamide eye drops (Allergan S.p.A., Rome, Italy) immediately before the light exposure. Each animal was kept separately in a small cage and placed in the middle of a custom-made light box apparatus (dimensions 72 × 61 × 52 cm). Light intensity was measured through a digital illuminance meter (Dr. Meter, Ahern Ave, Union City, CA, USA). Rats were exposed to diffused 1000 lux cool-white light continuatively for 24 h emitted from six light-emitting diode bulbs. The temperature of the apparatus was controlled by a cooling aeration system based on a small air fan and maintained at (25 ± 1.5 °C). After light exposure, the rats were returned to the dim cyclic light environment. Two days later, rats underwent to electroretinography (ERG) and subsequent sacrifice by a lethal dose of sodium pentobarbital.

2.5. Electroretinography

Control and LD rats were dark-adapted overnight and anesthetized by intraperitoneal injection of 30 mg/kg sodium pentobarbital. Pupils were dilated with a topical drop of 1%

tropicamide (Allergan S.p.A.) and a heating pad was used to keep the body temperature at 37.5 °C. The electrophysiological signals were recorded through silver/silver chloride corneal ring electrodes inserted under the lower eyelids avoiding visual field obstruction. Saline solution drops were intermittently instilled to prevent ocular surface dryness and clouding. Each corneal electrode was referred to a needle electrode inserted subcutaneously at the level of the corresponding frontal region. The ground electrode was inserted subcutaneously at the tail root. The scotopic responses were evoked by a 10 cd-s/m^2 flash intensity delivered with a Ganzfeld stimulator (Biomedica Mangoni, Pisa, Italy). After the scotopic stimulation, rats were adapted to a background light intensity of 30 cd/m^2 for 10 min. Photopic, cone-mediated responses, were recorded at 3 cd-s/m^2 flash stimuli. The average of 20 consecutive responses was considered for the photopic ERG analyses. The interval between light flashes was adjusted to appropriate times that allowed response recovering (20 s for scotopic responses, 3 s for photopic responses). Responses were collected simultaneously from both eyes, amplified at 1000 gain, and filtered with a bandpass of 0.2 to 500 Hz before being digitized at 5 kHz rate with a data acquisition device (Biomedica Mangoni). All ERG waveforms were analyzed using a customized program (Biomedica Mangoni). Noise amplitude was evaluated by measuring the electrical activity in absence of light stimuli. In compliance with the International Society for Clinical Electrophysiology guidelines, the b-wave amplitude was measured from the trough of the a-wave to the peak of the b-wave or, if no a-wave was detectable, from the pre-stimulus baseline.

2.6. Immunohistochemistry

Eyeballs were immersion-fixed in 4% paraformaldehyde in 0.1 M phosphate-buffered saline (PBS) for 2 h at room temperature, transferred to 25% sucrose in 0.1 M PBS and stored at 4 °C. After being embedded in cryo-gel medium, fixed eyes were cut into 10 µm thick coronal sections and mounted onto positive charged slides. Immunostaining was performed by incubating mounted sections with mouse monoclonal anti-rhodopsin (ab5417, Abcam, Cambridge, UK; dilution 1:200), rabbit polyclonal anti-cone arrestin (AB15282, Sigma-Aldrich, St. Louis, MO, USA; dilution: 1:200), rabbit monoclonal anti-glial fibrillary acid protein (GFAP; ab207165, Abcam; dilution: 1:400) and rabbit monoclonal anti-ionized calcium-binding adapter molecule 1 (Iba-1; ab178846, Abcam; dilution: 1:200) antibodies diluted in 0.1% *v/v* Triton X-100 in 0.1 M PBS overnight at 4 °C. After being rinsed, mounted sections were incubated with appropriate goat polyclonal anti-mouse conjugated with Alexa-Fluor 488 (A-11001, Thermo Fisher Scientific, Waltham, MA, USA; dilution: 1:200), goat polyclonal anti-rabbit conjugated with Alexa-Fluor 555 (ab150078, Abcam; dilution: 1:200) or goat polyclonal anti-rabbit conjugated with Alexa-Fluor 488 (ab150077, Abcam; dilution: 1:200) secondary antibodies diluted in 0.1% *v/v* Triton X-100 in 0.1 M PBS for 2 h at room temperature. Then, retinal sections were coverslipped with Fluoroshield mounting medium containing 4′, 6-diamidino-2-phenylindole (DAPI; Abcam). The image acquisition was performed using an epifluorescence microscope (Ni-E; Nikon-Europe, Amsterdam, The Netherlands) equipped with a 20× plan apochromat objective and a digital camera (DS-Fi1 c; Nikon-Europe). Levels of the immunohistochemical signal were quantified by averaging the fluorescence intensity of five coronal sections randomly chosen from each retina (six retinas per group). Four images per section were quantified by using the analysis tool of Adobe Photoshop. Quantification was performed in a masked manner. Images were then turned into grayscale, normalized for the background and analyzed for the mean gray levels to quantify the immunofluorescence intensity for each marker. The outer nuclear layer (ONL) thickness (extending from the interface between the outer plexiform layer and the inner segment layer) was measured in five sections for each retina (six retinas per group) and four images in each section were sampled.

2.7. Western Blot

Eyes were enucleated, retinas were dissected and stored at −80 °C. Samples were lysed with RIPA lysis buffer (Santa Cruz Biotechnology, Dallas, TX, USA) supplemented

with proteinase and phosphatase inhibitor cocktails (Roche Applied Science, Indianapolis, IN, USA). Protein content was quantified by Micro BCA Protein Assay (Thermo Fisher Scientific, Waltham, MA, USA). Samples containing 30 µg of proteins were subjected to SDS-PAGE (4–20%; Bio-Rad Laboratories, Inc, Hercules, CA, USA) and gels were transblotted onto nitrocellulose membranes (Bio-Rad Laboratories, Inc). After a blocking phase with either 5% skim-milk or 4% bovine serum albumin (BSA), membranes were incubated overnight at 4 °C with the primary antibodies listed in Table 1. Then, blots were incubated for 2 h at room temperature with appropriate HRP-conjugated secondary antibodies (rabbit anti-goat, sc-2768, Santa Cruz Biotechnology; rabbit anti-mouse, A9044, Sigma-Aldrich; goat anti-rabbit, 170–6515, Bio-Rad Laboratories, Inc; all at 1:5000). Blots were developed by the Clarity Western enhanced chemiluminescence substrate (Bio-Rad Laboratories, Inc). Blot images were acquired with the ChemiDoc XRS+ (Bio-Rad Laboratories, Inc). The optical density (OD) of the target bands (Image Lab 3.0 software; Bio-Rad Laboratories, Inc) were normalized for the relative OD of β-actin as a loading control or nuclear factor kappa-light-chain-enhancer of activated B cells (NF-κB) p65 as appropriate. Although their reactivity with rat antigens is not reported, cleaved caspase 3, Nfr2 and NF-kB antibodies are apparently selective also for rats as reported in the operating instructions of the customer. This is also in line with previous studies in which these antibodies were used in rat samples [27,28].

Table 1. Primary antibodies list used in the Western blot analysis.

Antibody	Dilution	Source	Catalogue
Rabbit monoclonal anti-Bax	1:500	Abcam	ab182733
Rabbit polyclonal anti-Bcl-2	1:500	Abcam	ab194583
Rabbit polyclonal anti-cleaved caspase 3	1:500	Abcam	ab2302
Rabbit monoclonal anti-Nrf2	1:300	Abcam	ab62352
Rabbit polyclonal anti-HO-1	1:500	Abcam	ab13243
Rabbit polyclonal anti-pNF-kB p65 (Ser 536)	1:100	Santa Cruz Biotechnology	sc-33020
Rabbit polyclonal anti-NF-kB p65	1:1000	Abcam	ab16502
Mouse monoclonal anti-IL-6	1:100	Santa Cruz Biotechnology	sc-57315
Goat polyclonal anti-IL-10	1:100	Santa Cruz Biotechnology	sc-1783
Mouse monoclonal anti-β-actin	1:2500	Sigma-Aldrich	A2228

2.8. Statistical Analysis

Statistical analyses were performed using the Graph Pad Prism 8.0.2 software (GraphPad Software, Inc, San Diego, CA, USA). Differences between groups were tested using two-tailed *t*-test or one-way ANOVA followed by Newman–Keuls multiple comparison post hoc test. Differences with $p < 0.05$ were considered significant. All data are expressed as mean ± SD of the indicated *n* values.

3. Results

3.1. Plasma, Choroid and Retinal Levels of Lutein and C3G

After 7 days of administration of either lutein (5.2 mg/Kg) or C3G (4.0 mg/Kg), their levels were measured in plasma, choroid and retina in order to establish whether both compounds reached the choroidal vascular plexus to be conveyed to the retina. As shown in Figure 1A, plasma levels of lutein (11.8 ± 0.5 ng/mL) were lower than those of C3G (15.56 ± 2.9 ng/mL; $p = 0.044$). Lutein concentration was higher in the retina than in the choroid (15.9 ± 3.1 vs. 11.7 ± 1.1 ng/mg), while the opposite occurred for C3G (6.4 ± 1.4 vs. 9.47 ± 2.1 ng/mg). Choroid levels of lutein and C3G were similar, while retinal levels of lutein were higher than those of C3G ($p = 0.0017$; Figure 1B).

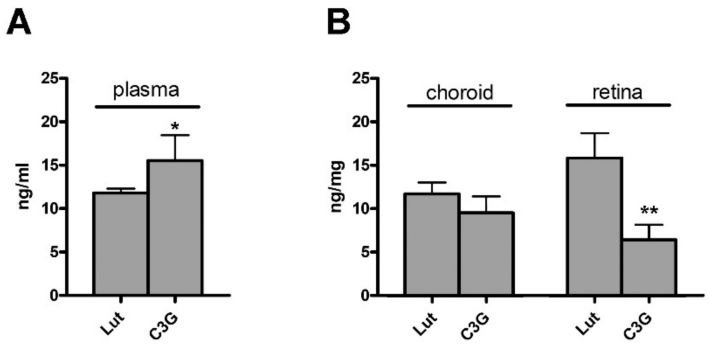

Figure 1. Plasma, choroid and retina concentration of lutein and C3G after 1 week of administration. (**A**) Mean total lutein and C3G concentration measured in plasma. (**B**) Mean total lutein and C3G concentration measured in choroid and retina. Data are expressed as mean ± SD (n = 4). Differences between groups were tested for statistical significance using two-tailed t-test. * $p < 0.05$; ** $p < 0.01$ versus lutein.

3.2. Combined Efficacy of Lutein and C3G on Oxidative Stress

As shown in Figure 2, in untreated LD rats, protein levels of Nrf2 were upregulated in response to light stimulation (control 1.0 ± 0.075; LD 2.4 ± 0.24; $p < 0.0001$). As a consequence of Nrf2 upregulation, HO-1 was increased, as compared to control rats (control 1.0 ± 0.07, LD 2.12 ± 0.24; $p < 0.0001$). Compared to untreated LD rats, pretreatment with either lutein or C3G resulted in a 40% decrease in the protein levels of Nrf2 (+Lut 1.63 ± 0.16, $p < 0.0001$; +C3G 1.62 ± 0.098, $p < 0.0001$) and HO-1 (+Lut 1.56 ± 0.2, $p = 0.0070$; +C3G 1.46 ± 0.24, $p = 0.0017$), which still remained about 50 % higher than in controls (+Lut $p = 0.0059$; +C3G $p = 0.025$). The pretreatment with lutein in combination with C3G resulted in a much stronger decrease in Nrf2 (+Lut/C3G 1.06 ± 0.14, $p < 0.0001$) and HO-1 levels (+Lut/C3G 1.07 ± 0.13, $p < 0.0001$) which returned to levels similar to those measured in control rats.

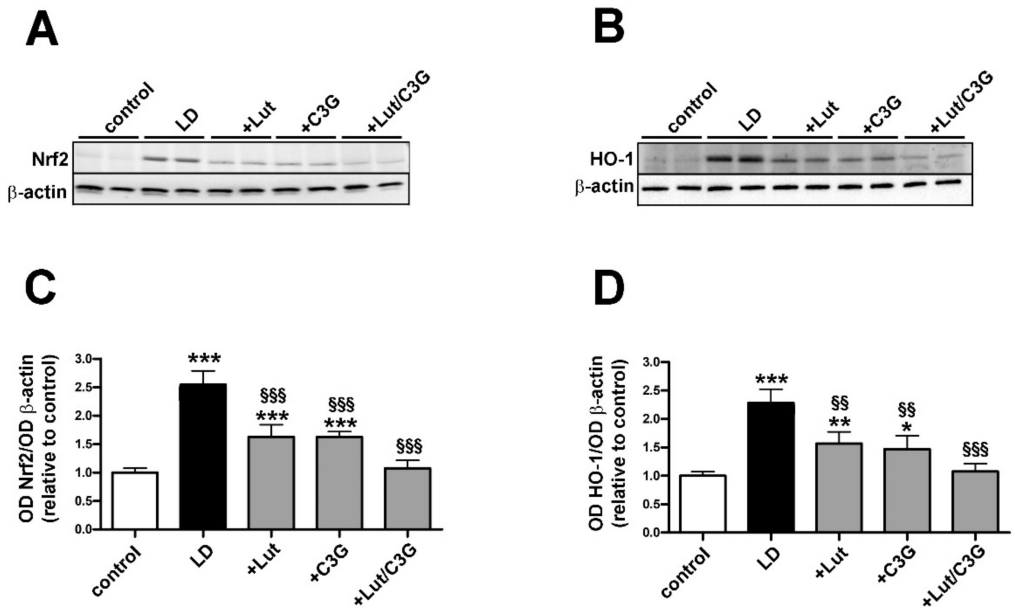

Figure 2. Individual and combined effects of lutein and C3G on oxidative stress markers. (**A**,**B**) Representative Western blots from retinal homogenates of control and LD rats untreated or pretreated with either lutein, C3G or their combination. (**C**,**D**) Densitometric analysis of nuclear factor erythroid 2-related factor 2 (Nrf2) and heme oxygenase-1 (HO-1) immunoblots. The expression of Nrf2 and HO-1 was normalized to the loading control β-actin. Data are expressed as mean ± SD (n = 6). Differences

between groups were tested for statistical significance using one-way ANOVA followed by the Newman–Keuls multiple comparison post-hoc test. * $p < 0.05$; ** $p < 0.01$; *** $p < 0.001$ versus control; §§ $p < 0.01$; §§§ $p < 0.001$ versus LD.

3.3. Combined Efficacy of Lutein and C3G on Inflammatory Response

As shown in Figure 3, LD rats displayed upregulated levels of pro-inflammatory markers including the phosphorylated form of the nuclear factor kappa-light-chain-enhancer of activated B cells (NF-kB; LD 1.76 ± 0.21, $p < 0.0001$) and interleukin-6 (IL-6; LD 1.96 ± 0.16, $p < 0.0001$), while the anti-inflammatory cytokine IL-10 was downregulated (LD 0.55 ± 0.06, $p < 0.0001$). Pretreatment with either lutein or C3G reduced by about 25% both phosphorylated NF-kB (+Lut 1.39 ± 0.09, $p = 0.0106$; +C3G 1.33 ± 0.15, $p = 0.0029$) and IL-6 (+Lut 1.47 ± 0.17, $p = 0.0014$, +C3G 1.50 ± 0.08, $p = 0.0024$) in concomitance with a 60% increase in IL-10 levels (+Lut 0.79 ± 0.06, $p = 0.0034$; +C3G 0.80 ± 0.05, $p = 0.0020$) as compared to untreated LD rats. After pretreatment with lutein and C3G, the levels of pro-inflammatory NF-kB (+Lut/C3G 0.99 ± 0.08, $p = 0.98$) and IL-6 (+Lut/C3G 1.04 ± 0.14, $p = 0.97$) and anti-inflammatory IL-10 (+Lut/C3G 1.03 ± 0.11, $p = 0.98$) did not differ from those measured in controls.

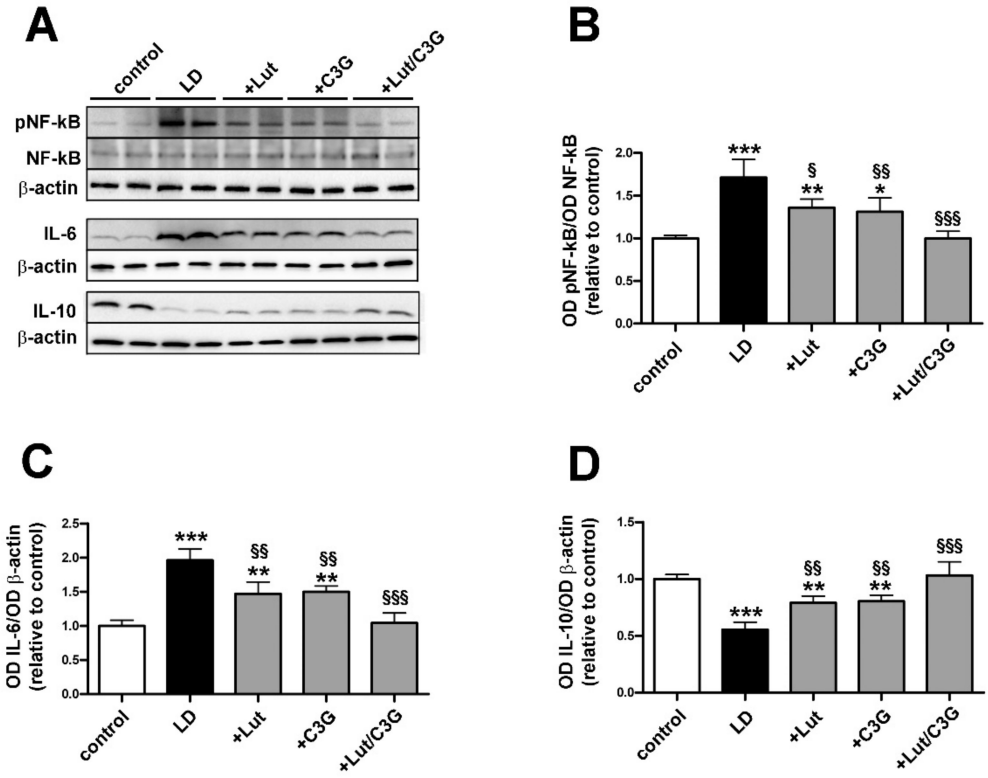

Figure 3. Individual and combined effects of lutein and C3G on inflammatory markers. (**A**) Representative Western blots. (**B**–**D**) Densitometric analysis of the phosphorylation levels of nuclear factor kappa-light-chain-enhancer of activated B cells (NF-kB), interleukin (IL)-6 and IL-10. The expression of pNF-kB was normalized to the level of NF-kB, while the expression of IL-6 and IL-10 was relative to the loading control β-actin. Data are expressed as mean ± SD ($n = 6$). Differences between groups were tested for statistical significance using one-way ANOVA followed by the Newman–Keuls multiple comparison post hoc test. * $p < 0.05$; ** $p < 0.01$; *** $p < 0.001$ versus control; § $p < 0.05$; §§ $p < 0.01$; §§§ $p < 0.001$ versus LD.

3.4. Combined Efficacy of Lutein and C3G on Gliosis and Microglial Activation

Oxidative stress and inflammation promote Müller cell gliosis as characterized by GFAP upregulation. In addition, the activation of microglia, as identified by Iba-1 upregu-

lation, further contributes to the inflammatory response. As shown in Figure 4A, in control retinas, GFAP immunoreactivity was confined to the ganglion cell layer (GCL) while in untreated LD rats, Müller cells showed extensive GFAP immunolabeling along their processes spreading across retinal layers. GFAP-positive processes were less evident, but still detectable in retinas of lutein- or C3G-treated rats. On the contrary, in retinas of rats pretreated with lutein and C3G in combination, GFAP immunoreactivity in vertical processes was undetectable resulting confined to the GCL, similarly to controls. Quantitative analysis of fluorescence intensity showed that in untreated LD rats, GFAP immunoreactivity was increased as compared to controls (LD; 9.70 ± 1.12, $p < 0.0001$). Individual administration of lutein or C3G reduced GFAP intensity (+Lut; 4.88 ± 0.45, $p < 0.0001$; +C3G; 4.68 ± 1.79, $p < 0.0001$) with no difference among single compounds. In contrast, the pretreatment with their combination resulted in a further decrease of GFAP immunofluorescence that became 85% lower than in untreated LD rats (+Lut/C3G; 1.13 ± 0.44, $p < 0.0001$) with no statistical difference from control rats ($p = 0.98$; Figure 4B). As shown in Figure 4A, Iba-1 immunolabeling was weakly represented in the inner retinal layers of control retinas, with arborizing processes likely associated to inactive microglia. In contrast, Iba1 immunoreactivity was more prominent in the retina of untreated LD rats with enlarged amoeboid-shaped immunopositive cells localized in INL, ONL and subretinal space. Pretreatment with either lutein or C3G partially prevented microglial activation as determined by decreased Iba1-immunolabeled cells, while no evidence of activated microglia was observed when the compounds were given in combination. As shown by the quantitative analysis of fluorescence intensity, in untreated LD rats, Iba-1 was increased compared to controls (LD; 6.90 ± 1.96, $p < 0.0001$). Iba1 immunofluorescence was reduced by about 47% after the administration of either lutein or C3G compared to LD rats (+Lut 3.76 ± 0.24, $p = 0.0001$; +C3G 3.50 ± 0.67, $p < 0.0001$), while their combination preserved Iba1 immunoreactivity to control levels ($p = 0.95$; Figure 4C).

3.5. Combined Efficacy of Lutein and C3G on Photoreceptor Degeneration

Representive images of retinal sections immunolabeled with rhodopsin or cone arrestin and counterstained with DAPI are shown in Figure 5A. Retinas of untreated LD rats showed a prominent decrease ONL thickness compared to control (LD 28.8 ± 3.03 μm, $p < 0.0001$; Figure 5B), as a consequence of photoreceptor loss. Photoreceptors were partially protected following individual pretreatment with lutein or C3G compared to LD (+Lut 40.80 ± 4.02 μm, $p = 0.027$; +C3G 42.40 ± 7.3 μm, $p = 0.010$). No evidence of photoreceptor loss was observed after combined pretreatment (+Lut/C3G 52.00 ± 5.38 μm, $p = 0.96$). Untreated LD rats showed a similar residual expression of rhodopsin (LD 0.26 ± 0.02, $p < 0.0001$) and cone arrestin (LD 0.25 ± 0.02 $p < 0.0001$) compared to control. After individual treatments with lutein or C3G, the immunofluorescence levels of both rhodopsin (+Lut 0.66 ± 0.06, $p = 0.0016$; +C3G 0.62 ± 0.13, $p = 0.0044$) and cone arrestin (+Lut 0.69 ± 0.11, $p < 0.0001$; +C3G 0.71 ± 0.13, $p < 0.0001$) were partially preserved compared to those in LD rats. In contrast, retinas of light-exposed rats treated with lutein and C3G in combination displayed a well-organized and abundant expression of rhodopsin (+Lut/C3G 0.91 ± 0.24, $p = 0.84$) and cone arrestin (+Lut/C3G 0.89 ± 0.15, $p = 0.55$) at levels similar to control (Figure 5C,D).

We investigated whether the dietary combination of lutein and C3G might affect the activation of selected components in the apoptotic pathway that is known to be dysregulated in LD rats [29]. A major checkpoint in the apoptotic pathway is the ratio of pro-apoptotic (Bax) to anti-apoptotic (Bcl-2), playing a key role in the apoptotic pathway. As shown by the representative blots in Figure 5E and the densitometric analysis in Figure 5F,G the Bax/Bcl-2 ratio was increased in untreated LD rats compared to control (LD 2.23 ± 0.21, $p < 0.0001$) with upregulated levels of the pro-apoptotic Bax and stable levels of the anti-apoptotic Bcl-2 (Figure 5F). Downstream to the increased Bax/Bcl-2 ratio, levels of caspase 3 increased in LD rats compared to control (LD 1.96 ± 0.24, $p < 0.0001$; Figure 5G). Treatment with lutein or C3G attenuated the increase in Bax/Bcl-2 ratio (+Lut 1.68 ± 0.22, $p = 0.0048$; +C3G

0.58 ± 0.20, $p = 0.0010$) and the caspase level (+Lut 1.56 ± 0.12, $p = 0.048$; +C3G 1.47 ± 0.13, $p = 0.018$) compared to LD untreated rats. The combined treatment further reduced the levels of Bax/Bcl-2 ratio (+Lut/C3G 0.90 ± 0.12, $p < 0.0001$) and caspase 3 (+Lut/C3G 1.06 ± 0.21, $p < 0.0001$) compared to LD rats, reaching values that were comparable to those measured in controls.

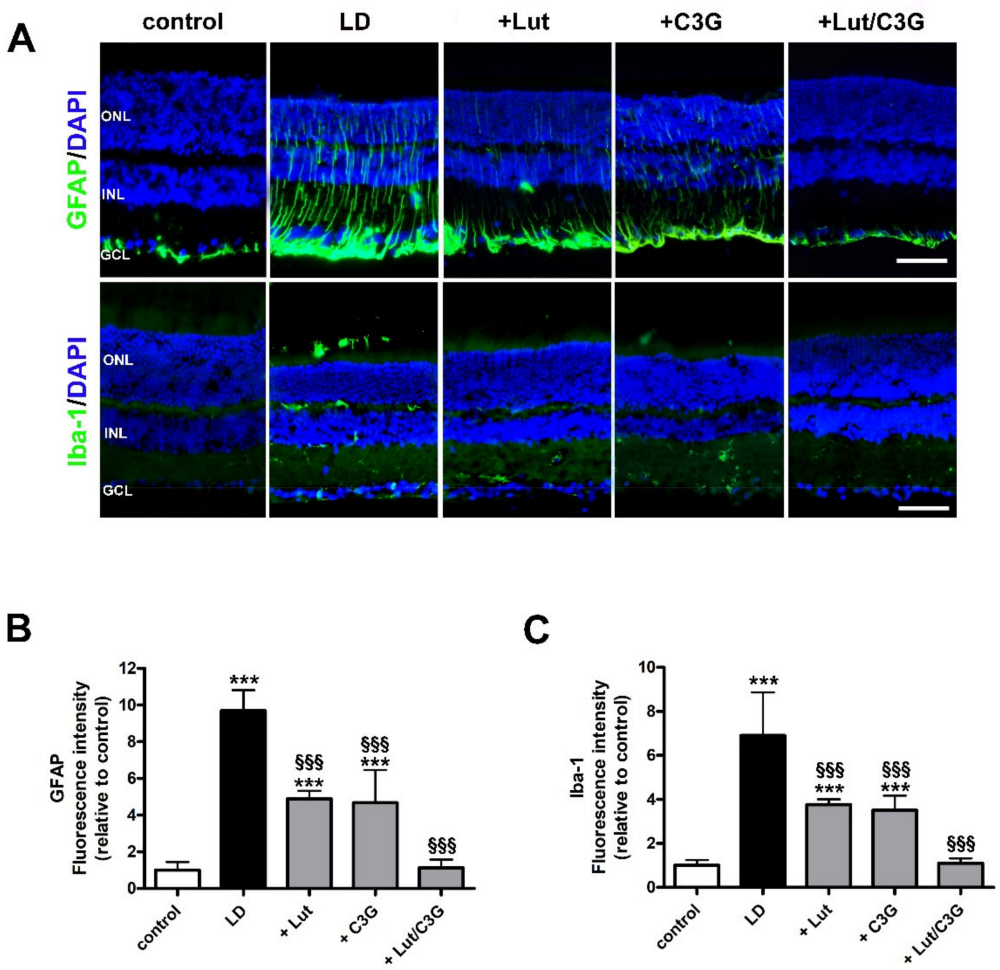

Figure 4. Individual and combined effects of lutein and C3G on gliosis and microglial activation. (**A**) Representative images of retinal sections from control and LD rats untreated or pretreated with either lutein, C3G or their combination immunolabeled for glial fibrillary acidic protein (GFAP; green) and ionized calcium binding adaptor molecule 1 (Iba-1; green). Sections are counterstained with DAPI to highlight retinal nuclear layers. (**B**,**C**) Quantitative analysis of fluorescence intensity. GCL, ganglion cell layer; INL, inner nuclear layer; ONL, outer nuclear layer. Scale bar, 50 μm ($n = 6$ retinas per group). Data are expressed as mean ± SD. Differences between groups were tested for statistical significance using one-way ANOVA followed by the Newman–Keuls multiple comparison post hoc test. *** $p < 0.001$ versus control; §§§ $p < 0.001$ versus LD.

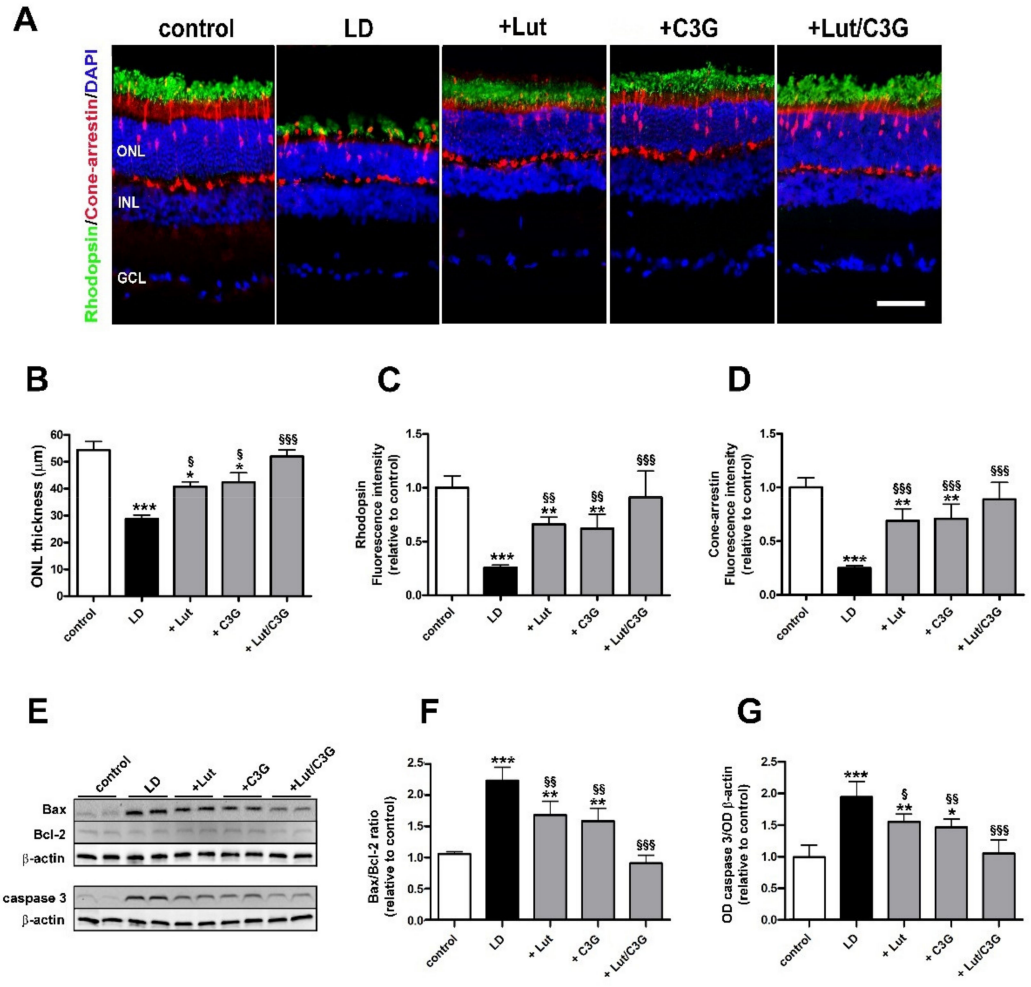

Figure 5. Individual and combined effects of lutein and C3G on photoreceptor degeneration. (**A**) Representative images of retinal sections from control and LD rats untreated or pretreated with either lutein, C3G or their combination immunolabeled for rhodopsin (green) and cone-arrestin (red). Retinal nuclear layers are highlighted by the DAPI counterstaining. (**B**) Quantitative analysis of ONL thickness. (**C**,**D**) Quantitative analysis of rhodopsin and cone-arrestin immunofluorescence intensity. GCL, ganglion cell layer; INL, inner nuclear layer; ONL, outer nuclear layer. Scale bar, 50 µm ($n = 6$ retinas per group). (**E**) Representative Western blots of Bax, Bcl-2 and active caspase 3 from each experimental group. (**F**,**G**) Densitometric analysis of the Bax/Bcl-2 ratio and active caspase 3. The expression of active caspase 3 was relative to the loading control β-actin. Data are expressed as mean ± SD. Differences between groups were tested for statistical significance using one-way ANOVA followed by the Newman-Keuls multiple comparison post-hoc test. * $p < 0.05$; ** $p < 0.01$; *** $p < 0.001$ versus control; § $p < 0.05$; §§ $p < 0.01$; §§§ $p < 0.001$ versus LD.

3.6. Combined Efficacy of Lutein and C3G on Retinal Function

In additional experiments aimed at evaluating whether protective efficacy of dietary combination on photoreceptor loss were accompanied by ameliorated visual function, LD rats treated with lutein and C3G either alone or in combination were subjected to comprehensive ERG analyses to assess outer and inner retinal function. Under scotopic conditions, the a-wave reflects the activity of rods while the b-wave reflects the activity of bipolar and Müller cells. As shown by scotopic ERG responses in Figure 6A and quantitative analysis of both a- and b-wave amplitudes in Figure 6B,C, in untreated LD rats, displayed a reduced amplitude of a-wave (LD 61.00 ± 15.46, $p < 0.0001$) and b-wave (LD 220.60 ± 25.26, $p < 0.0001$) compared to those measured in controls (control a-wave 248.4 ± 17.95 µV; b-wave 588.20 ± 17.60 µV). The pretreatment with either lutein or C3G

administered alone partially preserved the a-wave (+Lut 104.8 ± 17.55 µV, $p = 0.039$; +C3G 120.6 ± 17.42 µV, $p = 0.0033$) and b-wave amplitudes (+Lut 319.4 ± 26.08 µV, $p = 0.0008$; +C3G 357.00 ± 24.36 µV, $p < 0.0001$) compared with untreated LD rats. Lutein in combination with C3G completely preserved the a-wave (+Lut/C3G 214.0 ± 36.01 µV, $p = 0.14$) and b-wave amplitudes (+Lut/C3G 534.40 ± 54.46 µV, $p = 0.10$), resulting in amplitudes similar to those of controls.

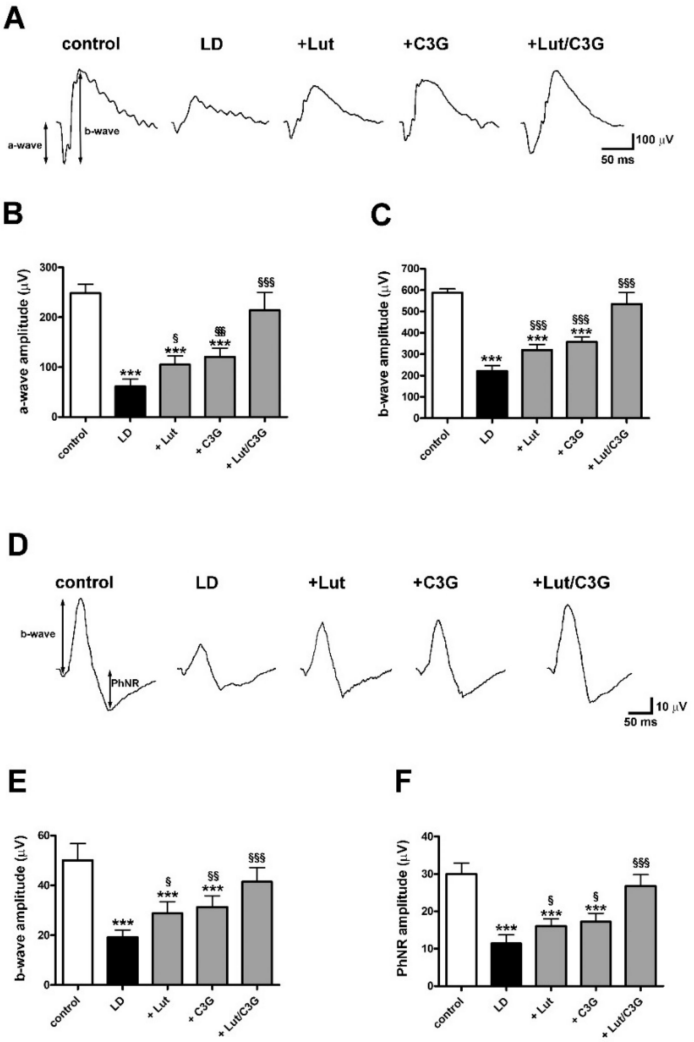

Figure 6. Individual and combined effects of lutein and C3G on scotopic and photopic full field electroretinogram (ERG). (**A**) Representative ERG waveforms showing scotopic a- and b-waves from control and LD rats untreated or pretreated with either lutein, C3G or their combination. (**B**,**C**) Quantitative analysis of scotopic a- and b-wave amplitudes. (**D**) Representative ERG waveforms showing photopic b-waves and photopic negative response (PhNR). (**E**,**F**) Quantitative analysis of photopic b-wave and PhNR amplitudes. Data are expressed as mean ± SD. Differences between groups were tested for statistical significance using one-way ANOVA followed by the Newman–Keuls multiple comparison post hoc test ($n = 6$ animals per group). *** $p < 0.001$ versus control; § $p < 0.05$; §§ $p < 0.01$; §§§ $p < 0.001$ versus LD.

Under photopic conditions, additional measurements included the b-wave, which indirectly reflects the cone activity since the a-wave cannot be measured reliably, and the PhNR, a negative-going wave following the b-wave that originates in the inner retinal layer and is correlated with RGC activity [30]. As shown by photopic ERG responses in Figure 6D and quantitative analysis of b-wave and PhNR amplitudes in Figure 6E,F,

in untreated LD rats, the photopic b-wave (LD 19.20 ± 2.95 μV, $p < 0.0001$) and the PhNR (LD 11.40 ± 2.30 μV, $p < 0.0001$) were both reduced in amplitude compared to control (control b-wave 50.00 ± 6.78 μV; PhNR 30.00 ± 2.91 μV). Lutein or C3G administered alone partially prevented the photopic ERG dysfunction, with both b-wave (+Lut 28.80 ± 4.60 μV, $p = 0.047$; +C3G 31.40 ± 4.45 μV, $p = 0.0089$) and PhNR amplitudes (+Lut 16.00 ± 2.00 μV, $p = 0.044$; +C3G 17.20 ± 2.28 μV, $p = 0.013$) higher than those in untreated LD rats. The lutein and C3G combination completely preserved the photopic ERG responses in both b-wave (+Lut/C3G 41.40 ± 5.77 μV, $p = 0.094$) and PhNR amplitudes (+Lut/C3G 26.80 ± 3.03 μV, $p = 0.30$) to control levels.

3.7. Efficacy of a Pre-Formulated Mixture on Light-Induced Retinal Damage

After having established the efficacy of the combined treatment of lutein and C3G, we investigated how their effects could be modulated in a more sophisticated blend of functional nutrients. In particular, the efficacy of a mixture including lutein and C3G together with verbascoside and zinc was evaluated at two different doses. As shown in Figure 7A, rats pretreated with a low dose of the mixture showed a significant reduction in upregulated levels of Nrf2 (+Mixture low 1.34 ± 0.13, $p = 0.010$) and HO-1 (+Mixture low 1.31 ± 0.08, $p = 0.0048$) as compared to untreated LD rats. After pretreatment with a high dose of the mixture, the levels of Nrf2 (+Mixture high 1.05 ± 0.13, $p = 0.95$) and HO-1 (+Mixture high 0.86 ± 0.04, $p = 0.75$) did not differ from those measured in controls.

Representative images of retinal sections immunolabeled with GFAP and Iba-1 are shown in Figure 7B, while the quantitative analysis of immunostaining is shown in Figure 7C–E. After low dose of the mixture, the ONL thickness was greater than in untreated LD rats (+Mixture low 38.20 ± 2.58 μm, $p = 0.0065$), while the high dose of the mixture completely prevented the light-induced ONL decrease as compared to control (+Mixture high 52.60 ± 5.59 μm, $p = 0.42$; Figure 7C). As shown in Figure 7D,E, the pretreatment at low dose partially prevented the increase in GFAP (+Mixture low 2.28 ± 0.28, $p = 0.0023$) and Iba-1 immunostaining (+Mixture low 2.71 ± 0.32, $p = 0.0071$) compared to untreated LD rats. After high dose pretreatment, GFAP (+Mixture high 1.35 ± 0.29, $p = 0.47$) and Iba-1 immunostaining (+Mixture high 1.36 ± 0.22, $p = 0.45$) was not different from control rats.

Figure 8 shows how light exposure led to a decrease in the amplitude of both scotopic a-wave (LD 85.20 ± 19.23 μV, $p < 0.0001$) and b-wave (LD 216.70 ± 53.22 μV, $p < 0.0001$), and photopic b-wave (LD 18.00 ± 4.47 μV, $p < 0.0001$) and PhNR (LD 14.00 ± 2.46 μV, $p < 0.0001$) as compared to control. The mixture at low dose attenuated the reduction in the amplitude of scotopic (+Mixture low a wave 139.2 ± 23.93 μV, $p = 0.046$; b-wave 334.40 ± 50.54 μV, $p = 0.048$) and photopic waves (+Mixture low b-wave 29.00 ± 3.35 μV, $p = 0.012$; PhNR 19.00 ± 2.01 μV $p = 0.024$) as compared to LD rats. The pretreatment with the mixture at high dose prevented such amplitude reduction maintaining both scotopic (+Mixture high a wave 189.6 ± 30.63 μV, $p = 0.20$; b-wave 527.90 ± 70.66 μV, $p = 0.025$) and photopic ERG responses (+Mixture high b-wave 38.00 ± 4.25 μV, $p = 0.14$; PhNR 23.50 ± 2.01 μV, $p = 0.25$) to control levels suggesting preservation of photoreceptors from death.

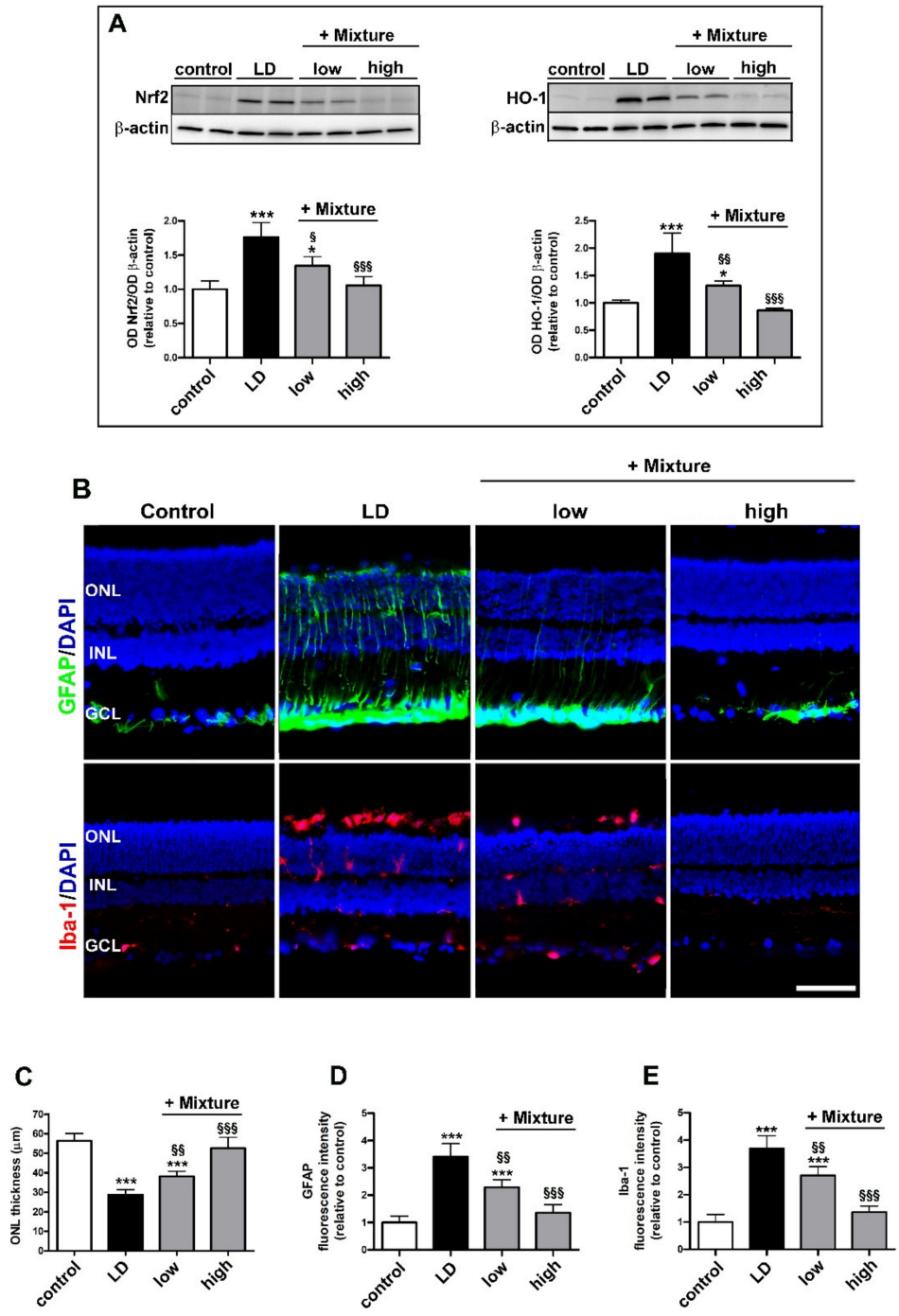

Figure 7. Effects of pre-formulated mixture on oxidative markers, gliosis and microglial activation. (**A**) Western blots and densitometric analysis of Nrf2 and HO-1 in retinal homogenates of control and LD rats untreated or pretreated with the mixture at low or high dosage. (**B**) Representative images of retinal sections immunolabeled for GFAP (green) and Iba-1 (red) and counterstained with DAPI (blue). (**C**) Quantitative analysis of ONL thickness. (**D**,**E**) Quantitative analysis of GFAP and Iba1 immunofluorescence intensity. Scale bar, 50 μm (n = 6 retinas per group). Data are expressed as mean ± SD. Differences between groups were tested for statistical significance using one-way ANOVA followed by the Newman–Keuls multiple comparison post hoc test. * $p < 0.05$; *** $p < 0.001$ versus control; § $p < 0.05$; §§ $p < 0.01$; §§§ $p < 0.001$ versus LD.

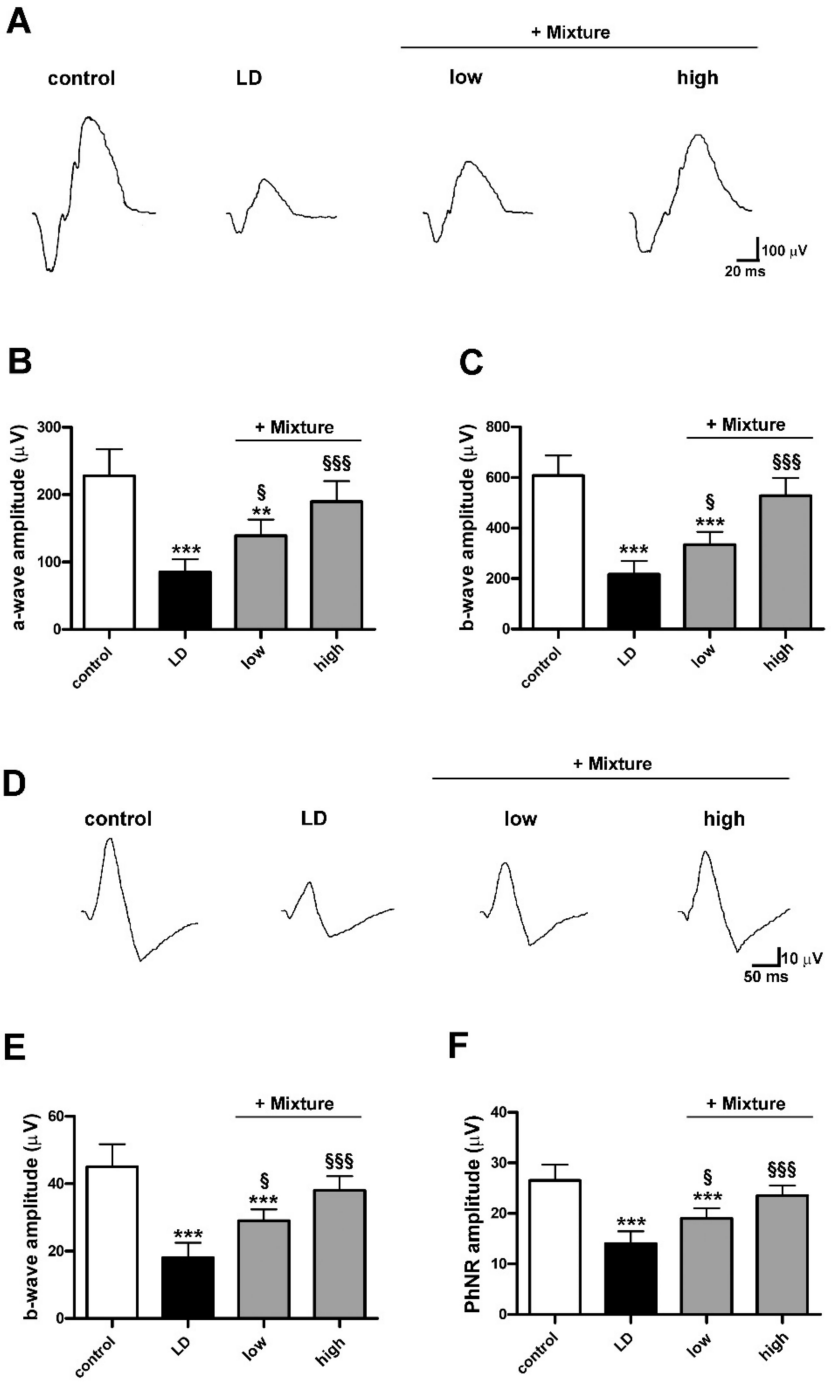

Figure 8. Effects of pre-formulated mixture on scotopic and photopic full field electroretinogram (ERG). (**A**) Representative ERG waveforms showing scotopic a- and b-waves from control and LD rats untreated or pretreated with the mixture at low and high dosage. (**B**,**C**) Quantitative analysis of scotopic a- and b-wave amplitudes. (**D**) Representative ERG waveforms showing photopic b-waves with photopic negative response (PhNR). (**E**,**F**) Quantitative analysis of photopic b-wave and PhNR amplitudes. Data are expressed as mean ± SD. Differences between groups were tested for statistical significance using one-way ANOVA followed by the Newman–Keuls multiple comparison post hoc test (n = 6 animals per group). ** $p < 0.01$; *** $p < 0.001$ versus control; § $p < 0.05$; §§§ $p < 0.001$ versus LD.

4. Discussion

Food supplements or dietary interventions including antioxidant compounds are used frequently to prevent retinal diseases [6]. In experimental models of light induced retinal damage, there is indication that diet and dietary supplements with lutein and C3G can be beneficially used against light-associated oxidative stress and inflammatory processes [4,31]. In patients, dietary administration of antioxidants has been shown to reduce the incidence of oxidative stress-related eye diseases [32], although several studies provided conflicting results [33,34]. However, there is little information about whether the combination of lutein and C3G has superior efficacy over a single free supplementation. How their combined efficacy would be modulated in a more sophisticated blend of functional nutrients including additional antioxidant compounds has also been investigated.

4.1. Light-Induced Retinal Damage

The eye has evolved several mechanisms to protect the retina from light-induced damage. For instance, macular pigments including lutein confer additional protection to the retina through their ability to absorb high-energy blue light. However, prolonged exposures to high light intensities will cause injury to the eye, a feature that is mimicked in the model of light-induced retinal damage. Exposure to very intense light irradiation for an extended period may result in chemical changes in retinal cells thus ultimately leading to cell death [35]. The importance of light-induced phototoxicity has gained attention in the last years, considering that long-term exposure to video displays and light-emitting diodes may trigger morphological and functional alterations of the retina thus contributing to the increase in the incidence of retinal diseases [36].

The rat model of light damage is characterized by the activation of the Nrf2 antioxidant pathway, as indicated by the present results and previous findings [37,38]. This is a homeostatic response aimed at counteracting the light-induced overproduction of ROS in the retina. However, in pathological conditions, ROS production overcomes the endogenous antioxidant capacity, thus promoting the onset of oxidative stress that, in turn, triggers inflammation, gliosis and microglia activation culminating in the apoptotic death of retinal cells [39]. The activation of the apoptotic cascade is paralleled by photoreceptor loss as determined by a drastic decrease in ONL thickness. As a consequence of photoreceptor loss, both scotopic and photopic ERG responses are reduced in amplitude thus indicating a drastic impairment of the visual function, in line with previous reports [26].

4.2. Preventive Efficacy of Antioxidant Compounds

With a global increasing rate of light-induced degenerative diseases of the retina, it is important to develop preventive methods to mitigate light-related manifestations and curb the progression of retinal damage. In this respect, dietary regimens rich in antioxidant compounds including lutein or C3G have been reported to actively counteract light-induced retinal damages. In particular, lutein plays a crucial role acting not only as an important regulator of redox balance, but also as a structural molecule in cell membranes and short wavelength light filter in retinal tissues [40]. Similarly, C3G has been established to act as a stabilizer of free radicals by its hydrogen donating ability and also to promote the regeneration and synthesis of rhodopsin [41]. As shown by the present findings, after dietary administration, lutein and C3G are detected in the plasma and ocular tissues in line with previous results [42,43]. The evaluation of lutein and C3G in ocular tissues has been preliminary to the analysis of their efficacy since it allowed to determine whether each compound effectively reaches the ocular tissues where their efficacy to prevent light-induced damage has been tested. Several studies suggest that high blood levels of lutein or C3G are associated with reduced risk of ocular diseases suggesting the beneficial effects of their dietary intake [44,45]. Since lutein and C3G cannot be synthesized by the human body, their plasma levels can only be ensured through food intake or dietary supplements. They are delivered to the retina by the choroidal vascular plexus. In the retina, we found lutein levels higher than those of C3G although their choroidal levels were similar. Reduced levels

of C3G in the retina can be attributed to its degradation leading to the formation of the corresponding phenolic acids [46]. Lutein and C3G may exert their antioxidant activity acting as both radical scavengers and antioxidant defense inducers via Nrf2 activation [47,48]. However, how antioxidants preferentially act as radical scavengers or Nrf2 inducers is yet to be elucidated. In our experimental conditions, the LD-triggered increase in Nrf2 and HO-1 levels, demonstrating the activation of the antioxidant system, was almost prevented by the pre-treatment with Lutein and C3G. This is likely to derive from the accumulation of both compounds in the retina following their 7-days preventive administration which allowed to buffer the LD-driven increase in free radical formation and decreasing the upstream ROS-driven activation of the Nrf2-HO-1 pathway. However, the contribution of a preventive activation of the Nrf2 antioxidant pathway further preventing the LD-driven ROS accumulation cannot be excluded.

Reduced activity of Nrf2/HO-1 correlates with the inhibition of inflammatory processes, as demonstrated by the decreased phosphorylation of NF-kB and the partial recovery of cytokine levels. The antioxidant and the anti-inflammatory properties of lutein or C3G result in effective but incomplete preservation of both rods and cones that is reflected in ameliorated visual function, in line with previous findings [4,49]. Lutein or C3G, when administered alone, similarly ameliorate the pathological signs of retinal damage. In contrast, their combined administration provides synergistic efficacy to protect the retina from light damage. In particular, lutein and C3G exert a multitarget role by hampering major retinal events activated by light, as demonstrated by the general reduction in upregulated levels of oxidative and pro-inflammatory markers associated with neuroprotective effects and recovered visual function. In particular, the finding that the combined administration of lutein and C3G preserves scotopic and photopic ERG is indicative of its neuroprotective efficacy on both photoreceptor and post-receptor cells, including bipolar cells and retinal ganglion cells [50].

Multicomponent formulae of antioxidant compounds, which are available without a prescription, are widely used by many people as preventive therapy for eye diseases. Several studies support the protective role of nutraceutical mixtures in ocular health although their benefits as putative therapeutical strategies are still limited and sometimes controversial. Different mixtures of antioxidant nutrients have been proven to protect the retina from light, although superior efficacy of a combination over a single free supplementation is not obvious [51]. In fact, the total antioxidant capacity of a complex mixture is likely to depend on either the antagonistic or synergistic interaction among the different compounds. In particular, the antagonism occurs when the sum of the effects is less than the mathematical sum that would be predicted from individual components [52]. On the other hand, the combination of antioxidant compounds with complementary action may play an important role to optimize their action. For instance, in the rd10 mouse model of retinitis pigmentosa, combined antioxidant compounds positively interact with each other to ameliorate retinal functionality and morphology [53]. In this respect, our focus on photoreceptors as the main targets of light damage and Müller cells as targets of inflammation with a prominent expression of GFAP and Iba-1 by microglial cells, does not exclude the involvement of additional cell types. In particular, both Müller cells and ON-center bipolar cells are involved in the generation of the b-wave (ON-center bipolar hypothesis) and they are affected by light exposure as a consequence of photoreceptor damage [54]. Here, we provide the first evidence that a mix of antioxidant compounds including zinc and verbascoside in addition to lutein and C3G, effectively protects photoreceptor cells against light-induced damage thus preventing some secondary changes that are likely to be induced in the inner retina, as demonstrated by restored ERG. In this respect, the extracellular currents that generate the b-wave either originate directly in ON-bipolar cells or reflect potassium-induced changes in the membrane potential of Müller cells enveloping them. In addition, the b-wave is also affected by light-induced activity in third-order retinal neurons (amacrine cells and RGCs) as demonstrated by the PhNR, a negative-going wave

following the b-wave that originates in the inner retinal layer in response to photopic conditions and is correlated with RGC activity [30].

In addition to the protective efficacy of lutein in combination with C3G, zinc and verbascoside have been reported individually as active compounds against retinal diseases. Zinc is an essential microelement that plays a main role in maintaining normal ocular function by serving as an antioxidant [55], and its supplementation is reported to slow down the progression of age-related macular degeneration [56]. Verbascoside is a glycoside present in many medicinal herbs and possesses anti-oxidative, anti-inflammatory and neuroprotective properties [57]. Despite its poor bioavailability, there is evidence that diet supplementation with verbascoside reduces oxidative stress in ocular tissues and fluids, while in vitro verbascoside inhibits apoptotic death of retinal cells [58,59]. The synergistic effects of antioxidant mixtures may increase the bioavailability of partnering compounds, further improving treatment outcomes. In addition, the bioactivity of each individual component may occur at different levels of the same signaling cascade or activate different pathways thus leading to multi-target and multifunctional effects [21].

5. Conclusions

Taken together, the present evidence that combined administration of lutein, C3G, verbascoside and zinc successfully ameliorates retinal dysfunction by acting as a major antioxidant compound can now offer new perspectives not only for implementing our knowledge on the effectiveness of dietary supplements in counteracting light-induced retinal damage, but also for eventually expanding complementary nutritional interventions. As shown in the schematic representation of Figure 9, the present data demonstrate the ability of lutein, C3G, verbascoside and zinc to preserve visual function by preventing retinal cell apoptosis through a major antioxidant action leading to reduced levels of pro-inflammatory markers. The beneficial efficacy of the multicomponent formula would also encourage the development and consumption of foods and/or supplements rich in these compounds.

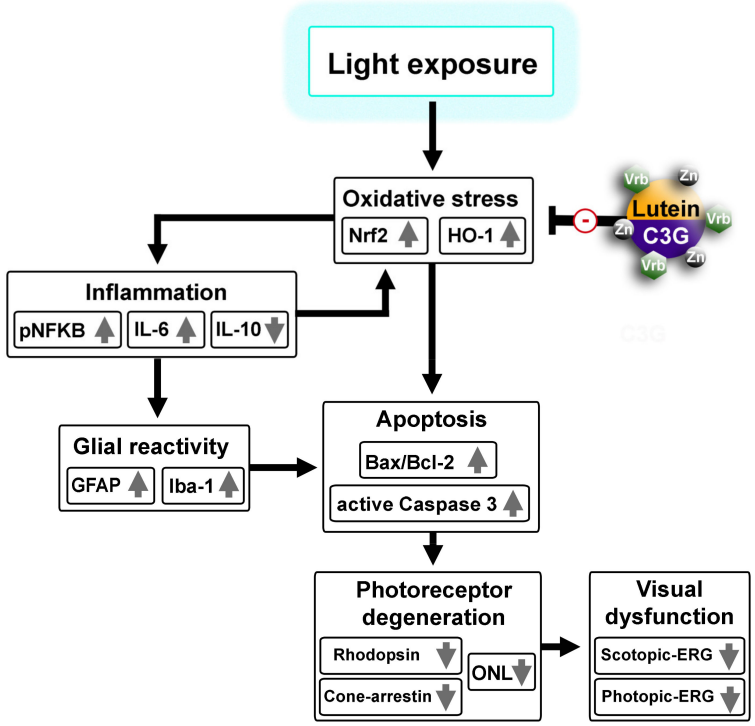

Figure 9. Schematic diagram showing possible mechanisms through which a nutraceutical blend containing lutein, cyanidin-3-glucosid (C3G), zinc (Zn) and verbascoside (Vrb) prevents light induced oxidative stress and the downstream cascade leading to photoreceptor degeneration and visual dysfunction.

Author Contributions: Conceptualization, D.R., P.B. and M.C.; methodology, R.A., A.C., A.M. and S.P.; validation, A.C. and A.M.; formal analysis, R.A. and A.C.; investigation, R.A., A.C., A.M., S.P. and R.C.; resources, M.D.M.; data curation, R.A., A.C. and M.C.; writing—original draft preparation, R.A., P.B. and M.C.; writing—review and editing, R.A., M.D.M., D.R., P.B. and M.C.; supervision, M.C.; project administration, D.R., P.B. and M.C.; funding acquisition, M.D.M. and M.C. All authors have read and agreed to the published version of the manuscript.

Funding: This research was funded by grants from Sooft Italia, SpA (Montegiorgio, FM, Italy) to M.C. and M.D.M.

Institutional Review Board Statement: The experimental protocol was approved by the Commission for Animal Wellbeing of the University of Pisa (permit number: 133/2019-PR, 14 February 2019).

Informed Consent Statement: Not applicable.

Data Availability Statement: The data presented in this study are available on request from the corresponding author.

Acknowledgments: The critical reading of the manuscript by Giuseppe Guarnaccia (ESASO, Switzerland) is greatly acknowledged. The authors also wish to thank Tiziana Cintio for animal assistance.

Conflicts of Interest: M.C. and M.D.M. received a study grant from Sooft Italia SpA. D.R., S.P. and R.C. are employees of Sooft Italia SpA. Sooft Italia SpA had no direct role in the collection, analyses or interpretation of data or in the decision to publish the results. R.A, A.C., A.M. and P.B. declare no conflict of interest.

References

1. Bungau, S.; Abdel-Daim, M.M.; Tit, D.M.; Ghanem, E.; Sato, S.; Maruyama-Inoue, M.; Yamane, S.; Kadonosono, K. Health Benefits of Polyphenols and Carotenoids in Age-Related Eye Diseases. *Oxid. Med. Cell. Longev.* **2019**, *2019*, 9783429. [CrossRef] [PubMed]
2. Chen, Y.; Okano, K.; Maeda, T.; Chauhan, V.; Golczak, M.; Maeda, A.; Palczewski, K. Mechanism of all-trans-retinal toxicity with implications for stargardt disease and age-related macular degeneration. *J. Biol. Chem.* **2012**, *287*, 5059–5069. [CrossRef] [PubMed]
3. Maeda, T.; Maeda, A.; Matosky, M.; Okano, K.; Roos, S.; Tang, J.; Palczewski, K. Evaluation of potential therapies for a mouse model of human age-related macular degeneration caused by delayed all-trans-retinal clearance. *Investig. Ophthalmol. Vis. Sci.* **2009**, *50*, 4917–4925. [CrossRef] [PubMed]
4. Wang, Y.; Huo, Y.; Zhao, L.; Lu, F.; Wang, O.; Yang, X.; Ji, B.; Zhou, F. Cyanidin-3-glucoside and its phenolic acid metabolites attenuate visible light-induced retinal degeneration in vivo via activation of Nrf2/HO-1 pathway and NF-κB suppression. *Mol. Nutr. Food Res.* **2016**, *60*, 1564–1577. [CrossRef]
5. Salehi, B.; Martorell, M.; Arbiser, J.L.; Sureda, A.; Martins, N.; Maurya, P.K.; Sharifi-Rad, M.; Kumar, P.; Sharifi-Rad, J. Antioxidants: Positive or Negative Actors? *Biomolecules* **2018**, *8*, 124. [CrossRef] [PubMed]
6. Wang, P.; Chin, E.K.; Almeida, D. Antioxidants for the Treatment of Retinal Disease: Summary of Recent Evidence. *Clin. Ophthalmol.* **2021**, *15*, 1621–1628. [CrossRef]
7. Ikonne, E.U.; Ikpeazu, V.O.; Ugbogu, E.A. The potential health benefits of dietary natural plant products in age related eye diseases. *Heliyon* **2020**, *6*, e04408. [CrossRef] [PubMed]
8. Kim, J.; Jin, H.L.; Jang, D.S.; Jeong, K.W.; Choung, S.Y. Quercetin-3-O-α-l-arabinopyranoside protects against retinal cell death via blue light-induced damage in human RPE cells and Balb-c mice. *Food Funct.* **2018**, *9*, 2171–2183. [CrossRef]
9. Sahin, K.; Akdemir, F.; Orhan, C.; Tuzcu, M.; Gencoglu, H.; Sahin, N.; Ozercan, I.H.; Ali, S.; Yilmaz, I.; Juturu, V. (3R, 3′R)-zeaxanthin protects the retina from photo-oxidative damage via modulating the inflammation and visual health molecular markers. *Cutan. Ocul. Toxicol.* **2019**, *38*, 161–168. [CrossRef]
10. Shang, Y.M.; Wang, G.S.; Sliney, D.H.; Yang, C.H.; Lee, L.L. Light-emitting-diode induced retinal damage and its wavelength dependency in vivo. *Int. J. Ophthalmol.* **2017**, *10*, 1912202.
11. Li, L.H.; Lee, J.C.; Leung, H.H.; Lam, W.C.; Fu, Z.; Lo, A. Lutein Supplementation for Eye Diseases. *Nutrients* **2020**, *12*, 1721. [CrossRef]
12. Liu, J.; Zhou, H.; Song, L.; Yang, Z.; Qiu, M.; Wang, J.; Shi, S. Anthocyanins: Promising Natural Products with Diverse Pharmacological Activities. *Molecules* **2021**, *26*, 3807. [CrossRef] [PubMed]
13. Eisenhauer, B.; Natoli, S.; Liew, G.; Flood, V.M. Lutein and Zeaxanthin-Food Sources, Bioavailability and Dietary Variety in Age-Related Macular Degeneration Protection. *Nutrients* **2017**, *9*, 120. [CrossRef] [PubMed]
14. Mares, J. Lutein and Zeaxanthin Isomers in Eye Health and Disease. *Annu. Rev. Nutr.* **2016**, *36*, 571–602. [CrossRef] [PubMed]
15. Liu, T.; Liu, W.H.; Zhao, J.S.; Meng, F.Z.; Wang, H. Lutein protects against β-amyloid peptide-induced oxidative stress in cerebrovascular endothelial cells through modulation of Nrf-2 and NF-κb. *Cell Biol. Toxicol.* **2017**, *33*, 57–67. [CrossRef]
16. Chang, J.; Zhang, Y.; Li, Y.; Lu, K.; Shen, Y.; Guo, Y.; Qi, Q.; Wang, M.; Zhang, S. NrF2/ARE and NF-κB pathway regulation may be the mechanism for lutein inhibition of human breast cancer cell. *Future Oncol.* **2018**, *14*, 719–726. [CrossRef] [PubMed]

17. Bernstein, P.S.; Li, B.; Vachali, P.P.; Gorusupudi, A.; Shyam, R.; Henriksen, B.S.; Nolan, J.M. Lutein, zeaxanthin, and meso-zeaxanthin: The basic and clinical science underlying carotenoid-based nutritional interventions against ocular disease. *Prog. Retin. Eye Res.* **2016**, *50*, 34–66. [CrossRef]
18. Harborne, J.B.; Williams, C.A. Anthocyanins and other flavonoids. *Nat. Prod. Rep.* **2001**, *18*, 310–333. [CrossRef]
19. Bosch-Morell, F.; Villagrasa, V.; Ortega, T.; Acero, N.; Muñoz-Mingarro, D.; González-Rosende, M.E.; Castillo, E.; Sanahuja, M.A.; Soriano, P.; Martínez-Solís, I. Medicinal plants and natural products as neuroprotective agents in age-related macular degeneration. *Neural Regen Res.* **2020**, *15*, 2207–2216.
20. Pawlowska, E.; Szczepanska, J.; Koskela, A.; Kaarniranta, K.; Blasiak, J. Dietary Polyphenols in Age-Related Macular Degeneration: Protection against Oxidative Stress and Beyond. *Oxid. Med. Cell. Longev.* **2019**, *2019*, 9682318. [CrossRef]
21. Leena, M.M.; Silvia, M.G.; Vinitha, K.; Moses, J.A.; Anandharamakrishnan, C. Synergistic potential of nutraceuticals: Mechanisms and prospects for futuristic medicine. *Food Funct.* **2020**, *11*, 9317–9337. [CrossRef] [PubMed]
22. Sanz, M.M.; Johnson, L.E.; Ahuja, S.; Ekström, P.A.; Romero, J.; van Veen, T. Significant photoreceptor rescue by treatment with a combination of antioxidants in an animal model for retinal degeneration. *Neuroscience* **2007**, *145*, 1120–1129. [CrossRef] [PubMed]
23. Kohno, H.; Chen, Y.; Kevany, B.M.; Pearlman, E.; Miyagi, M.; Maeda, T.; Palczewski, K.; Maeda, A. Photoreceptor proteins initiate microglial activation via Toll-like receptor 4 in retinal degeneration mediated by all-trans-retinal. *J. Biol. Chem.* **2013**, *288*, 15326–15341. [CrossRef] [PubMed]
24. Rashid, K.; Wolf, A.; Langmann, T. Microglia Activation and Immunomodulatory Therapies for Retinal Degenerations. *Front. Cell. Neurosci.* **2018**, *12*, 176. [CrossRef]
25. Nair, A.B.; Jacob, S. A simple practice guide for dose conversion between animals and human. *J. Basic Clin. Pharm.* **2016**, *7*, 27–31. [CrossRef] [PubMed]
26. Riccitelli, S.; Di Paolo, M.; Ashley, J.; Bisti, S.; Di Marco, S. The Time courses of Functional, Morphological, and Molecular Changes Triggered by Light Exposure in Sprague-Dawley Rat Retinas. *Cells* **2021**, *10*, 1561. [CrossRef]
27. Ma, H.; Qin, S.; Zhao, S. Osteoarthritis is Prevented in Rats by Verbascoside via Nuclear Factor kappa B (NF-kB) Pathway Downregulation. *Med. Sci. Monit.* **2020**, *26*, e921276. [CrossRef]
28. Xu, G.; Guo, J.; Sun, C. Eucalyptol ameliorates early brain injury after subarachnoid haemorrhage via antioxidant and anti-inflammatory effects in a rat model. *Pharm. Biol.* **2021**, *59*, 114–120. [CrossRef]
29. Wenzel, A.; Grimm, C.; Samardzija, M.; Remé, C.E. Molecular mechanisms of light-induced photoreceptor apoptosis and neuroprotection for retinal degeneration. *Prog. Retin. Eye Res.* **2005**, *24*, 275–306. [CrossRef]
30. Marmoy, O.R.; Viswanathan, S. Clinical electrophysiology of the optic nerve and retinal ganglion cells. *Eye Lond.* **2021**. [CrossRef]
31. Yang, J.; Li, D.; Zhang, Y.; Zhang, L.; Liao, Z.; Aihemaitijiang, S.; Hou, Y.; Zhan, Z.; Xie, K.; Zhang, Z. Lutein protected the retina from light induced retinal damage by inhibiting increasing oxidative stress and inflammation. *J. Funct. Foods* **2020**, *73*, 104107. [CrossRef]
32. Braakhuis, A.; Raman, R.; Vaghefi, E. The Association between Dietary Intake of Antioxidants and Ocular Disease. *Diseases* **2017**, *5*, 3. [CrossRef]
33. AREDS2 Research Group; Chew, E.Y.; Clemons, T.; SanGiovanni, J.P.; Danis, R.; Domalpally, A.; McBee, W.; Sperduto, R.; Ferris, F.L. The Age-Related Eye Disease Study 2 (AREDS2): Study design and baseline characteristics (AREDS2 report number 1). *Ophthalmology* **2012**, *119*, 2282–2289.
34. Piermarocchi, S.; Saviano, S.; Parisi, V.; Tedeschi, M.; Panozzo, G.; Scarpa, G.; Boschi, G.; Lo Giudice, G. Carmis Study Group Carotenoids in Age-related Maculopathy Italian Study (CARMIS): Two-year results of a randomized study. *Eur. J. Ophthalmol.* **2012**, *22*, 216–225. [PubMed]
35. Hunter, J.J.; Morgan, J.I.; Merigan, W.H.; Sliney, D.H.; Sparrow, J.R.; Williams, D.R. The susceptibility of the retina to photochemical damage from visible light. *Prog. Retin. Eye Res.* **2012**, *31*, 28–42. [CrossRef] [PubMed]
36. Ouyang, X.; Yang, J.; Hong, Z.; Wu, Y.; Xie, Y.; Wang, G. Mechanisms of blue light-induced eye hazard and protective measures: A review. *Biomed. Pharm.* **2020**, *130*, 110577. [CrossRef] [PubMed]
37. Okamoto, T.; Kawashima, H.; Osada, H.; Toda, E.; Homma, K.; Nagai, N.; Imai, Y.; Tsubota, K.; Ozawa, Y. Dietary Spirulina Supplementation Protects Visual Function From Photostress by Suppressing Retinal Neurodegeneration in Mice. *Transl. Vis. Sci. Technol.* **2019**, *8*, 20. [CrossRef] [PubMed]
38. Tanito, M.; Agbaga, M.P.; Anderson, R.E. Upregulation of thioredoxin system via Nrf2-antioxidant responsive element pathway in adaptive-retinal neuroprotection in vivo and in vitro. *Free Radic. Biol. Med.* **2007**, *42*, 1838–1850. [CrossRef]
39. Domènech, E.B.; Marfany, G. The Relevance of Oxidative Stress in the Pathogenesis and Therapy of Retinal Dystrophies. *Antioxidants* **2020**, *9*, 347. [CrossRef]
40. Arunkumar, R.; Gorusupudi, A.; Bernstein, P.S. The macular carotenoids: A biochemical overview. *Biochim. Biophys. Acta Mol. Cell Biol. Lipids* **2020**, *1865*, 158617. [CrossRef]
41. Tena, N.; Martín, J.; Asuero, A.G. State of the Art of Anthocyanins: Antioxidant Activity, Sources, Bioavailability, and Therapeutic Effect in Human Health. *Antioxidants* **2020**, *9*, 451. [CrossRef] [PubMed]
42. Matsumoto, H.; Nakamura, Y.; Iida, H.; Ito, K.; Ohguro, H. Comparative assessment of distribution of blackcurrant anthocyanins in rabbit and rat ocular tissues. *Exp. Eye Res.* **2006**, *83*, 348–356. [CrossRef] [PubMed]

43. Sato, Y.; Kobayashi, M.; Itagaki, S.; Hirano, T.; Noda, T.; Mizuno, S.; Sugawara, M.; Iseki, K. Pharmacokinetic properties of lutein emulsion after oral administration to rats and effect of food intake on plasma concentration of lutein. *Biopharm. Drug Dispos.* **2011**, *32*, 151–158. [CrossRef] [PubMed]
44. Khoo, H.E.; Ng, H.S.; Yap, W.S.; Goh, H.; Yim, H.S. Nutrients for Prevention of Macular Degeneration and Eye-Related Diseases. *Antioxidants* **2019**, *8*, 85. [CrossRef] [PubMed]
45. Nomi, Y.; Iwasaki-Kurashige, K.; Matsumoto, H. Therapeutic Effects of Anthocyanins for Vision and Eye Health. *Molecules* **2019**, *24*, 3311. [CrossRef]
46. Vitaglione, P.; Donnarumma, G.; Napolitano, A.; Galvano, F.; Gallo, A.; Scalfi, L.; Fogliano, V. Protocatechuic acid is the major human metabolite of cyanidin-glucosides. *J. Nutr.* **2007**, *137*, 2043–2048. [CrossRef] [PubMed]
47. Kamoshita, M.; Toda, E.; Osada, H.; Narimatsu, T.; Kobayashi, S.; Tsubota, K.; Ozawa, Y. Lutein acts via multiple antioxidant pathways in the photo-stressed retina. *Sci. Rep.* **2016**, *6*, 30226. [CrossRef]
48. Sukprasansap, M.; Chanvorachote, P.; Tencomnao, T. Cyanidin-3-glucoside activates Nrf2-antioxidant response element and protects against glutamate-induced oxidative and endoplasmic reticulum stress in HT22 hippocampal neuronal cells. *BMC Complement. Med. Ther.* **2020**, *20*, 46. [CrossRef]
49. Sasaki, M.; Yuki, K.; Kurihara, T.; Miyake, S.; Noda, K.; Kobayashi, S.; Ishida, S.; Tsubota, K.; Ozawa, Y. Biological role of lutein in the light-induced retinal degeneration. *J. Nutr. Biochem.* **2012**, *23*, 423–429. [CrossRef]
50. Randazzo, J.; Zhang, Z.; Hoff, M.; Kawada, H.; Sachs, A.; Yuan, Y.; Haider, N.; Kador, P. Orally active multi-functional antioxidants are neuroprotective in a rat model of light-induced retinal damage. *PLoS ONE* **2011**, *6*, e21926. [CrossRef] [PubMed]
51. Prieto, M.A.; Curran, T.P.; Gowen, A.; Vázquez, J.A. An efficient methodology for quantification of synergy and antagonism in single electron transfer antioxidant assays. *Food Res. Int.* **2015**, *67*, 284–298. [CrossRef]
52. Olszowy, M.; Dawidowicz, A.L.; Jóźwik-Dolęba, M. Are mutual interactions between antioxidants the only factors responsible for antagonistic antioxidant effect of their mixtures? Additive and antagonistic antioxidant effects in mixtures of gallic, ferulic and caffeic acids. *Eur. Food Res. Technol.* **2019**, *245*, 1473–1485. [CrossRef]
53. Olivares-González, L.; Velasco, S.; Campillo, I.; Salom, D.; González-García, E.; Soriano Del Castillo, J.M.; Rodrigo, R. Nutraceutical Supplementation Ameliorates Visual Function, Retinal Degeneration, and Redox Status in rd10 Mice. *Antioxidants* **2021**, *10*, 1033. [CrossRef] [PubMed]
54. Dong, C.J.; Hare, W.A. Contribution to the kinetics and amplitude of the electroretinogram b-wave by third-order retinal neurons in the rabbit retina. *Vis. Res.* **2000**, *40*, 579–589. [CrossRef]
55. Kamińska, A.; Romano, G.L.; Rejdak, R.; Zweifel, S.; Fiedorowicz, M.; Rejdak, M.; Bajka, A.; Amato, R.; Bucolo, C.; Avitabile, T.; et al. Influence of Trace Elements on Neurodegenerative Diseases of The Eye-The Glaucoma Model. *Int. J. Mol. Sci.* **2021**, *22*, 4323. [CrossRef] [PubMed]
56. Blasiak, J.; Pawlowska, E.; Chojnacki, J.; Szczepanska, J.; Chojnacki, C.; Kaarniranta, K. Zinc and Autophagy in Age-Related Macular Degeneration. *Int. J. Mol. Sci.* **2020**, *21*, 4994. [CrossRef] [PubMed]
57. Wu, L.; Georgiev, M.I.; Cao, H.; Nahar, L.; El-Seedi, H.R.; Sarker, S.D.; Xiao, J.; Lu, B. Therapeutic potential of phenylethanoid glycosides: A systematic review. *Med. Res. Rev.* **2020**, *40*, 2605–2649. [CrossRef]
58. Chen, Q.; Xi, X.; Zeng, Y.; He, Z.; Zhao, J.; Li, Y. Acteoside inhibits autophagic apoptosis of retinal ganglion cells to rescue glaucoma-induced optic atrophy. *J. Cell. Biochem.* **2019**, *120*, 13133–13140. [CrossRef]
59. Mosca, M.; Ambrosone, L.; Semeraro, F.; Casamassima, D.; Vizzarri, F.; Costagliola, C. Ocular tissues and fluids oxidative stress in hares fed on verbascoside supplement. *Int. J. Food Sci. Nutr.* **2014**, *65*, 235–240. [CrossRef] [PubMed]

tvst

Glaucoma

Efficacy of a Spearmint (*Mentha spicata* L.) Extract as Nutritional Support in a Rat Model of Hypertensive Glaucoma

Rosario Amato[1], Alessio Canovai[1], Alberto Melecchi[1], Samanta Maci[2], Filipa Quintela[2], Brenda A. Fonseca[3], Maurizio Cammalleri[1,4], and Massimo Dal Monte[1,4]

[1] Department of Biology, University of Pisa, Pisa, Italy
[2] Kemin Human Nutrition and Health, a Division of Kemin Foods L.C., Lisbon, Portugal
[3] Kemin Foods, L.C., Des Moines, IA, USA
[4] Interdepartmental Research Center Nutrafood "Nutraceuticals and Food for Health," University of Pisa, Pisa, Italy

Correspondence: Massimo Dal Monte, Department of Biology, University of Pisa, via San Zeno, 31, Pisa 56127, Italy. e-mail: massimo.dalmonte@unipi.it

Received: July 10, 2023
Accepted: October 11, 2023
Published: November 2, 2023

Keywords: retinal ganglion cells; electroretinogram; oxidative stress; inflammation; neuroprotection

Citation: Amato R, Canovai A, Melecchi A, Maci S, Quintela F, Fonseca BA, Cammalleri M, Dal Monte M. Efficacy of a spearmint (*Mentha spicata* L.) extract as nutritional support in a rat model of hypertensive glaucoma. Transl Vis Sci Technol. 2023;12(11):6, https://doi.org/10.1167/tvst.12.11.6

Purpose: Glaucoma is an eye–brain axis disorder characterized by loss of retinal ganglion cells (RGCs). Although the role of intraocular pressure (IOP) elevation in glaucoma has been established, the reduction of oxidative stress and inflammation has emerged as a promising target for neuronal tissue–supporting glaucoma management. Therefore, we evaluated the effect of a proprietary spearmint extract (SPE) on RGC density, activity, and neuronal health markers in a rat model of hypertensive glaucoma.

Methods: Animals were divided in four groups: untreated healthy control and three glaucomatous groups receiving orally administered vehicle, SPE-low dose, or SPE-high dose for 28 days. Ocular hypertension was induced through intracameral injection of methylcellulose at day 15. At day 29, rats underwent electroretinogram (ERG) recordings, and retinas were analyzed for RGC density and markers of neural trophism, oxidative stress, and inflammation.

Results: SPE exerted dose-dependent response benefits on all markers except for IOP elevation. SPE significantly improved RGC-related ERG responses, cell density, neurotrophins, oxidative stress, and inflammation markers. Also, in SPE-high rats, most of the parameters were not statistically different from those of healthy controls.

Conclusions: SPE, a plant-based, polyphenolic extract, could be an effective nutritional support for neuronal tissues.

Translational Relevance: These results suggest that SPE not only may be a complementary approach in support to hypotensive treatments for the management of glaucoma but may also serve as nutritional support in other ocular conditions where antioxidant, anti-inflammatory, and neuroprotective mechanism are often disrupted.

Introduction

Glaucoma, a neurodegenerative disorder, is one of the leading causes of blindness and is estimated to affect more than 76 million people worldwide, with that number expected to reach over 111 million by 2040.[1] The disease affects both the eye and brain with typically irreversible neural damage. In its various subtypes (primary open-angle glaucoma, primary angle-closure glaucoma, normotensive glaucoma, etc.), its global prevalence is estimated at 3.5% of the population 40 to 80 years of age.[2] Data from a meta-analysis conducted in 2022 reported a pooled prevalence estimate of primary open-angle glaucoma in Europe of 2.60% (95% confidence interval, 1.90–3.56) with expected growth associated with a progressively aging population in Western countries.[3] Glaucoma is mainly characterized by a progressive optic neuropathy, including chronic axonal damage and retinal ganglion cell (RGC) loss. The complex pathophysiology behind the RGC degeneration is comprised of a series of

genetic, metabolic, and environmental factors and consequently requires a multifactorial approach to glaucoma management.[4]

Intraocular pressure (IOP) elevation represents one of the most recurrent risk factors driving glaucomatous progression and RGC neurodegeneration.[5] Thus, the reduction of ocular hypertension represents the main target for the pharmaceutical treatments currently in use with significant but not resolutive effects.[6] This highlights the significance of contributing pathophysiological mechanisms other than IOP elevation that equally drive the disease progression or etiology (such as in normotensive glaucoma). This necessitates the understanding of these other mechanisms and the development of solutions to mitigate these effects.

Current research advancing this understanding links glaucoma to degeneration of the central nervous system (CNS), moving it away from being considered just a traditional eye disease. A recent review assessing the morphological and functional changes affecting the CNS in glaucoma[7] reported structural alterations along the visual pathway and in numerous cognitive functions outside the visual pathway, such as for visual memory, working memory, attention, and motor coordination. These observations suggest that independent mechanisms of neurodegeneration in glaucoma are potentially affecting neural tissues in addition to the known anterograde and/or retrograde neuronal degeneration.[7–9] Recent evidence also suggests that metabolic stress and bioenergetic insufficiency play key roles in the progression of glaucoma ultimately resulting in RGC degeneration through the promotion of oxidative stress and inflammation.[10,11] Furthermore, levels of neurotrophic factors such as brain-derived neurotrophic factor (BDNF) and nerve growth factor (NGF) could play a key role in the progression of glaucoma.[12] BDNF indeed plays a vital role in RGC physiology, protecting RGCs in conditions of ocular hypertension, hypoxia, or glucose deprivation, whereas the role of NGF is less clear, as NGF binds two different receptors that evoke opposite effects.[13] Nonetheless, when neurotrophin support is lacking, the induction of apoptotic death of RGCs has been described.[14] RGCs are supplied with neurotrophins produced locally in the retina but also in the brain, and these neurotrophins are delivered to RGCs through retrograde transport, which is impaired in the early stages of glaucoma, thus leading to a deficiency in the trophic support of RGCs.[12] Therefore, the use of antioxidant, anti-inflammatory, and/or neurotrophic support solutions as complementary approaches for the management of this condition is gaining increasing attention. In this context, a proprietary spearmint extract (SPE), marketed as Neumentix (Kemin Foods, L.C., Des Moines, IA), which is a polyphenol-rich ingredient derived from patented lines of spearmint (*Mentha spicata* L.) plants,[15–17] could provide suitable nutritional support. Multiple preclinical studies with SPE have demonstrated that SPE can reduce markers of oxidative stress and inflammation and promote neuroprotection in neural tissue.[18–20] Furthermore, SPE has been shown to modulate brain neurotransmitters in the mouse and promote neurogenesis in rat hippocampal neurons.[21,22] Clinical research has additionally shown that the extract is well tolerated and supports cognitive function improvements in both healthy young and older people.[23–27] Specifically, the oral administration of SPE for 12 weeks has been shown to improve working memory, attention, and agility compared to placebo. Additionally, SPE in combination with green tea extract has been shown to improve sleep quality and next-day concentration, decision-making, working memory, and reaction time in healthy young people. Furthermore, there is biological plausibility that SPE offers cognitive and sleep benefits by supporting the underlying health of neuronal tissue. Recent animal models of glaucomatous conditions induced by optic nerve crush or methylcellulose (MCE)-induced ocular hypertension indicate that dietary interventions including SPE counteract the inflammatory processes and morpho-functional alterations of glaucoma.[28,29] These studies suggest that SPE could be a potential candidate for providing nutritional support for ocular neural tissues.

Hence, the objective of this study was to determine the effect of oral supplementation of SPE at two doses on RGC degeneration in terms of retinal dysfunction and cell loss, following IOP elevation in a rat model of MCE-induced hypertensive glaucoma. In this model, the increase in IOP results in a sudden elevation of inflammatory and oxidative stress markers that in glaucoma patients may require a considerable amount of time to occur. Nevertheless, it can still provide valuable information about the mechanisms involved in glaucoma and preliminary data on how they can potentially be modulated by nutritional intervention. Scotopic and photopic electroretinogram (ERG) and pattern ERG (PERG) were used to evaluate retinal function, and RGC density was measured by immunohistochemistry for RNA-binding protein with multiple splicing (RBPMS), a selective RGC marker in the mammalian retina.[30] Levels of neurotrophins, BDNF, and NGF, which are known to promote neuronal survival and synapsis plasticity in the CNS[31,32] and RGC survival,[13] were measured to assess direct neuroprotective effects. Finally, levels of markers of oxidative stress, of cellular antioxidant defense, and of neuroinflammation in the retina were measured to ascertain the

antioxidant and anti-inflammatory effects of the SPE intervention.

Materials and Methods

Animals

Forty male Sprague Dawley rats (8 weeks old, about 300 g) were purchased from Envigo Italy (San Pietro al Natisone, Italy). Each rat was kept in a regulated environment (23°C ± 1°C, 50% ± 5% humidity) with 12-hour light/dark cycles (lights on at 08:00 AM) and fed with a standard diet (2018 Teklad Global Diets; Envigo Italy) and water ad libitum. Rats were housed one per cage to avoid motor restraints. Before the study started, all rats were acclimatized for 7 days to handling and tonometry. Animals were managed in agreement with the ARVO Statement for the Use of Animals in Ophthalmic and Vision Research. The study follows the European Communities Council Directive (2010/63/UE) and the Italian guidelines for animal care (DL 26/14). The experimental protocol was authorized by the Commission for Animal Wellbeing of the University of Pisa (protocol no. 4/2022) and by the Ministry of Health (protocol no. 307/2022-PR). The principles of the 3Rs (replacement, reduction, and refinement) for ethical use of animals in scientific research were utilized to reduce both the number and suffering of the animals.

Rats were randomly divided into four groups as follows: one group (10 rats) of healthy controls (control, rats receiving no MCE injection and no supplementation; group 1), and three groups of glaucomatous rats (10 rats/group) receiving MCE injection and randomized to oral supplementation with vehicle (MCE + vehicle; group 2); low-dose SPE (MCE + SPE-low; group 3); and high-dose SPE (MCE + SPE-high; group 4).

Rat Model of Hypertensive Glaucoma

The induction of ocular hypertension was performed in agreement with published procedures.[33,34] Briefly, 2% MCE w/v in sterile saline was prepared to obtain a solution viscosity ranging from 3500 to 5600 cps. Rats were anesthetized with an intraperitoneal injection of sodium pentobarbital (30 mg/kg) and injected into the anterior chamber with 15 µL of the MCE solution in both eyes using a Hamilton syringe equipped with an 18-gauge needle. The needle was inserted in the iridocorneal angle at about 1 mm from the ora serrata and oriented parallel to the iris surface. After the slow injection of MCE (1-minute duration), the needle was kept in place for 1 minute to avoid MCE outpours. Immediately after the injection of MCE, antibiotic eyedrops were instilled in order to prevent the occurrence of endophthalmitis. The animals were kept under continuous monitoring during the whole period of anesthesia for possible alterations in the breathing frequency up to the complete recovery. Each rat was daily monitored during the following 3 days for any alterations in ocular tissues (corneal opacity, cataracts, conjunctivitis, or hyphema).

Dietary Supplementation

SPE (marketed as Neumentix by Kemin Foods, L.C., Des Moines, IA) is a proprietary ingredient sourced from patented, non–genetically modified organism (GMO) lines of native spearmint (*Mentha spicata* L.) grown in the United States and developed by using traditional plant breeding methodologies. These plants are capable of accumulating >100 mg/g rosmarinic acid (RA) on a dry-weight basis, a much higher concentration compared to that reported for traditional spearmint, with RA content in the range of 7.1 to 58.5 mg/g.[15,35] Ultra-high performance liquid chromatography–mass spectrometry analysis of SPE shows that the product has a characteristic and consistent phenolic fingerprint and contains a powerful assortment of phenolic compounds including, but not limited to, RA, salvianolic acid, caffeic acid, caftaric acid, quinic acid, and lithospermic acid.[15] SPE is standardized to 14.5% to 17.5% RA and 24% to 37% total phenolics.

In the present study, SPE was tested at low (SPE-low) and high (SPE-high) doses corresponding to half or full dosages found to exert cognitive benefits in clinical trials,[23–25,27] taking into account the difference in the metabolism of the two species (man and rat)[36] and the dose used in previous preclinical studies.[18–21] SPE-high was administered at 93.0 mg/kg body weight per day, corresponding to a human daily dose of 15 mg/kg body weight (900 mg/d for a 60-kg person). SPE-low was administered at 46.5 mg/kg body weight per day, corresponding to a human daily dose of 7.5 mg/kg body weight (450 mg/d for a 60-kg person). High- and low-dose solutions of SPE were freshly prepared every day in distilled water immediately before the treatment. In particular, SPE was dissolved at 93 mg/mL in distilled water (vehicle) in order to obtain the stock solution to be administered for the high dose. Hence, the low-dose solution containing SPE at 46.5 mg/mL was prepared by performing 1:2 dilution of the high-dose solution. Equal amounts of low- and high-dose solutions (volume administered 300 µL) were administered daily by oral gavage for 14 days before

and 14 days after the MCE injection. Animals were routinely observed during the treatment period both before and after the MCE injection. In particular, eating and drinking behaviors and the possible occurrence of postural signs of distress (hunching, huddling, crouching, rigidity) were monitored up to 15 minutes after administration of the product.

Measurement of IOP

A time-dependent IOP profile was built for each group in order to test the effect of the oral supplementation on the ocular hypertension. IOP was non-invasively assessed daily using rebound tonometry (Tonolab; iCare Finland Oy, Helsinki, Finland) before and after MCE injections in every group for the period under investigation (28 days). Multiple sampling procedures (5–10 readings) were performed at the same range of time during the day.

Measurement of RGC Activity

The effect of the oral supplementation with SPE on the glaucomatous RGC dysfunction was analyzed at day 29 with ERG recording, in agreement with published procedures.[37] In particular, two main functional output related with RGC activity were analyzed: photopic negative response (PhNR) and PERG. These two procedures provide information regarding the inner retinal response in the context of the overall light-adapted retinal activity (PhNR) and specific RGC activity (PERG). These two parameters were analyzed both per se and in relation with the overall retinal activity as assessed by scotopic ERG. The ERG recording was performed at the endpoint of the study using a commercially available setup (Retimax Advanced; CSO, Firenze, Italy). After dark adaptation overnight, each rat was anesthetized by an intraperitoneal injection of sodium pentobarbital (30 mg/kg) and gently restrained in a custom-made holder with an unobstructed visual field. ERG responses were recorded using silver/silver chloride corneal electrodes. A reference electrode was inserted on the forehead, and a ground electrode was inserted at the base of the tail. Corneal moisture was maintained along the ERG routine by instilling balanced salt solution every 15 minutes. Scotopic ERG responses were retrieved following a single 10-cd·s/m^2 flash stimulus over a dark background delivered by a Ganzfeld light source. Then, the rats underwent light adaptation to 30-cd·s/m^2 rod-saturating background light for 10 minutes before photopic ERG responses were recorded using a 3-cd·s/m^2 stimulus delivered over the same background light. The responses to 10 consecutive stimuli with an interstimulus interval of 3 seconds were recorded and averaged. PERG recordings were then performed by delivering pattern stimuli consisting of 0.05-c/° black and white bars reversing at 1 Hz presented at 98% contrast. The pattern stimuli were administered through a light-emitting diode display with a mean luminance of 50 cd/m^2 aligned at about 20 cm from the corneal surface. A total of 200 signals were averaged. The ERG waveforms were analyzed for their consistency and evaluated for signal processing and noise filtering. In the photopic ERG waveforms, the PhNR was identified as the first negative deflection after the b-wave. The PERG waveforms were analyzed using Retimax Scientific 7.0.4 software (CSO) to retrieve the amplitude of positive (N35–P50) and negative (P50–N95) components. The amplitudes of PhNR and PERG and the latency of PERG were considered to be analytical parameters related to RGC function.

Retina Collection

Immediately after the ERG recordings, the rats were euthanized, and the retinas were dissected from other ocular tissues by microsurgical procedures. One retina from each mouse was used for immunohistochemistry; the other was divided in four quadrants that were immediately frozen in liquid nitrogen. For each retina, the four quadrants were randomly assigned to one of four groups: group 1, for western blot and the evaluation of 4-hydroxynonenal (4-HNE) levels; group 2, for the evaluation of malondialdehyde (MDA) levels; group 3, for the evaluation of 8-hydroxy-deoxyguanosine (8-OH-dG) levels; group 4, for the evaluation of glutathione (GSH) levels.

RGC Immunohistochemistry and Quantification

The effect of SPE on the glaucomatous RGC loss was evaluated by analyzing the RGC density using immunofluorescence. Briefly, isolated retinas were immersion-fixed in 4% w/v paraformaldehyde and stored at 4°C. Retinas underwent whole-mount immunostaining for RBPMS, using a guinea pig polyclonal antibody (ABN1376; Merck KGaA, Darmstadt, Germany) at 1:100 dilution for 72 hours, followed by 48-hour incubation with a fluorescein-conjugated donkey anti-guinea pig secondary antibody (AP193F; Merck KGaA) at 1:80 dilution. After being processed, retinas were analyzed with an epifluorescence microscope (Ni-E; Nikon Europe, Amsterdam, The Netherlands) equipped with a 20 × plan achromat objective, a digital camera (DS-Fi1c; Nikon Europe), and a motorized stage for organ whole-mount recon-

struction. The derived images were automatically analyzed for the RBPMS-positive cell density following the sampling of four radially opposite images at two different radial eccentricities (center = 0.5 mm, periphery = 4 mm from the optic disc) in order to determine the average density of RGCs in peripheral and central retina.

Western Blot

Retina quadrants were lysed with radioimmunoprecipitation assay lysis buffer (Santa Cruz Biotechnology, Dallas, TX) added with phosphatase and proteinase inhibitor cocktails (1:100 dilution; Roche Applied Science, Indianapolis, IN), and protein concentration was measured using a Micro BCA Protein Assay Kit (Thermo Fisher Scientific, Waltham, MA). For each sample, 20 µg of proteins were separated by sodium dodecyl sulfate–polyacrylamide gel electrophoresis using 4% to 20% polyacrylamide gels (Bio-Rad Laboratories, Hercules, CA) that were subsequently transblotted onto nitrocellulose membranes (Bio-Rad Laboratories). Blots were blocked with 5% skim milk for 1 hour and then individually incubated overnight with the following primary antibodies: rabbit monoclonal raised against BDNF (1:1000 dilution, ab108319; Abcam, Cambridge, UK) or NGF (1:1000 dilution, ab52918; Abcam); rabbit polyclonal raised against nuclear factor erythroid 2–related factor 2 (Nrf2; 1:300 dilution, ab92946; Abcam), heme oxygenase-1 (HO-1; 1:500 dilution, ab13243; Abcam), nuclear factor kappa-light-chain-enhancer of activated B cells (NF-κB; 1:1000 dilution, ab16502; Abcam), or the phosphorylated form of NF-κB (pNF-κB; 1:1000 dilution, sc-33020; Santa Cruz Biotechnology); mouse monoclonal raised against interleukin (IL)-6 (1:500 dilution; sc-57315; Santa Cruz Biotechnology) or β-actin (1:2500 dilution, A2228; Merck KGaA); hamster monoclonal raised against IL-1β (1:100 dilution, sc-12742; Santa Cruz Biotechnology); or goat polyclonal antibody raised against IL-10 (1:100 dilution, sc-1783; Santa Cruz Biotechnology). Blots were then incubated for 2 hours with the appropriate horseradish peroxidase–conjugated secondary anti-rabbit, anti-mouse, anti-hamster, or anti-goat antibodies, diluted 1:5000 (Santa Cruz Biotechnology). Membranes were visualized using the Clarity Western ECL Substrate (Bio-Rad Laboratories). Images were acquired using the ChemiDoc XRS+ (Bio-Rad Laboratories). The optical density (OD) relative to the target bands was evaluated (Image Lab 3.0 software; Bio-Rad Laboratories) and normalized to the corresponding OD of β-actin or NF-κB as appropriate.

Measurement of Oxidative Stress Markers

Oxidative stress in the retina was measured by evaluating the levels of common markers. MDA and 4-HNE are products of lipid peroxidation, and 8-OH-dG is generated by oxidative damage to DNA; their levels have been found to increase in glaucoma patients.[38] GSH is a major endogenous antioxidant in the retina whose levels have been found to decrease in both hypertensive and normotensive glaucoma patients.[39] The levels of MDA, 4-HNE, 8-OH-dG, and GSH were evaluated using commercially available kits: Lipid Peroxidation (MDA) Assay Kit (ab118970, Abcam), Lipid Peroxidation (4-HNE) Assay Kit (ab238538, Abcam), 8-Hydroxy 2 Deoxyguanosine ELISA Kit (ab201734, Abcam), and GSH+GSSG/GSH Assay Kit (Colorimetric) (ab239709, Abcam), according to the manufacturer's instructions.

Data Analysis

In adherence with the 3R principles for the ethical use of animals in scientific research, a priori power analysis was performed (G*Power 3.0.10, www.gpower.hhu.de). Sample size was calculated considering $\alpha = 0.05$, an effect size of at least 0.6 (an effect size sufficiently high to evaluate relevant differences among groups), and a statistical power of at least 0.80. Animal treatments were performed in a non-blinded fashion. Investigators performing ERG, immunohistochemistry, western blot, and measurement of oxidative stress markers were blinded to the treatment group. Blinding was performed by assigning a numerical coded identifier to the samples. Unblinding was done after data collection. Data analysis of IOP and ERG results provided the average of the two eyes as representative measures from each rat. Data were analyzed by the Shapiro–Wilk test to verify their normal distribution. Statistical significance was evaluated with Prism 8.0.2 (GraphPad Software, San Diego, CA) using one-way analysis of variance (ANOVA) followed by Tukey's post hoc test. Data are expressed as means ± SEM of the reported n values. Differences with $P < 0.05$ were considered statistically significant.

Results

Spearmint Extract Does Not Affect MCE-Induced Ocular Hypertension

Animals were routinely observed during the treatment period both before and after the MCE injection. In particular, eating and drinking behaviors and

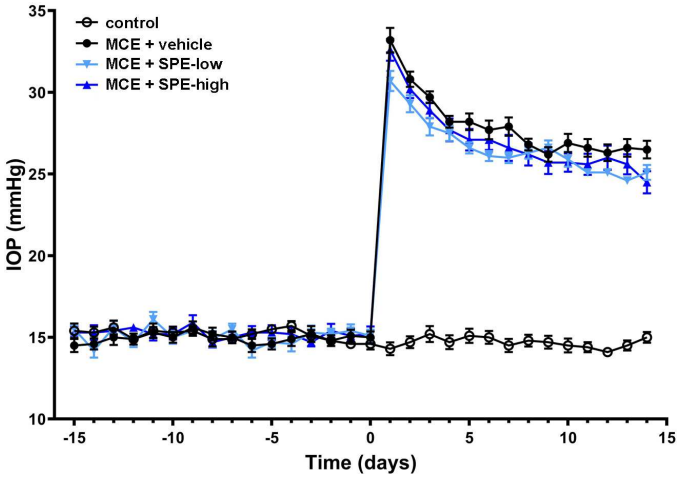

Figure 1. Values of intraocular pressure. MCE injection increased IOP and SPE did not affect increased IOP. Data are shown as mean ± SEM ($n = 10$ for each group). Day 0 corresponds to the day of MCE intraocular injection. Healthy controls did not receive a MCE injection.

the possible occurrence of postural signs of distress were monitored up to 15 minutes after administration of the product. As shown in Figure 1, the IOP profiles in all of the MCE-treated rats, assessed by rebound tonometry, revealed a significant increment in IOP levels, reaching a peak of about 34 mmHg within 24 hours after the MCE injection. Hereinafter, IOP gradually decreased over time, although it maintained higher levels as compared to healthy controls, thus confirming the reliability of the model in reproducing a glaucomatous-like ocular hypertension throughout the time window under analysis. Glaucomatous rats treated with either low- or high-dose SPE displayed IOP profiles comparable to those of vehicle-treated glaucomatous controls, without any significant difference in either the early IOP peak or its following gradual decrement.

Spearmint Extract Exerts a Dose-Dependent Beneficial Effect in RGC-Related ERG Parameters

Scotopic ERG was performed to assess the overall photoreceptor activity, reflected by the scotopic a-wave, and the overall post-receptor activity, reflected by the scotopic b-wave, at the end of the study. As expected, neither scotopic ERG parameter was significantly affected following either the MCE injection or the supplementation regimens (Figs. 2A–2C). Similarly, the photopic b-wave, reflecting the cone-specific overall post-receptor activity, displayed no alterations in amplitude in any experimental group (Figs. 3A, 3B). In contrast, the PhNR amplitude, reflecting RGC-specific activity, was significantly decreased in vehicle-treated MCE rats as compared to the healthy controls (Figs. 3A, 3C). The loss in PhNR amplitude was dose-dependently attenuated following SPE intervention. The definitive establishment of RGC functional alterations in glaucomatous rats derives from assessment of PERG responses. In vehicle-treated MCE rats, amplitudes in both N35–P50 and P50–N95 components were halved compared to the healthy controls (Fig. 4). SPE administration resulted in significant dose-dependent protection of the amplitude of both N35–P50 and P50–N95 components of the PERG response.

Spearmint Extract Preserves RGC Density Following MCE-Induced IOP Elevation in a Dose-Dependent Manner

As shown in Figure 5, the immunostaining of RBPMS in whole-mount retinas revealed the typical difference in RGC density between the peripheral and central portion of the retina. The intracameral injection of MCE produced a proportional loss of RGC density in both central and peripheral retina. Oral supplementation with SPE resulted in a significant dose-dependent preservation of RGC density at both central and peripheral retinal locations. Furthermore, in glaucomatous rats supplemented with high-dose SPE, RGC density in the central retina was not statistically different from that in healthy controls.

Spearmint Extract Promotes the Maintenance of Neural Trophism Under MCE-Induced Glaucomatous Stress in a Dose-Dependent Manner

Neural trophism was evaluated by analyzing the protein levels of BDNF and NGF as crucial neurotrophins involved in the maintenance of RGC viability. As demonstrated by the western blot analysis shown in Figure 6, retinal levels of both BDNF and NGF significantly decreased after the intracameral injection of MCE compared to levels observed in healthy control rats. As compared to vehicle-treated MCE rats, animals receiving SPE at both doses displayed a significant dose-dependent increase in neurotrophin supply.

Spearmint Extract Counteracts the MCE-Induced Oxidative Stress in a Dose-Dependent Manner

The effect of SPE in counteracting MCE-induced oxidative stress was analyzed by colorimetric analyses

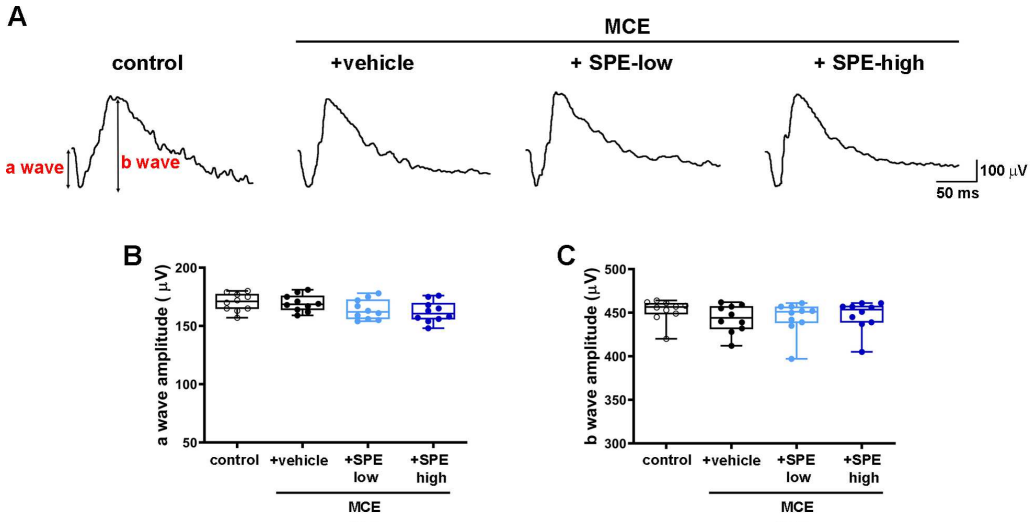

Figure 2. SPE did not affect scotopic ERG. (**A**) Representative ERG waveforms recorded at a light intensity of 10 cd·s/m^2 in control rats and in rats injected with MCE fed with either vehicle or SPE. (**B**, **C**) Scotopic a-wave (**B**) and b-wave (**C**) amplitudes. Photoreceptor and post-receptor responses to a light flash were not influenced by MCE or SPE, as evidenced by the invariance of both a- and b-wave amplitudes. Data are shown as box plots with minimum to maximum whiskers ($n = 10$ for each group).

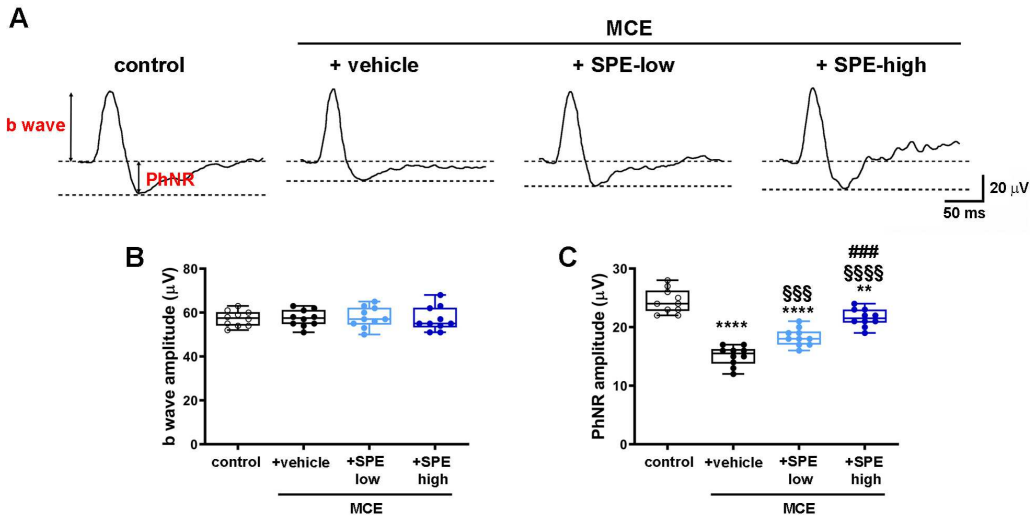

Figure 3. SPE did not affect photopic b-wave amplitude, but it attenuated the MCE-induced reduction of PhNR amplitude. (**A**) Representative ERG waveforms recorded using a 3 cd·s/m^2 stimulus on a 30 cd·s/m^2 rod-saturating background light in control rats and in rats injected with MCE which were fed with either vehicle or SPE. (**B**) Photopic b-wave amplitude. (**C**) PhNR amplitude. MCE reduced PhNR amplitude, an effect that was attenuated by SPE in a dose-dependent manner. Data are shown as box plots with minimum to maximum whiskers ($n = 10$ for each group). $^{**}P < 0.01$and $^{****}P < 0.0001$ versus control; $^{§§§}P < 0.001$and $^{§§§§}P < 0.0001$ versus MCE; $^{###}P < 0.001$ versus SPE-low (one-way ANOVA followed by the multiple-comparison Tukey's test).

and western blot. In particular, the colorimetric analysis was performed to evaluate the levels of oxidation-deriving products including MDA, 8-OH-dG, and 4-HNE, as well as depletion of the endogenous antioxidant GSH. Western blot was used to assess the levels of Nrf2, the master transcriptional regulator of genes involved in cellular antioxidant response, and of HO-1, one of the main Nrf2 target genes (Fig. 7). Retinal levels of MDA (Fig. 7A), 8-OH-dG (Fig. 7B), and 4-HNE (Fig. 7C) were significantly increased in rats receiving the intracameral injection of MCE, paralleled by a significant depletion of GSH (Fig. 7D). SPE resulted in a statistically significant dose-dependent inhibition of oxidative stress-related phenomena, with the high SPE dose able to restore 4-HNE and

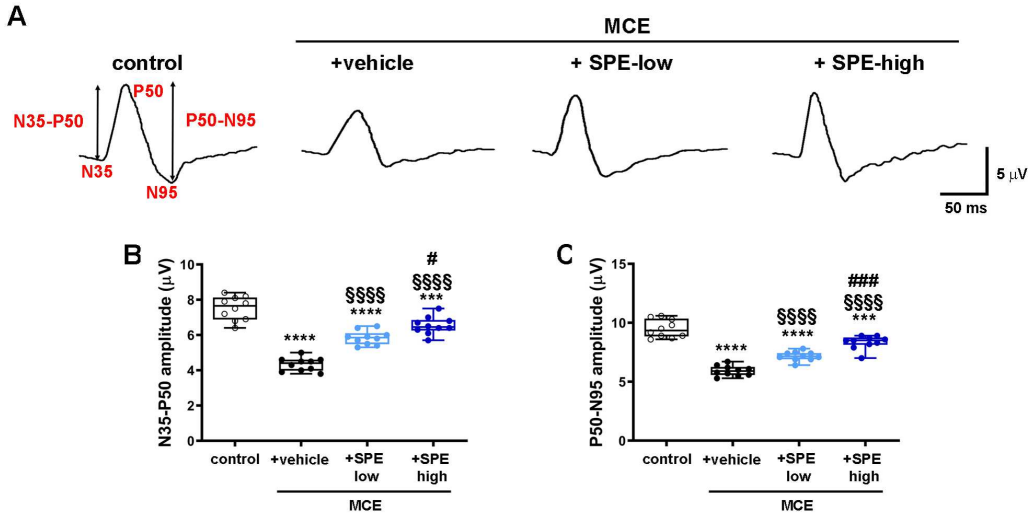

Figure 4. SPE attenuated the MCE-induced reduction of PERG amplitude. (**A**) Representative PERG traces showing the two negative peaks (N35 and N95) and the positive peak P50 in control rats and in rats injected with MCE fed with either vehicle or SPE. (**B**, **C**) Mean amplitudes of the N35–P50 (**B**) and P50–N95 (**C**) waves. MCE reduced the amplitude of both waves, an effect that was substantially attenuated by SPE in a dose dependent manner. Data are shown as box plots with minimum to maximum whiskers ($n = 10$ for each group). $^{***}P < 0.001$ and $^{****}P < 0.0001$ versus control; $^{§§§§}P < 0.0001$ versus MCE; $^{\#}P < 0.05$ and $^{\#\#\#}P < 0.001$ versus SPE-low (one-way ANOVA followed by the multiple-comparison Tukey's test).

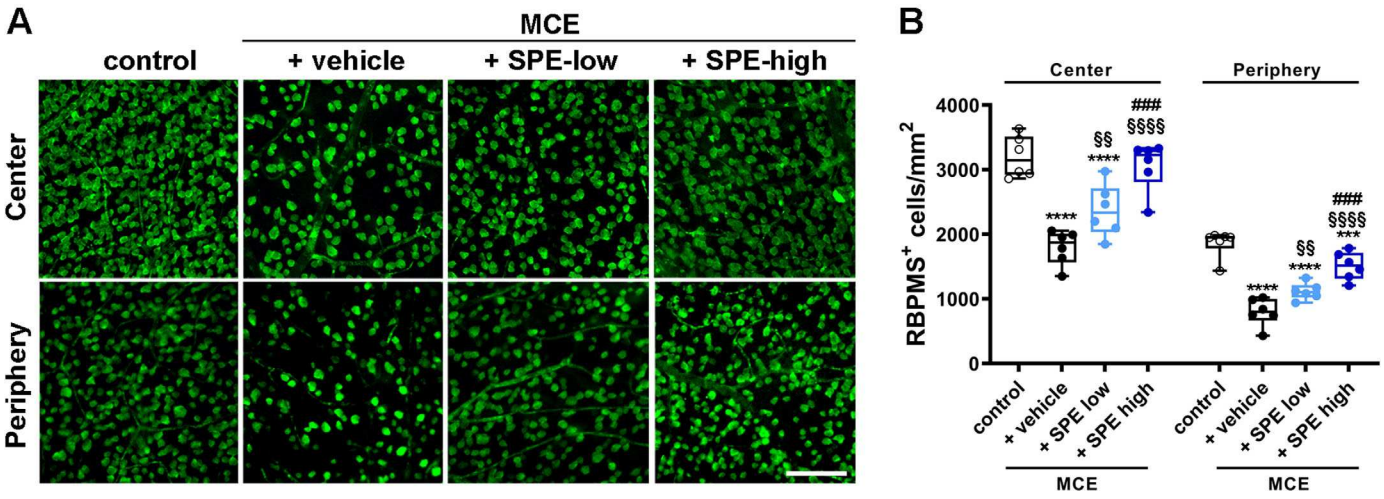

Figure 5. SPE prevented the MCE-induced reduction of RGC density. (**A**) Representative images of RBPMS staining in central and peripheral areas of retinas from control rats and rats injected with MCE which were fed with either vehicle or SPE. *Scale bar*: 100 µm. (**B**) Analysis of RBPMS-positive cell density, differentially sampled from the peripheral and central areas of the retina. MCE reduced RGC density, an effect that was attenuated or prevented by SPE in a dose-dependent manner. Data are shown as box plots with minimum to maximum whiskers ($n = 10$ for each group). $^{***}P < 0.001$ and $^{****}P < 0.0001$ versus control; $^{§§}P < 0.01$ and $^{§§§§}P < 0.0001$ versus MCE; $^{\#\#\#}P < 0.0001$ versus SPE dose (one-way ANOVA followed by the multiple-comparison Tukey's test).

GSH to healthy control levels. The MCE-induced increase in oxidative products was reflected in the induction of the cellular antioxidant response as demonstrated by the rise in Nrf2 (Figs. 7E, 7F) and subsequent increase in HO-1 (Figs. 7E, 7G) protein levels. The effect of SPE in counteracting MCE-induced oxidative stress status was also supported by the related dose-dependent attenuation of the cellular antioxidant response. MCE-induced increments of HO-1 levels were substantially attenuated by low- and high-dose SPE. Furthermore, high-dose SPE completely restored Nrf2 to the levels observed in healthy control animals.

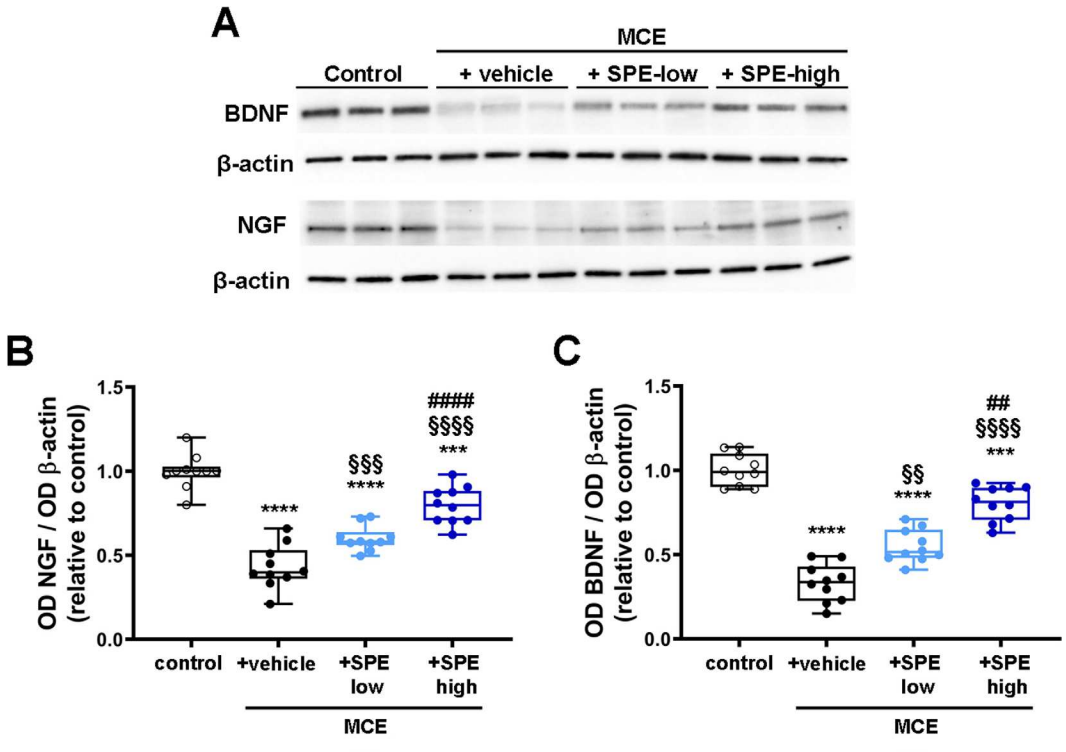

Figure 6. SPE attenuated the MCE-induced reduction in neurotrophin levels. (**A**) Representative western blots from retinal homogenates of control rats or rats that received MCE which were fed with either vehicle or SPE. (**B**, **C**) Densitometric analysis of the levels of BDNF (**B**) and NGF (**C**). MCE resulted in decreased levels of both BDNF and NGF, effects that were substantially attenuated by SPE in a dose-dependent manner. Data are shown as box plots with minimum to maximum whiskers ($n = 10$ for each group). $^{***}P < 0.001$ and $^{****}P < 0.0001$ versus control; $^{§§}P < 0.01$, $^{§§§}P < 0.001$, and $^{§§§§}P < 0.0001$ versus MCE; $^{\#\#}P < 0.01$ and $^{\#\#\#\#}P < 0.0001$ versus SPE dose (one-way ANOVA followed by the multiple-comparison Tukey's test).

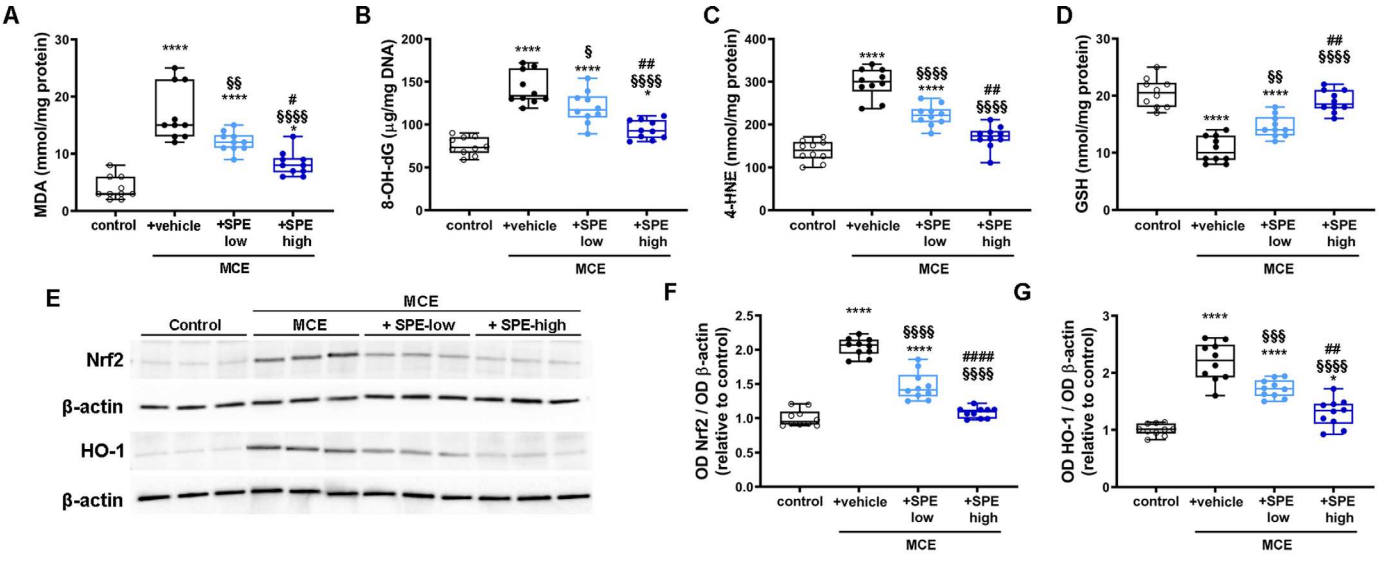

Figure 7. SPE prevented MCE-induced oxidative stress and the subsequent cellular antioxidant response. (**A**–**D**) Levels of oxidative stress biomarkers in control rats or rats that received MCE fed with either vehicle or SPE. MCE resulted in increased levels of MDA (**A**), 8-OH-dG (**B**), and 4-HNE (**C**) and in decreased levels of GSH (**D**). These effects were almost completely prevented or substantially attenuated by SPE in a dose-dependent manner. (**E**) Representative western blots from retinal homogenates of control rats or rats that received MCE fed with either vehicle or SPE. (**F**, **G**) Densitometric analysis of the levels of Nrf2 (**F**) and HO-1 (**G**). MCE resulted in increased levels of both Nrf2 and HO-1, effects that were completely prevented or attenuated by SPE in a dose-dependent manner. Data are shown as box plots with minimum to maximum whiskers ($n = 10$ for each group). $^{*}P < 0.05$ and $^{****}P < 0.0001$ versus control; $^{§}P < 0.05$, $^{§§}P < 0.01$, and $^{§§§§}P < 0.0001$ versus MCE; $^{\#}P < 0.05$ and $^{\#\#}P < 0.01$ versus SPE-low (one-way ANOVA followed by the multiple-comparison Tukey's test).

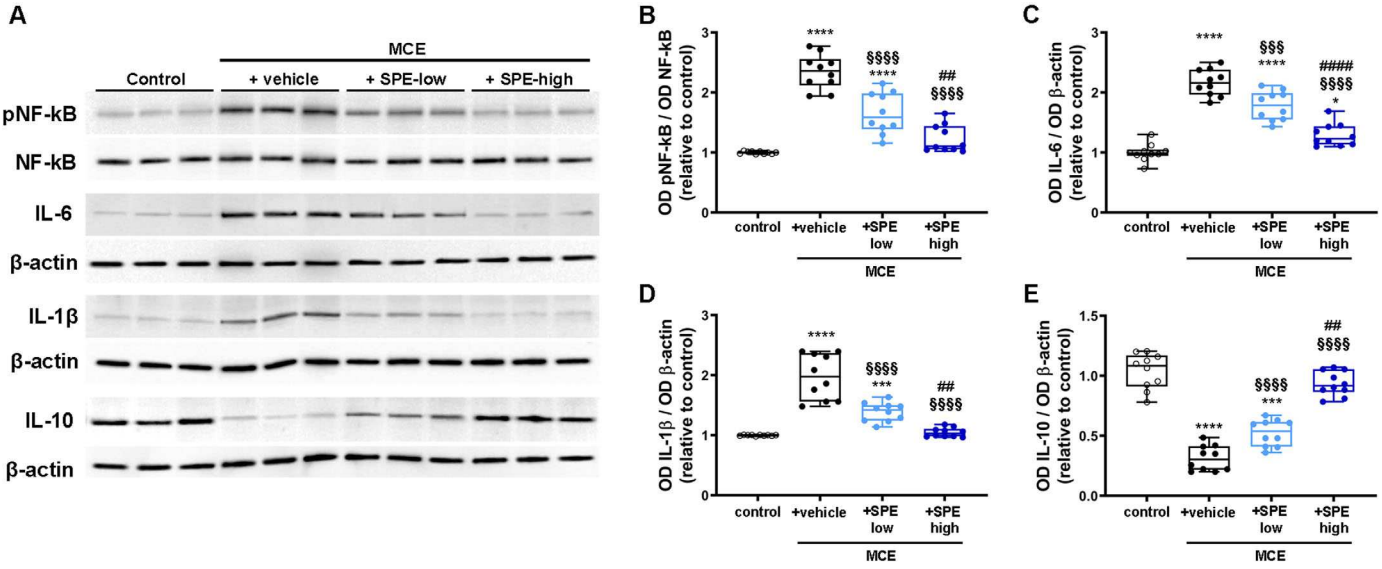

Figure 8. SPE prevented the MCE-induced increase in inflammatory response. (**A**) Representative western blots from retinal homogenates of control rats or rats that received MCE which were fed with either vehicle or SPE. (**B**–**E**) Densitometric analysis of the levels of the phosphorylated form of NF-κB (**B**), IL-6 (**C**), IL-1β (**D**), and IL-10 (**E**). MCE resulted in increased levels of the phosphorylated form of NF-κB, IL-6, and IL-1β and in decreased levels of IL-10. These effects were completely prevented or substantially attenuated by SPE in a dose-dependent manner. Data are shown as box plots with minimum to maximum whiskers ($n = 10$ for each group). $^{*}P < 0.05$, $^{***}P < 0.001$, and $^{****}P < 0.0001$ versus control; $^{\S\S}P < 0.01$ and $^{\S\S\S\S}P < 0.0001$ versus MCE; $^{\#}P < 0.01$, $^{\#\#}P < 0.01$, and $^{\#\#\#\#}P < 0.0001$ versus SPE-low (one-way ANOVA followed by the multiple-comparison Tukey's test).

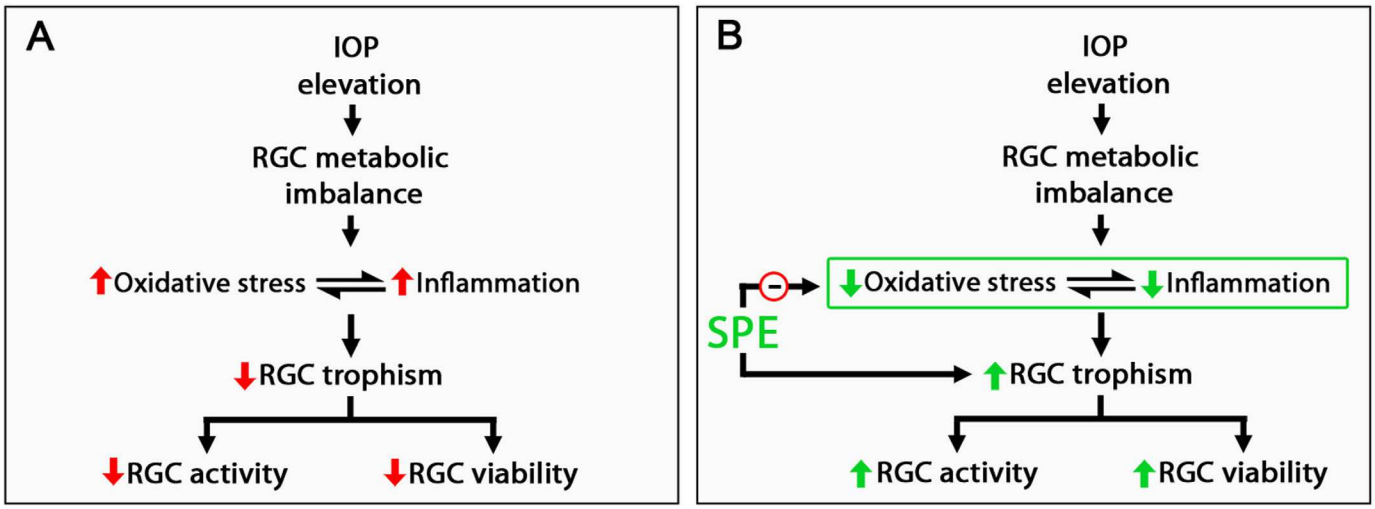

Figure 9. Schematic representation of SPE effects on glaucoma pathophysiological mechanisms. (**A**) In glaucoma, several factors coincide, either increasing IOP or not, to create an imbalance in the metabolic activity of RGCs. The increase in oxidative stress and inflammation, two processes that mutually interact one another, as well as the consequent reduction in RGC trophism, lead to a reduction in RGC activity and viability. (**B**) SPE likely exerts an antioxidant effect due to the scavenging properties of its main component, RA, and other spearmint polyphenols, thus inhibiting the IOP-induced increases in oxidative stress. The inhibition of oxidative processes consequently impacts the inflammatory response and reduces inflammation, thus decreasing the RGC metabolic alterations that typically occur in both hypertensive and normotensive glaucoma. The restoration of the metabolic balance is reflected by the enhancement of RGC neural trophism which correlates with the preservation of both cell activity and viability.

Spearmint Extract Counteracts the MCE-Induced Inflammatory Response in a Dose-Dependent Manner

Inflammatory processes involved in RGC degeneration were analyzed by testing the levels of the active (phosphorylated) form of NF-κB, as one of the master transcriptional regulators of the pro-inflammatory response, and the related levels of pro- and anti-inflammatory cytokines. The western blot shown in Figure 8 revealed that the intracameral injection of MCE resulted in an incremental increase in the phosphorylated form of NF-κB (pNF-κB) (Figs. 8A, 8B), which was paralleled by an increase in pro-inflammatory cytokines IL-6 (Figs. 8A, 8C) and IL-1β (Figs. 8A, 8D) and a significant decrease in the anti-inflammatory cytokine IL-10 (Figs. 8A, 8E). Oral supplementation with SPE exerted a significant dose-dependent inhibition of the pro-inflammatory processes, as demonstrated by the significant decrease in pNF-κB with subsequent reduced levels of IL-6 and IL-1β, and the increase in anti-inflammatory cytokine IL-10 compared to vehicle-treated MCE rats. In this context, the high dose of SPE returned pNF-κB, IL-1β, and IL-10 to healthy control levels.

Discussion

Despite many reports describing successful neuroprotection in animal models of glaucoma, the clinical translatability of their results has been extremely limited, possibly because no single model recapitulates all aspects of glaucoma.[40] However, thanks to basic research, our understanding of the molecular basis of glaucoma pathogenesis is continually increasing, thus opening the door to the development of effective neuroprotective strategies and to their clinical translation. Here, we observed that SPE reduces glaucoma-induced retinal dysfunction acting downstream of the IOP elevation with no effects on IOP itself. In fact, all groups receiving MCE injections exhibited elevated IOP, providing evidence for the validity of the MCE model for reproducing a glaucomatous-like ocular hypertension. Animals exposed to both low- and high-dose SPE showed reduced RGC loss and attenuated functional impairment as a result of the increased IOP. Importantly, the preservation of RGC function and cell density was dose dependent. Exploration of potential underlying mechanisms for the neuroprotection revealed significant, dose-dependent decreases in markers of oxidative stress and inflammation along with the novel finding that oral supplementation with a natural plant extract led to elevated levels of the neurotrophins BDNF and NGF under the glaucomatous conditions.

Glaucoma provides a model of neurodegeneration in which IOP elevation represents one of the most recurrent and acknowledged risk factors promoting and associated with glaucomatous progression and RGC neurodegeneration.[5] Glaucoma is understood to be a multifactorial condition influenced by other mechanisms such as oxidative stress, inflammation, and lack of neural trophic support. In addition, progression of neurodegenerative disease is influenced by genetics, environmental risk factors, and nutritional support, evidenced by the fact that some individuals with elevated IOP never develop glaucoma.

In addition to being commonly monitored as a clinical parameter for the diagnosis and follow-up of glaucoma, IOP elevation currently represents the main target for pharmaceutical treatments attempting to counteract glaucoma progression.[6] Despite the efficacy of this approach in influencing glaucomatous neurodegeneration, obvious limitations have emerged regarding the actual resolutive effects of treatments targeting IOP reduction and their applicability to IOP-independent glaucomatous neurodegeneration.[41] In effect, IOP elevation is not an overall feature of all glaucoma subgroups because it could manifest later in the progression of the disease or even not occur, as in the case of normotensive glaucoma. These discrepancies would highlight the limitations of current IOP-exclusive treatment strategies for glaucoma management and strengthen the need to seek complementary treatment strategies to counteract IOP-independent neurodegenerative mechanisms.

Recent advancements in the understanding of neurodegenerative phenomena in glaucoma have pointed to a central role of RGC metabolic imbalance as an early alteration promoting neural complications and cell death in preliminary stages of the disease.[42] In effect, RGCs are known to display high metabolic needs to fulfill their role in the visual pathway, making them particularly susceptible to metabolic stress and bioenergetic insufficiency.[43] Altered metabolism in RGCs would result in mitochondrial dysfunction, thus promoting abnormal surges of reactive oxygen species, ultimately promoting oxidative cell damage.[11] Moreover, oxidative stress triggers the activation of inflammatory processes, further promoting cell damage and contributing to the loss of RGC activity and viability.[10] Finally, cell loss in the retina coupled with restricted retrograde transportation in the RGC axon could result in reduced RGC neurotrophin levels.[44] Therefore, metabolic imbalances of RGCs could contribute to inflammatory, oxidative, and

apoptotic damages seen during the early stages of glaucoma.

As shown in this study, the RGC oxidative, inflammatory and neurotrophic damage typical of glaucomatous conditions is well reproduced by the MCE model of glaucoma. In effect, the increase in IOP promotes selective RGC dysfunction, as demonstrated by the decreased amplitude of the RGC-specific ERG, in agreement with previous studies in rodents.[28,33] These alterations correlate with the loss of RGC density and decreased levels of neurotrophins. In line with the central role played by oxidative stress in glaucomatous phenomena,[45] MCE-induced losses in RGC activity and viability are associated with an increased oxidative stress paralleled by significant induction of the inflammatory response.

The emerging roles played by oxidative stress, inflammation, and neurotrophic depletion in the genesis and progression of glaucomatous neurodegeneration have opened up the possibility of using complementary supplementation of bioactive nutrients with antioxidant, anti-inflammatory, and neurotrophic properties, given their beneficial effects on the preservation of RGC activity and viability without treatment invasiveness.[46] In this respect, the use of SPE as a bioactive ingredient for the complementary nutritional support in the management of glaucoma represents a promising option, given its high content in antioxidant/anti-inflammatory polyphenols. SPE has already displayed significant beneficial effects on age-related cognitive decline in healthy subjects, as well as on neural damages in a mouse model of stroke. These conditions, as well as glaucoma, share increases in oxidative stress and inflammation as common denominators.[18–20]

The present data demonstrate that oral supplementation with SPE starting at 2 weeks before MCE injection diminished (at low dose) or completely prevented (at high dose) IOP-induced neurodegeneration, as evidenced by the maintenance of both RGC density and RGC activity. Together with previous findings demonstrating the efficacy of SPE in the context of a multicomponent formulation,[28] the present results point on the effectiveness of SPE, either alone or in combination, in counteracting glaucoma-associated neurodegeneration. In addition to its ameliorative effects on RGC activity and viability, SPE does not induce any changes in the normal outer retinal function, as ERG parameters related to the activity of photoreceptors or second-order retinal neurons are unaltered. Of note, SPE exerts neuroprotection independently from any hypotensive effect, suggesting that it acts on downstream effectors that are affected by an increase in IOP. In this respect, because SPE is rich in RA and other polyphenol compounds such as salvianolic and lithospermic acid, which are known for their anti-inflammatory and antioxidant properties,[47,48] the effects of SPE on NF-κB activity and inflammatory cytokines, as well as on markers of oxidative stress, could be expected. However, the finding that GSH levels may be completely preserved by SPE is noteworthy, as it indicates that this polyphenol-rich ingredient may restore the non-enzymatic antioxidant endogenous defenses, which act as rapid inactivators of radicals and oxidants. Nevertheless, the novel finding that SPE may attenuate the reduced production or availability of neurotrophins seen in the glaucomatous condition is of particular importance. In fact, the lack of neurotrophin supply to RGCs is a mechanism common to different retinal neurodegenerative diseases[13,49] and the use of neurotrophins to counteract retinal degeneration has been widely discussed.[50] Furthermore, neurotrophins are key for neuronal cell survival and synaptic plasticity in the optical system and are involved in learning and memory processes.[31,32] The metabolic and neurotrophic imbalances in retinal tissues can be related to the morphological and functional changes along the visual pathway and in numerous brain areas outside the visual pathway known to affect the CNS in glaucoma.[7]

The present finding, therefore, may open the door for the use of SPE supplementation as nutritional support in patients with glaucoma, as well as for patients suffering from other neurodegenerative retinal conditions such as retinitis pigmentosa, age-related macular degeneration, or optic neuritis.[51–53] Moreover, the effect of SPE in the preservation of neurotrophin levels under neural stress conditions may further expand the suitability of including this ingredient in nutritional support dedicated to brain disorders, in which altered neurotrophism classically drives neurovascular breakout.[54] Although this is currently a hypothesis that requires specific investigations, the effects of SPE previously observed on the blood–brain barrier[18] and in models of stroke[19] may point on this direction. Nevertheless, the present results regarding SPE effects on neurotrophins provide an additional proposed mechanism for the cognitive function benefits already observed in clinical trials with SPE.[23,25]

If viewed from a translational perspective, the present study has potential limitations that are linked to the model used here. In the rat, IOP-induced RGC damage occurs over a short period of time, whereas the same damage in humans requires years to manifest. In addition, because MCE blocks aqueous humor outflow, the model used here could be related to primary angle-closure glaucoma, which affects only a

quarter of the glaucoma population despite being the cause of about 50% of glaucoma-related blindness.[55] Another potential limitation is that here we observed a neuroprotective effect of SPE starting with a prophylactic approach; therefore, whether SPE may produce similar results when given only in a therapeutic setting has yet to be proven. Furthermore, it is not obvious what the best time window is in which to start SPE administration in humans not affected by glaucoma in order to obtain effects similar to those observed here. The effects of SPE on the mechanisms underpinning glaucoma development in the MCE rat model are summarized in Figure 9.

Conclusions

The present findings demonstrate the efficacy of SPE, a plant-based clinically studied nootropic ingredient, as a promising nutritional support in modulating neuroprotective mechanisms relevant for the management of glaucoma symptoms. The data emphasize the IOP-independent effects of SPE in reducing markers of oxidative stress and inflammation and promoting neurotrophism, thus highlighting the possibility of its application, either alone or in combination with other ingredients (as already reported in the literature), as a complementary approach in support of hypotensive treatments aimed at optimizing the management of glaucoma. We are aware that an important limitation in the clinical management of glaucoma is establishing the actual risk of glaucoma development in patients, as the diagnosis emerges in relatively advanced stages of the disease. However, a growing body of evidence has recently highlighted the possibility of identifying, over the progression of glaucoma in patients, the so-called "critical period." It would correspond to oxidative stress- and inflammatory-related RGC dyshomeostasis preceding cell loss that could be detected with the use of sensitive electrophysiological tests such as PERG.[56]

Acknowledgments

The authors thank Tiziana Cintio for her assistance with animal housing and care. These data were presented (E-abstract 3880242) at the ARVO meeting held in New Orleans, LA, in April 2023.

Supported by a grant from Kemin Foods, L.C. (Des Moines, IA) to MDM. Kemin Foods, L.C., had no direct role in the collection, analyses, or interpretation of the data.

Disclosure: **R. Amato**, None; **A. Canovai**, None; **A. Melecchi**, None; **S. Maci**, (E); **F. Quintela**, (E); **B.A. Fonseca**, (E); **M. Cammalleri**, None; **M. Dal Monte**, (F)

References

1. Allison K, Patel D, Alabi O. Epidemiology of glaucoma: the past, present, and predictions for the future. *Cureus*. 2020;12:e11686.
2. Tham YC, Li X, Wong TY, Quigley HA, Aung T, Cheng CY. Global prevalence of glaucoma and projections of glaucoma burden through 2040: a systematic review and meta-analysis. *Ophthalmology*. 2014;121:2081–2090.
3. Gallo Afflitto G, Aiello F, Cesareo M, Nucci C. Primary open angle glaucoma prevalence in Europe: a systematic review and meta-analysis. *J Glaucoma*. 2022;31:783–788.
4. Kang JM, Tanna AP. Glaucoma. *Med Clin North Am*. 2021;105:493–510.
5. Vernazza S, Oddone F, Tirendi S, Bassi AM. Risk factors for retinal ganglion cell distress in glaucoma and neuroprotective potential intervention. *Int J Mol Sci*. 2021;22:7994.
6. Kuo CY, Liu CJL. Neuroprotection in glaucoma: basic aspects and clinical relevance. *J Pers Med*. 2022;12:1884.
7. Nuzzi R, Vitale A. Cerebral modifications in glaucoma and macular degeneration: analysis of current evidence in literature and their implications on therapeutic perspectives. *Eye Brain*. 2021;13:159–173.
8. Lawlor M, Danesh-Meyer H, Levin LA, Davagnanam I, De Vita E, Plant GT. Glaucoma and the brain: trans-synaptic degeneration, structural change, and implications for neuroprotection. *Surv Ophthalmol*. 2018;63:296–306.
9. Adornetto A, Rombolà L, Morrone LA, et al. Natural products: evidence for neuroprotection to be exploited in glaucoma. *Nutrients*. 2020;12:3158.
10. Baudouin C, Kolko M, Melik-Parsadaniantz S, Messmer EM. Inflammation in glaucoma: from the back to the front of the eye, and beyond. *Prog Retin Eye Res*. 2021;83:100916.
11. Kimura A, Namekata K, Guo X, Noro T, Harada C, Harada T. Targeting oxidative stress for treatment of glaucoma and optic neuritis. *Oxid Med Cell Longev*. 2017;2017:2817252.

12. Lambuk L, Mohd Lazaldin MA, Ahmad S, et al. Brain-derived neurotrophic factor-mediated neuroprotection in glaucoma: a review of current state of the art. *Front Pharmacol*. 2022;13:875662.
13. Fudalej E, Justyniarska M, Kasarełło K, Dziedziak J, Szaflik JP, Cudnoch-Jędrzejewska A. Neuroprotective factors of the retina and their role in promoting survival of retinal ganglion cells: a review. *Ophthalmic Res*. 2021;64:345–355.
14. Kimura A, Namekata K, Guo X, Harada C, Harada T. Neuroprotection, growth factors and BDNF-TrkB signalling in retinal degeneration. *Int J Mol Sci*. 2016;17:1584.
15. Cirlini M, Mena P, Tassotti M, et al. Phenolic and volatile composition of a dry spearmint (*Mentha spicata* L.) extract. *Molecules*. 2016;21:1007.
16. Greaves J, Narasimhamoorthy B, Wildgen S, Barkley R, Ruden S. Spearmint plant denominated KI-MsEM0110. US patent US9545075B2, January 17, 2017.
17. Narasimhamoorthy B., Greaves J., Wildgen S., Barkley R., Ruden S. Spearmint plant denominated KI-MsEM0042. US patent US9545076B2, January 17, 2017.
18. Bian Y, Yamashita T, Taira Y, et al. A polyphenolic complex attenuates inflammatory response and blood-brain barrier disruption. *Curr Neurovasc Res*. 2020;17:286–293.
19. Taira Y, Yamashita T, Bian Y, et al. Antioxidative effects of a novel dietary supplement Neumentix in a mouse stroke model. *J Stroke Cerebrovasc Dis*. 2020;29:104818.
20. Farr S, Fonseca B, Herrlinger K, et al. Selective reduction of oxidative stress markers in the SAMP8 mouse brain by a distinct spearmint extract with antioxidant properties. In: *American Academy of Neurology (AAN) 67th Annual Meeting Abstracts* (abstract P4.078). Minneapolis, MN: American Academy of Neurology.
21. Zhang Y, Jia X, Chen X, et al. L-theanine and Neumentix mixture improves sleep quality and modulates brain neurotransmitter levels in mice. *Ann Palliat Med*. 2021;10:4572–4581.
22. Fonseca BA, Herrlinger KA. The effects of a proprietary spearmint extract on neurogenesis rates in rat hippocampal neurons. *Neurology*. 2016:84:7–105.
23. Falcone PH, Nieman KM, Tribby AC, et al. The attention-enhancing effects of spearmint extract supplementation in healthy men and women: a randomized, double-blind, placebo-controlled, parallel trial. *Nutr Res*. 2019;64:24–38.
24. Falcone PH, Tribby AC, Vogel RM, et al. Efficacy of a nootropic spearmint extract on reactive agility: a randomized, double-blind, placebo-controlled, parallel trial. *J Int Soc Sports Nutr*. 2018;15:58.
25. Herrlinger KA, Nieman KM, Sanoshy KD, et al. Spearmint extract improves working memory in men and women with age-associated memory impairment. *J Altern Complement Med*. 2018;24:37–47.
26. Tubbs AS, Kennedy KER, Alfonso-Miller P, Wills CCA, Grandner MA. A randomized, double-blind, placebo-controlled trial of a polyphenol botanical blend on sleep and daytime functioning. *Int J Environ Res Public Health*. 2021;18:3044.
27. Nieman KM, Sanoshy KD, Bresciani L, et al. Tolerance, bioavailability, and potential cognitive health implications of a distinct aqueous spearmint extract. *J Funct Food Health Dis*. 2015; 5:165–187.
28. Cammalleri M, Dal Monte M, Amato R, Bagnoli P, Rusciano D. A dietary combination of forskolin with homotaurine, spearmint and B vitamins protects injured retinal ganglion cells in a rodent model of hypertensive glaucoma. *Nutrients*. 2020;12:1189.
29. Locri F, Cammalleri M, Dal Monte M, Rusciano D, Bagnoli P. Protective efficacy of a dietary supplement based on forskolin, homotaurine, spearmint extract, and group B vitamins in a mouse model of optic nerve injury. *Nutrients*. 2019;11:2931.
30. Rodriguez AR, Pérez de Sevilla Müller L, Brecha NC. The RNA binding protein RBPMS is a selective marker of ganglion cells in the mammalian retina. *J Comp Neurol*. 2014;522:1411–1443.
31. Wang H, Wang R, Thrimawithana T, et al. The nerve growth factor signaling and its potential as therapeutic target for glaucoma. *Biomed Res Int*. 2014;2014:759473.
32. Li Y, Li F, Qin D, et al. The role of brain derived neurotrophic factor in central nervous system. *Front Aging Neurosci*. 2022;14:986443.
33. Dal Monte M, Cammalleri M, Amato R, et al. A topical formulation of melatoninergic compounds exerts strong hypotensive and neuroprotective effects in a rat model of hypertensive glaucoma. *Int J Mol Sci*. 2020;21:9267.
34. Dal Monte M, Cammalleri M, Pezzino S, et al. Hypotensive effect of nanomicellar formulation of melatonin and agomelatine in a rat model: significance for glaucoma therapy. *Diagnostics (Basel)*. 2020;10:138.
35. Narasimhamoorthy B, Zhao LQ, Liu X, Yang W, Greaves JA. Differences in the chemotype of two native spearmint clonal lines selected for ros-

marinic acid accumulation in comparison to commercially grown native spearmint. *Ind Crop Prod*. 2015;63:87–91.
36. Reagan-Shaw S, Nihal M, Ahmad N. Dose translation from animal to human studies revisited. *FASEB J*. 2008;22:659–661.
37. Porciatti V. Electrophysiological assessment of retinal ganglion cell function. *Exp Eye Res*. 2015;141:164–170.
38. Chang D, Sha Q, Zhang X, et al. The evaluation of the oxidative stress parameters in patients with primary angle-closure glaucoma. *PLoS One*. 2011;6:e27218.
39. Gherghel D, Mroczkowska S, Qin L. Reduction in blood glutathione levels occurs similarly in patients with primary-open angle or normal tension glaucoma. *Invest Ophthalmol Vis Sci*. 2013;54:3333–3339.
40. Guymer C, Wood JPM, Chidlow G, Casson RJ. Neuroprotection in glaucoma: recent advances and clinical translation. *Clin Exp Ophthalmol*. 2019;47:88–105.
41. Weinreb RN, Aung T, Medeiros FA. The pathophysiology and treatment of glaucoma: a review. *JAMA*. 2014;311:1901–1911.
42. Casson RJ, Chidlow G, Crowston JG, Williams PA, Wood JPM. Retinal energy metabolism in health and glaucoma. *Prog Retin Eye Res*. 2021;81:100881.
43. Inman DM, Harun-Or-Rashid M. Metabolic vulnerability in the neurodegenerative disease glaucoma. *Front Neurosci*. 2017;11:146.
44. Quigley HA, McKinnon SJ, Zack DJ, et al. Retrograde axonal transport of BDNF in retinal ganglion cells is blocked by acute IOP elevation in rats. *Invest Ophthalmol Vis Sci*. 2000;41:3460–3466.
45. Tezel G. Oxidative stress in glaucomatous neurodegeneration: mechanisms and consequences. *Prog Retin Eye Res*. 2006;25:490–513.
46. Garcia-Medina JJ, Rubio-Velazquez E, Lopez-Bernal MD, et al. Glaucoma and antioxidants: review and update. *Antioxidants (Basel)*. 2020;9:1031.
47. Luo C, Zou L, Sun H, et al. A review of the anti-inflammatory effects of rosmarinic acid on inflammatory diseases. *Front Pharmacol*. 2020;11:153.
48. Nadeem M, Imran M, Aslam Gondal T, et al. Therapeutic potential of rosmarinic acid: a comprehensive review. *Appl Sci*. 2019;9:3139.
49. Gokoffski KK, Peng M, Alas B, Lam P. Neuroprotection and neuro-regeneration of the optic nerve: recent advances and future directions. *Curr Opin Neurol*. 2020;33:93–105.
50. Daly C, Ward R, Reynolds AL, Galvin O, Collery RF, Kennedy BN. Brain-derived neurotrophic factor as a treatment option for retinal degeneration. *Adv Exp Med Biol*. 2018;1074:465–471.
51. Amadoro G, Latina V, Balzamino BO, et al. Nerve growth factor-based therapy in Alzheimer's disease and age-related macular degeneration. *Front Neurosci*. 2021;15:735928.
52. Khan RS, Ross AG, Willett K, et al. Amnion-derived multipotent progenitor cells suppress experimental optic neuritis and myelitis. *Neurotherapeutics*. 2021;18:448–459.
53. Rocco ML, Calzà L, Aloe L. NGF and retinitis pigmentosa: structural and molecular studies. *Adv Exp Med Biol*. 2021;1331:255–263.
54. da Silva Meirelles L, Simon D, Regner A. Neurotrauma: the crosstalk between neurotrophins and inflammation in the acutely injured brain. *Int J Mol Sci*. 2017;18:1082.
55. Wright C, Tawfik MA, Waisbourd M, Katz LJ. Primary angle-closure glaucoma: an update. *Acta Ophthalmol*. 2016;94:217–225.
56. Porciatti V, Chou TH. Using noninvasive electrophysiology to determine time windows of neuroprotection in optic neuropathies. *Int J Mol Sci*. 2022;23:5751.

Canovai *et al.*
Acta Neuropathologica Communications (2023) 11:146
https://doi.org/10.1186/s40478-023-01642-6

Acta Neuropathologica Communications

RESEARCH

Open Access

Pyrroloquinoline quinone drives ATP synthesis in vitro and in vivo and provides retinal ganglion cell neuroprotection

Alessio Canovai[1,2], James R. Tribble[1], Melissa Jöe[1], Daniela Y. Westerlund[1], Rosario Amato[2], Ian A. Trounce[3], Massimo Dal Monte[2] and Pete A. Williams[1*]

Abstract

Retinal ganglion cells are highly metabolically active requiring strictly regulated metabolism and functional mitochondria to keep ATP levels in physiological range. Imbalances in metabolism and mitochondrial mechanisms can be sufficient to induce a depletion of ATP, thus altering retinal ganglion cell viability and increasing cell susceptibility to death under stress. Altered metabolism and mitochondrial abnormalities have been demonstrated early in many optic neuropathies, including glaucoma, autosomal dominant optic atrophy, and Leber hereditary optic neuropathy. Pyrroloquinoline quinone (PQQ) is a quinone cofactor and is reported to have numerous effects on cellular and mitochondrial metabolism. However, the reported effects are highly context-dependent, indicating the need to study the mechanism of PQQ in specific systems. We investigated whether PQQ had a neuroprotective effect under different retinal ganglion cell stresses and assessed the effect of PQQ on metabolic and mitochondrial processes in cortical neuron and retinal ganglion cell specific contexts. We demonstrated that PQQ is neuroprotective in two models of retinal ganglion cell degeneration. We identified an increased ATP content in healthy retinal ganglion cell-related contexts both in in vitro and in vivo models. Although PQQ administration resulted in a moderate effect on mitochondrial biogenesis and content, a metabolic variation in non-diseased retinal ganglion cell-related tissues was identified after PQQ treatment. These results suggest the potential of PQQ as a novel neuroprotectant against retinal ganglion cell death.

Keywords Pyrroloquinoline quinone (PQQ), Mitochondria, Metabolism, Metabolomics, ATP, Retinal ganglion cell, Retina, Optic nerve, Neuroprotection

Introduction

Retinal ganglion cells (RGCs) are the output neurons of the retina, the axons of which form the optic nerve, connecting the eye to the brain. RGCs are highly metabolically and physiologically active cells, requiring a constant supply of ATP to ensure proper function. A finely regulated metabolism and perfectly balanced mitochondrial function are fundamental to maintain ATP at a physiological level. Imbalances in these mechanisms can be detrimental to RGC viability by depleting ATP, rendering RGCs susceptible to damage [1]. Altered metabolism and mitochondrial abnormalities have been reported to

*Correspondence:
Pete A. Williams
pete.williams@ki.se
[1] Division of Eye and Vision, Department of Clinical Neuroscience, St. Erik Eye Hospital, Karolinska Institutet, Stockholm, Sweden
[2] Department of Biology, University of Pisa, Pisa, Italy
[3] Department of Surgery, Centre for Eye Research Australia, Royal Victorian Eye and Ear Hospital, Ophthalmology, University of Melbourne, Melbourne, VIC, Australia

occur early in the pathogenesis of many optic neuropathies, including glaucoma, autosomal dominant optic atrophy (ADOA), and Leber hereditary optic neuropathy (LHON), where progressive RGC dysfunction and degeneration are typical hallmarks of disease [2–8]. Reducing bioenergetic insufficiency by buffering metabolic stress, positively regulating mitochondrial mechanisms, and restoring ATP levels have all been demonstrated to be neuroprotective to RGCs [7, 9]. A treatment that can prevent metabolic dysfunction and arrest RGC degeneration is highly sought after. There is strong potential for bioenergetic compounds which could be supplemented in diet, adjuvant to existing medication to increase RGC resilience, and with better side effect profiles.

Pyrroloquinoline quinone (PQQ) is a quinone cofactor first described in bacterial dehydrogenases [10]. It has been considered as a 'new vitamin' given its nutritional importance on mammalian growth, reproduction, and development demonstrated by a wide range of abnormalities when PQQ is absent in the diet [11, 12]. PQQ is not synthetized de novo in mammals, but is instead present in several foods, such as parsley, green pepper, spinach, kiwi, and soybeans, thus giving the possibility to consume PQQ through dietary supplementation [13]. PQQ administration has a good safety profile, with a median LD50 of 0.5–2.0 g/kg in rats, and no signs of toxic effects when treated long term via oral gavage [14]. This suggests a strong potential for PQQ as a compound to support retinal ganglion cell health.

Several studies have reported an effect of PQQ on metabolism and mitochondrial mechanisms, acting as an enzyme cofactor [15], regulating nicotinamide adenine dinucleotide (NAD) content [16], increasing oxidative phosphorylation (OXPHOS) and ATP production [17], and altering mitochondrial dynamics and content through the regulation of pathways particularly involved in mitochondrial biogenesis [18, 19]. However, such effects are highly context-dependent and heterogeneous, dictating the necessity to study, in depth, the mechanism of PQQ in specific systems. Although there is some evidence suggesting a putative neuroprotection of PQQ in models of acute damage in the central nervous system (CNS) [20–23], the role of PQQ in metabolism and mitochondrial content in a neuronal context has not been extensively investigated.

In this study, we explored neuroprotection exerted by PQQ in models of RGC degeneration where bioenergetic capacity is compromised. Given the reported ability of PQQ to provide bioenergetic support in other systems, we hypothesized that PQQ could provide neuroprotection by bolstering bioenergetic support. Supporting this hypothesis, we demonstrate that PQQ is neuroprotective in two models of RGC degeneration. In addition, we identify that PQQ administration leads to increased neuronal ATP content in RGC-related tissues both in in vitro and in vivo models. Although we identified a mild effect exerted by PQQ on mitochondrial biogenesis and content, we report a metabolic variation in non-diseased RGC-related tissues. Taken together, these results suggest a potential role of PQQ as a novel neuroprotective compound to improve RGC resilience.

Materials and methods

Animal strain and husbandry

All breeding and experimental procedures were managed in accordance with the Association for Research for Vision and Ophthalmology Statement for the Use of Animals in Ophthalmic and Research. Individual study protocols were accepted by Stockholm's Committee for Ethical Animal Research (10389-2018). Animals were housed in a regulated environment, (12 h light/12 h dark cycle) and fed with food and water ad libitum. C57BL/6J (B6J) and MitoV (strain information detailed below) mouse strains were bred and used at 12–20 weeks of age. PQQ disodium salt (Mitsubishi Gas Chemical Company Inc., Tokyo, Japan) was dissolved in DMSO and diluted in Hank's balanced salt solution (without $CaCl_2$, $MgCl_2$ and phenol red) (HBSS; Gibco). Mice were treated with either vehicle (HBSS) or 20 mg/kg PQQ i.p. either for a single injection (short-term) or chronically every 48 h for 2 weeks (long-term) as further indicated. In a subset of experiments, PQQ was dissolved in drinking water at the concentration of 0.2 mg/mL in order to obtain a daily administration of 20 mg/kg considering an individual mean drinking volume of 3 mL/day. Water was protected from light as PQQ is light sensitive.

Retina axotomy explant model

A retinal axotomy model was performed as previously reported [7]. Briefly, B6J mice (n = 13) were euthanized by cervical dislocation, retinas immediately dissected in ice-cold HBSS and flat mounted on inserts for cell culture (Millicell 0.4 µm pore; Merck) with ganglion cell layer (GCL) up. Retinas were cultured (37 °C, 5% CO_2) in media composed of Neurobasal-A supplemented with 2 mM L-glutamate (GlutaMAX, Gibco), 2% B27, 1% N2, and 1% penicillin/streptomycin (Gibco) in 6-well culture plates. After 2 days, half of the media volume was replaced. For PQQ treated retinas, PQQ was dissolved in the culture media to a concentration of 50 or 100 µM. Retinas were removed from culture to be further processed after 3 days ex vivo (DEV). For controls (0 DEV), eyes were enucleated and retinas directly fixed and processed for immunofluorescent labelling.

Intravitreal rotenone model

Rotenone induced retinal degeneration model was performed following established protocols [7]. B6J mice (n = 20) underwent anesthesia by an intraperitoneal injection of mixed ketamine (37.5 mg/kg) and medetomidine hydrochloride (1.25 mg/kg). Two µl of 10 mM rotenone diluted in DMSO (all Sigma-Aldrich) or DMSO only (control) was bilaterally injected into the vitreous using a 33G tri-beveled needle on a 10 µl glass syringe (WPI). For PQQ treated retinas, PQQ (20 mg/kg) i.p. was administered 24 h prior to and immediately after rotenone injection. Mice were euthanized by cervical dislocation 24 h after rotenone injection and eyes were immediately isolated for further analyses.

Analysis of RGC death and degeneration

Loss of RGCs, loss of nuclei, and nuclear shrinkage in retinal explants (n = 5 retinas from 0 DEV, 9 from 3 DEV, 4 from 3 DEV + 50 µM, 6 from 3 DEV + 100 µM) and rotenone injected retinas (n = 9 DMSO, 9 DMSO + PQQ, 10 rotenone and 9 rotenone + PQQ) were assessed by immunofluorescence through RBPMS and DAPI labelling of flat mounts. Retinal explants at 3 DEV were fixed in 3.7% PFA for 30 min, detached from the cell culture insets and transferred on slides. Eyes from the animals injected with rotenone were fixed in PFA at the same concentration for 1 h immediately after enucleation. Retinas were then dissected in ice-cold HBSS and transferred onto slides. Tissues were isolated using a hydrophobic barrier pen (VWR) and permeabilized with 0.5% Triton X-100 (VWR) in 1 M PBS for 1 h. After blocking in 2% bovine serum albumin (BSA, Fisher Scientific) in 1 M PBS for 1 h, retinas were immunolabelled with rabbit polyclonal anti-RBPMS (NBP2-20112, Novusbio, 1:500) primary antibody at 4 °C overnight. Thereafter, retinas were rinsed by 5 washes in 1 M PBS for 5 min each before labelling with Alexa Fluor 568 conjugated goat anti-rabbit secondary antibody (A11011, Invitrogen, 1:500) for 4 h at room temperature. Tissue was then washed as before and counterstained with DAPI (1 µg/mL in 1 M PBS) for 10 min. After being rinsed once in PBS, tissue was mounted with Fluoromount-G and glass coverslips (Invitrogen). Nail-varnish was used to seal the slides which were kept at 4 °C until further imaging. The acquisition of the images was performed on a Leica DMi8 microscope with a CoolLED pE-300 white LED-based light source and a Leica DFC7000 T fluorescence color camera (all Leica). Six images per retina (40× magnification) were acquired equidistantly at 0, 2, 4, 6, 8, and 10 o'clock from a superior to inferior line through the optic nerve head at an eccentricity of around 1000 µm. Images were cropped to 100 µm × 100 µm squares and the cell counter plugin in Fiji was used to count RBPMS + cells and DAPI nuclei (only round nuclei were considered, thus discarding vascular endothelium). The mean of cell counts per retina was measured across the 6 images and expressed as a density per 0.01 mm^2. For the measurement of nuclear diameter, 30 nuclei from RBPMS-positive cells (or in as many surviving cells in the image) per cropped image were quantified using the line tool, providing an average diameter. The mean diameter from each cropped image was then averaged across the 6 images to obtain a final average diameter per retina.

Luminometry-based ATP and NAD assays

ATP or NAD content was analyzed in vitro and in vivo following a similar protocol. In order to assess how quickly PQQ could be used by cells in vitro to increase ATP and NAD content, ATP and NAD assays were run on treated brain cortex first to make a dose–response curve and then on retina, optic nerve and superior colliculus exposed to a single concentration. A total of 4 hemispheres were harvested from the whole cortex of B6J mice. Each hemisphere was transferred to 800 µl of dispase (5000 U; Corning) and incubated on a Thermomixer C heating block (Eppendorf) at 37 °C, 350 rpm for 30 min before being dissociated by gentle trituration. Cell concentration was calculated by cell counting on a C-Chip hemocytometer (NanoEntek) and each cell suspension was diluted to 2 million cells/mL. Seven aliquots of each cell suspension for each sample were incubated with different concentrations of PQQ (0.1, 0.5, 1, 5, 10, 50 µM) for 2 h at 37 °C, 5% CO_2. Cells maintained in HBSS for the same time were used as controls. Samples were then homogenized for 15 s at 30,000 min^{-1} (VDI 12, VWR) and ATP or NAD content was measured using a luminometry-based assay (CellTiter-Glo® Luminescent Cell Viability Assay for ATP, NAD/NADH Glo-™ for NAD; Promega). Reagents of the kit were prepared according to the manufacturer's instructions. Equal volumes (50 µl) of sample (reaching a concentration of 100,000 cells/well) and working reagent were combined in a 96-well plate (Nunc™ F96 MicroWell™ White Polystyrene plate, Thermo Fisher Scientific). Luminescence was measured using a Tecan Infinite 200 at approximately 10 min for ATP and 1 h for NAD from initial mixing according to the manufacturer's instructions. To exclude any possible interaction between PQQ and ATP working reagent, the assay was run on PQQ solutions diluted in HBSS without cell lysates as a positive control, demonstrating no change in luminescence with increasing concentrations of PQQ (Additional file 2: Fig. 1). To measure the in vitro ATP content on treated retina, optic nerve and superior colliculus, 5 B6J mice

were euthanized by cervical dislocation, whole eyes enucleated, and retinas dissected in HBSS. The brain was removed, and the superior colliculus was isolated. Optic nerves were cut at 3 mm from the end proximal to the eye, left and right segments were collected in two different samples and stored at 4 °C in HBSS until further processing. Retinas from left and right eyes were pooled to form a single sample. Retinas and superior colliculi were dissociated in 500 and 800 µl of dispase respectively and processed as described above. Cells from dissociated retinas and superior colliculi, as well as isolated optic nerve segments, were incubated with 50 µM PQQ for the same time and in the same conditions as above. The bioluminescent assay was then conducted as previously described. The assessment of ATP and NAD content in vivo was performed on B6J mice (n = 36) treated short-term with an injection of either vehicle or 20 mg/kg PQQ. A cohort of animals (n = 12) was administered with either water or PQQ dissolved in drinking water at the same dose. Animals were euthanized at 24, 48, 72 h after the injection and 24 h after the water administration. Brains, retinas, optic nerves, and superior colliculi were collected and processed as described above. A direct homogenization after the cell dilution was performed and the luminescent assay was run with the same procedure previously indicated.

Trypan Blue assay

Cell viability was assessed by Trypan Blue staining. Cells from brain cortex were obtained and diluted as above. Samples were incubated with 50 µM PQQ for 2 h, stained with 0.4% Trypan Blue dye (Thermo Fisher Scientific) and counted on a hemocytometer (NanoEntek).

JC-1 staining

To measure the short-term effects of PQQ on mitochondrial membrane potential (ΔΨ), JC-1 staining on treated brain cortical cells (dose–response), or retina, optic nerve and superior colliculus (single dose) was performed according to previous protocols with some variations [24]. Briefly, a total of 4 hemispheres from whole cortexes of B6J mice were harvested and brain cortical cells were obtained as described above. Cell suspensions were diluted at a concentration of 1 million cells/mL, then aliquots from each sample were incubated with solutions of PQQ at different concentrations (0.5, 5, 50 µM) for 2 h. At the last 30 min of incubation, JC-1 (Thermo Fisher Scientific, dissolved in DMSO) was added at a final concentration of 2 µM and cells were kept in the dye until the end of PQQ incubation. Cells were washed from the dye, resuspended in HBSS and 50 µl of sample was loaded on a 96-well plate (Nunc™ F96 MicroWell™ White Polystyrene plate, Thermo Fisher Scientific) in an alternate manner to avoid interference between adjacent wells. Fluorescence at 535 nm (green; monomer) and 590 nm (red; aggregate) was measured using a Tecan Infinite 200 and ΔΨ levels were expressed as the ratio of red to green fluorescence. To measure ΔΨ levels in treated retina, optic nerve and superior colliculus, B6J mice (n = 8 for retinas, 5 for the other tissues) were euthanized and the tissues collected as described in the previous section. Cells from retinas and superior colliculi were diluted at a concentration of 1 million cells/mL and incubated with 50 µM PQQ for 2 h. JC-1 was administered at the same concentration and times used for cortical cells. Optic nerves were incubated with PQQ for 1 h, homogenized in PQQ at 8000 min^{-1} speed (VDI 12, VWR) and incubated with 2 µM JC-1 for 30 min at 37 °C for a total of 2 h of incubation in PQQ. Fluorescence was measured as previously described.

Mitochondrial isolation and individual mitochondrial complex activity assays

A total of 6 hemispheres from whole brain cortexes of B6J mice were isolated and dissociated as previously detailed. Cells were then diluted at a concentration of 4 million cells/mL and incubated with 50 µM PQQ for 2 h. Thereafter, mitochondria were extracted using the Thermo Scientific™ Mitochondria Isolation Kit for Cultured Cells (Thermo Fisher Scientific) according to the manufacturer's instructions. Isolated mitochondria were then suspended in 80 µL of mitochondrial isolation buffer (220 mM mannitol, 70 mM sucrose, 10 mM Tris–HCL, 1 mM EDTA, pH = 7.2) and protein content quantified by Pierce™ Detergent Compatible Bradford Assay Kit (Thermo Fisher Scientific). Samples were then sonicated with 3 pulses of 3 s each at ~ 4 W, aliquoted and kept at − 80 °C until further processing. Assays to evaluate the activity of individual mitochondrial complexes were performed according to the protocols described in the supplementary materials from [25], with some adjustments for plates and plate reader. All the assays were performed in a 96 well plate (Sarstedt) and the readings run using a Tecan Infinite 200. Briefly, for the Complex (C) II assay, 20–80 µg/mL of mitochondrial proteins were incubated in 20 mM succinate, 2 µg/mL rotenone, 2 µg/mL antimycin A, 2 mM KCN, 50 µM DCPIP (all Sigma-Aldrich) in potassium buffer for 10 min and then the reduction of DCPIP was measured after the addition of 10 mM DB (Sigma-Aldrich) at 595 nm for 3 min. To assess the activity of CIII, 20 µg/mL of mitochondrial proteins were incubated in 50 µM decylubiquinol, 2 mM KCN, 50 µM cytochrome C (Cyt C) (all Sigma-Aldrich) in sucrose/Tris buffer and the reduction of Cyt C was monitored at 550 nm for 3 min. To account for CIII-independent Cyt C reduction, samples were run both without or with 2 µg/mL antimycin A. Regarding the CIV assay,

10 µg/mL of mitochondrial proteins were mixed with 20 µM ferrocytochrome c (FeCyt C) in degassed potassium buffer, and the oxidation of FeCyt C was measured at 550 nm for 3 min. For the citrate synthase (CS) assay, 20 µg/mL of mitochondrial proteins were incubated with 100 µM DTNB, 300 µM acetyl-CoA and 500 µM oxaloacetate (Sigma-Aldrich) in Tris buffer, and the reduction of DTNB was checked at 415 nm for 3 min. The enzyme activity was calculated by the formula: enzyme activity (nmol min^{-1} mg^{-1}) = (ΔAbsorbance/min × 1000)/[(extinction coefficient × volume of sample used in mL) × (sample protein concentration in mg mL^{-1})] [26]. The ΔAbsorbance/min was derived from the slope of the linear phase of the reaction. The specific activity of CIII was calculated by subtracting the activity without antimycin A minus the one in presence of the inhibitor. The activities of CII, III and IV were normalized to the CS.

Quantitative real-time PCR

B6J treated with either vehicle or 20 mg/kg PQQ i.p. either short-term (n = 7 mice for 24 h, 8 for the other time points) or long-term (n = 16 mice) were euthanized by cervical dislocation. For the short-term treatment, retinas were collected 24, 48 and 72 h after the injection, whereas for the long-term administration retinas and optic nerves were harvested 15 days after the starting point. Eyes were enucleated and retinas dissected in ice-cold HBSS. A second operator isolated the optic nerves from the brain and cut around the optic chiasm. A single retina comprised of a sample, whereas left and right optic nerve segments were pooled together to make a unique sample. All the samples were then snap frozen in dry ice and stored at − 80 °C until further processing. A total RNA extraction was performed homogenizing retinas and optic nerves in 350 µl buffer RLT (Qiagen) with 1% β-mercaptoethanol (Fisher Scientific) and using a QIAshredder kit (Qiagen) according to the manufacturer's instructions. A column-based kit (RNeasy Mini Kits, Qiagen) was used to extract RNA according to the manufacturer's instructions. Isolated RNA was suspended in nuclease-free water and RNA concentration was quantified using a NanoDrop™ One (Thermo Fisher Scientific). cDNA was generated starting from 1 µg of input RNA through an iScript™ cDNA Synthesis Kit and a MyIQ thermocycler (both Bio-Rad) and stored at − 20 °C. Quantitative real-time PCR was performed at the CFX96 Touch Real-Time PCR Detection System thermocycler (Bio-Rad) using SsoAdvanced Universal SYBR Green Supermix (Bio-Rad), cDNA (15 ng for retina; 3 ng for optic nerve) and the appropriate DNA templates (Prime PCR Assay, *mus musculus*, Bio-Rad): *mt-Co2*, *Rsp18*, *Pgc-1α*, *Tfam*, *Ndufb8*, *Sdhb*, *Uqcrc2*, *mt-Co1*, *Atp5a1*. The protocol used comprised of a 3 min activation and denaturation step at 95 °C, followed by an amplification stage composed by 50 cycles of a 15 s denaturation at 95 °C and 1 min annealing, and plate read at 60 °C. Data was exported and opened in the software CFX manager (Bio-Rad) to visualize the amplification and melting curves. The expression levels were calculated by the ΔΔCt method. The mtRNA/nuRNA ratio was calculated using *mt-Co2* and *Rsp18* as the reference mitochondrial and nuclear gene, respectively, as described in [27]. *Rsp18* was used as housekeeping gene when the expression of the other genes was calculated.

Western blot

B6J mice (n = 16) treated with intraperitoneal injections of either vehicle or 20 mg/kg PQQ long-term were euthanized by cervical dislocation after 15 days from the starting point. Eyes were enucleated and retinas dissected in ice-cold HBSS. A second operator isolated the optic nerves from the brain and segments were obtained by cutting right before the optic chiasm. Left and right retinas or optic nerves from the same animal were pooled to make a single sample. All the samples were then snap frozen in dry ice and stored at − 80 °C until further processing. Samples were lysed in RIPA buffer (Santa Cruz Biotechnology) supplemented with phosphatase and proteinase inhibitor cocktails (Roche Applied Science). Protein content was measured by Micro BCA protein assay (Thermo Fisher Scientific). Equal micrograms of proteins per sample (10 µg for retinas; 20 µg for optic nerves) were separated by SDS-PAGE (4–20%; Bio-Rad) and gels were transblotted onto nitrocellulose membranes (Bio-Rad). Membranes were blocked with either 4% BSA (Sigma-Aldrich) or 5% skim milk in TBS/Tween for 1 h at room temperature and incubated overnight at 4 °C with mouse monoclonal total OXPHOS rodent WB antibody cocktail (ab110413, Abcam, 1:250, recognizing 5 different targets: NDUFB8, SDHB, UQCRC2, mt-CO1, ATP5a) or mouse monoclonal anti-β-actin antibody (A2228, Sigma-Aldrich, 1:2500). Afterward, membranes were incubated for 2 h at room temperature with the solution of HRP-conjugated rabbit polyclonal anti-mouse antibody (A9044, Sigma-Aldrich, 1:5000). Rat heart mitochondrial extract provided by the manufacturer (ab110341, Abcam) was diluted at 1:200 and used as a positive control. Clarity western chemiluminescence substrate (Bio-Rad) was used to develop blots, and images were acquired by the ChemiDoc™ Imaging System (Bio-Rad). Protein levels of the target bands were expressed by normalizing the optical density (OD) of the target calculated by Image Lab 6.0 software (Bio-Rad) to the corresponding OD of β-actin as loading control.

Mitochondrial morphological analyses

To image and analyze mitochondrial morphology, retinal and optic nerve cryo-sections were cut from MitoV mice (n = 8) treated for 2 weeks in vivo with either vehicle or 20 mg/kg PQQ i.p. The MitoV mouse strain is on a B6J background and expresses YFP under a rat neuron-specific *Eno2* promoter. YFP is localized to mitochondria through a *Cox8a* gene-targeting signal fused to the YFP N-terminus. This line was selected due to its specificity in inner retinal expression (defined MitoV for visual tissue) [7]. The strain has been further characterized in previous reports [7]. Mice were euthanized after 15 days from the first injection and eyes enucleated. The brain was isolated with the attached optic nerves. Tissues were fixed in 3.7% PFA for 24 h and cryo-protected by immersion in 30% sucrose solution. Eyes were directly frozen in optimal cutting temperature medium (Sakura) on dry ice, whereas optic nerves were separated from the brain and then included in the same medium. Blocks were maintained at −80 °C until use. Eyes and optic nerves were cryo-sectioned in 20 µm-thick coronal and longitudinal sections respectively using a cryostat (Cryostar NX70, Thermo Scientific). All the sections were stored at −20 °C until further processing. Cryo-sections were then air dried for 15 min and rehydrated in 1 M PBS for 5 min before following the protocol. Tissues were isolated using a hydrophobic barrier pen (VWR), permeabilized with 0.1% Triton X-100 (VWR) in 1 M PBS for 1 h and blocked in 2% BSA (Fisher Scientific) in 1 M PBS for 1 h. Sections were then immunolabelled with chicken polyclonal anti-GFP (ab13970, Abcam, 1:500) and rabbit polyclonal anti-TOMM20 (ab78547, Abcam, 1:500) primary antibodies at 4 °C overnight. Anti-GFP primary antibody was used to limit loss of signal from potential bleaching of YFP. Thereafter, sections were rinsed with 5 × 5 min washes in 1 M PBS and stained with Alexa Fluor 488 conjugated goat anti-chicken (A11039, Invitrogen, 1:500) and Alexa Fluor 568 conjugated goat anti-rabbit (A11011, Invitrogen, 1:500) secondary antibodies for 4 h at room temperature. Tissue was washed as before and counterstained with DAPI (1 µg/mL in 1 M PBS) for 10 min. After being rinsed once in PBS, tissue was mounted using Fluoromount-G and glass coverslips (Invitrogen). Nail-varnish was used to seal the slides. Images were acquired using confocal imaging on a Zeiss LSM-980 Airy (63×, 1.5 × optical zoom, image size 89.8 × 89.8 µm, 0.07 µm pixel size, z-stacks with 0.23 µm optimal interval). Images from retinal sections were acquired from central retina at ~ 500 µm lateral to the optic nerve head. Images from optic nerve sections were acquired from areas around the optic chiasm used for reference. Alexa Fluor 488 conjugated and Alexa Fluor 568 conjugated secondary antibodies targeting anti-GFP and anti-TOMM20 primary antibodies respectively were imaged. DAPI channel was also imaged for reference purposes in retinal samples. Retinal images encompassed nerve fiber layer (NFL), GCL and inner plexiform layer (IPL). Mitochondrial particles were reconstructed in 3D using Imaris software (version 9.3.1). NFL/GCL and IPL were cropped for the analyses and reconstructed separately with different settings. Volume reconstructions were performed using the surface tool and volumes under 125 voxels were filtered and discarded from subsequent analysis to reduce noise. Volume, surface area, sphericity (including prolate and oblate dimensions) of each mitochondrial particle were calculated by the software and plotted either individually or as an average per retina or optic nerve. For volume and surface area, an average of both mean and sum of each parameter was calculated. Mean volume, volume sum, mean surface area and surface area sum in each retina were normalized to the number of either GFP or TOMM20 positive cells and then to the volume crop in NFL/GCL, or to only volume crop in IPL. The same parameters were normalized to the volume crop in the optic nerve images.

Metabolomics

B6J mice (n = 10 animals) treated with a single i.p. injection of either vehicle or 20 mg/kg PQQ were euthanized by cervical dislocation after 24 h from the treatment. Eyes were enucleated and retinas were immediately dissected in ice cold HBSS, wiped dry, weighed and frozen on dry ice. A second investigator isolated the optic nerves immediately after death. Optic nerves were cut at 3 mm from the end proximal to the eye and frozen as for retinas. Each sample comprised a single retina or an isolated optic nerve segment. Tissue was stored at −80 °C and shipped kept in dry ice to the Swedish Metabolomics Centre for sample processing. 200 µl of extraction buffer (80:20 v/v MeOH:H_2O) including internal standards were added to the tubes together with 1 tungsten bead. Tissues were shaken at 30 Hz for 3 min in a mixer mill and samples were then centrifuged at 4 °C, 18620 g for 10 min. Afterwards, 200 µl of the supernatant was transferred to micro vials and evaporated to dryness in a speed-vac concentrator. Samples were stored at −80 °C and small aliquots of the remaining supernatants were pooled and used to create quality control (QC) samples. Prior to the analysis, samples were re-suspended in 10 + 10 µl methanol and elution solvent A. The samples were analyzed in batches according to a randomized run order. Each batch of samples was first analyzed in positive mode. After all samples within a batch had been analyzed, the instrument was switched to negative mode and a second injection of each sample was performed. The chromatographic separation was performed on an Agilent

1290 Infinity UHPLC-system (Agilent Technologies, Waldbronn, Germany). 2 µl of each sample were injected onto an Atlantis Premier BEH-Z-HILIC VanGuard FIT (1.7 µm, 2.1×50 mm) column (Waters Corporation, Milford, MA, USA) held at 40 °C. The HILIC gradient elution solvents were (A) 10 mM ammonium formate, 5 µM Medronic acid in H_2O, pH 9 and (B) 90:10 Acetonitrile: [10 mM ammonium formate in H_2O], pH 9. Chromatographic separation was achieved using a linear gradient (flow rate of 0.4 mL/ min): min 0 = 90% B, min 6 = 80% B, min 9.5 = 20% B, min 11 = 90% B. The flow rate was then increased to 0.7 mL/min for 2 min, held at this rate for 0.5 min, and further reduced to 0.4 mL/min for 0.5 min before the next injection. Compounds were detected with an Agilent 6546 Q-TOF mass spectrometer equipped with a jet stream electrospray ion source operating in positive or negative ion mode. MSMS analysis was run on the QC samples for identification purposes. All data preprocessing was performed using the Agilent MassHunter Profinder version B.10.0 SP1 (Agilent Technologies Inc., Santa Clara, CA, USA). Sixty-three (retina) or seventy-three (optic nerves) low molecular weight metabolites that could be certified with standards were detected. The quantification of the metabolites was calculated as area under the curve of the mass spectrometry peak and normalized first to an internal standard for negative and positive runs, then for the weight of the tissue for retinal samples. Data were analyzed and graphs were made using MetaboAnalyst [version 5.0; 28, 29] and R. All data were subject to Pareto scaling [30]. Hierarchical clustering (HC) (Spearman, Average) was used to create the dendrograms. Correlation heatmaps were created using Spearman rank correlation. Principal component analysis (PCA) was performed in R (4.1.0) using the *factoextra* package. Comparisons between groups were analyzed by two-sample t-tests with an adjusted *p* value (false discovery rate, FDR), using a cutoff of 0.05 considered significant. Quantitative pathway analysis was performed using the *Mus musculus* KEGG library in MetaboAnalyst and a background metabolome of all detected metabolites.

Statistical analysis

Graph Pad Prism 8.0.2 software and R were used for the statistical analyses. A Shapiro Wilk test was used to test the normality of the data. A Student's t-test or one-way ANOVA (followed by Tukey's multiple comparison post hoc test) were applied as appropriate to analyze normally distributed data. A Mann–Whitney test was used to analyze non-normally distributed data. For individual mitochondrial particles morphology, a linear mixed effects model through the lme4 package in R was applied when multiple observations come from the same retina or optic nerve, in order to reduce p value inflation and intra-class correlation [31–33]. Differences with $p < 0.05$ were considered significant. For the box plots, the median is represented by the center hinge with upper and lower hinges indicating the first and third quartiles, whereas whiskers denote 1.5 times the interquartile range. All the graphs were made in R or using MetaboAnalyst 5.0 for dendrograms and correlation heatmaps.

Results

PQQ is neuroprotective in different models of RGC-related damage

Since RGCs strictly rely on a perfectly controlled metabolism and PQQ has been demonstrated to regulate the cellular bioenergetic balance [15–19], we hypothesized that PQQ could protect RGCs under stress/injury which compromise bioenergetic capacity. We first evaluated the effects of PQQ in an ex vivo model of RGC injury, which reproduces an axon-specific insult by separating the retina from the optic nerve [7, 34]. Significant RGC loss was detected after 3 days ex vivo (DEV), as assessed by counting cells positive for RBPMS (a specific marker of RGCs). Administration of PQQ via the culture media at both 50 and 100 µM provided a significant preservation of RGC density under stress condition (Fig. 1A, B). The administration of PQQ was effective in counteracting the loss of DAPI positive nuclei, however the nuclear shrinkage was only partially prevented at the highest dose (Additional file 3: Fig. 2A, B).

To further explore PQQ neuroprotection, we next tested the ability of PQQ to protect RGC against Complex I inhibition in a model of RGC degeneration induced by rotenone. In this model, retinal cell death is induced by the inhibition of mitochondrial Complex I triggered by an intravitreal injection of rotenone, resulting in a rapid degeneration of retinal neurons [7, 35]. A significant RGC and retinal cell loss, as well as nuclear shrinkage, were identified after 24 h from the rotenone injection (Fig. 1C, D; Additional file 3: Fig. 2C, D). While the administration of PQQ was effective in preventing RGC and retinal cell loss, the nuclear shrinkage was persisting in retinas of PQQ-treated mice although significantly attenuated (Fig. 1C, D; Additional file 3: Fig. 2C, D). These data support a neuroprotective role of PQQ against a range of different stressors, such as RGC axonal damage and severe mitochondrial dysfunction.

PQQ increases ATP content and alters mitochondrial membrane potential in cortical neurons and RGCs in vitro

As PQQ has been reported to influence metabolism and regulate the cellular bioenergetic balance in several systems [15–19], we investigated the effect of PQQ on neuronal ATP production. We initially assessed if PQQ was rapidly utilized by measuring the ATP content in

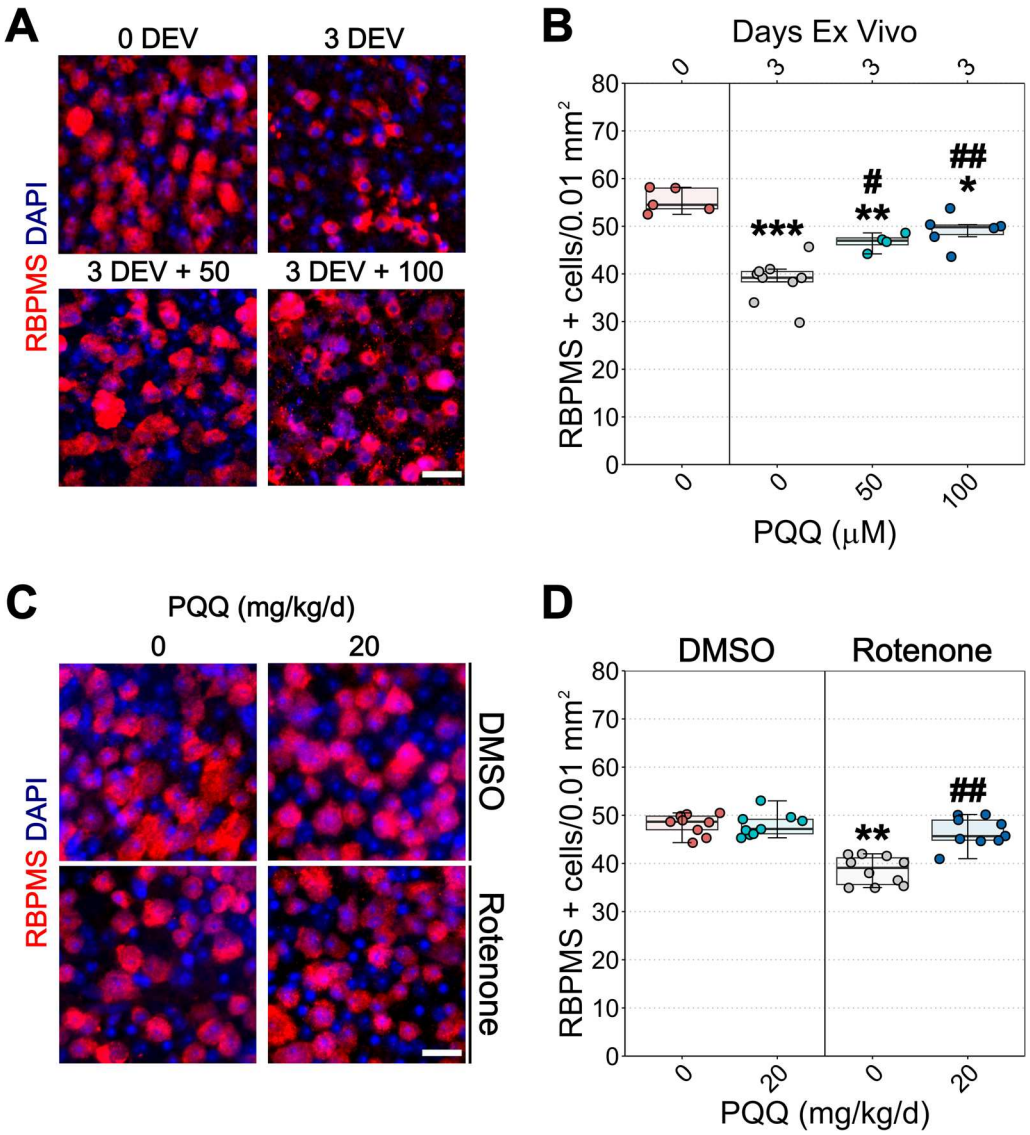

Fig. 1 Effects of PQQ administration on RGC survival in ex vivo and in vivo models of RGC stress. **A** Representative images of retinas cultured ex vivo, immunolabeled for RNA-binding protein with multiple splicing (RBPMS, red) and counterstained with DAPI (blue). Retinal explants were cultured in either basic or supplemented media with either 50 or 100 µM PQQ for 3 days ex vivo (DEV). Control retinas (0 DEV) were directly fixed and processed after the dissection. **B** Quantification of RBPMS positive cell density per 0.01 mm^2. n = 5 (0 DEV), 9 (3 DEV), 4 (3 DEV + 50 µM PQQ), 6 (3 DEV + 100 µM PQQ) retinas. **C** Representative images of retinas from mice injected with either DMSO or rotenone and treated with either vehicle or 20 mg/kg PQQ. Flat mount retinas were immunolabeled for RBPMS (red) and counterstained with DAPI (blue). **D** Quantification of RBPMS positive cell density per 0.01 mm^2. n = 9 DMSO, 9 DMSO + PQQ, 10 rotenone and 9 rotenone + PQQ retinas. Scale bar = 20 µm. *$p < 0.05$, **$p < 0.01$ and ***$p < 0.001$ versus 0 DEV (explants) or DMSO (rotenone model); $^{\#}p < 0.01$ and $^{\#\#}p < 0.001$ versus 3 DEV (explants) or rotenone (rotenone model)

dissociated brain cortical cells. Cortical cells were incubated with increasing concentrations of PQQ (0.1, 0.5, 1, 5, 10, 50 µM) for 2 h and ATP levels assessed. A significant dose-dependent increase in ATP content was demonstrated in cortical cells from concentrations at 0.5 µM, reaching > 50-fold the untreated control at the highest dose tested (Fig. 2A) without a loss of viability (Additional file 4: Fig. 3). As NAD is a key cofactor involved in metabolism and ATP synthesis, we assessed if the short incubation with PQQ might promote NAD synthesis. However, PQQ effect on generating ATP in vitro appeared not predominantly dependent on NAD synthesis, since NAD content was not significantly influenced following the incubation

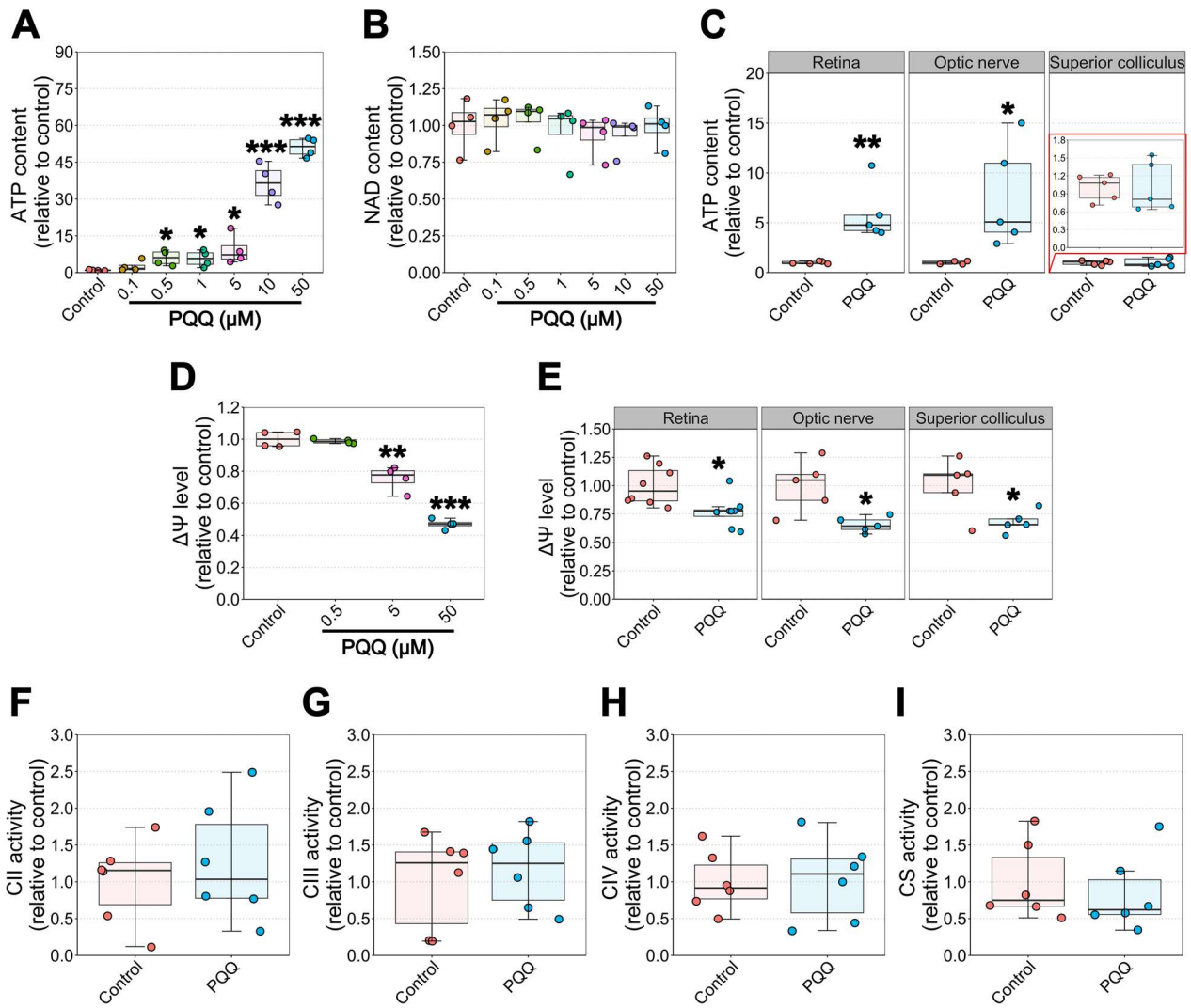

Fig. 2 Effects of PQQ administration on ATP, NAD, mitochondrial membrane potential levels and mitochondrial function in vitro. **A** ATP and **B** NAD content in dissociated mouse brain cortical cells incubated with different doses of PQQ (0.1, 0.5, 1, 5, 10, 50 μM) for 2 h. n = 4 different cell suspensions from different hemispheres. **C** ATP content in dissociated retinal and superior colliculus cells and in isolated optic nerves incubated with 50 μM PQQ for 2 h. The red inset shows a zoom of the graph related to the ATP content in superior colliculus. n = 5 retinal replicates made by 2 pooled retinas, 5 optic nerve replicates made of isolated segments cut to 3 mm length, 5 superior colliculus replicates. **D** Mitochondrial membrane potential (ΔΨ) levels in dissociated brain cortical cells incubated with several concentrations of PQQ (0.5, 5, 50 μM) for 2 h. n = 4 different cell suspensions from different hemispheres. **E** ΔΨ levels in dissociated retinal and superior colliculus cells and in isolated optic nerves incubated with 50 μM PQQ for 2 h. n = 8 retinal replicates made by 2 pooled retinas, 5 optic nerve replicates made of isolated segments cut to 3 mm length, 5 superior colliculus replicates. **F**–**I** Mitochondrial Complex (**C**) II (**F**), III (**G**), IV (**H**) and citrate synthase (CS; **I**) activity in dissociated cortical cells incubated with 50 μM PQQ for 2 h. n = 6 different cell suspensions from different hemispheres. *$p < 0.05$, **$p < 0.01$ and ***$p < 0.001$ versus control

with PQQ (Fig. 2B). To support these findings in an RGC specific context we next assessed if PQQ at 50 μM (where the highest ATP increase was demonstrated) provided a similar ATP increase in RGC-related tissues. Dissociated retinal cells and optic nerve confirmed the increase in ATP as seen in cortical neurons (Fig. 2C).

To further investigate the mechanisms behind PQQ's rapid ATP increase in vitro, we assessed mitochondrial membrane potential (ΔΨ) in cortical cells incubated with PQQ for 2 h. The levels of ΔΨ dose-dependently reduced in PQQ-incubated cells, decreasing to 47% of the control at 50 μM (Fig. 2D). The decline in ΔΨ levels was further confirmed in dissociated retina, optic nerve, or superior colliculus incubated at a dose of 50 μM (Fig. 2E), suggesting that, together with a concomitant increase in ATP levels, mitochondrial potential may be dissipated to produce ATP [24]. Since ΔΨ is highly influenced by the activity of mitochondrial complexes and enzymes from

tricarboxylic acid (TCA) cycle (such as citrate synthase; CS), we next assessed a direct interaction between PQQ and each individual mitochondrial complex. Mitochondria were isolated from cortical cells incubated with PQQ and spectrophotometric assays to measure the activity of Complexes II–IV (CII, CIII, CIV) and CS were performed. No significant change in individual complexes and citrate synthase activity was detected suggesting that PQQ does not act directly in the mitochondrion itself (Fig. 2F–I). Taken together, these data suggest that cells from CNS and RGC-related tissues can quickly use PQQ and increase their ATP content.

PQQ modulates ATP and NAD content in visual system tissues in vivo

We next assessed whether the administration of PQQ in vivo leads to similar effects on metabolism. Adult B6J mice were treated with PQQ and the levels of ATP and NAD in visual system tissues were assessed following a single intraperitoneal injection of 20 mg/kg PQQ. A significant increase in ATP levels in retina, optic nerve, and superior colliculus (a major target for RGC axons in the brain) from PQQ-treated animals was identified after 24 h. Higher levels of ATP in PQQ-treated mice were also detected in retinas and superior colliculi after 48 and 72 h (Fig. 3A). PQQ administration significantly increased NAD levels in the superior colliculus after 24 and 72 h from the treatment, whilst having no effect on the other tissues at all the time points analyzed (Fig. 3B).

Since we confirmed an increase in ATP in vivo after the treatment with PQQ, we next assessed the efficacy of PQQ when administered in normal drinking water. However, ATP and NAD levels were not elevated by dietary PQQ (except for a significant increase in superior colliculus NAD), suggesting ineffective bioavailability of PQQ orally (Additional file 5: Fig. 4).

PQQ exerts a mild effect on mitochondrial content and morphology in RGCs

ATP production is strictly dependent on mitochondrial activity and content, and PQQ has been previously reported to regulate mitochondrial biogenesis through the activation of peroxisome proliferator-activated receptor-gamma coactivator alpha (PGC-1α) and the expression of mitochondrial transcription factor A (TFAM) [18, 19]. We initially assessed this short-term transcriptional activation of mitochondrial biogenesis in the whole retina at the same time points where ATP increases were identified in vivo. We performed qPCR to assess the mtRNA:nuRNA ratio, which provides an estimate of the number of mitochondrial genome copies, an early hallmark of mitochondrial biogenesis and an indicator of the number of mitochondria [27]. The expression of *Pgc-1α* and *Tfam* were also assessed. Short-term treatment with PQQ did not effect mtRNA:nuRNA or *Pgc-1α* and *Tfam* mRNA levels, suggesting that a single injection of PQQ is not adequate to induce transcriptional variations in retinal mitochondrial biogenesis (Additional file 6: Fig. 5).

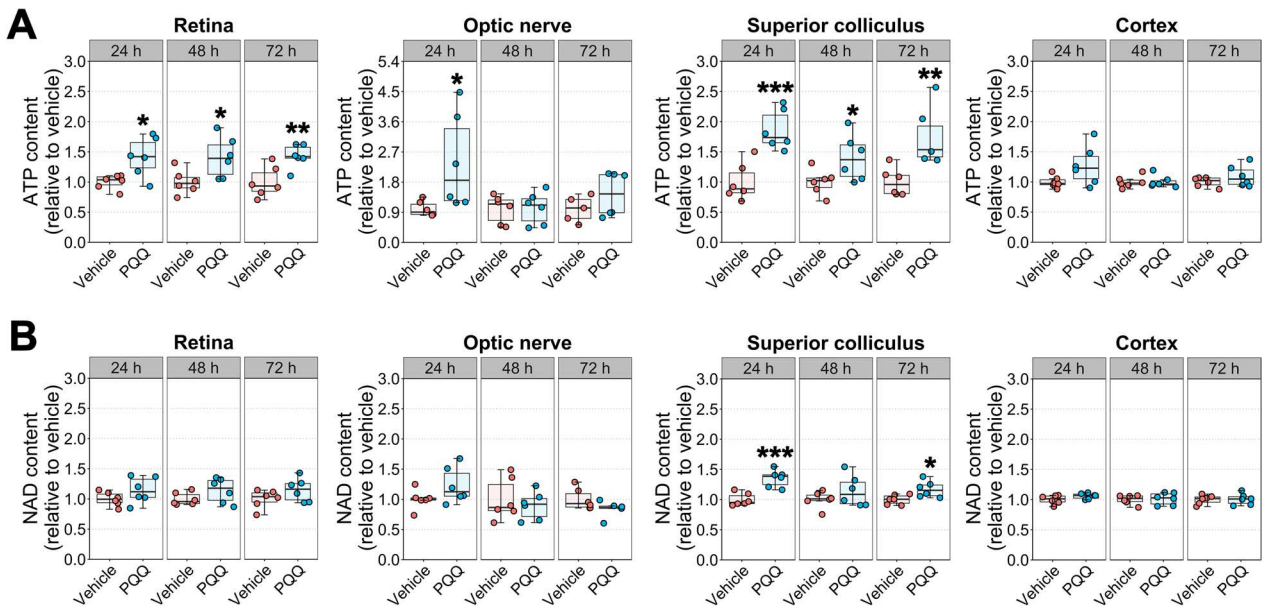

Fig. 3 Effects of PQQ administration on ATP and NAD levels in visual system tissues in vivo. **A** ATP and **B** NAD content in retina, optic nerve, superior colliculus, and brain cortex from animals treated with either vehicle or a single injection of 20 mg/kg PQQ assessed after 24, 48 or 72 h from the treatment. n = 6 animals per group for each time point. *$p < 0.05$, **$p < 0.01$ and ***$p < 0.001$ versus vehicle

We next questioned whether transcriptional regulation of mitochondria is activated if PQQ was administered chronically. In addition to *Pgc-1α*, *Tfam*, and the mtRNA:nuRNA ratio, we quantified the expression of individual mitochondrial complexes-related genes in retinal samples to further assess an influence on mitochondrial content. mRNA levels of *Ndufb8* (CI), *Sdhb* (CII), *Uqcrc2* (CIII), *mt-Co1* (CIV), *Atp5a1* (CV; ATP synthase) were assessed. Chronic administration of PQQ had no effect on either retinal mtRNA:nuRNA ratio or *Pgc-1α* and *Tfam* mRNA, suggesting that PQQ is not effective in triggering mitochondrial biogenesis transcriptionally short-term or long-term (Fig. 4A, B). However, PQQ-treated retinas displayed a significant increase in *Ndufb8* mRNA levels, without a change in other mitochondrial markers (Fig. 4C). Since whole retinas contain different mixed cell populations, we next assessed if PQQ could induce a similar response in the optic nerve, which is an RGC enriched tissue (RGC axons). A significant decrease in mtRNA:nuRNA ratio, as well as *Ndufb8* and *mt-Co1* mRNA levels, was identified in optic nerves from PQQ-injected mice (Fig. 4D–F). To further confirm these molecular regulations, protein levels were quantified by Western blot to assess if the observed transcriptional changes were strictly correlated with variations in protein levels. A significant increase in NDUFB8 protein levels was demonstrated in retinas from PQQ-treated animals, suggesting that its transcriptional regulation consequently results in its protein translation (Fig. 4G; Additional file 7: Fig. 6A, C). However, no changes in the levels of mitochondrial complexes were identified in the optic nerve after PQQ treatment (Fig. 4H; Additional file 7: Fig. 6B, D).

We next assessed whether mitochondrial morphological remodeling occurs following tissue mRNA and metabolic changes. We first assessed the effects of PQQ on gross mitochondrial morphology reconstructing TOMM20-positive mitochondrial particles in retinal GCL/NFL, IPL and in optic nerve. Mice were administered 20 mg/kg of PQQ via i.p. for 2 weeks and then euthanized and their tissue processed for high resolution confocal microscopy. No change in total mitochondrial morphology was observed following PQQ administration in the retina (Fig. 5; Additional file 8: Fig. 7) whereas optic nerves from PQQ-treated mice displayed a significant decrease in individual mitochondrial particle total surface area and changes to sphericity (Fig. 7A–I). A similar trend was identified at an average level per optic nerve (Additional file 10: Fig. 9A–E). As TOMM20 positive particles are representative of mitochondria from multiple cell types, we next determined whether there was an RGC-specific response in these tissues using our recently published mitochondrial reporter mouse which expresses YFP under a rat neuron-specific *Eno2* promoter and localized to mitochondria through a *Cox8a* gene-targeting signal fused to the YFP N-terminus. This strain is called MitoV (V for visual system) and the expression of YFP is specifically restricted to RGCs in the inner retina (with the expression in a subset of bipolar neurons and photoreceptors in the outer retina) [7]. A significant increase in individual sphericity was observed in the GCL of PQQ treated retinas, whereas no differences were detected in all the other parameters analyzed (Fig. 6). Taken as an average, all morphological parameters were similar between vehicle- and PQQ- treated mice (Additional file 9: Fig. 8). In the optic nerve, the administration of PQQ resulted in no changed individual particles morphology, although on average the mean volume and the volume sum were significantly increased (Fig. 7J–R; Additional file 10: Fig. 9F–J). Taken together, all the changes identified both at the molecular and morphological level may reflect some heterogeneity and variability across tissues and within conditions, suggesting that the overall effect of PQQ administration results in only a mild effect on mitochondrial content.

PQQ modifies the metabolic profiles in non-diseased RGCs

Because we identified a mild effect of PQQ on mitochondrial content and that the ATP levels may be regulated by a crosstalk of several metabolic processes, we set out to determine whether PQQ administration

(See figure on next page.)

Fig. 4 Effects of PQQ administration on molecular regulation of mitochondrial content in vivo. **A** mtRNA/nuRNA ratio in retinal samples from animals treated with either vehicle or 20 mg/kg PQQ long-term, calculated using the expression of *mt-Co2* and *Rsp18* as mitochondrial and nuclear reference gene, respectively. **B**, **C** *Pgc-1a*, *Tfam* (**B**) and *Ndufb8*, *Sdhb*, *Uqcrc2*, *mt-Co1* and *Atp5a1* (**C**) mRNA levels in whole retinas from animals injected long-term with either vehicle or 20 mg/kg PQQ. *Rsp18* was used as housekeeping gene. n = 15 retinas per group. **D** mtRNA/nuRNA ratio in optic nerve samples from animals treated long-term with either vehicle or 20 mg/kg PQQ, calculated using the same genes described in **A** as mitochondrial and nuclear reference genes. **E**, **F** *Pgc-1a*, *Tfam* (**E**) and *Ndufb8*, *Sdhb*, *Uqcrc2*, *mt-Co1* and *Atp5a1* (**F**) mRNA levels in optic nerves from animals treated long-term with either vehicle or 20 mg/kg PQQ. *Rsp18* was used as housekeeping gene. n = 8 optic nerves per group. **G**, **H** Representative blots and densitometric analysis of NDUFB8, SDHB, UQCRC2, mt-CO1 and ATP5a protein levels in retinas (**G**) and optic nerves (**H**) from vehicle and PQQ treated animals. Protein levels were expressed as the optical density (OD) of the target normalized for the respective OD of β-actin used as loading control. n = 8 samples per group. *$p < 0.05$, **$p < 0.01$ and ***$p < 0.001$ versus vehicle

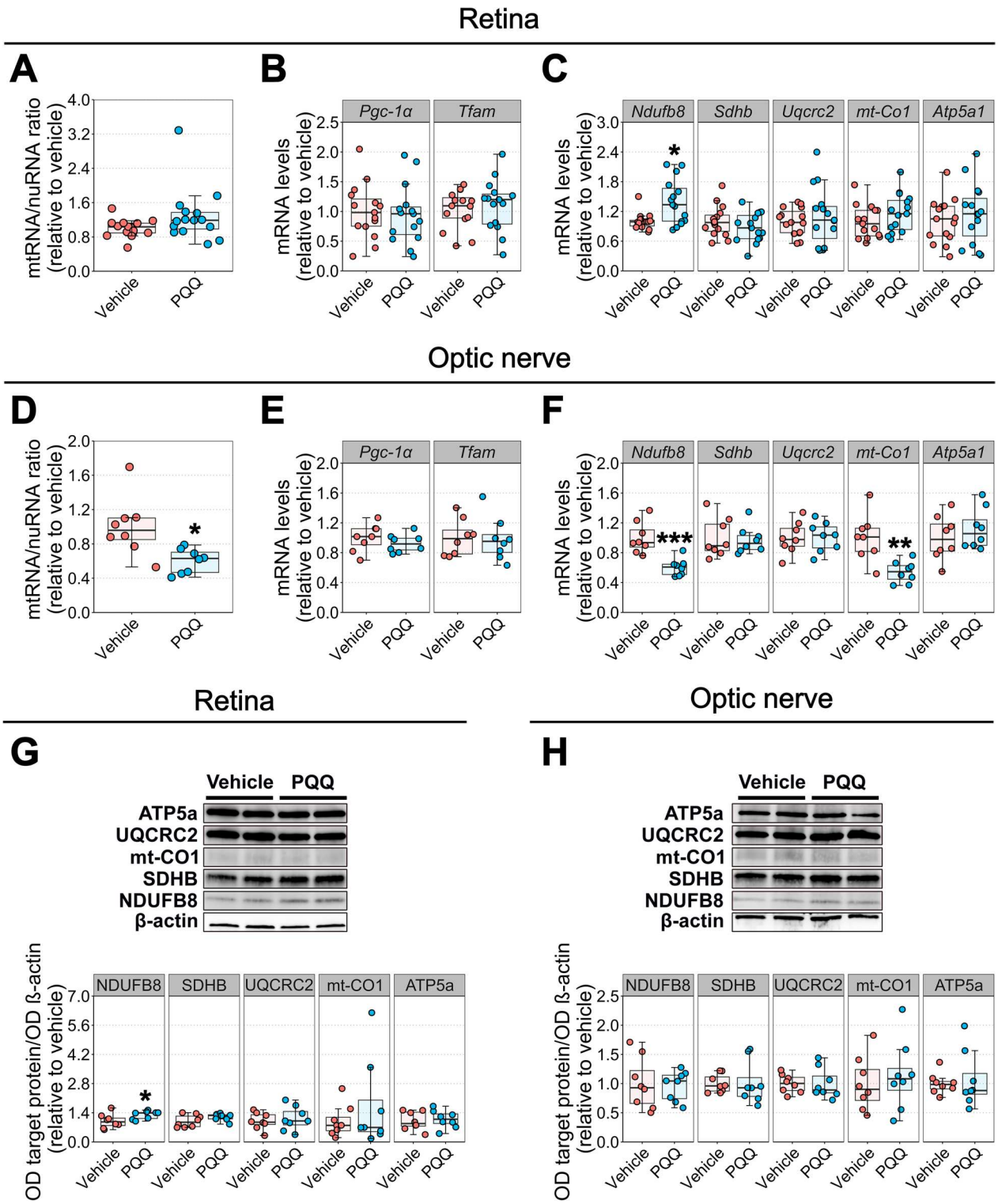

Fig. 4 (See legend on previous page.)

altered the metabolic profile of RGCs under basal conditions. To achieve this, we performed metabolomics across retinas and optic nerves collected from mice treated with a single injection of PQQ after 24 h from the injection using a low molecular weight enriched metabolomics protocol (identifying 63 low molecular

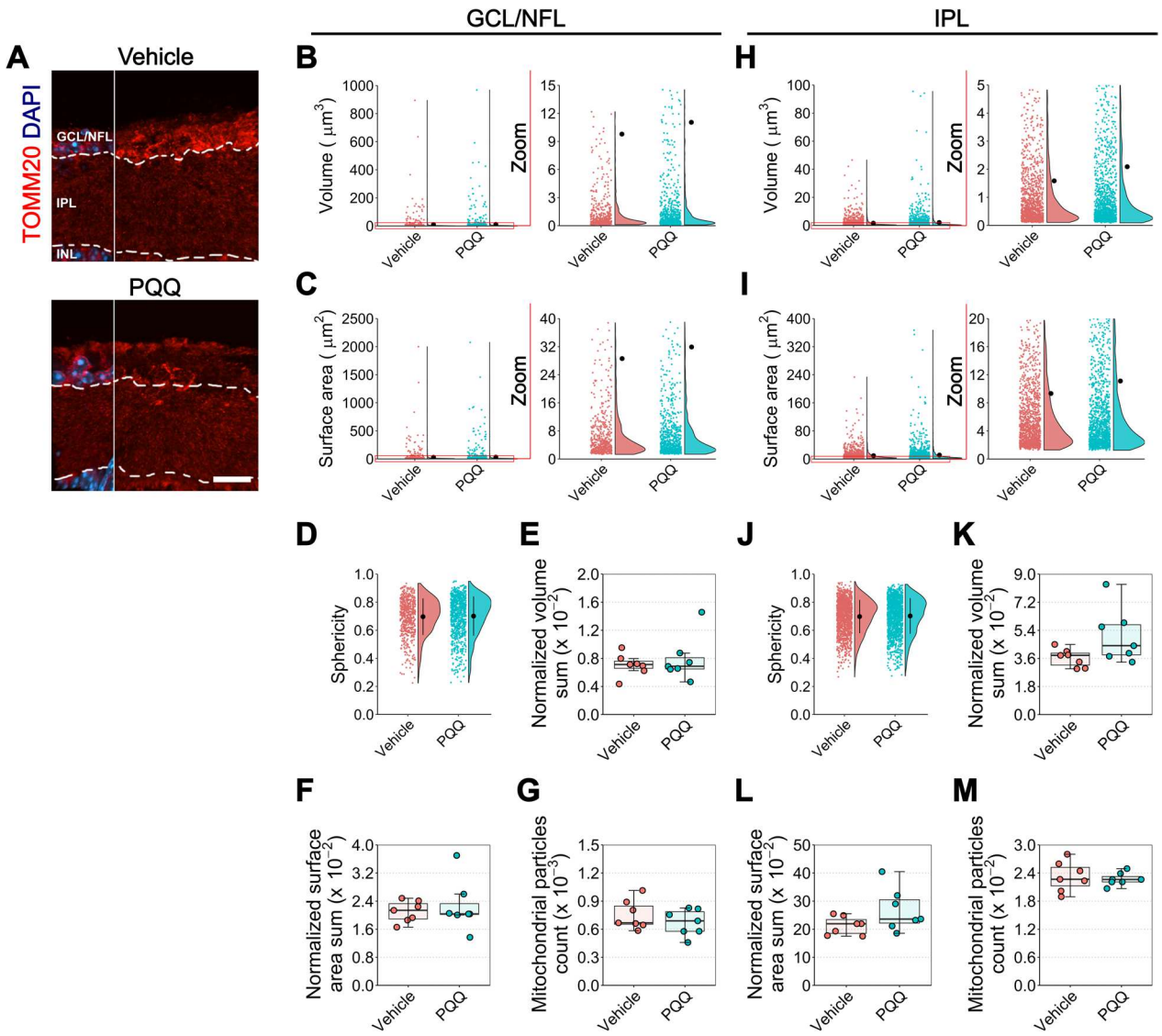

Fig. 5 Effects of PQQ administration on retinal gross mitochondrial morphology in vivo. **A** Representative images of retinal cross sections from animals treated long-term with either vehicle or 20 mg/kg PQQ immunolabeled for TOMM20 (red) and counterstained with DAPI (blue). The DAPI was used for reference to crop GCL/NFL from IPL. Dashed lines demark the boundaries between GCL/NFL, IPL and INL on retinal sections. **B**–**D** Violin plots representing individual volume (**B**), surface area (**C**) and sphericity (**D**) of TOMM20-positive mitochondrial particles in GCL/NFL of vehicle or PQQ-treated animals. n = 555 vehicle and 812 PQQ disconnected particles from 7 different retinas per group. **E**–**G** Averaged volume sum (**E**), surface area sum (**F**) and count (**G**) per retina of TOMM20-positive mitochondrial particles in GCL/NFL. n = 7 retinas per group. **H**–**J** Violin plots showing individual TOMM20-positive mitochondrial particles volume (**H**), surface area (**I**) and sphericity (**J**) in IPL of vehicle or PQQ-treated animals. n = 1318 vehicle and 1361 PQQ disconnected particles from 7 different retinas per group. **K**–**M** Averaged volume sum (**K**), surface area sum (**L**) and count (**M**) per retina of TOMM20-positive mitochondrial particles in IPL. n = 7 retinas per group. For individual parameters, individual values of disconnected particles from each retina were analyzed together and a linear mixed effects model was applied to account for the multiple observations that come from the same sample. Scale bar = 20 µm. GCL, ganglion cell layer; INL, inner nuclear layer; IPL, inner plexiform layer; NFL, nerve fiber layer. The red zoom depicts the inset of data points to optimally visualize the data distribution

weight metabolites in the retina and 73 enriched in the optic nerve with high accuracy and confidence; Additional file 1: Data 1). Hierarchical clustering (HC) of both conditions and individual samples identified some heterogeneity across and within conditions in retinal samples, overall suggesting similarities between retinas from vehicle- and PQQ- treated mice. However, the division between samples in optic nerve was largely distinguished (Fig. 8A; Additional file 11: Fig. 10). Principal component analysis (PCA) confirmed a complete

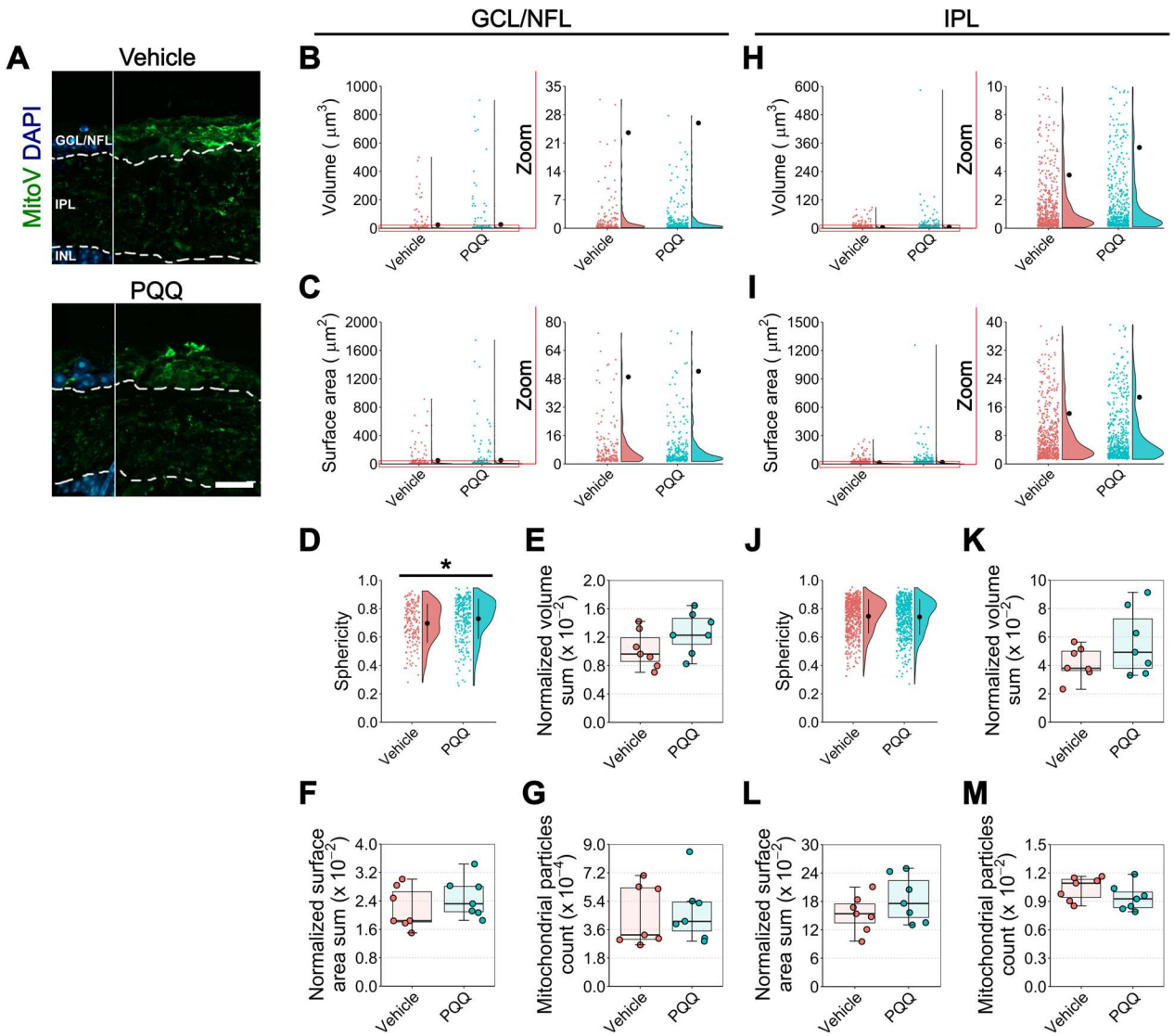

Fig. 6 Effects of PQQ administration on RGC-specific retinal mitochondrial morphology in vivo. **A** Representative images of retinal cross sections from MitoV animals treated long-term with either vehicle or 20 mg/kg PQQ immunolabeled for YFP (an antibody anti-GFP was used to limit loss of signal from potential bleaching of YFP; the staining is indicated here as MitoV) (green) and counterstained with DAPI (blue). The DAPI was used for reference to crop GCL/NFL from IPL. Dashed lines demark the boundaries between GCL/NFL, IPL and INL on retinal sections. (B-D) Violin plots depicting individual volume (**B**), surface area (**C**) and sphericity (**D**) of MitoV-positive mitochondrial particles in GCL/NFL of animals treated with either vehicle or PQQ. n = 176 vehicle and 268 PQQ disconnected particles in 7 different retinas per group. **E**–**G** Averaged volume sum (**E**), surface area sum (**F**) and count (**G**) per retina of MitoV-positive mitochondrial particles in GCL/NFL. n = 7 retinas per group. **H**–**J** Violin plots showing individual volume (**H**), surface area (**I**) and sphericity (**J**) of MitoV-positive mitochondrial particles in IPL of vehicle and PQQ-treated animals. n = 600 vehicle and 552 PQQ disconnected particles in 7 different retinas per group. **K**–**M** Averaged volume sum (**K**), surface area sum (**L**) and count (**M**) per retina of MitoV-positive mitochondrial particles in IPL. n = 7 retinas per group. For individual parameters, individual values of disconnected particles from each retina were analyzed together and a linear mixed effects model was applied to account for the multiple observations that come from the same sample. Scale bar = 20 µm. GCL, ganglion cell layer; INL, inner nuclear layer; IPL, inner plexiform layer; NFL, nerve fiber layer. The red zoom depicts the inset of data points to optimally visualize the distribution of the data. *$p < 0.05$ versus vehicle

overlap between groups in retina, whilst identifying a clear separation of samples in the optic nerve (Fig. 8B). This suggests that PQQ exerts differing effects on the two tissues studied. Administration of PQQ resulted in 5 changed metabolites in the retina (2 increased, 3 decreased) and 18 in the optic nerve (12 increased, 6 decreased) (Fig. 8C, D; Additional file 1: Data 1). Comparison of changed metabolites across tissues identified AMP as a commonly changed metabolite, although demonstrating an increase in the retina and a decrease

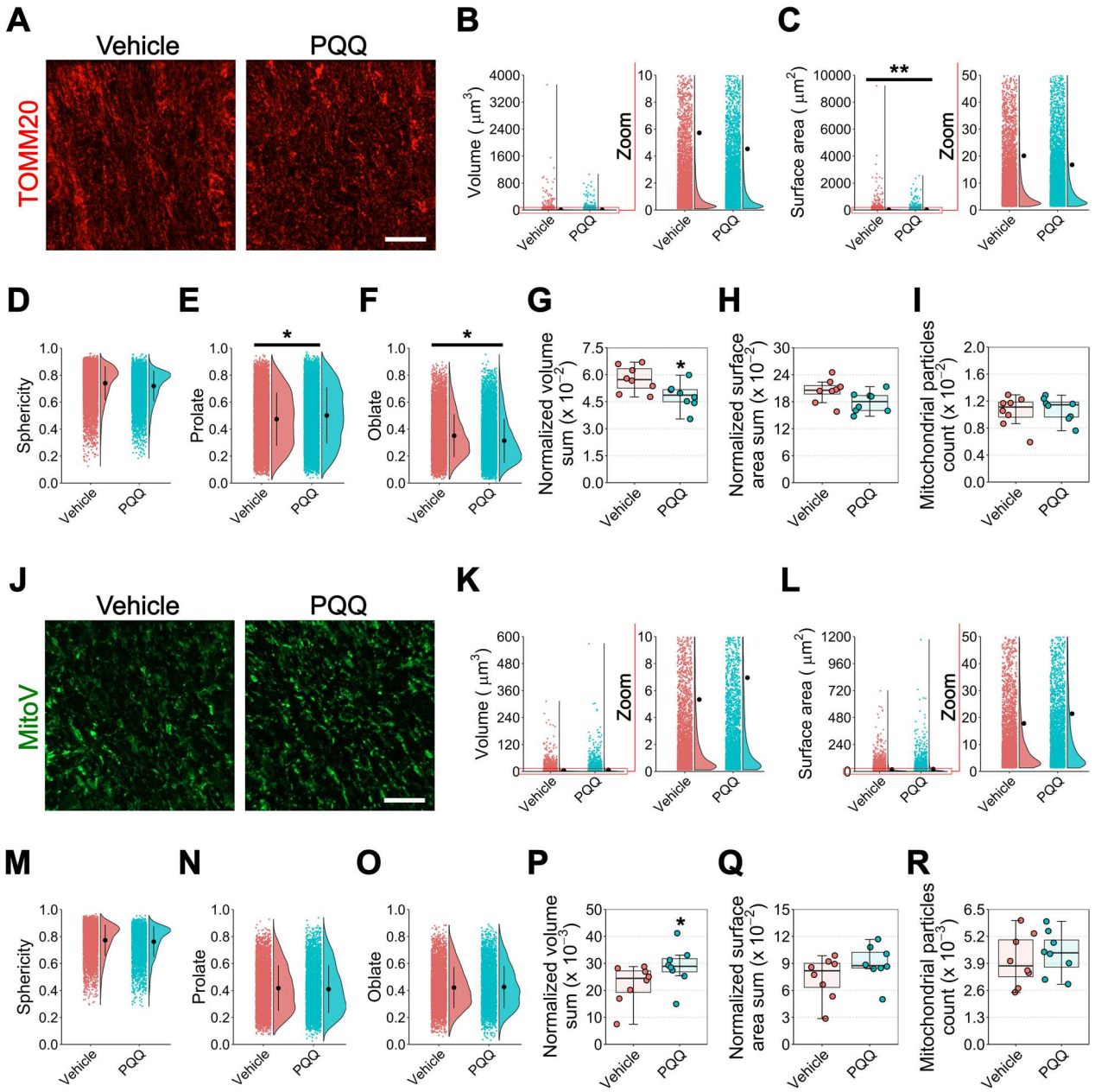

Fig. 7 Effects of PQQ administration on general and RGC-specific mitochondrial morphology in the optic nerve in vivo. **A** Representative images of optic nerve longitudinal sections from MitoV animals treated long-term with either vehicle or 20 mg/kg PQQ immunolabeled for TOMM20 (red). **B**–**F** Violin plots showing individual volume (**B**), surface area (**C**), sphericity (**D**), prolate (**E**) and oblate (**F**) of TOMM20-positive mitochondrial particles in optic nerves from vehicle- or PQQ-treated animals. n = 9338 vehicle and 9293 PQQ disconnected particles in 8 different optic nerves per group. **G**–**I** Averaged volume sum (**G**), surface area sum (**H**) and count (**I**) per optic nerve of TOMM20-positive particles. n = 8 optic nerves per group. **J** Representative images of optic nerve longitudinal sections from MitoV animals treated long-term with either vehicle or 20 mg/kg PQQ immunolabeled for YFP (an antibody anti-GFP was used to limit loss of signal from potential bleaching of YFP; the staining is indicated here as MitoV) (green). **K**–**O** Violin plots representing individual volume (**K**), surface area (**L**), sphericity (**M**), prolate (**N**), oblate (**O**) of MitoV-positive particles in optic nerves of vehicle and PQQ-treated animals. n = 4378 vehicle and 3947 PQQ disconnected particles in 8 different optic nerves per group. **P**–**R** Averaged volume sum (**P**), surface area sum (**Q**) and count (**R**) per optic nerve of MitoV-positive particles. n = 8 optic nerves per group. For individual parameters, individual values of disconnected particles from each optic nerve were analyzed together and a linear mixed effects model was applied to account for the multiple observations that come from the same sample. Scale bar = 20 µm. The red zoom depicts the inset of data points to optimally visualize the data distribution. *$p < 0.05$ and **$p < 0.01$ versus vehicle

in the optic nerve (Fig. 8E). Pathway analysis revealed that PQQ-induced metabolite modifications are predicted to have a minimal impact on retinal pathways, whilst significantly affecting phenylalanine metabolism, and arginine, phenylalanine, tyrosine, and tryptophan biosynthesis in the optic nerve (Fig. 8F; Additional file 1: Data 1).

Taken together, our data support the potential for PQQ as an adjuvant supplement for human retinal diseases. As our study provides strong data for injectable routes, but not for oral routes, further development is required if PQQ is to be properly administered at the target doses orally in humans.

Discussion

RGCs require strict control of ATP content due to their high activity levels. This requires the maintenance of functional mitochondria to provide a continuous supply of ATP predominantly derived from OXPHOS in mitochondria [1, 36]. An imbalance in mitochondrial metabolism results in bioenergetic insufficiency, rendering RGCs susceptible to neurodegeneration. Altered metabolism and mitochondrial dysfunction occur early in the pathogenesis of many retinal diseases such as glaucoma, ADOA, and LHON [2–8]. Improving metabolic and mitochondrial function to increase ATP content has been effective in counteracting RGC damage and reducing the progression of neurodegeneration [7, 37], suggesting the potential of ATP boosters as therapeutic compounds against RGC-related neurodegenerative diseases.

Our data demonstrate that PQQ administration drives an increase in ATP content in vitro in cells isolated from both cortical neurons and RGC-relevant tissues, suggesting that PQQ can be rapidly utilized to enhance the concentration of ATP. Despite similar effects in vitro, in vivo administration of PQQ provided a differential effect on ATP generation in visual system tissues as compared with cortex likely depending on possible differences in drug uptake across blood-retinal barrier as compared with blood–brain barrier [38]. In this respect, while ATP content in the cortex remained unaltered, the ATP-boosting effect of PQQ was consistently obtained in visual system tissues, with a sustained elevation of ATP over 3 days after administration. The potential role of PQQ as a potent inducer of ATP synthesis with durable effects was identified over the whole RGC-trajectory through the visual system including retina containing RGC soma and dendrites, optic nerve containing RGC axons, and superior colliculus containing RGC terminals. Noteworthy, variation in ATP content may not undoubtedly attributed to changes in RGC energetic balance but rather be the result of the integration of neural, glial and vascular cell types in each of the visual system tissues, whose different composition might explain the variability in response and time identified across these tissues. The variability in ATP-boosting effect of PQQ was also demonstrated by differences in its influence on NAD pool, one of the primary factors influencing ATP generation rate of OXPHOS. In this respect, PQQ's effect on ATP generation appeared unrelated with changes in NAD pool in retina and optic nerve, while a significant increment in NAD pool was evident in superior colliculus.

Promoting mitochondrial biogenesis is a key mechanism to bolster OXPHOS and ATP production by modulating the number of functional mitochondria. In previous studies on Hepa1-6, HepG2 and NIH/3T3 cell lines, PQQ has been reported to bolster ATP production by stimulating mitochondrial biogenesis through the activation of PGC-1α, a major transcriptional coactivator of several biogenesis-related factors, among which TFAM plays an important role in mitochondrial DNA replication and repair [18, 19, 39, 40]. However, PQQ effect appears to be cell and system dependent, with different outcomes depending on the cell line and the doses tested [18, 19, 40]. In this respect, our data demonstrated that either mitochondrial content or the expression of *Pgc-1α* and *Tfam* were not altered in visual system tissues following short- or long-term administration of PQQ, thus suggesting that the ATP-boosting effect of PQQ is likely independent of mitochondrial biogenesis mechanisms. On the other hand, the short-term ATP-boosting activity of PQQ was associated with a significant variation in mitochondrial membrane potential, apparently unrelated to a direct effect on OXPHOS complexes activity.

(See figure on next page.)

Fig. 8 Effects of PQQ administration on metabolic profile of non-diseased RGC- related tissues in vivo. **A**, **B** Dendrograms (**A**) and principal component analysis (PCA; **B**) of retinal and optic nerve samples collected from mice treated with either vehicle or a single injection of 20 mg/kg PQQ after 24 h. **C**, **D** Bar chart (**C**) and volcano plots (**D**) indicating respectively the number and the increase/decrease of significantly changed metabolites in retinas and optic nerves from PQQ-treated animals compared to their vehicle-injected controls (FDR < 0.05; red = increased in PQQ, blue = decreased). **E** Euler plot and heatmaps showing commonly changed metabolites across tissues. The red and the blue in the heatmaps indicates respectively the highest and the lowest value by row. **F** KEGG pathway analysis indicating the predicted affected pathways based on the detected changed metabolites in retinas and optic nerves from PQQ-treated mice. Pathways were highlighted in red when FDR < 0.05 and annotated when the impact was high. The size of the points indicates the pathways hits, underlining the number of the metabolites detected within the pathway. n = 10 retinas or optic nerves per group

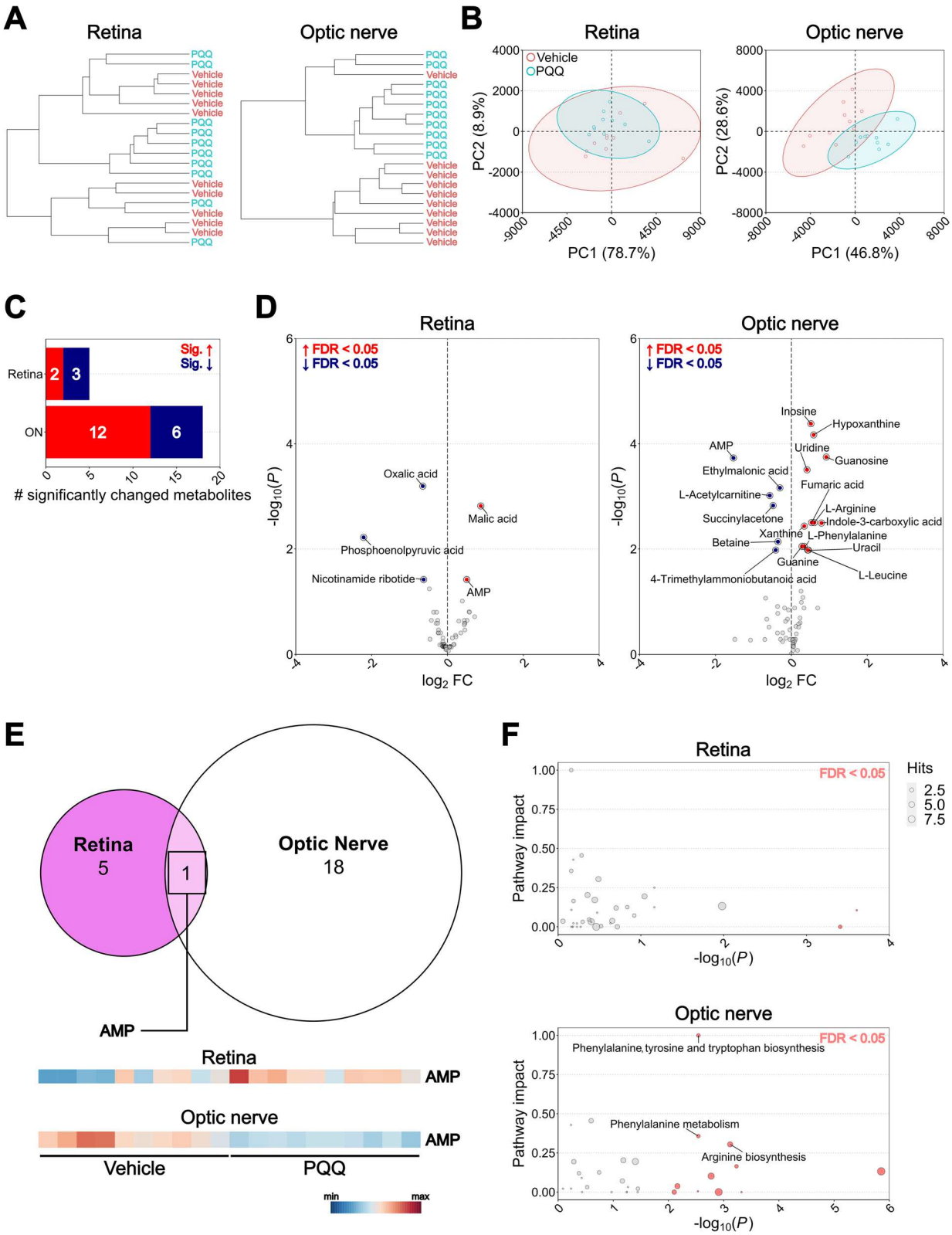

Fig. 8 (See legend on previous page.)

The long-term administration of PQQ resulted in a mild but significant influence on transcription and translation of mitochondrial complex-related markers together with a subtle variation in gross mitochondrial morphology. Taken together, these results suggest that the ATP-boosting activity of PQQ only partially consists in a direct effect on mitochondrial content and function, at least in healthy conditions.

To identify alternative metabolic mechanisms involved in ATP-boosting effects of PQQ, we performed low molecular weight metabolomics in retina and optic nerve. We demonstrated a clear distinction between untreated and PQQ-treated optic nerve, suggesting a PQQ-mediated change in metabolic profile. Pathway analysis predicted impact on phenylalanine metabolism, and arginine, phenylalanine, tyrosine, and tryptophan biosynthesis. Changes in such pathways have also emerged in the metabolome profile of retina and optic nerve after the administration of nicotinamide, another relevant ATP-boosting compound providing strong neuroprotection in the retina via a metabolic mechanism [7]. Most of the metabolites displaying a significant increment following PQQ administration are strictly involved in anaplerotic mechanisms providing substrates to improve local ATP generation by fueling glycolysis or TCA cycle and OXPHOS [41]. In particular, the PQQ-dependent increase of L-arginine and fumarate can be derived from the metabolization of argininosuccinate in a reaction catalyzed by the argininosuccinate lyase [42]. Fumarate supports the activity of the TCA cycle and could contribute to the increased PQQ-mediated ATP content. Fumarate and its derivatives have also been demonstrated to exert antioxidant effects by regulating the activation of antioxidant pathways and resulting in enhanced cytoprotective cellular resistance to free radicals [43, 44]. Similarly, L-arginine may act as precursor of several endogenous polyamines reported to be neuroprotective in neurological and retinal diseases through the regulation of antioxidant, anti-inflammatory and anti-apoptotic mechanisms [45–49]. The antioxidant effects of both metabolites may further influence ATP production. In effect, end products of oxidative stress-induced lipid peroxidation have been reported to alter ATP synthase subunits resulting in impaired enzyme activity with reduced conversion of ADP to ATP and energy depletion [50, 51]. Reducing oxidative stress may therefore indirectly buffer the depletion of ATP under stress, suggesting an additional role of these metabolites in regulating the ATP pool but may not explain an increase in ATP seen in un-stressed systems. Low molecular weight metabolomics also revealed a PQQ-driven increment in L-leucine, a branched-chain amino acid which has multiple functions in the brain involving the metabolism of key neurotransmitters (glutamate), protein synthesis, and energy production [52]. L-leucine has been reported to induce ATP synthesis alone or in combination with other branched-chain amino acids by improving glycolysis and protecting RGCs from degeneration in a model of glaucoma, suggesting a potential metabolic substrate involved in the bioenergetic support of RGCs [53]. In addition to a, likely direct, effect in regulating ATP levels, the metabolism of L-leucine might provide carbon skeletons to increase energy substrates fueling TCA cycle, such as acetyl-CoA, and ketone bodies (acetoacetyl-CoA) synthesis [54]. Ketone bodies in turn may be used by astrocytes, neurons, and oligodendrocytes to further obtain acetyl-CoA under conditions of metabolic stress and glucose deprivation, resulting in improved metabolism, ATP production and RGC protection over stress [55, 56]. Supporting this, a ketogenic diet has been demonstrated to be neuroprotective in an experimental mouse model of glaucoma, with improved RGC survival, ameliorated axonal transport, and reduced gliosis [56]. Glial cells have the capacity to metabolize branched-chain amino acids, and neurons may use these metabolites either in vitro or in vivo under severe mitochondrial dysfunction to replenish TCA pool intermediates, suggesting a likely alternative way to promote metabolism and regulate the local ATP pool [55, 57, 58].

During RGC injury, intracellular ATP seems to initially increase as an early adaptation to sustain the high energy demand generated by the insult, declining gradually over time as the damage persists [59]. RGCs rapidly use ATP to sustain the high cellular activity and axonal transport of proteins required for remodeling and maintenance of cell cytoskeleton under stress, hence requiring a quick ATP turnover to constantly have the necessary metabolic substrate for their functioning [60]. Thus, if ATP synthesis is inadequate in maintaining constant optimal ATP levels under stress, RGC consume most of the ATP pool leading to metabolic exhaustion over time. For this reason, energy-boosting strategies providing RGCs more ATP might be neuroprotective in the context of disease. Supplementation of exogenous ATP in models of RGC injury gave different results under different type of stress. Supporting this, a single supplementation of ATP at either high or low dose in a model of optic nerve crush failed to protect RGCs from death [59]. However, multiple administration of ATP encapsulated in liposomes has been effective in protecting RGC from degeneration in a model of retinal ischemia/reperfusion [61]. The discrepancy in the outcomes might depend on the administration route, the duration of the injury, and the poor stability of ATP which might require multiple supplementations to become effective, raising the question if increasing ATP directly by its exogenous

supplementation is an effective strategy to counteract RGC degeneration. Given its ability to increase local ATP content, PQQ might be a promising compound supplying RGCs with substrates counteracting stress-deriving bioenergetic insufficiency and the resultant neurodegeneration.

We tested the neuroprotective efficacy of PQQ in different models of RGC injury where bioenergetic capacity has been compromised. We initially assessed PQQ neuroprotection using an ex vivo model of retinal axotomy which results in Wallerian degeneration and loss of ATP with significant RGC degeneration 3 days post-axotomy [7, 34, 62, 63]. Our data demonstrated that the administration of PQQ confers RGC neuroprotection in this model, with an effective reduction of RGC cell loss and stress-related features such as nuclear shrinkage. The moderate PQQ neuroprotection reflects the complexity of factors regulating RGC degeneration in this context and might suggest that PQQ protection may act only on some of the neurodegenerative mechanisms in this model (e.g. supplementing ATP but not addressing neuroinflammation or caspase activity) [7, 34, 64]. Considering the ATP-boosting capacity of PQQ demonstrated in healthy conditions, a possible mechanism of PQQ neuroprotection may be ascribed, at least in part, to a likely counteraction of bioenergetic insufficiency through an increased ATP reservoir. To isolate and further investigate the potential contribution of PQQ in reducing RGC stress by regulating neuronal bioenergetic balance, we tested PQQ neuroprotection in a model where impaired bioenergetic capacity represents the principal insult driving RGC death. To test this we used an in vivo model of bioenergetic injury initiated by the inhibition of mitochondrial Complex I bioenergetic injury initiated by the inhibition of mitochondrial Complex I following intravitreal injection of rotenone [35, 65]. Rotenone injection induces acute mitochondrial damage, resulting in ATP depletion and oxidative stress which in turn cause RGC degeneration. This models a typical feature of RGC-specific retinal diseases such as glaucoma and genetic optic atrophies characterized by genetic mutations in mitochondrial-related genes as in the case of ADOA and LHON [2, 5, 6, 8]. The preservation of RGC-density and nuclear diameter resulting from PQQ administration supports the strong neuroprotective efficacy of PQQ. Since in this model RGC viability is strongly related to altered ATP reservoirs and PQQ has an ATP-boosting activity, the neuroprotective effects of PQQ are likely due to an amelioration of cell bioenergetic capacity by supporting ATP levels.

Conclusions

Taken in concert, our data demonstrate that PQQ is neuroprotective in different models of RGC stress. PQQ administration increases local ATP content and alters metabolic profiles in non-diseased visual system tissues. The prominent neuroprotective efficacy of PQQ against RGC damage under a variety of stressors is possibly related to its ATP boosting activity, although a clear correlation would need further investigations. The present findings support a potential role of PQQ as a novel neuroprotective compound used as adjuvant with other current therapies to improve RGC resilience with a low risk of side effects. Although our data demonstrated a negligible effect of short-term oral delivery, the dietary supplementation with PQQ still remains a valid option given the possibility to improve its bioavailability by favoring the mobility across body barriers (e.g. absorption in the gastrointestinal tract and blood–brain barrier permeability) and by designing slow-release formulations. Further studies are needed to identify the optimal dose and delivery system in humans to achieve similar effects in promoting ATP content in health and disease before PQQ could be considered ready for clinical use.

Abbreviations

ADOA	Autosomal dominant optic atrophy
ADP	Adenosine diphosphate
AMP	Adenosine monophosphate
ANOVA	Analysis of variance
ATP	Adenosine triphosphate
ATP5a1	ATP synthase F1 subunit alpha
BSA	Bovine serum albumin
CNS	Central nervous system
CS	Citrate synthase
Cyt C	Cytochrome C
DAPI	4′,6-Diamidino-2-phenylindole
DB	Decylubiquinone
DCPIP	2,6-Dichlorophenolindophenol
DEV	Days ex vivo
DMSO	Dimethyl sulfoxide
DTNB	5,5′-Dithiobis (2-nitrobenzoic acid)
FDR	False discovery rate
GCL	Ganglion cell layer
GFP	Green fluorescent protein
HBSS	Hank's balanced salt solution
HC	Hierarchical clustering
IPL	Inner plexiform layer
KEGG	Kyoto Encyclopedia of Genes and Genomes
LD50	Lethal dose 50
LHON	Leber hereditary optic neuropathy
mt-CO1	Mitochondrially Encoded Cytochrome C Oxidase I
NAD	Nicotinamide adenine dinucleotide
NADH	Nicotinamide adenine dinucleotide + hydrogen (reduced)
NDUFB8	NADH:Ubiquinone Oxidoreductase Subunit B8
NFL	Nerve fiber layer
OD	Optical density
OXPHOS	Oxidative phosphorylation
PBS	Phosphate-buffered saline
PCA	Principal component analysis
PFA	Paraformaldehyde

PGC-1α	Proliferator-activated receptor-gamma coactivator alpha
PQQ	Pyrroloquinoline quinone
RBPMS	RNA-binding protein with multiple splicing
RGC	Retinal ganglion cell
SDHB	Succinate dehydrogenase complex iron sulfur subunit B
TBS	Tris-buffered saline
TCA	Tricarboxylic acid
TFAM	Mitochondrial transcription factor A
TOMM20	Translocase of outer mitochondrial membrane 20
UQCRC2	Ubiquinol-cytochrome c reductase core protein 2
YFP	Yellow fluorescent protein

Supplementary Information

The online version contains supplementary material available at https://doi.org/10.1186/s40478-023-01642-6.

Additional file 1: Dataset 1. Raw mass spectrometry data (area under the curve), weight normalized results, comparisons, and pathway analysis.

Additional file 2: Figure 1. Assessment of PQQ interference on ATP assay in vitro. Luminescence of control samples with PQQ diluted in HBSS (control vehicle) at different concentrations (0.1, 0.5, 1, 5, 10, 50 µM) without cell lysates. n = 3 different replicates per group.

Additional file 3: Figure 2. Supplementary analysis of retinal cell survival in ex vivo and in vivo models of RGC stress. (A, B) Quantification of DAPI positive cell density per 0.01 mm^2 (A) and mean DAPI nuclear diameter (B) in GCL of retinas cultured ex vivo. Retinal explants were cultured in either basic or supplemented media with either 50 or 100 µM PQQ for 3 days ex vivo (DEV). Control retinas (0 DEV) were directly fixed and processed after the dissection. n = 5 (0 DEV), 7 (3 DEV), 4 (3 DEV + 50 µM PQQ), 6 (3 DEV + 100 µM PQQ) retinas. (C, D) Quantification of DAPI positive cell density per 0.01 mm^2 (C) and mean DAPI nuclear diameter (D) in GCL of retinas from animals injected either with DMSO (control) or rotenone and treated with vehicle or 20 mg/kg i.p. PQQ. n = 9 DMSO, 9 DMSO + PQQ, 10 rotenone and 9 rotenone + PQQ retinas. GCL, ganglion cell layer. $*p < 0.05$, $**p < 0.01$ and $***p < 0.001$ versus 0 DEV (explants) or DMSO (rotenone model); $^{\#}p < 0.01$ and $^{\#\#}p < 0.001$ versus 3 DEV (explants) or rotenone (rotenone model).

Additional file 4: Figure 3. Effects of PQQ administration on cell viability in vitro. Evaluation of PQQ cell toxicity in dissociated mouse brain cortical cells incubated with 50 µM PQQ for 2 h. Cells maintained in HBSS for the same time were used as controls. Toxicity was assessed by Trypan blue assay and quantified as the number of cells/mL. n = 3 different cell suspensions from different hemispheres.

Additional file 5: Figure 4. Effects of PQQ administration by drinking water on ATP and NAD levels in visual system tissues in vivo. (A) ATP and (B) NAD content in retina, optic nerve, superior colliculus and brain cortex measured from mice treated with either vehicle or 20 mg/kg PQQ diluted in drinking water after 24 h. n = 6 animals per group. $*p < 0.05$ versus vehicle.

Additional file 6: Figure 5. Effects of PQQ administration on short term transcriptional activation of mitochondrial biogenesis in vivo. (A) mtRNA/nuRNA ratio in whole retinal samples from animals treated with a single i.p. injection of either vehicle or 20 mg/kg PQQ, calculated using the expression of *mt-Co2* and *Rsp18* as mitochondrial and nuclear reference gene, respectively. mtRNA/nuRNA ratio was measured 24, 48 or 72 h after the treatment. (B) *Pgc-1a* and *Tfam* mRNA levels measured in whole retinas from animals injected with either vehicle or 20 mg/kg PQQ after 24, 48 or 72 h. *Rsp18* was used as housekeeping gene. n = 6 vehicle and 7 PQQ retinas for 24 h, 8 vehicle and 7 PQQ retinas for 48 h, 8 vehicle and 7 PQQ retinas for 72 h.

Additional file 7: Figure 6. Full quantified and uncropped representative blots of Western Blot data. (A, B) Full blots of markers of mitochondrial complexes (ATP5a, UQCRC2, mt-CO1, SDHB, NDUFB8; blots on the left) in either retinas (A) or optic nerves (B) from vehicle-or PQQ-treated animals. β-actin was used as loading control after membrane stripping and reprobing (blots on the right). The optical density (OD) of each marker was normalized for the relative OD of the β-actin to provide the quantification reported in Fig. 3G, H. Since total OXPHOS rodent WB antibody cocktail (ab110413, Abcam) used to detect bands recognizes 5 markers contemporarily, two different exposures were performed to obtain the optimal visualization of bands (top = lower exposure; bottom = higher exposure). Black arrows indicate which marker was quantified on each membrane (top = ATP5a, UQCRC2 and SDHB; bottom = mt-CO1 and NDUFB8). Rat heart mitochondrial extract provided by the manufacturer (ab110341, Abcam) was diluted at 1:200 and run as positive control (PC). (C, D) Uncropped membranes of the representative blots shown in Fig. 3G, H.

Additional file 8: Figure 7. Supplementary analysis of retinal gross mitochondrial morphology after PQQ administration in vivo. Individual (violin plots) and averaged (box plots) analysis of reconstructed TOMM20-postive particles in GCL/NFL (A-G) and IPL (H-N) in retinas of mice after long term treatment either with vehicle or PQQ. For individual parameters, a linear mixed effects model was applied to account for the multiple observations that come from the same retina. Individual parameters in GCL/NFL (555 vehicle and 812 PQQ) or in IPL (1318 vehicle and 1361 PQQ) were measured on disconnected TOMM20-positive particles from 7 different retinas per group. n = 7 retinas per group in the averaged graphs. GCL, ganglion cell layer. IPL, inner plexiform layer. NFL, nerve fiber layer.

Additional file 9: Figure 8. Supplementary analysis of RGC-specific retinal mitochondrial morphology after PQQ administration in vivo. Individual (violin plots) and averaged (box plots) analysis of reconstructed MitoV-positive particles in GCL/NFL (A-G) and IPL (H-N) in retinas of MitoV mice after long term treatment either with vehicle or 20 mg/kg PQQ. For individual parameters, a linear mixed effects model was applied to account for the multiple observations that come from the same retina. Individual parameters in GCL/NFL (176 vehicle and 268 PQQ) or in IPL (600 vehicle and 552 PQQ) were measured on disconnected MitoV-positive particles from 7 different retinas per group. n = 7 retinas per group in the averaged graphs. GCL, ganglion cell layer. IPL, inner plexiform layer. NFL, nerve fiber layer.

Additional file 10: Figure 9. Supplementary analysis of general and RGC-specific mitochondrial morphology in optic nerve in vivo. Averaged morphological parameters per sample in TOMM20- (A-E) or MitoV-positive (F-J) particles in optic nerves from MitoV mice treated long term with either vehicle or 20 mg/kg PQQ. n = 8 optic nerves per group. $*p < 0.05$ and $**p < 0.01$ versus vehicle.

Additional file 11: Figure 10. Hierarchical clustering of retinal and optic nerve individual samples based on the metabolic profiles derived from the low molecular weight metabolomics in vivo. Correlation heatmaps representing the hierarchical clustering of individual retinal and optic nerve samples collected from animals treated with a single injection of either vehicle or 20 mg/kg PQQ after 24 h. Heatmaps were created using the Spearman rank correlation on Metaboanalyst 5.0 platform (red = highest correlation, blue = lowest correlation). n = 10 retinas or optic nerves per group.

Acknowledgements

The authors would like to thank St. Erik Eye Hospital for financial support for research space and facilities, the staff at the Division of Eye and Vision's animal facility for their assistance in animal breeding and husbandry, and the Swedish Metabolomics Centre for metabolomics data generation.

Author contributions

AC—designed and performed experiments, analyzed data, wrote the manuscript; JRT—designed experiments, analyzed data, wrote the manuscript; MJ—performed experiments; DYW—performed experiments; RA—designed experiments, wrote the manuscript; IAT—designed experiments, wrote the manuscript; MDM—designed experiments, wrote the manuscript; PAW—conceived and designed experiments, analyzed data, wrote the manuscript. All authors read and approved the final manuscript.

Funding

Open access funding provided by Karolinska Institute. PAW is supported by Karolinska Institutet in the form of a Board of Research Faculty Funded Career

Position, by St. Erik Eye Hospital philanthropic donations, and Vetenskapsrådet 2018-02124 and 2022-00799. PAW is an Alcon Research Institute Young Investigator. IAT was supported by NHMRC grant GNT1159795. MDM is supported by a grant from the Italian Ministry of University and Research to the Department of Biology of the University of Pisa under the Department of Excellence 2023-2027 initiative, and by intramural funds of the University of Pisa.

Availability of data and materials
All data generated or analyzed during this study are included in this published article [and its supplementary information files].

Declarations

Ethics approval and consent to participate
All breeding and experimental procedures were undertaken in accordance with the Association for Research for Vision and Ophthalmology Statement for the Use of Animals in Ophthalmic and Research. Individual study protocols were approved by Stockholm's Committee for Ethical Animal Research (10389-2018).

Consent for publication
Not applicable.

Competing interests
The authors declare that they have no competing interests.

Received: 7 July 2023 Accepted: 23 August 2023
Published online: 08 September 2023

References

1. Casson RJ, Chidlow G, Crowston JG, Williams PA, Wood JPM (2021) Retinal energy metabolism in health and glaucoma. Prog Retin Eye Res 81:100881. https://doi.org/10.1016/j.preteyeres.2020.100881
2. Carelli V, Ross-Cisneros FN, Sadun AA (2004) Mitochondrial dysfunction as a cause of optic neuropathies. Prog Retin Eye Res 23(1):53–89. https://doi.org/10.1016/j.preteyeres.2003.10.003
3. Chao de la Barca JM, Simard G, Amati-Bonneau P, Safiedeen Z, Prunier-Mirebeau D, Chupin S, Gadras C, Tessier L, Gueguen N, Chevrollier A, Desquiret-Dumas V, Ferré M, Bris C, Kouassi Nzoughet J, Bocca C, Leruez S, Verny C, Miléa D, Bonneau D, Lenaers G, Martinez MC, Procaccio V, Reynier P (2016) The metabolomic signature of Leber's hereditary optic neuropathy reveals endoplasmic reticulum stress. Brain 139(11):2864–2876. https://doi.org/10.1093/brain/aww222
4. Chao de la Barca JM, Simard G, Sarzi E, Chaumette T, Rousseau G, Chupin S, Gadras C, Tessier L, Ferré M, Chevrollier A, Desquiret-Dumas V, Gueguen N, Leruez S, Verny C, Miléa D, Bonneau D, Amati-Bonneau P, Procaccio V, Hamel C, Lenaers G, Reynier P, Prunier-Mirebeau D (2017) Targeted metabolomics reveals early dominant optic atrophy signature in optic nerves of Opa1delTTAG/+ mice. Invest Ophthalmol Vis Sci 58(2):812–820. https://doi.org/10.1167/iovs.16-21116
5. Williams PA, Harder JM, Foxworth NE, Cochran KE, Philip VM, Porciatti V, Smithies O, John SW (2017) Vitamin B3 modulates mitochondrial vulnerability and prevents glaucoma in aged mice. Science 355(6326):756–760. https://doi.org/10.1126/science.aal0092
6. Tribble JR, Vasalauskaite A, Redmond T, Young RD, Hassan S, Fautsch MP, Sengpiel F, Williams PA, Morgan JE (2019) Midget retinal ganglion cell dendritic and mitochondrial degeneration is an early feature of human glaucoma. Brain Commun 1(1):fcz035. https://doi.org/10.1093/braincomms/fcz035
7. Tribble JR, Otmani A, Sun S, Ellis SA, Cimaglia G, Vohra R, Jöe M, Lardner E, Venkataraman AP, Domínguez-Vicent A, Kokkali E, Rho S, Jóhannesson G, Burgess RW, Fuerst PG, Brautaset R, Kolko M, Morgan JE, Crowston JG, Votruba M, Williams PA (2021) Nicotinamide provides neuroprotection in glaucoma by protecting against mitochondrial and metabolic dysfunction. Redox Biol 43:101988. https://doi.org/10.1016/j.redox.2021.101988
8. Strachan EL, Mac White-Begg D, Crean J, Reynolds AL, Kennedy BN, O'Sullivan NC (2021) The role of mitochondria in optic atrophy with autosomal inheritance. Front Neurosci 15:784987. https://doi.org/10.3389/fnins.2021.784987
9. Lopez Sanchez MI, Crowston JG, Mackey DA, Trounce IA (2016) Emerging mitochondrial therapeutic targets in optic neuropathies. Pharmacol Ther 165:132–152. https://doi.org/10.1016/j.pharmthera.2016.06.004
10. Hauge JG (1964) Glucose dehydrogenase of *Bacterium anitratum*: an enzyme with a Novel Prosthetic Group. J Biol Chem 239:3630–3639. https://doi.org/10.1016/S0021-9258(18)91183-X
11. Steinberg FM, Gershwin ME, Rucker RB (1994) Dietary pyrroloquinoline quinone: growth and immune response in BALB/c mice. J Nutr 124(5):744–753. https://doi.org/10.1093/jn/124.5.744
12. Steinberg F, Stites TE, Anderson P, Storms D, Chan I, Eghbali S, Rucker R (2003) Pyrroloquinoline quinone improves growth and reproductive performance in mice fed chemically defined diets. Exp Biol Med (Maywood) 228(2):160–166. https://doi.org/10.1177/153537020322800205
13. Kumazawa T, Sato K, Seno H, Ishii A, Suzuki O (1995) Levels of pyrroloquinoline quinone in various foods. Biochem J 307(Pt 2):331–333. https://doi.org/10.1042/bj3070331
14. Nakano M, Takahashi H, Koura S, Chung C, Tafazoli S, Roberts A (2014) Acute and subchronic toxicity studies of pyrroloquinoline quinone (PQQ) disodium salt (BioPQQ™) in rats. Regul Toxicol Pharmacol 70(1):107–121. https://doi.org/10.1016/j.yrtph.2014.06.024
15. Akagawa M, Minematsu K, Shibata T, Kondo T, Ishii T, Uchida K (2016) Identification of lactate dehydrogenase as a mammalian pyrroloquinoline quinone (PQQ)-binding protein. Sci Rep 6:26723. https://doi.org/10.1038/srep26723
16. Jonscher KR, Chowanadisai W, Rucker RB (2021) Pyrroloquinoline-quinone is more than an antioxidant: a vitamin-like accessory factor important in health and disease prevention. Biomolecules 11(10):1441. https://doi.org/10.3390/biom11101441
17. Ebeling MC, Polanco JR, Qu J, Tu C, Montezuma SR, Ferrington DA (2020) Improving retinal mitochondrial function as a treatment for age-related macular degeneration. Redox Biol 34:101552. https://doi.org/10.1016/j.redox.2020.101552
18. Chowanadisai W, Bauerly KA, Tchaparian E, Wong A, Cortopassi GA, Rucker RB (2010) Pyrroloquinoline quinone stimulates mitochondrial biogenesis through cAMP response element-binding protein phosphorylation and increased PGC-1alpha expression. J Biol Chem 285(1):142–152. https://doi.org/10.1074/jbc.M109.030130
19. Saihara K, Kamikubo R, Ikemoto K, Uchida K, Akagawa M (2017) Pyrroloquinoline quinone, a redox-active o-Quinone, stimulates mitochondrial biogenesis by activating the SIRT1/PGC-1α signaling pathway. Biochemistry 56(50):6615–6625. https://doi.org/10.1021/acs.biochem.7b01185
20. Zhang Y, Feustel PJ, Kimelberg HK (2006) Neuroprotection by pyrroloquinoline quinone (PQQ) in reversible middle cerebral artery occlusion in the adult rat. Brain Res 1094(1):200–206. https://doi.org/10.1016/j.brainres.2006.03.111
21. Zhang L, Liu J, Cheng C, Yuan Y, Yu B, Shen A, Yan M (2012) The neuroprotective effect of pyrroloquinoline quinone on traumatic brain injury. J Neurotrauma 29(5):851–864. https://doi.org/10.1089/neu.2011.1882
22. Zhang Q, Chen S, Yu S, Qin J, Zhang J, Cheng Q, Ke K, Ding F (2016) Neuroprotective effects of pyrroloquinoline quinone against rotenone injury in primary cultured midbrain neurons and in a rat model of Parkinson's disease. Neuropharmacology 108:238–251. https://doi.org/10.1016/j.neuropharm.2016.04.025
23. Sawmiller D, Li S, Mori T, Habib A, Rongo D, Delic V, Bradshaw PC, Shytle RD, Sanberg C, Bickford P, Tan J (2017) Beneficial effects of a pyrroloquinolinequinone-containing dietary formulation on motor deficiency, cognitive decline and mitochondrial dysfunction in a mouse model of Alzheimer's disease. Heliyon 3(4):e00279. https://doi.org/10.1016/j.heliyon.2017.e00279
24. Sivandzade F, Bhalerao A, Cucullo L (2019) Analysis of the mitochondrial membrane potential using the cationic JC-1 dye as a sensitive fluorescent probe. Bio Protoc 9(1):e3128. https://doi.org/10.21769/BioProtoc.3128
25. Van Bergen NJ, Blake RE, Crowston JG, Trounce IA (2014) Oxidative phosphorylation measurement in cell lines and tissues. Mitochondrion. https://doi.org/10.1016/j.mito.2014.03.003
26. Spinazzi M, Casarin A, Pertegato V, Salviati L, Angelini C (2012) Assessment of mitochondrial respiratory chain enzymatic activities on tissues

and cultured cells. Nat Protoc 7(6):1235–1246. https://doi.org/10.1038/nprot.2012.058
27. Quiros PM, Goyal A, Jha P, Auwerx J (2017) Analysis of mtDNA/nDNA ratio in mice. Curr Protoc Mouse Biol 7(1):47–54. https://doi.org/10.1002/cpmo.21
28. Xia J, Psychogios N, Young N, Wishart DS (2009) MetaboAnalyst: a web server for metabolomic data analysis and interpretation. Nucleic Acids Res 37(Web Server issue):W652-660. https://doi.org/10.1093/nar/gkp356
29. Xia J, Wishart DS (2011) Web-based inference of biological patterns, functions and pathways from metabolomic data using MetaboAnalyst. Nat Protoc 6(6):743–760. https://doi.org/10.1038/nprot.2011.319
30. van den Berg RA, Hoefsloot HC, Westerhuis JA, Smilde AK, van der Werf MJ (2006) Centering, scaling, and transformations: improving the biological information content of metabolomics data. BMC Genom 7:142. https://doi.org/10.1186/1471-2164-7-142
31. Bates DM, Mächler M, Bolker B, Walker S (2015) Fitting linear mixed-effects models using lme4. J Stat Softw 67(1):48. https://doi.org/10.18637/jss.v067.i01
32. Wilson MD, Sethi S, Lein PJ, Keil KP (2017) Valid statistical approaches for analyzing sholl data: mixed effects versus simple linear models. J Neurosci Methods 279:33–43. https://doi.org/10.1016/j.jneumeth.2017.01.003
33. Tribble JR, Kokkali E, Otmani A, Plastino F, Lardner E, Vohra R, Kolko M, André H, Morgan JE, Williams PA (2021) When is a control not a control? Reactive microglia occur throughout the control contralateral pathway of retinal ganglion cell projections in experimental glaucoma. Transl Vis Sci Technol 10(1):22. https://doi.org/10.1167/tvst.10.1.22
34. Enz TJ, Tribble JR, Williams PA (2021) Comparison of glaucoma-relevant transcriptomic datasets identifies novel drug targets for retinal ganglion cell neuroprotection. J Clin Med 10(17):3938. https://doi.org/10.3390/jcm10173938
35. Zhang X, Jones D, Gonzalez-Lima F (2006) Neurodegeneration produced by rotenone in the mouse retina: a potential model to investigate environmental pesticide contributions to neurodegenerative diseases. J Toxicol Environ Health A 69(18):1681–1697. https://doi.org/10.1080/15287390600630203
36. Muench NA, Patel S, Maes ME, Donahue RJ, Ikeda A, Nickells RW (2021) The influence of mitochondrial dynamics and function on retinal ganglion cell susceptibility in optic nerve disease. Cells 10(7):1593. https://doi.org/10.3390/cells10071593
37. Harun-Or-Rashid M, Pappenhagen N, Zubricky R, Coughlin L, Jassim AH, Inman DM (2020) MCT2 overexpression rescues metabolic vulnerability and protects retinal ganglion cells in two models of glaucoma. Neurobiol Dis 141:104944. https://doi.org/10.1016/j.nbd.2020.104944
38. Toda R, Kawazu K, Oyabu M, Miyazaki T, Kiuchi Y (2011) Comparison of drug permeabilities across the blood–retinal barrier, blood–aqueous humor barrier, and blood–brain barrier. J Pharm Sci 100(9):3904–3911. https://doi.org/10.1002/jps.22610
39. Jornayvaz FR, Shulman GI (2010) Regulation of mitochondrial biogenesis. Essays Biochem 47:69–84. https://doi.org/10.1042/bse0470069
40. Zhang J, Meruvu S, Bedi YS, Chau J, Arguelles A, Rucker R, Choudhury M (2015) Pyrroloquinoline quinone increases the expression and activity of Sirt1 and -3 genes in HepG2 cells. Nutr Res 35(9):844–849. https://doi.org/10.1016/j.nutres.2015.06.014
41. Owen OE, Kalhan SC, Hanson RW (2002) The key role of anaplerosis and cataplerosis for citric acid cycle function. J Biol Chem 277(34):30409–30412. https://doi.org/10.1074/jbc.R200006200
42. Morris SM Jr (2002) Regulation of enzymes of the urea cycle and arginine metabolism. Annu Rev Nutr 22:87–105. https://doi.org/10.1146/annurev.nutr.22.110801.140547
43. Linker RA, Lee DH, Ryan S, van Dam AM, Conrad R, Bista P, Zeng W, Hronowsky X, Buko A, Chollate S, Ellrichmann G, Brück W, Dawson K, Goelz S, Wiese S, Scannevin RH, Lukashev M, Gold R (2011) Fumaric acid esters exert neuroprotective effects in neuroinflammation via activation of the Nrf2 antioxidant pathway. Brain 134(Pt 3):678–692. https://doi.org/10.1093/brain/awq386
44. Ashrafian H, Czibik G, Bellahcene M, Aksentijević D, Smith AC, Mitchell SJ, Dodd MS, Kirwan J, Byrne JJ, Ludwig C, Isackson H, Yavari A, Støttrup NB, Contractor H, Cahill TJ, Sahgal N, Ball DR, Birkler RI, Hargreaves I, Tennant DA, Land J, Lygate CA, Johannsen M, Kharbanda RK, Neubauer S, Redwood C, de Cabo R, Ahmet I, Talan M, Günther UL, Robinson AJ, Viant MR, Pollard PJ, Tyler DJ, Watkins H (2012) Fumarate is cardioprotective via activation of the Nrf2 antioxidant pathway. Cell Metab 15(3):361–371. https://doi.org/10.1016/j.cmet.2012.01.017
45. Hong S, Lee JE, Kim CY, Seong GJ (2007) Agmatine protects retinal ganglion cells from hypoxia-induced apoptosis in transformed rat retinal ganglion cell line. BMC Neurosci 8:81. https://doi.org/10.1186/1471-2202-8-81
46. Hong S, Kim CY, Lee JE, Seong GJ (2009) Agmatine protects cultured retinal ganglion cells from tumor necrosis factor-alpha-induced apoptosis. Life Sci 84(1–2):28–32. https://doi.org/10.1016/j.lfs.2008.10.006
47. Dastan A, Kocer I, Erdogan F, Ates O, Kiziltunc A (2009) Agmatine as retinal protection from ischemia-reperfusion injury in guinea pigs. Jpn J Ophthalmol 53(3):219–224. https://doi.org/10.1007/s10384-009-0660-0
48. Xu W, Gao L, Li T, Shao A, Zhang J (2018) Neuroprotective role of agmatine in neurological diseases. Curr Neuropharmacol 16(9):1296–1305. https://doi.org/10.2174/1570159X15666170808120633
49. Abo El Gheit RE, Soliman NA, Badawi GA, Madi NM, El-Saka MH, Badr SM, Emam MN (2021) Retinoprotective effect of agmatine in streptozotocin-induced diabetic rat model: avenues for vascular and neuronal protection: Agmatine in diabetic retinopathy. J Physiol Biochem 77(2):305–320. https://doi.org/10.1007/s13105-021-00799-9
50. Hartl D, Schuldt V, Forler S, Zabel C, Klose J, Rohe M (2012) Presymptomatic alterations in energy metabolism and oxidative stress in the APP23 mouse model of Alzheimer disease. J Proteome Res 11(6):3295–3304. https://doi.org/10.1021/pr300021e
51. Ebanks B, Chakrabarti L (2022) Mitochondrial ATP synthase is a target of oxidative stress in neurodegenerative diseases. Front Mol Biosci 9:854321. https://doi.org/10.3389/fmolb.2022.854321
52. Fernstrom JD (2005) Branched-chain amino acids and brain function. J Nutr 135(6 Suppl):1539S-1546S. https://doi.org/10.1093/jn/135.6.1539S
53. Hasegawa T, Ikeda HO, Iwai S, Muraoka Y, Tsuruyama T, Okamoto-Furuta K, Kohda H, Kakizuka A, Yoshimura N (2018) Branched chain amino acids attenuate major pathologies in mouse models of retinal degeneration and glaucoma. Heliyon 4(2):e00544. https://doi.org/10.1016/j.heliyon.2018.e00544
54. Murín R, Hamprecht B (2008) Metabolic and regulatory roles of leucine in neural cells. Neurochem Res 33(2):279–284. https://doi.org/10.1007/s11064-007-9444-4
55. Edmond J, Robbins RA, Bergstrom JD, Cole RA, de Vellis J (1987) Capacity for substrate utilization in oxidative metabolism by neurons, astrocytes, and oligodendrocytes from developing brain in primary culture. J Neurosci Res 18(4):551–561. https://doi.org/10.1002/jnr.490180407
56. Harun-Or-Rashid M, Pappenhagen N, Palmer PG, Smith MA, Gevorgyan V, Wilson GN, Crish SD, Inman DM (2018) Structural and functional rescue of chronic metabolically stressed optic nerves through respiration. J Neurosci 38(22):5122–5139. https://doi.org/10.1523/JNEUROSCI.3652-17.2018
57. Motori E, Atanassov I, Kochan SMV, Folz-Donahue K, Sakthivelu V, Giavalisco P, Toni N, Puyal J, Larsson NG (2020) Neuronal metabolic rewiring promotes resilience to neurodegeneration caused by mitochondrial dysfunction. Sci Adv. 6(35):eaba8271. https://doi.org/10.1126/sciadv.aba8271
58. Salcedo C, Andersen JV, Vinten KT, Pinborg LH, Waagepetersen HS, Freude KK, Aldana BI (2021) Functional metabolic mapping reveals highly active branched-chain amino acid metabolism in human astrocytes, which is impaired in iPSC-derived astrocytes in Alzheimer's disease. Front Aging Neurosci 13:736580. https://doi.org/10.3389/fnagi.2021.736580
59. Zhu J, Li P, Zhou YG, Ye J (2020) Altered energy metabolism during early optic nerve crush injury: implications of Warburg-like aerobic glycolysis in facilitating retinal ganglion cell survival. Neurosci Bull 36(7):761–777. https://doi.org/10.1007/s12264-020-00490-x
60. Calkins DJ (2021) Adaptive responses to neurodegenerative stress in glaucoma. Prog Retin Eye Res 84:100953. https://doi.org/10.1016/j.preteyeres.2021.100953
61. Dvoriantchikova G, Barakat DJ, Hernandez E, Shestopalov VI, Ivanov D (2010) Liposome-delivered ATP effectively protects the retina against ischemia-reperfusion injury. Mol Vis 16:2882–2890
62. Howell GR, Libby RT, Jakobs TC, Smith RS, Phalan FC, Barter JW, Barbay JM, Marchant JK, Mahesh N, Porciatti V, Whitmore AV, Masland RH, John SW (2007) Axons of retinal ganglion cells are insulted in the optic

nerve early in DBA/2J glaucoma. J Cell Biol 179(7):1523–1537. https://doi.org/10.1083/jcb.200706181
63. Maddineni P, Kasetti RB, Patel PD, Millar JC, Kiehlbauch C, Clark AF, Zode GS (2020) CNS axonal degeneration and transport deficits at the optic nerve head precede structural and functional loss of retinal ganglion cells in a mouse model of glaucoma. Mol Neurodegener 15(1):48. https://doi.org/10.1186/s13024-020-00400-9
64. Tribble JR, Kastanaki E, Uslular AB, Rutigliani C, Enz TJ, Williams PA (2022) Valproic acid reduces neuroinflammation to provide retinal ganglion cell neuroprotection in the retina axotomy model. Front Cell Dev Biol 10:903436. https://doi.org/10.3389/fcell.2022.903436
65. Sasaoka M, Ota T, Kageyama M (2020) Rotenone-induced inner retinal degeneration via presynaptic activation of voltage-dependent sodium and L-type calcium channels in rats. Sci Rep 10(1):969. https://doi.org/10.1038/s41598-020-57638-y

Publisher's Note